Universidade de Aveiro
2023

RICARDO SAMPAIO OLIVEIRA

CABEÇO DE VIDE (CDV) SERPENTINES AND THEIR IMPLICATIONS FOR MARS

SERPENTINAS DE CABEÇO DE VIDE (CDV) E AS SUAS IMPLICAÇÕES EM MARTE

Universidade de Aveiro
2023

RICARDO SAMPAIO OLIVEIRA

CABEÇO DE VIDE (CDV) SERPENTINES AND THEIR IMPLICATIONS FOR MARS

SERPENTINAS DE CABEÇO DE VIDE (CDV) E AS SUAS IMPLICAÇÕES EM MARTE

Dissertação apresentada à Universidade de Aveiro para cumprimento dos requisitos necessários à obtenção do grau de Mestre em Engenharia Geológica, realizada sob a orientação científica da Doutora Slavka Carvalho Andrejkovičová, Investigadora Principal do Departamento de Geociências da Universidade de Aveiro, e sob coorientação do Doutor Fernando Joaquim Fernandes Tavares Rocha, Professor Catedrático do Departamento de Geociências da Universidade de Aveiro.

o júri

Presidente	Prof. Doutora Carla Alexandra de Figueiredo Patinha Professora Auxiliar da Universidade de Aveiro
Orientador	Doutora Slavka Carvalho Andrejkovičová Investigadora Principal da Universidade de Aveiro
Arguente	Prof. Doutor José Manuel Vaz Velho Barbosa Marques Professor Associado com Agregação do Instituto Superior Técnico da Universidade de Lisboa

agradecimentos

Não faria sentido iniciar os agradecimentos sem deixar um agradecimento especial a quem um simples "obrigado" nunca chegará. Aos meus pais, irmã e família, por todo o apoio e amor desde o primeiro dia da minha vida, por me permitirem estar nesta fase e nesta posição neste momento, e por estarem sempre presentes. Vocês foram, são e serão sempre uma das minhas maiores motivações. Esta é para vocês.

À minha Bruna, que nunca me deixa baixar os braços, que está sempre comigo, e que nunca me deixa cair. Nunca descansaste enquanto eu não desse o melhor de mim. Obrigado por todo o amor, carinho, por tudo, e por tudo o que ainda temos para viver.

Um sincero agradecimento, à Doutora Slavka Carvalho Andrejkovičová, orientadora, por todo o carinho, disponibilidade e incentivo demonstrados desde o primeiro dia. São poucas as palavras que conseguem descrever a sua mente criativa e científica. Encerro este capítulo da minha vida com um enorme sentimento de admiração por si e pelo enorme ser humano que você é. Estarei eternamente grato por toda a experiência e conhecimento compartilhado, por todas as aventuras vividas, pelo seu trabalho e, acima de tudo, por a ter conhecido.

Ao Professor Doutor Fernando Joaquim Fernandes Tavares Rocha, coorientador, por todas as conversas, disponibilidade, e pela forma sempre cativante em como consegue transmitir todo o seu conhecimento. Sem a sua ajuda, boa disposição e as suas ideias nada disto teria sido possível.

À Engenheira Denise Terroso, por todo o conhecimento partilhado, pela ajuda na realização de ensaios, na análise dos mesmos e em tudo o resto, e acima de tudo, pela constante força, motivação e amizade criada ao longo destes anos.

À Engenheira Cristina Sequeira, pela ajuda na realização de ensaios no seu laboratório, por toda a simpatia, disponibilidade e pela amizade criada.

Às "Biology girls": Doutora Inês Macário e Mestre Telma Veloso, pela vossa disponibilidade, pela partilha de conhecimento e pela vossa ajuda em algo completamente novo e inovador. Foram sempre incansáveis na procura de soluções e foi um gosto aprender e conviver com vocês.

À Junta de Freguesia de Cabeço de Vide e às Termas da Sulfúrea por toda a disponibilidade, ajuda e colaboração.

Ao Professor Doutor José Manuel Marques, por toda a disponibilidade, colaboração, simpatia e boa disposição na recolha e análise de amostras.

A todos os meus colegas e amigos que tornaram tudo possível, os momentos que vivemos durante estes anos nunca serão apagados da minha memória e será um orgulho relembrá-los mais tarde. A vocês, que sabem quem são, um sinceríssimo obrigado.

Ao Departamento de Geociências da Universidade de Aveiro e às suas pessoas, incluindo corpo técnico, docente e de investigação, que de certa forma contribuíram para a minha evolução académica, pessoal e profissional.

Obrigado a todos.

palavras-chave

Serpentinização; Alteração Hidrotermal; Geology; Cabeço de Vide (CdV); Análogo; Marte; Jezero Crater.

resumo

Serpentinas representam um grupo de minerais hidratados ricos em magnésio que se formam através de um processo geológico denominado serpentinização. Derivam, geralmente, da alteração de um determinado tipo de rocha, particularmente as rochas ultramáficas, na presença de água no estado líquido. Serpentinas têm uma importância significativa no estudo de vida em Marte, devido à sua capacidade de fornecer evidências de atividade antiga que envolve água, oferecem possíveis condições para vida microbiana, preservam compostos orgânicos e bio assinaturas, e guiam possíveis futuras explorações e missões de recuperação de amostras. Entender de forma detalhada a relevância das serpentinas no contexto geológico e astrobiológico de Marte é crucial para perceber e desvendar os mistérios que existem em relação à possível existência de vida no planeta Vermelho.

Tendo em conta a sua acessibilidade e serpentinização ativa, o complexo hidrotermal máfico/ultramáfico de Cabeço de Vide (CdV), Portugal, representa uma oportunidade única para a investigação de rochas na Terra com serpentinização continental, dando ênfase ao facto dos ultramáficos de CdV não serem ofiolitos, mas sim associados à intrusão de um plutão máfico/ultramáfico (Rocha et al., 2017; Marques et al., 2008, 2018). Neste contexto, CdV é proposto como um ambiente mineralógico excelente para estudo como análogo de Marte, especialmente considerando as deteções de serpentinas no local de aterragem da missão Mars 2020 (Perseverance), Jezero Crater.

Esta dissertação tem como principais objetivos o estudo detalhado das rochas ultramáficas de Cabeço de Vide, especificamente do furo AC2, no que toca a características texturais e mineralógicas, assim como a caracterização das águas recolhidas da ribeira, fontes e furos na área de estudo, de forma a entender os processos de interação água-rocha que ocorrem em profundidade. De forma a obter tais resultados, técnicas como difração de raios-X (XRD), fluorescência de raios-X (XRF), espetroscopia de reflectância total atenuada de infravermelho por transformada de Fourier (ATR-FTIR) e microscopia eletrónica de varrimento (SEM) foram utilizadas, que vão fornecer uma base de dados detalhada das características dos minerais que compõem as rochas ultramáficas e os seus derivativos serpentinizados, que representam vários graus e etapas de serpentinização. Toda esta informação será bastante útil para registar a evolução composicional nos minerais durante o processo de serpentinização, assim como fornecer um contexto maior nas serpentinas em Terra como uma abordagem importante para perceber em detalhe os processos geológicos em Marte.

Os resultados obtidos confirmaram a importância das interações rocha-água que ocorrem em profundidade em Cabeço de Vide, enquanto corroboram toda a informação que enfatiza as semelhanças litológicas entre a área de estudo e Jezero Crater, Marte, através da identificação de carbonatos, esmectites, serpentinas, óxidos de ferro, entre outros. Com a presente dissertação, conclui-se que o complexo hidrotermal máfico-ultramáfico de Cabeço de Vide e as suas serpentinas enfatizam a importância do estudo e completa compreensão do papel dos processos de serpentinização no estudo de potencial vida microbiana.

keywords

Serpentinization, Hydrothermal Alteration, Geology, Cabeço de Vide (CdV), Analog, Mars, Jezero Crater.

abstract

Serpentines are a group of hydrous magnesium-rich silicate minerals that are formed through a geological process called serpentinization. They are typically derived from the alteration of certain types of rocks, particularly ultramafic rocks, in the presence of liquid water. Serpentines hold significant importance for the study of life on Mars as they provide evidence of past water activity, offer potentially habitable environments for microbial life, preserve organic compounds and biosignatures, and guide future exploration and sample return missions. Understanding the role of serpentines in the Martian geological and astrobiological context is crucial for unraveling the mysteries surrounding the potential existence of life on the Red Planet.

Because of its accessibility and active serpentinization, the hydrothermally altered mafic-ultramafic complex from Cabeço de Vide (CdV), Portugal, provides a unique opportunity for the investigation and study of continental serpentinized rocks on Earth, emphasizing the fact that CdV ultramafics are not ophiolites, but associated with the intrusion of a mafic/ultramafic pluton (Rocha et al., 2017; Marques et al., 2008, 2018). In this context, CdV is proposed as an excellent mineralogical environment to study as a Mars analog, especially as serpentine detections have been reported at the selected Mars 2020 (Perseverance) rover landing site, Jezero Crater.

The two fundamental objectives within this document are a more detailed study of the CdV ultramafic rocks, specifically from drill core AC2, in what concerns textural and mineralogical features, and the characterization of waters collected from streams, springs and boreholes in the study area, in order to fully understand the water-rock interaction process occurring at depth. To achieve such results, techniques like X-Ray Diffraction (XRD), X-Ray Fluorescence (XRF), Attenuated Total Reflectance Fourier-transform infrared spectroscopy (ATR-FTIR), and Scanning Electron Microscopy (SEM) were used, which will provide a detailed database concerning the compositional features of the minerals making up the ultramafic rocks and their serpentinized derivatives exhibiting variable degrees of serpentinization. Such information will be of great usefulness to record compositional evolution in minerals during the serpentinization process, as well as providing a greater context on the serpentine bodies on Earth as an important approach to understand geochemical processes on Mars.

The results obtained confirmed the importance of water/rock interactions occurring at depth in Cabeço de Vide, while corroborating all the information that emphasizes the lithological similarities between the study area and Jezero Crater, with the identification of carbonates, smectites, serpentines, iron oxides, and others. This thesis concludes that the Cabeço de Vide mafic-ultramafic hydrothermal complex and its serpentines emphasize the importance of studying and fully understanding the role of serpentinization processes in the study of potential microbial life.

Contents

List of Figures

List of Tables

List of Acronyms

Al – Aluminium
Atg – Antigorite
Amp – Amphibole
ATR - FTIR – Attenuated Total Reflectance Fourier-transform Infrared Spectrometry
C – Carbon
Ca – Calcium
Cal – Calcite
CdV – Cabeço de Vide
CH_4 – Methane
Chl – Chlorite
CO_2 – Carbon Dioxide
Cr – Cromium
Crl – Chrysotile
CRISM – Compact Reconnaissance Imaging Spectrometer for Mars
Fe – Iron
Fsp – Feldspar
H – Hydrogen Atom
H_2 – Hydrogen Molecule
H_20 – Water
Hbl – Hornblende
ICP-MS – Inductively Coupled Plasma Mass Spectrometry
K – Potassium
K-Fs – K-Feldspar
Lz – Lizardite
LIBS – Laser Induced Breakdown Spectroscopy
LOI – Loss on Ignition
Mag. – Magnification
Mag-Mgh – Magnetite-Maghemite
MAVEN – Mars Atmosphere and Volatile Evolution
Mca – Mica
Mg – Magnesium
Mn – Manganese
MRO – Mars Reconnaissance Orbiter
MSL – Mars Science Laboratory
N.d. – Not detected.
Ni – Nickel
O – Oxygen
Phl – Phlogopite
Prh – Prehnite
Rt – Rutile
SAM – Sample Analysis on Mars
SEM – Scanning Electron Microscope
Si – Silica
Sme – Smectite
Srp – Serpentine
Ti – Titanium
Tlc – Talc
UV – Ultraviolet
XRD – X-Ray Diffraction
XRF – X-Ray Fluorescence
Zn – Zinc

1. Introduction

Studying life on Earth unravels the complex processes that led to the emergence and evolution of life on our own planet. This knowledge is fundamental to help us explore the possibility of life arising elsewhere in the universe and further understand the conditions required for its existence. The existence of planets outside our solar system (Mayor and Queloz, 1995) and the existence of low-temperature hydrothermal fields, two fundamental discoveries made between 1995 and 2001, revealed to launch research efforts in serpentinization processes that are now recognized as one if not the most important metamorphic hydration reactions for explanations of the origin of life (Holm et al., 2015). Ever since the unique physical and chemical environments on Earth relative to other planets of our solar system have been acknowledged, we – humans – have been questioning whether there are similar conditions in other stellar systems of the universe (Müntener, 2010).

Studying life outside the planet we currently live on holds significant importance, showing profound scientific, philosophical and societal implications, expanding our understanding of the universe, our origins, and our place within it. It drives scientific progress, fosters innovation, and ignites our collective imagination. By studying life on other planets, we can gain insights into the origins of life itself. If life is found elsewhere, it would provide evidence that life can effectively emerge under different conditions and increase our understanding of the processes that lead to the development of life forms. It also helps to gain insights about what can be our next chapter, where scientists can identify habitable zones, explore the potential for life beyond earth and assess the presence of water or organic molecules by studying the environments of other celestial bodies such as exoplanets or moons (Steele et al., 2022). Investigating life on other planets can provide insights into the potential diversity of life forms. Understanding different biological systems and organisms could clarify the possibilities of adapting and thriving in extreme environments. This knowledge could be extremely important for future human missions to space or for addressing challenges on Earth, such as climate change or the search for alternative energy sources, like hydrogen and methane (Holm et al., 2015). Overall, the search for life beyond Earth captivates everyone's attention and inspires curiosity. It encourages people to contemplate humanity's place in the cosmos, stimulates interest in science and promotes international cooperation in space exploration. The quest to find extraterrestrial life can unite people from diverse backgrounds and cultures, fostering a shared sense of wonder and discovery (Schwarzenbach et al., 2014).

Serpentines represent a group of hydrous magnesium-rich silicate minerals that typically derive from the alteration particularly of ultramafic rocks in the presence of water, through a reaction called serpentinization. Serpentinization is a process that is common on Earth in locations where olivine-enriched bedrock is in contact with liquid water, generally in active tectonic margins such as obducted ocean-floor sequences and

at slow-spreading centers (Früh-Green et al., 2004). However, continental occurrences of active serpentinization on Earth are rare. This process occurs in the presence of H_2O and CO_2 fluids, resulting in the production of significant quantities of hydrogen (H_2 – a metabolic energy source, by reduction of water during iron oxidation and resulting reducing conditions), methane (CH_4) and lesser quantities of other hydrocarbons in the vent fluids (Kelley et al., 2001). These are some of the key elements for life as we know it. This is of extreme interest for the global research community focused on the study of the origin of life given the previously found episodic CH_4 plumes and the detection of organic molecules in Gale Crater on Mars (Webster et al, 2018; Eigenbrode et al., 2018), and most recently the discovery of diverse organic-mineral associations in Jezero Crater (Sharma et al., 2023).

Data from Jezero Crater Floor samples, Mars, identified diversity of minerals that include olivine, pyroxene and feldspar, in conjunction with aqueous alteration products including serpentines, smectites and carbonates (Dobrea and Clark, 2019; Simon et al., 2023). Following the study of Rocha et al. (2017), all the mentioned minerals with the exception of feldspars were also present in Cabeço de Vide (CdV), the study area, what points to similar geological processes leading to serpentinization in both locations. Cabeço de Vide, where serpentinization-rodingitization processes affected an Ordovician age cumulate-type structure (Marques et al., 2018), presents itself as an optimal mineralogical environment to study as Mars analog, since serpentinization has been proposed as a formation mechanism of Jezero Crater (Mars 2020/Perseverance rover landing site) carbonates (Brown et al., 2020; Simon et al., 2023), also indicating to the geological similarities between CdV and Jezero Crater, emphasizing the fact that CdV ultramafics are not ophiolites, but associated with the intrusion of mafic/ultramafic pluton (Rocha et al., 2017; Marques et al., 2008, 2018).

1.1. Objectives

The two fundamental objectives within this document are a more detailed study of the CdV ultramafic rocks, specifically from drill core AC2, in what concerns both textural and mineralogical features, and the characterization of waters collected from streams, springs and boreholes in the study area, allowing to put forward a genetic model for the serpentinization process and the water-rock interaction process occurring at depth.

Petrographic and geochemical characterization will provide a detailed database concerning the compositional features of the minerals making up the ultramafic rocks and their serpentinized derivatives exhibiting variable degrees of serpentinization. Petrography and mineral chemistry will also provide the means to establish serpentinization reactions, to study their products in detail, and to infer the most relevant physical conditions to their occurrence.

Processes related to serpentinization have a paramount astrobiological potential and for this reason, the other fundamental goal of this thesis is focused on the biosignature preservation potential in minerals of CdV. For life to have emerged from carbon dioxide, rocks, and water on the early Earth, a sustained source of chemically transducible energy was essential. The serpentinization process is emerging as an increasingly likely source of that energy (Russel et al., 2010).

All these findings will be a crucial contribution to update knowledge on serpentization of CdV ultramafics and be used as an analog to Mars, particularly for Perseverance mission in Jezero Crater. Furthermore, this information can be exceptionally valuable to serve as inventory or library of data for a future Mars Sample Return Mission, like the one scheduled for around 2030. Also, up to date, there is a lack of scientific papers related to understanding of geological processes leading to serpentinization on Earth with emphasis to those on Mars, so this document pretends to clarify a crucial missing link on understanding the actual geological processes leading to serpentinization of CdV ultramafic rocks.

1.2. Structure of the Thesis

This thesis is divided into six main chapters:

Chapter 1 is where this thesis is introduced, along with its main objectives, briefly describing the main topics discussed and referencing some of the most important works made in the study area Cabeço de Vide.
Chapter 2 succinctly describes the historical context of space exploration, defines what serpentines are and the importance of studying serpentines and the serpentinization process, integrating serpentines in Mars missions and referencing relevant Mars analogs studied in the pass, finalizing this topic with a summary of why Cabeço de Vide is a good Mars analog.
Chapter 3 presents a geographical and geological summary of the study area, as well as a concise summary of the hydrogeological features of Cabeço de Vide.
Chapter 4 characterizes the materials and methods used to accomplish the main objectives of this thesis, describing where samples were collected and how they were prepared, as well as all the techniques used.
Chapter 5 features the discussion and interpretation of the main results obtained by each technique used to analyse each sample that allow us to investigate the capabilities of CdV samples as Mars analogs.
Chapter 6 refers the main final considerations made from this thesis, including some suggestions for future work and development to be made, with a view to enrich the contents of this thesis.

Finally, **chapters 7 and 8** present the bibliographic references used during this thesis and the attachments, respectively.

2. State of the Art

2.1. Historical context

The history of space exploration is a fascinating journey that spans decades and involves a series of significant milestones achieved by various nations and organizations. It started with Sputnik 1, the first artificial satellite launched in 1957, marking the beginning of the space age and ignited a space race between the United States of America and the Soviet Union, with other historical milestones such as the first human spaceflight by Yuri Gagarin and the Apollo 11 Moon landing (Figure 1). All these milestones and achievements have reshaped our understanding of the universe, driven technological innovation, fostered international cooperation and ignited inspiration across the globe. This journey continues as we push the boundaries of human exploration, paving the way for a future where the mysteries of space are unraveled, and our horizons continue to expand.

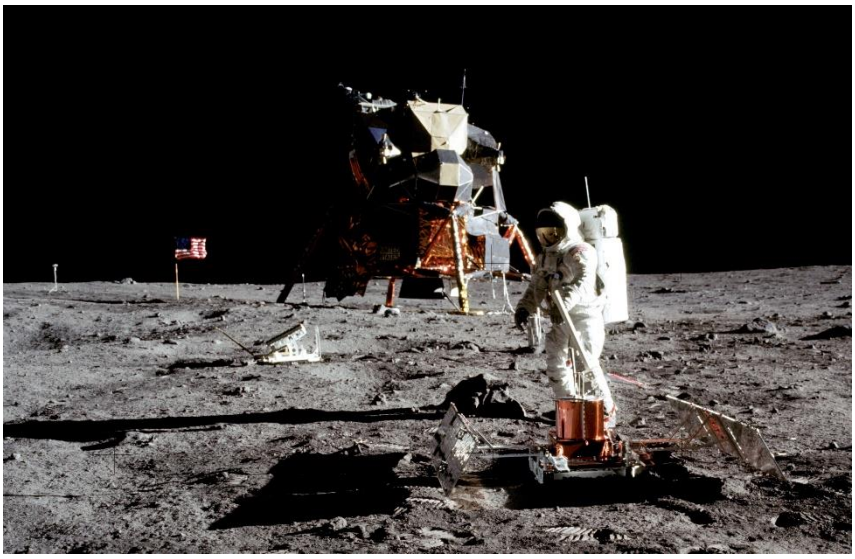

Figure 1: Apollo 11 landing site (Source: NASA).

Between 1995 and 2001, two fundamental discoveries in the existence of planets outside of the solar system (Mayor and Queloz, 1995) along with the existence of low-temperature hydrothermal fields have driven research efforts in serpentinization processes that are nowadays recognized as possibly the most important metamorphic reactions to explain the origin of life. The discovery that the undifferentiated crust of terrestrial planets like Mars and the early Earth consists mainly of mafic and ultramafic rocks has sparked a growing fascination with understanding the origins of life both on our planet and beyond. This has fueled a new interdisciplinary research direction called astrobiology, and recent efforts on Mars reinforced the importance of serpentinization on the Red Planet in the formation of molecular hydrogen and methane. Undoubtedly comprehending the process of serpentinization of ultramafic rocks plays a crucial role in connecting life sciences with solid earth processes, as it may be the fundamental process for prebiotic and biotic environments on extraterrestrial planetary bodies (Müntener, 2010).

Currently, the space trip to Mars is no longer science fiction based on the dreams of scientists and creative children but a present and current reality in the achievement of human history. The 21st century witnessed many international organizations attempting and achieving orbital launches and landing missions on the Red Planet, more than 56 million kilometers away from the Earth. However, no human being has set foot on an astronomical body other than Earth since 1972.

The landing process on Mars requires a difficult technique, and among 18 landing attempts, only eight attempts achieved their procedural goal. NASA sent various orbiters, including the Mars Odyssey (2001), the Mars Reconnaissance Orbiter (MRO, 2005) and the Mars Atmosphere and Volatile Evolution (MAVEN, 2015), together with the European Space Agency (ESA), with Mars Express (2003) and the ExoMars Trace Gas Orbiter (TGO or ExoMars Orbiter, 2016), this last one in collaboration with the Russian Roscosmos agency (Kim, 2022). NASA's Mars Rovers revealed to be extremely important in expanding our knowledge of the Red Planet, revealing its geological past and technological challenges of exploration, with access to raw images from Mars and other useful information. These missions have pushed the boundaries of technology, laid the groundwork for future exploration, both human and robotic, and advancing our understanding of Mars' geology, climate, and potential habitability. NASA's fleet of Martian Rovers is summarized in Table 1, and pictures on Figure 2.

Table 1: NASA's rovers, missions and information summary.

Mission	Spacecraft	Launch Date	Outcome	Other Information
Mars Pathfinder	Sojourner	04/12/1996	Successful	Operated for 84 days
Spirit	Spirit	10/06/2003	Successful	Operated for 2208 sols
Opportunity	Opportunity	08/07/2003	Successful	Operated for 5351 sols
Mars Science Laboratory (MSL)	Curiosity	26/11/2011	**Operational**	Landed on 6th August 2012
Mars 2020	Perseverance	30/07/2020	**Operational**	Landed on 18th February 2021

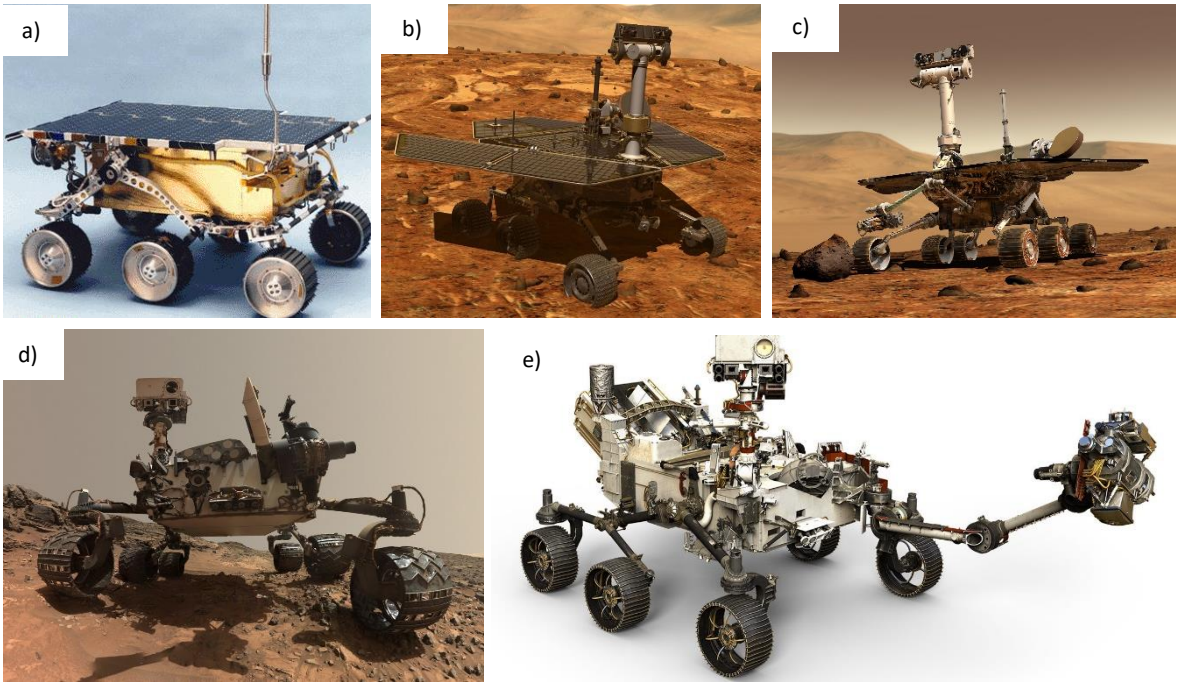

Figure 2: NASA's fleet of Martian Rovers: a) Sojourner; b) Spirit; c) Opportunity; d) Curiosity; and e) Perseverance (Source: NASA).

2.2. Serpentines

Serpentines are considered to be a mineral interface between the solid Earth, the hydrosphere and the biosphere (Müntener, 2010). The serpentinization process is today recognized as a vital water-rock interaction responsible for the production of secondary minerals, hyperalkaline water and gases, with major implications in geophysics (seismic velocities and changes in mantle rock rheology), geochemistry (geochemical fluxes and carbon cycle), biology and astrobiology. Generally, serpentine formation occurs during hydrothermal alteration of ultramafic rocks and takes place over a wide range of temperatures between 400-800°C, while being only marginally reliant on pressure (Iyer, 2007).

Structurally, serpentine minerals are 1:1 trioctahedral phyllosilicates with the general chemical formula $Mg_3Si_2O_5(OH)_4$. Si^{4+} in the tetrahedral sheet can be substituted for Al^{3+} and Fe^{3+}, while Mg^{2+} in the octahedral sheet may be substituted for Fe^{2+}, Fe^{3+}, Cr, Al, Ni and Mn (Iyer, 2007). The main serpentine minerals can be distinguished by their crystal structure. Lizardite consists of planar layers (Figure 3 A), while chrysotile consists of scrolled layers which tend to form cylindrical shapes (Figure 3 B). Antigorite possesses a modulated structure in which the 1:1 layer periodically reverses itself (Figure 3 C). Lizardite is more susceptible to accept substitution than chrysotile and is more enriched in Al. A lack of octahedral sites in antigorite results in a loss of Mg and $(OH)_4$ relative to Si^{4+} and is therefore more enriched in Si (O'Hanley, 1996; Mével, 2003).

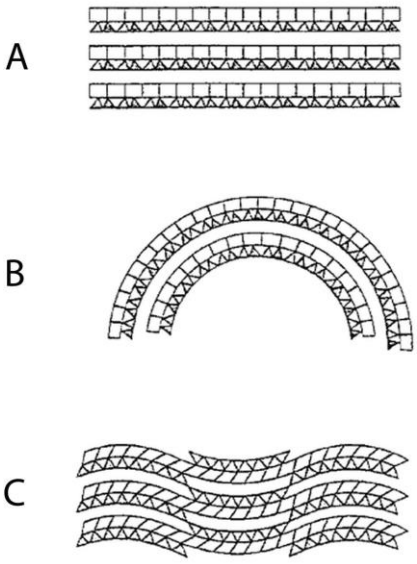

Figure 3: Representation of crystallographic structures of serpentine minerals: Lizardite (A), Chrysotile (B) and Antigorite (C) (Mével, 2003).

Summarizing, serpentinization is a geochemical process in which primary ferromagnesian minerals such as olivine ($(Mg,Fe)_2SiO_4$) and pyroxene ($(Mg,Fe)SiO_3$) are hydrated and transformed to form serpentine group minerals (lizardite, chrysotile and antigorite), following equation 1, brucite magnetite, Ni-Fe alloys, talc, chlorite and tremolite/actinolite. The serpentinization process occurs in the presence of H_2O and CO_2 fluids, resulting in the production of significant quantities of hydrogen that, with successive carbon I reduction via Fischer-Tropsch Type reactions (equation 5), more specifically the Sabatier reaction between carbon dioxide and hydrogen, may lead to the generation of abiotic methane (CH_4) and lesser quantities of long-chain hydrocarbons (Iyer, 2007). This is of vital interest for the global research community focused on the origin of life given the episodic CH_4 plumes (Webster et al., 2018) and the detection of a wide diversity of organic molecules largely found in minerals associated with aqueous processes in Jezero Crater, within the Máaz and Séitah formations (Sharma et al., 2023).

In a half reaction, iron hydroxide, produced via hydration of the iron-endmember of olivine (fayalite), undergoes subsequent oxidation of Fe^{2+}, producing magnetite and hydrogen gas (equation 2). It is important to note that the hydration of olivine and clinopyroxenes also releases OH^- ions resulting in highly alkaline fluids, which can emerge from fractures in the ultramafic rocks. Under basic conditions, including the presence of inorganic carbon, Ca^{2+} and Mg^{2+} form, respectively, calcium (equation 3) and magnesium carbonate (eq. 4) (Szponar et al., 2013).

$$3Fe_2SiO_4 + 5Mg_2SiO_4 + 9H_2O \rightarrow \mathbf{3Mg_3Si_2O_5(OH)_4} + Mg(OH)_2 + 2Fe(OH)_2 \quad (1)$$

Faylite *Fosterite* ***Serpentine*** *Brucite* *Iron (II) Hydroxide*

$$3Fe(OH)_2 \rightarrow \mathbf{Fe_3O_4} + 2H_2O + \mathbf{H_2} \quad (2)$$

Magnetite *Hydrogen*

$$Ca^{2+} + CO_3^{2-} \rightarrow \mathbf{CaCO_3}\,(s) \quad (3)$$

Calcium carbonate

$$Mg^{2+} + 2HCO_3^- \rightarrow \mathbf{MgCO_3}(s) + CO_2 + H_2O \quad (4)$$

Magnesium Carbonate

$$CO_2 + 4H_2 \rightarrow \mathbf{CH_4} + 2H_2O \quad (5)$$

Methane

During serpentinization, Fe^{3+} is produced and goes into both tetrahedral and octahedral sites in serpentine structure, and Fe^{3+} content increases in octahedral sites before tetrahedral sites, in time, as shown in Figure 4 (Marcaillou et al., 2011). Fe^{3+} present in serpentine can stabilize the crystal structure and coupled substitution of Fe^{3+} for Si^{4+} in tetrahedral sites and Fe^{3+} for Mg^{2+} in octahedral sites is one method of charge-balancing the structures. Fe^{3+} substitution in tetrahedral sites is favoured in low Si environments such as where the protolith is ultramafic. Throughout this Fe^{3+} production and substitution into the serpentine structure, first in octahedral and then in both octahedral and tetrahedral sites, H_2 is produced (O'Hanley and Dyar, 1993).

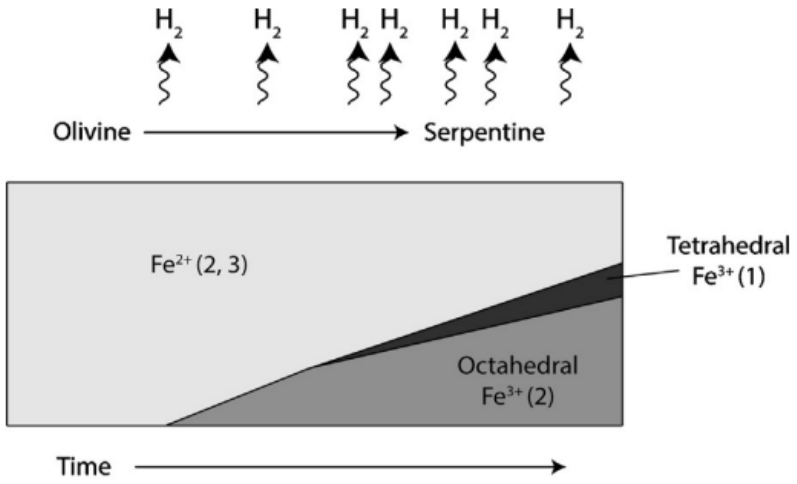

Figure 4: Diagram showing relative proportions of Fe^{2+} and tetrahedral and octahedral Fe^{3+} in serpentine with time during serpentinization, determined experimentally by Marcaillou et al. (2011). H_2 is produced during this process (Source: Greenberger et al., 2015).

Serpentinization generally occurs in slow expansion mid-ocean ridges and continental ophiolite tectonic environment system. Ophiolites are sections of the oceanic crust and upper mantle that have suffer obduction onto continental crust, that can yield ground waters with unique chemistry that are ultrabasic (pH>10) (Barnes et al., 1967). Ophiolites can originate from other tectonic events, including expansion and mantle plume-related activities. Most studies of physical and chemical characteristics of serpentinization events are typically from ophiolite regions. The degree of serpentinization depends on many factors such as fluid source, temperature, water/rock ratio, etc. (Wang et al., 2014). Complete serpentinization of a peridotite results in a water uptake of 13 to 15% by weight and a volume increase of around 40%, considering the fact that peridotite is a type of ultramafic igneous rock, is the main rock type found in the Earth's mantle and is primarily composed of olivine, with smaller amounts of pyroxenes and amphiboles. These changes can influence the rheology of the rock and therefore play a massive role in the formation of detachment faults and strain localization along serpentinized fault planes (Iyer, 2007). The serpentinization process is more efficient in fractured rocks, since they allow faster percolation of water and this process can occur at temperatures lower than 315°C, forming serpentine minerals, iron oxides and H_2 (Moody, 1976).

2.2.1. Serpentine textures

Generally, serpentine minerals have sub-microscopic grain sizes and can only be identified through X-Ray Diffraction analysis or electron microscopy (O'Hanley, 1996). Under the polarizing microscope, serpentine textures have been discussed in detail by Wicks and Whittaker (1977) and O'Hanley (1996) and are divided into three distinct categories: Pseudomorphic textures preserve the texture present in the precursor sock, while non-pseudomorphic textures do not. Transitional textures preserve some of the textures previously present in the protolith.

After alteration of the primary mineralization, serpentine forms pseudomorphic textures and serpentine pseudomorph called *bastite*, after the alteration of pyroxenes and amphiboles, talc and micas. Pseudomorphic textures of serpentine after alteration of olivine are described as mesh or hourglass textures. In mesh textures (Figure 5 (a)), serpentine is present in the mesh rim with relict olivine grains or optically distinct serpentine in the mesh cores. The outer edge of the mesh rim is representative of a grain boundary or even a fracture within the grain. The mesh rim serpentine consists of parallel, apparent fibers perpendicular to the contact between the mesh rim and mesh core. In hourglass textures, however, the olivine grains are generally smaller and therefore serpentine is indistinguishable from the mesh rim and is related to fractures. Non-pseudomorphic textures are divided into interlocking and interpenetrating textures (Figure 5 (b)). Interlocking textures consist of equant grains of serpentine and may consist of antigorite, lizardite and/or chrysotile, while where serpentine in interpenetrating textures consist of optically distinguishable, elongated blades of antigorite (O'Hanley, 1996).

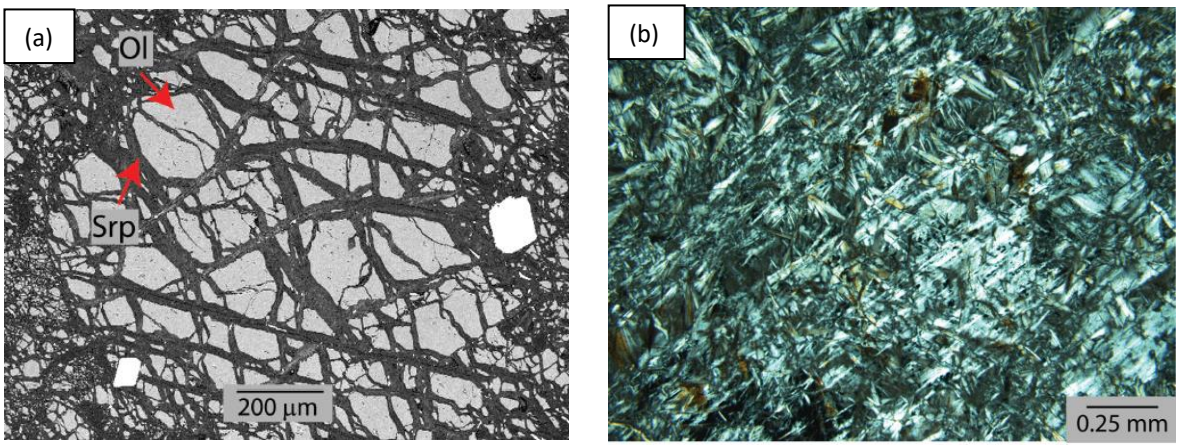

Figure 5: (a) Image of a pseudomorphic mesh texture in a dunite, where Serpentine (Srp) forms at the mesh rims surrounding relict mesh cores of olivine (Ol); (b) Photomicrograph of a non-pseudomorphic interpenetrating texture in serpentinites (Adapted from Iyer, 2007).

2.2.2. Serpentinization links to life

On Earth, on a more global scale, serpentinization of mantle and deep hot crustal rocks appears to be a significant process, mainly in crustal development in zones of relatively low magmatic supply, like the Mid-Atlantic Ridge. For this reason, for life to emerge from CO_2, rocks, and water on the early Earth, a sustained source of chemically transducible energy was essential. The serpentinization process is emerging as an increasingly likely source of that energy, so a wide body of research has recently demonstrated the importance of active serpentinization driven by meteoric water, occurring in peridotites already emplaced on the continents. Serpentinization of ultramafic crust would have continuously supplied hydrogen, methane, and ammonia, along with calcium and traces of acetate (Russel et al., 2014).

According to Kelley et al. (2001), zones of active serpentinization are known to foster dense microbial communities, surviving on the products of these reactions, in the absence of other energy sources, like solar or volcanic. Hydrogen (H_2) can be directly used as an electron donor in the metabolism of many chemoautotrophic organisms, like the methanogens at the Lost City Hydrothermal Field, that use H_2 to fix Carbon Dioxide (CO_2) and produce Methane (CH_4) and H_2O. These extreme environments and the chemistry and mineralogy that exist in them point to potential links to prebiotic chemistry and are often discussed as interesting environments for key steps in the origin of life on Earth (e.g., Russel et al., 2010). Considering serpentine forms in this particular setting and generally results in the release of bioaccessible H_2, it can be considered a unique environment indicator mineral. In this regard, the identification of serpentine indicates that serpentinization occurred and that H_2, as well as short-chained organics, were likely released (Amador et al., 2018).

2.3. Importance of studying serpentines and serpentinization

In 2016, the European AstRoMap project reported on the state of the art of astrobiology in the scientific world and introduced us to the first ever European roadmap for astrobiology research. In this context, astrobiology is seen as the study of the origin, evolution and distribution of life in what regards cosmic evolution, including habitability in the Solar System and beyond. This roadmap consists of five main research topics, and the third includes "Rock-Water-Carbon Interactions, Organic Synthesis on Earth, and Steps to Life". Research Topic 3 focuses on the fact that geology and geochemistry specifically provide the boundary conditions to fully understand life on Earth, which is the best-studied planet so far and it is a great example for more distant systems. On the planetary scale, the main energy dissipation process on metal-rich planets such as Earth is serpentinization. The first key objective of this research topic focuses on a better characterization and understanding of the dynamic redox interactions between rock, water and carbon in their geological context on planets and moons. As mentioned previously, during the serpentinization process, water and carbon dioxide fluids circulate through hydrothermal systems, reacting chemically with rocks present. Electrons leave their native iron and nickel source and they're transferred to water in order to generate H_2, an important source of energy. In a similar way, carbon dissolved in the circulating water reacts to generate reduced carbon compounds (Horneck et al., 2016).

The overturning of the mantle by solid-state convection currently supports the Earth's biosphere. The recycling of oxidized crustal Fe^{3+} in exchange for mantle Fe^{2+} strike to rejuvenate the reducing power of the crust. The majority of this reducing power originates from serpentinization. Life thrives in Earth's deep subsurface. Approximately 15% of the total biosphere is estimated to be this buried biome's biomass. Part of this is associated with the lithotrophic organisms that survive from the oxidation of iron, and it is supposed that autotrophic communities in the deep subsurface form some of the support for associated heterotrophs. This possibility of abundance of lithotrophs is a big reason why the global scientific community is optimistic that life exists within other worlds. Serpentinization is a direct fuel for life and driver for redox disequilibria needed for metabolism since it could serve as a source of hydrogen. Slower processes of serpentinization may have persisted on other planets, like Mars, after they lost accretional and tidal heat, due to percolation of fluids into microfractures over long periods of time. Even if the geodynamic cycles of other planets in the Solar System are less well understood, it seems likely that if life is present in other worlds, serpentinization has some role in supporting it (Vance et al., 2020).

Serpentines play a crucial role in the study of life on Mars mainly due to their significance as potential habitats for past or present microbial life, and future exploration and sample return missions, like the only scheduled by NASA for around 2030. Since serpentines are a type of mineral formed through the hydration and alteration of certain types of rocks, such as ultramafic rocks, in the presence of water, the presence of serpentines on Mars provide evidence of past water activity, a key ingredient for the existence of life as we

know it. The detection of serpentines is a strong indicator that water was once present on the Martian surface, since the first serpentine detection on Mars, in Nili Fossae, as reported by Ehlmann et al. (2009). Serpentine minerals, such as lizardite, antigorite and chrysotile, have unique chemical properties that make them potentially suitable for supporting microbial life. These minerals can act as hosts for essential elements and nutrients necessary for life, such as carbon, nitrogen and phosphorus. They can also provide protection against ultraviolet radiation, which is particularly important for microbial survival on Mars due to its thin atmosphere and lack of a robust ozone layer (Ehlmann et al., 2009).

As mentioned previously, serpentine-rich environments on Earth are known to harbor a diverse range of microbial life, even in extreme conditions, hence the emphasis given to this main characteristic of the serpentinization process. Similar environments on Mars could provide special places where microbial life could potentially exist. The interaction between water, minerals, and organic compounds within serpentine formations creates favorable conditions for the emergence and preservation of life. Studying these environments on Mars can offer important insights into the habitability of the Red Planet. The serpentinization process involves the incorporation of the mentioned organic compounds into the mineral structure, effectively protecting them from degradation. This preservation potential makes serpentines excellent targets for astrobiological investigations on Mars, as they could potentially contain evidence of ancient microbial life or organic molecules that could hint at the existence of past or even present life (Amador et al., 2018).

Most recently, the OSIRIs-REx mission (launched on September 8, 2016) targeted Bennu, an asteroid made of primitive materials with potential to provide information about the building blocks of the early Solar System. This was the first ever U.S. mission to collect a sample from an asteroid and deliver it to Earth with great success on September 24th, 2023. Previous remote sensing data identified, through mineral quantification, phyllosilicates: primarily Mg-rich serpentine, with smaller amounts of cronstedtite (Fe-rich serpentine) and saponite (smectite), along with magnetite and carbonates (Breitenfeld et al., 2022). NASA's preliminary results from the asteroid's material confirmed the presence of serpentine, magnetite, carbonates and sulfates (Figure 6). These results also showed that almost 5 wt.% of the mass of Bennu is carbon and also an extremely important abundance of organics. These preliminary results are crucial for future analyses, in order to further extend our knowledge on how our solar system was formed and how the precursor materials to life may have been seeded on Earth (NASA Press Release: Revealing the OSIRIs-REx Asteroid Sample; Minute 38:30).

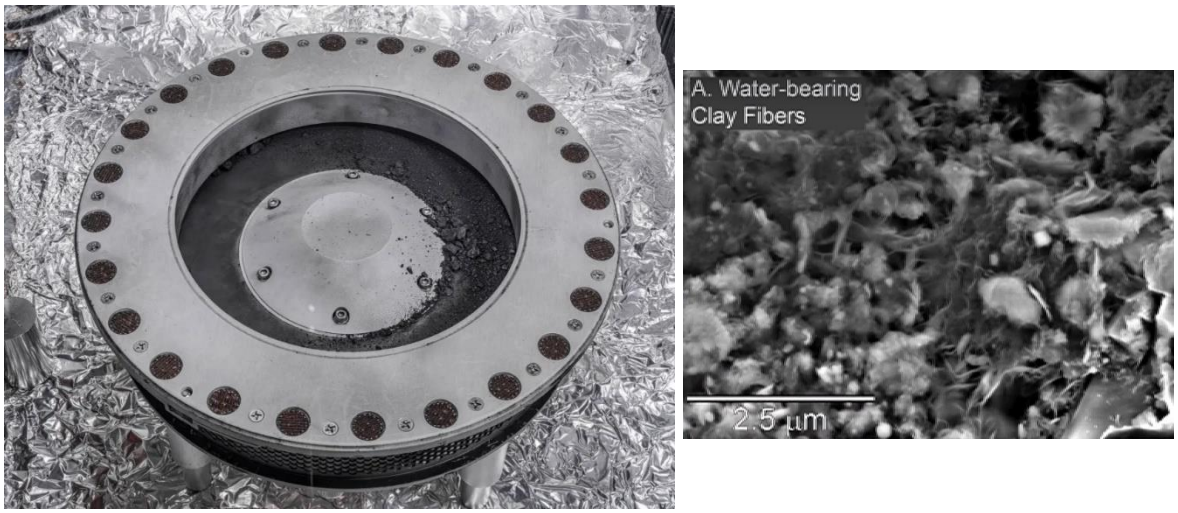

Figure 6: On the left, a view of outside of the OSIRIS-REx sample collector. Sample material from Bennu can be seen on the middle right. The bulk sample is located inside. Serpentine minerals were identified by SEM analysis (right) (Source: NASA).

Finally, the identification and characterization of serpentines on Mars guided previous and current missions, can guide future ones and the search for signs of life. Serpentine-rich regions were targeted for in situ exploration, as seen in Mars 2020 mission, where Perseverance rover was deployed in Jezero Crater, in Nili Fossae region of Mars, to conduct detailed investigations, including sample collection and analysis. The collection of serpentine samples and their potential return to Earth through sample return missions will enable more sophisticated and comprehensive studies in well-equipped laboratories, where scientists can utilize advanced analytical techniques to search for signs of life.

All this information emphasizes the fact that studying serpentinization processes on Earth hold significant importance for the study of life on Mars as they provide evidence of past water activity, offer potentially habitable environments for microbial life, preserve organic compounds and biosignatures and guide future exploration and sample return missions. Understanding the role of serpentines and serpentinization of ultramafic rocks in the Martian geological and astrobiological context is crucial to link life sciences with solid Earth processes and may be the fundamental process for prebiotic and biotic environments on extraterrestrial planetary bodies (Müntener, 2010).

2.4. Integration of serpentines in Mars 2020 mission

Over the past several decades, orbital and landed spacecraft data have provided an abundance of data that is extremely important to the study of all the geological processes that could have happened on the Red Planet. Mars' earlier missions found traces of a distant past existence of liquid water on Mars. Perseverance's older cousin Curiosity Rover explored the possible habitability of Mars, where it found nutrients and energy sources, such as nitrogen, hydrogen, sulfur, carbon, oxygen and phosphorus, that microbes could have used, establishing the fact that Mars indeed had regions that could have been favorable conditions for life to develop, in the ancient past (Eigenbrode et al., 2018; Vasavada, 2022). Figure 7 shows NASA's Perseverance landing sites, in relation to previous successful Mars missions.

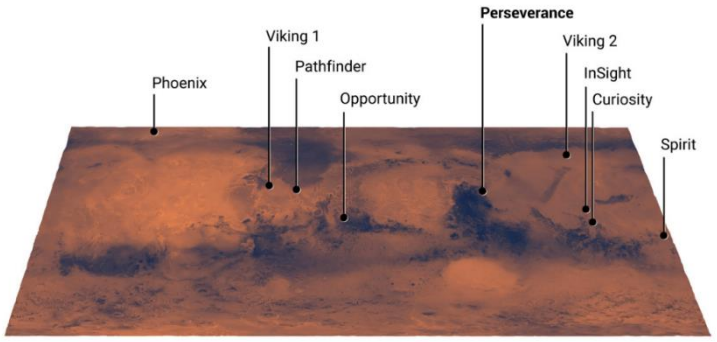

Figure 7: NASA's Perseverance rover landing site, in relation to the previous successful Mars Missions by NASA (Source: NASA/JPL-Caltech).

Scientists believe that Jezero Crater was once flooded with water and was an ancient river delta. The landing site selection process involved mission team members and scientists from all over the world, as they carefully examined more than sixty possible landing sites, each with its own unique features. Jezero Crater is an approximately 45km diameter impact crater located in the Nili Fossae region of Mars and was formed in the late-Noachian to mid-Noachian (3.7 – 4.1 billion years ago) (Goudge et al., 2015). It is located within the Isidis basin region of Mars, where an ancient meteorite impact left behind a large crater approximately 1200 kilometers across, in an event known as the Isidis impact. Crustal material in the Nili Fossae region consists of both units emplaced prior to the Isidis basin forming event and Isidis-related materials, including extensive brecciated units and impact melt (Zastrow and Glotch, 2021). The Nili Fossae region also shows evidence of a variety of other geologic processes subsequent to the formation of the Isidis impact basin, including fluvial activity and volcanism. The combination of all these events is believed to create environments friendly to life, as there is evidence of ancient river flow into Jezero, forming a delta that has long since been dry (Goudge et al., 2015). The Mars Reconnaissance Orbiter's CRISM instrument, that uses detectors that see in visible, infrared and near-infrared wavelengths to map the kind of mineral residue that is present where water once existed, has revealed that this interest site contains a wide mineralogical diversity, like clays, which only form in the presence of water (Goudge et al., 2019).

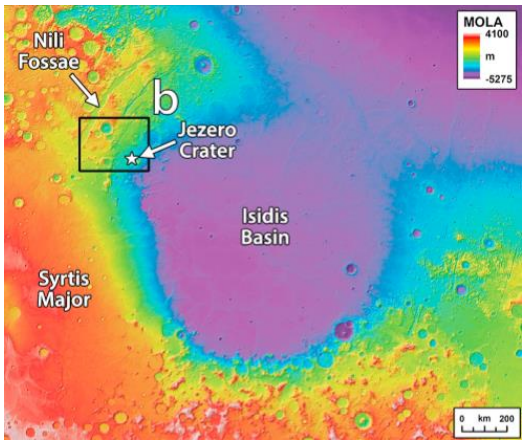

Figure 8: Location map for Jezero Crater, in the Nili Fossae region of Mars, within Isidis Basin (Goudge et al., 2015).

Fasset and Head (2005) first described evidence for a paleolake within Jezero Crater, as they identified the inlet and outlet valleys feeding and draining a basin enclosed by a topographic contour approximately 250 meters above the current crater floor. This contour sits at an elevation of -2395 m relative to the Mars datum and determines the minimum level of ponding inside the crater prior to breaching to form the outlet valley. Also important is the identification of two main distributary fan deposits present at the mouth of each inlet valley. Every described characteristic is well shown in Figure 9.

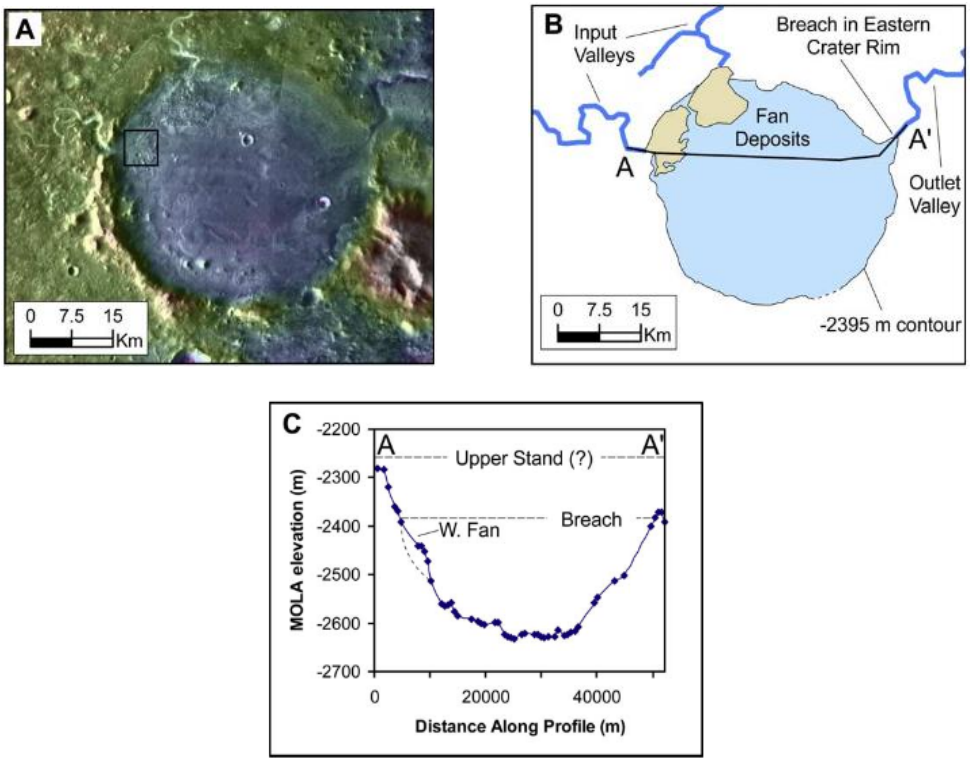

Figure 9: A) represents a THEMIS IR daytime mosaic of the fan deposits in Jezero Crater, Mars, with false color topography. B) shows a sketch map of the crater and fan, where the -2395m contour outlines the crater interior and the input and output valleys are represented. C) represents the A-A' profile showing the relative elevations of the western fan, crater interior and breach point (Fasset and Head, 2005).

For the reasons described previously, Jezero Crater was selected as the landing site for the most recent Mars 2020 mission. On February 18, 2021, NASA's Perseverance Rover (Figure 10) made its final descent to the Red Planet, after being launched July 30, 2020. Perseverance's four main science objectives include:

- **Looking for Habitability**: by identifying past environments that are capable of supporting microbial life.
- **Seeking Biosignatures**: by searching for signs of possible ancient microbial life in those habitable environments, especially a certain type of rocks known to preserve signs of life over time, like serpentines.
- **Collecting and Catching Samples**: using the rovers special drill to collect core samples of Martian rock and soil and storing them in seal tubes for future pickup missions that would bring these samples back to Earth for further detailed analysis.
- **Preparing for Humans**: by testing oxygen production from the CO_2-rich Martian atmosphere.

Figure 10: Perseverance Rover. Source: NASA/JPL-Caltech.

Jezero Crater has been subject to previous extensive photogeological and spectroscopic studies. These studies identified a variety of geological and mineralogical units of astrobiological interest, including km-scale deposits of carbonates, phyllosilicates and sulfates. The three fan/delta features in Jezero all exhibit distinct spectral signatures, but, specifically, the western delta is the most complex and exhibits clear regions enriched in different primary and secondary minerals, including Fe/Mg-smectites, low-Ca pyroxene, feldspar and olivine and carbonate signatures. Within the Mars 2020 landing ellipse, spectral data identified a wide variety of minerals was identified, including primary mafic minerals (feldspar, olivine and pyroxene) and aqueous alteration products (serpentine, smectite and carbonates) (Dobrea and Clark, 2019).

All the information about Jezero Crater and its mineralogy shows evidence that water carried clay minerals from the surrounding area into the crater lake formed by ancient river channels. Conceivably, microbial life could have lived in Jezero during one or more of these wet times. This is exactly one of the reasons why Mars 2020 mission was designed: to search for signs of potential ancient life through biosignatures. A biosignature can be defined as an object, substance and/or pattern whose origin specifically requires a biological agent. Identifying a biosignature in a rock depends not only on whether that signature could be identified by its inherent properties (e.g., chemical composition, mineralogy), it also depends upon understanding the geologic context in which the potential biosignature occurs (Dobrea and Clark, 2019; Horgan et al., 2020; Brown et al., 2020).

Spectral diversity observed in the sedimentary rocks along the stratigraphy of the delta front of Jezero Crater at certain locations preserve a record of variable aqueous conditions, especially variability in redox conditions, during deposition and post-depositional alteration by diagenetic fluids, and thus may be sites of enhanced organic matter preservation. These factors show that an early aqueous environment on Mars may have been favorable for the preservation of potential biosignatures (Núñez et al., 2023; Broz et al., 2023).

The relation between Jezero Crater and serpentines shows the importance of serpentine and serpentinization processes in relation to life and Mars 2020 mission, given the fact that serpentines have a unique ability to preserve organic compounds and biosignatures. The serpentinization process involves the incorporation of organic compounds into the mineral structure, effectively protecting them from degradation. This preservation potential made serpentines excellent targets for astrobiological investigations on Mars, as they can potentially contain evidence of ancient microbial life or organic molecules that could hint at the existence of past or present life (Comellas et al., 2023).

The Mars 2020 Perseverance rover is currently traversing up an ancient river delta near the edge of Jezero Crater, which is part of the Nilli Fossae region where serpentine minerals were detected previously from orbit using CRISM data from the Mars Reconnaissance Orbiter (MRO). The SuperCam instrument onboard this rover has analyzed targets with potential serpentine, as there are currently still some uncertainties in the

identification of serpentine using current SuperCam LIBS data and calibration, since there are other phyllosilicates and clays that have similar features and absorption bands in infra-red reflectance spectra (Comellas et al., 2023).

Most recently, surface investigations revealed landscape-to-microscopic textural, mineralogical and geochemical evidence for igneous lithologies. Jezero Crater samples collected confirmed previous spectral data, containing major rock-forming minerals such as pyroxene, olivine and feldspar, accessory minerals including oxides and phosphates, and evidence of various degrees of aqueous activity in the form of water-soluble salt, carbonates, sulfate, iron oxides and iron silicate minerals (Simon et al., 2023). A summary of the minerals identified with the visible and near-infrared spectrometer of SuperCam on the Crater floor is shown on Figure 11, showing how mineralogically complex a small region of Jezero Crater can be.

Máaz		Clinopyroxene[a,b]
		Fe-oxyhydroxide(s) (e.g., ferrihydrite, akaganeite[c])
		Fe^{3+}-phyllosilicate (nontronite or hisingerite likely)
		Monohydrated Mg-sulfate
		Al or Si–OH-mineral (Al-phyllosilicate and/or hydrated silica)
		Mg–OH mineral (smectite, serpentine, talc, and/or brucite) and/or carbonate—minor
Séítah	Pitted	Fe-oxyhydroxide(s) (e.g., ferrihydrite)
		Fe^{3+}-phyllosilicate (nontronite or hisingerite)
	Nonpitted	Olivine[a,b]
		Clinopyroxene
		Fe^{3+}-mineral (nontronite or hisingerite)[b]
		Mg–OH mineral (Mg-smectite, serpentine, talc and/or brucite)[b]
		Fe/Mg-carbonates[a,b]
		Fe-oxyhydroxide(s) (e.g., ferrihydrite)
		Monohydrated Mg-sulfate
		Al or Si–OH-mineral (Al-phyllosilicate and/or hydrated silica)[b]
Soils	Fine (μm-sized)	Pyroxene
		Olivine
		Hydration
	Coarse (μm–mm-sized)	Olivine
		Fe^{3+}-mineral (nontronite or hisingerite likely)
		Mg–OH mineral (Mg-smectite, serpentine, talc, and/or brucite)
Dust		Fe-oxides

Figure 11: Summary of minerals identified in Máaz and Séithah regions of Mars, as well as Martian Soils and Dust adjacent to the formations studied in Jezero Crater (Adapted from Mandon et al., 2023).

SHERLOC Instrument (Scanning Habitable Environments with Raman and Luminescence for Organics and Chemicals) detection of organic molecules in abraded targets from the Máaz and Séitah formations in the Jezero Crater floor are correlated with minerals that have undergone substantial aqueous processing, suggesting that organic molecules may have been abiotically aqueously deposited or synthesized within these altered materials within the crater floor. This information on organic molecules can unveil new insights into the organic geochemical cycle on Mars, through future confirmation of organic origin and specific identification of these molecules by laboratorial analysis on Earth (Sharma et al., 2023).

Considering this information, the fact that the Perseverance rover is currently collecting samples for a future Mars Samples Return Mission is extremely important, as this will allow samples from Mars to be analyzed by the finest laboratorial scientists and equipment for the very first time, in order to constrain the crater chronology of Mars and the global evolution of the planet's interior, for understanding the processes that formed Jezero Crater floor units, and for constraining the style and duration of the aqueous activity in Jezero Crater, past habitability, and cycling of organic elements present in this particular region of Mars (Simon et al., 2023).

2.5. Mars analogs and Cabeço de Vide as Mars analog

Mars analogs are environments on Earth that share certain characteristics with Mars, making them extremely valuable tools for studying and understanding fully the conditions, processes and potential habitability of the Martian surface. These analogs play a crucial role in advancing our knowledge of Mars and its potential for past and present life. They provide researchers with the opportunity to study various environmental conditions that exist on Mars, such as extreme cold, low atmospheric pressure, arid landscapes and high levels of radiation, while allowing scientists to test and calibrate instruments and technologies designed for Mars exploration.

A number of studies have been conducted all around the world on Mars analogs, emphasizing the extreme conditions present in Mars, like on the Atacama Desert, in Northern Chile, the driest and oldest desert on Earth, that has been largely investigated for almost 20 years as a Martian analog. This environment showed the presence of microorganisms in its specific conditions, like extreme aridity, high UV radiation and highly saline soils, confirming the fact that this area is an extremely important analog target and that molecular mechanisms are able to tolerate extreme conditions, like Mars (Azua-Bustos et al., 2022).

Steele et al. (2022) documented the study made in the Martian meteorite ALH 84001 (Allan Hills 84001), examining carbonates and silicates present to characterize the nature of water-rock reactions on early Mars. This study found complex refractory organic material associated with mineral assemblages that formed by mineral carbonation and serpentinization reactions and concluded that the two potentially distinct mechanisms of abiotic organic synthesis operated on early Mars during the late Noachian period, 3.9 to 4.1 billion years ago, all this making relations between this meteorite and implications for organic synthesis, since serpentinization is an abiotic organic synthesis mechanism, and Martian habitability, indicating that Mars hosted abiotic organic synthesis reactions for most of its history.

Studies focused on analogs for understanding the role of serpentinization, carbonates and serpentines on Mars include studies on the geochemistry of a continental site of serpentinization associated with ophiolites (Szponar et al., 2013) on the aqueous alteration of ultramafic rocks in Oman (Ehlmann et al., 2012), serpentines on Sri Lanka (Vithanage et al., 2014; Barbato et al., 2019; Karunatillake et al., 2021) and the known case of the Lost City hydrothermal field (Lang and Brazelton, 2020).

Ehlmann et al. (2012) focused on CRISM imaging and in-situ investigations by the Spirit rover, relating them to the Samail ophiolite complex in Oman. Waters participating in serpentinization at depth lose Mg to serpentine and carbonate precipitates, producing hydrogen gas, becoming highly alkaline and acquiring calcium from reaction with the pyroxene-bearing peridotite. Upon release of these waters back at the surface, calcium reacts with bicarbonate supplied by dissolution of atmospheric carbon dioxide to form calcium-rich

carbonates near springs. Karunatillake et al. (2021) reports an important study on variations in the Sri Lanka serpentine outcrops mineralized between the Highland Complex (HC) and Vijayan Complex (VC) of that area, following previous work made by Barbato et al. (2019), and Vithanage et al. (2014) about metal release from serpentine soils in Sri Lanka.

The Lost City hydrothermal field is a prime example of the biological potential of serpentinization. Microbial life is prevalent throughout the Lost City chimneys, powered by the hydrogen gas and organic molecules produced by serpentinization and its associated geochemical reactions. For this reason, this hydrothermal field is perhaps the most famous and most heavily researched site of active serpentinization. However, initial results from the first microbiological investigation of these rock cores have revealed a much lower biological content compared with the Lost City chimneys (Lang and Brazelton, 2020).

Even if the mentioned studies achieved great and interesting results, they share a big gap that this thesis pretends to fill. These previously cited serpentines and others have been proposed as Mars analogs but either they are studied as analogs for methane production from ophiolites (e.g., Tablelands Ophiolite in Eastern Canada; Szponar et al., 2013) or the authors focus on carbonate detections on chemical variations of serpentines at the microscale (e.g., Sri Lanka; Barbato et al., 2019).

According to Dobrea and Clark (2019), most of spectral data work on Jezero Crater was focused on restraining spectral signature to one spectrally dominant mineral and associating each geological unit to that specific mineral, when in reality minerals normally occur together in aggregates, and their composition provides really important information on its origin. This spectral orbital data of Jezero Crater identified a wide mineral diversity, including olivines, pyroxenes, feldspars, serpentines, smectites and carbonates (Figure 12). Olivines found are primarily associated with mantling and ripple-bearing units; High and low calcium pyroxene were identified, where high calcium (augite) is more common, occurring in association with olivine-bearing rippled units, in addition to low calcium pyroxene (pigeonite) found in discrete outcrops on the western side of the crater; Feldspar (bytownite) was identified occurring in association with carbonate-bearing outcrops located by the crater's rim, as well as in association with olivine in the outcrops on the crater floor; serpentines were detected, with the observed spectra being more consistent with lizardite. Smectites are broadly distributed throughout the site, dominantly present on the fan deposit; Carbonates are most spectrally dominant associated with light toned outcrops occurring both inside and outside the western part of the Jezero Crater (Dobrea and Clark, 2019; Ehlmann et al., 2009).

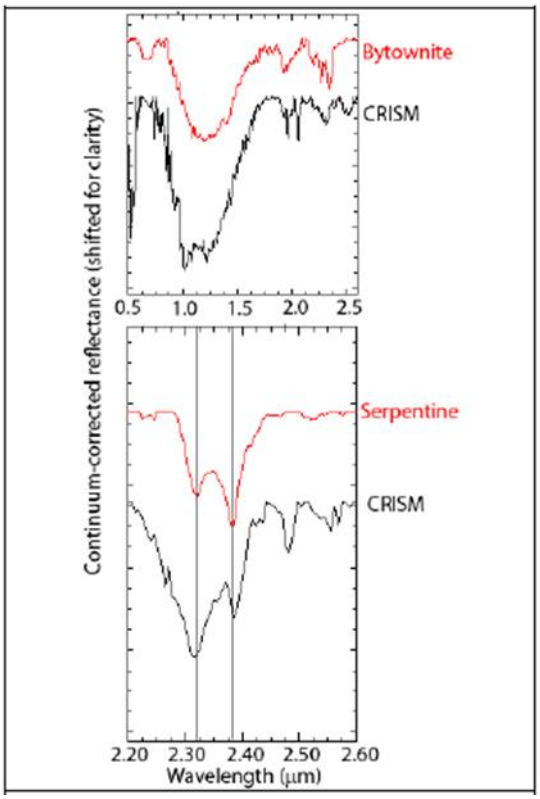

Figure 12: Corrected spectra of bytownite in red and CRISM spectrum of carbonate-bearing unit (Top); Similar comparison between serpentine, in red, and CRISM average on the crater rim, in black (Source: Dobrea and Clark, 2019).

All the minerals mentioned previously to be on Jezero Crater are also present in Cabeço de Vide, the study area, emphasizing the importance of the study of whole-rock samples in CdV as a possible source of information for present and future Mars missions. This information is tremendously important because, until now, CdV has been studied as a Mars analog due to the unique composition of the waters present in this area, per example Marques (2008, 2018, 2019). Etiope et al. (2013) also reported a new case of methane of apparent abiotic origin in continental serpentinized ultramafic rocks in Cabeço de Vide, revealed by the presence of methane and ethane in hyperalkaline mineral waters present in CdV boreholes (AC3 and AC5). This case study confirmed the fact that methane (CH_4) from serpentinized ultramafic rocks can be transported by hyperalkaline fluids linked to deep circulation of meteoric waters.

Preliminary studies on CdV geological features have already been reported (Rocha et al., 2017), focusing on the mineralogical evidence of hydrothermal alteration in the study area and fully understanding the actual geological processes leading to serpentinization of CdV ultramafic rocks. This study area is extremely important to study a Martian analog, as Cabeço de Vide ultramafics are not ophiolites, but associated with the intrusion of mafic/ultramafic pluton of Alter do Chão (Marques et al., 2008, 2018; Rocha et al., 2017).

3. Geographical and Geological Setting of the Study Area

3.1. Geographical Setting

The area of interest is located in Cabeço de Vide (CdV), a city located in Portalegre, in the NE part of the Alentejo Region of mainland Portugal. The geological and hydrogeological interest zone is situated in Termas da Sulfúrea, a spa area open since 1855, promoted in 1935 by the Cabeço de Vide parish council with a significant infrastructure investment and improvement. CdV is located between Alter do Chão and Monforte, close to the central section of the Portugal-Spain border (Gonçalves, 1973).

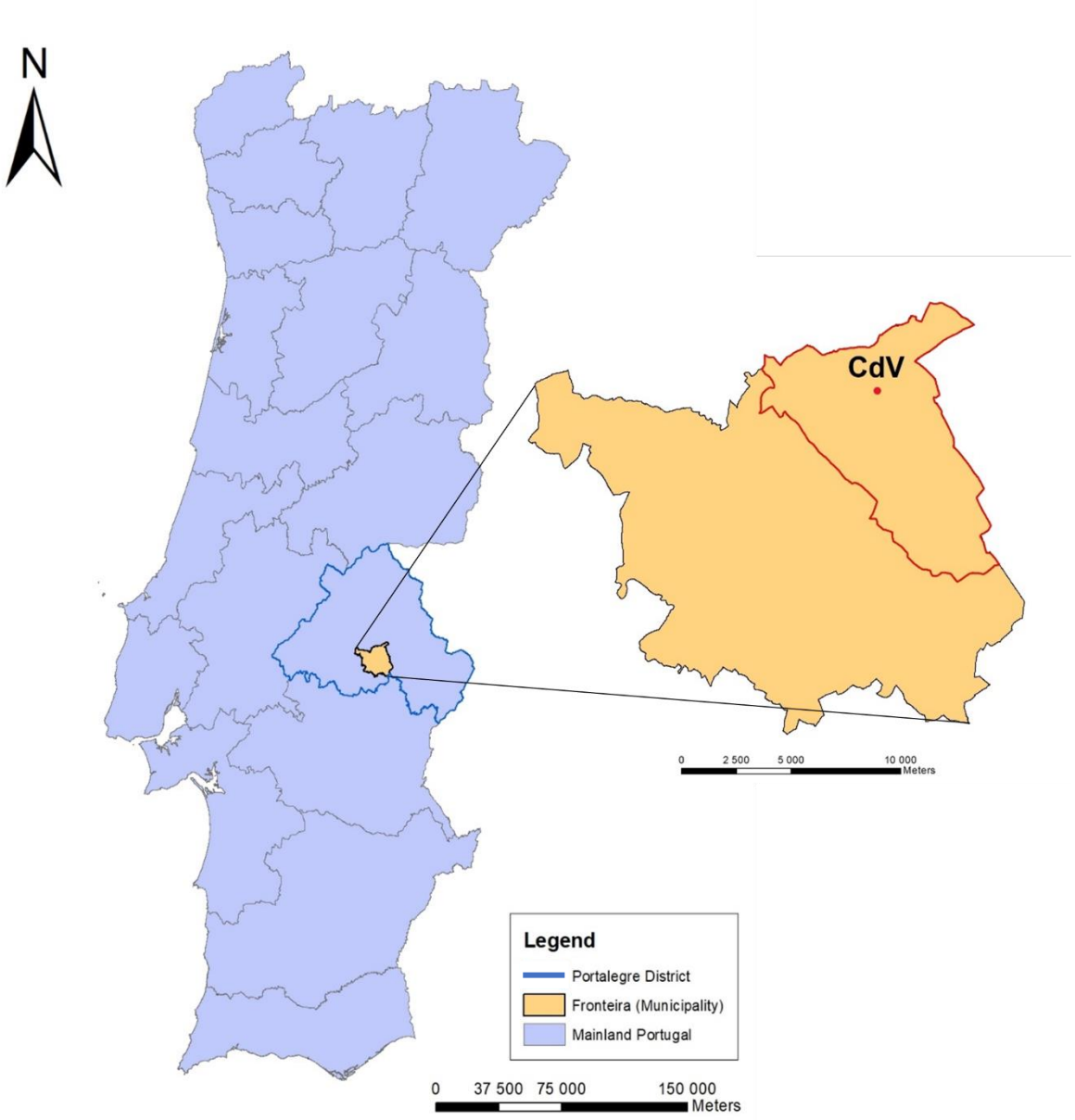

Figure 13: Geographical location of Fronteira municipality and Cabeço de Vide in mainland Portugal.

3.2. Geological Setting

The study area is situated in the southern region of the Ossa Morena Zone (OMZ), of the Iberian Hercynian belt, more precisely in the Alter do Chão-Elvas Domain. The Blastomilonitic belt, through the Alter do Chão thrust, limits the Northeast sector of this domain, while the southern limit is related to the Juromenha thrust (Gonçalves, 1973). This Zone represents a complex evolution of a continental margin during the Late Paleozoic associated to the convergence and collision of two large continental masses, Gondwana and Laurasia (Dallmeyer and Quesada, 1992). Cabeço de Vide thermal spa is located in the Alter-do-Chão pluton, a ring-like intrusion with a NW-SE elongated shape following the Variscan orientation, where the Lower Cambrian carbonate sequence suffered metamorphosis by the local mafic and ultramafic intrusions (Marques et al., 2008).

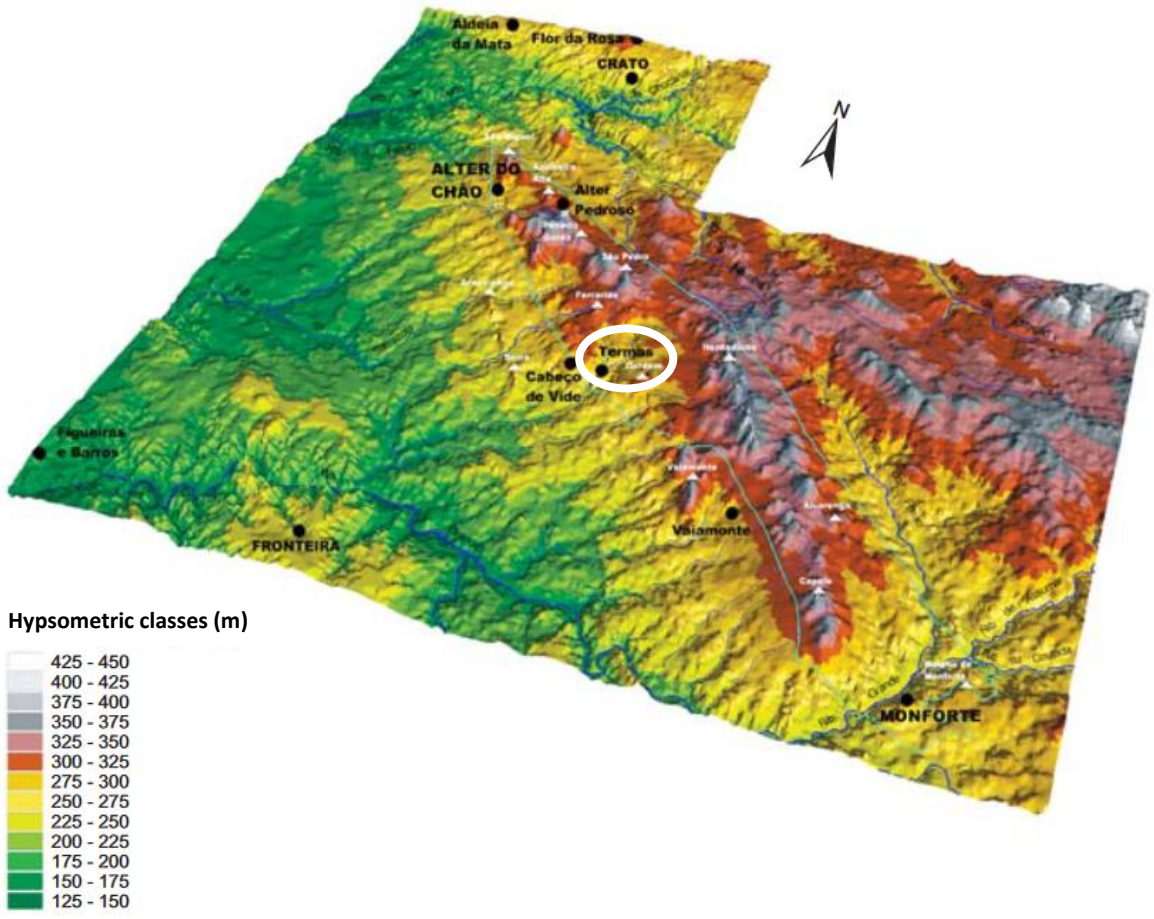

Figure 14: Geomorphological digital model of the Monforte-Alter do Chão Aquifer System with 10x elevation. Termas da Sulfúrea area is highlighted in the map with a white circle (Adapted from: Fernandes & Francés 2010).

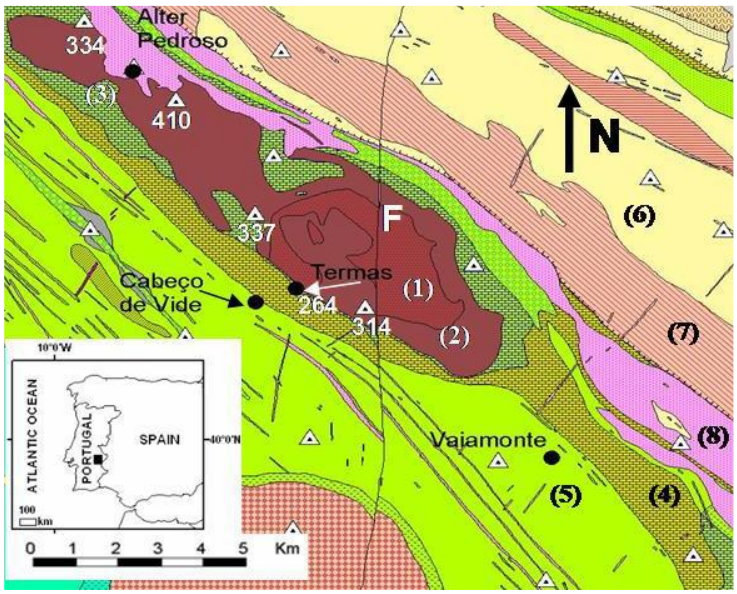

Figure 15: Representation of the location and geological map of Cabeço de Vide area (Marques et al., 2008).

CdV spring and borehole mineral waters (Figure 15) issue at the intrusive contact between the mafic and ultramafic rocks (1 and 2) and the carbonate sequence (4), associated with the main regional NNE-SSW trending fault (F). Several other distinct geological formations can be found and observed in the surroundings of the study region, including Precambrian metamorphic rocks (6) (schists and greywackes), Cambrian chloritized schists, quartzites, greywackes (5) and orthogneisses dated at 466 ± 10 Ma and some hyperalkaline syenites, that are the most representative ones (Marques et al., 2008, 2018).

In Cabeço de Vide, everything points to two different intrusive episodes: one dominantly ultrabasic and a posterior one with gabbroic nature (Pinto et al., 2003). The peridotite facies contain olivine, pyroxene and some plagioclase (altered by zeolites) and they are mostly serpentinized and/or show high grades of alteration of olivine to magnetite and serpentine, including strong chloritization of pyroxenes. The gabbroic lithologies differentiate from the previous facies since they don't show a metamorphism grade as intense as the one shown in ultrabasic rocks, and they are composed mainly of olivine, plagioclase and some hornblende (Pinto et al., 2006).

Serpentinites represent structures that would have originally been composed, almost exclusively, of olivine (dunites), despite representing strongly altered lithologies (serpentinized and through magnetitization), therefore the ultramafic rocks range from serpentinites to partially serpentinized dunites. Most commonly, the serpentinized ultramafic rocks contain serpentine minerals (lizardite, antigorite and chrysotile), magnetite, residual chromite, brucite and carbonates. Excessive quantities of antigorite are shown by the presence of lighter layers in the more altered areas (Pinto et al., 2006). Mafic rocks outcropping in the

surroundings of the ultramafic core are mostly coarse-to fine-grained gabbros with Ca-plagioclase, Ti-clinopyroxene, olivine and some Al-hornblende (Costa et al., 1993).

Costa et al. (1993) suggests two major theories: i) serpentinization of the ultramafics and rodingitization of the gabbros seem to be simultaneous, partly complementary hydrothermal mechanisms and ii) serpentinization-rodingitization processes in the Alter-do-Chão massif took place at low-pressure conditions and over a wide range of temperatures, evolving from amphibolite to upper prehnite-pumpellyite facies.

This thesis focuses on whole-rock samples from AC2, a nearly vertical borehole, close to the contact between the serpentinized peridotite and carbonate host-rocks. According to Ribeiro da Costa & Barriga, (2020), it is expected to find serpentinites between depths of 30 and 120 meters, as they represent a major portion of this drill core.

The presence of rock porosity and/or presence of faults or fractures in this hydrogeochemical system influences the growth of microorganisms, a fact that highlights the astrobiological importance of Cabeço de Vide. Compared with other Portuguese mineral waters, Cabeço de Vide mineral waters present an unusual hydrochemistry, as they are chloride rich, oxydrilic and sulphidric. Its mineralization was possibly acquired under hydrothermal conditions, during the circulation of the meteoric waters through the fissures of the ante-hercynian igneous rocks present in the study area. The emergency is controlled by the valley of the Ribeira de Cabeço de Vide and by the contact between the massif of ultramafic/mafic rocks and the Cambrian carbonate sequence.

Hydrogeologically, the Monforte-Alter do Chão aquifer system results from the hydraulic connection between two main shallow aquifer systems that can be found in the interest area:

1. A fissured/fractured aquifer system formed by the serpentines outcropping in the region. These serpentines formed through hydration of olivine-rich ultramafic rocks at relatively low temperatures. The typical combination of minerals products from serpentinization processes results in a dark green to black rock whose groundwater flow is determined by the fissure/fracture network (Marques, 2018). Most local surface (e.g., Ribeira sample, from CdV stream) and shallow (e.g., AC3 and AC5 boreholes) groundwaters discharging from the serpentinites belong to the Mg-HCO_3 type (Marques, 2008). Serpentine dissolution might be the reason why high concentrations of Mg^{2+} and SiO_2 were found in the local Mg-HCO_3-type waters (e.g., Barnes et al., 1967).
2. The fissured/karstified Cambrian limestone aquifer system of Monforte-Alter-do-Chão, which also includes the fractured gabbroic geological formations of the Mafic Complex of Alter do Chão-Cabeço de Vide. In this aquifer system, groundwater circulation appears to be strongly influenced by the fissure/fracture network that affects both geological formations, with no difference in behavior

between the dominant limestones and the gabbros (Fernandes & Francés, 2010). Groundwaters issued within the limestones are Ca-HCO_3–type waters, with neutral of slightly basic pH, and medium-to-high mineralization. This type of water is associated with gabbroic rocks and some springs are situated at the geological contact with the metamorphized limestones (Marques et al., 2019).

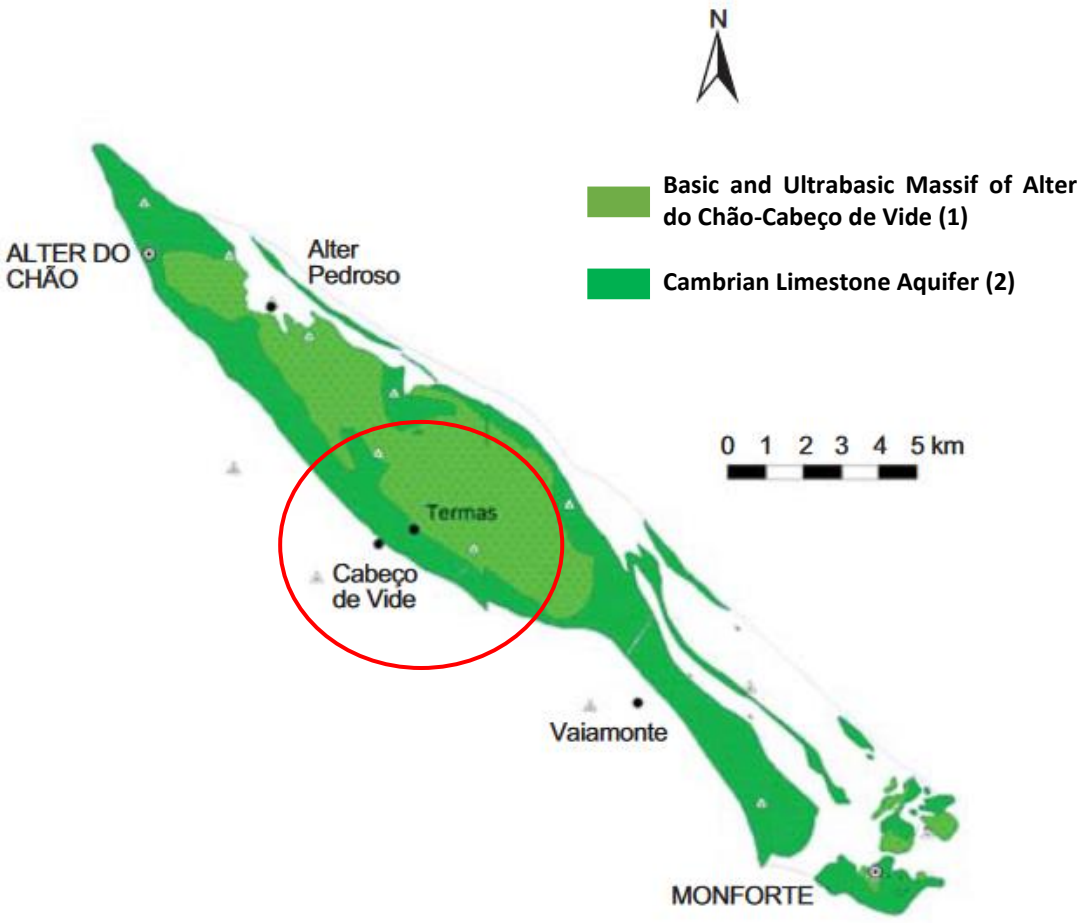

Figure 16: Hydrogeological fitting of the two aquifer systems in Cabeço de Vide, highlighted with a red circle (Adapted from Fernandes & Francés, 2010).

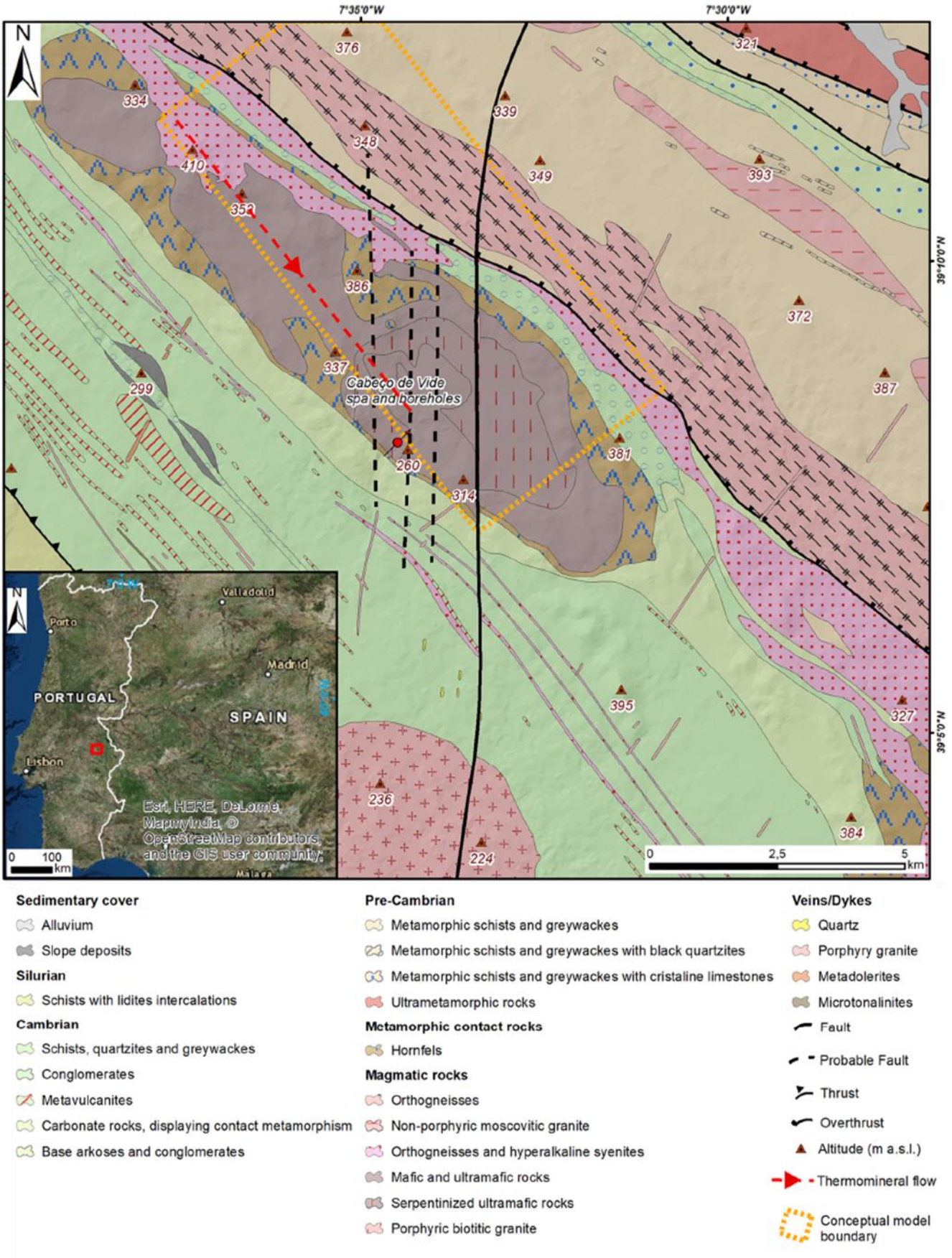

Figure 17: Location and geological map of the CdV region (Marques et al., 2018).

All this information is very important when studying Cabeço de Vide (CdV) and it helps us understand the phenoms that happen in this region, since CdV mineral waters have attracted significant scientific attention for a long time, due to its uncommon chemical composition and complex geological and hydrogeological conditions (Ferreira & Mendonça, 1990). Studies that establish a relation between Mars and the study area focus mainly on the characteristics of the water of the spa and boreholes. The unique features of these waters are produced due to the weathering of serpentinized and gabbroic rocks. Such type of groundwaters infiltrate at depth, along major faults, and evolve to hyperalkaline thermomineral waters, resulting from hydration of olivine and pyroxene, from fissured/fractured dunite rocks, in a deeper and closed system (Marques et al., 2019).

One of the main goals of the Mars 2020 mission is to collect Martian rock and soil samples through a drilling device and store them in sealed tubes for pickup by a future mission that would bring them back to Earth for more detailed analysis, so the information collected on rock and soil samples from terrestrial Mars analog samples is crucial for interpretation of the data acquired by rovers on Mars. This document studies and focuses not only on the hydrogeological characteristics of Cabeço de Vide, but also on the geological features of this region, studying water samples from springs and boreholes, along with core samples collected, as an analog for the study of possible past and present life on Mars. As mentioned previously, CdV is proposed as an excellent mineralogical environment to study as a Mars analog, as serpentine detections have been reported at the Mars 2020 Perseverance rover landing site, Jezero Crater (Vance et al., 2020). The simultaneous presence of serpentines, pyroxene, olivine, smectite and carbonates in both Cabeço de Vide (Rocha et al., 2017) and Jezero Crater (Simon et al., 2023) emphasize the mineralogical similarities between both sites, as serpentinization has also been proposed as a formation mechanism of Jezero Crater carbonates (Brown et al., 2020)

4. Materials and Methods

4.1. Sample Location

Rock samples from mineral water exploration borehole AC2 were collected for chemical and minero-petrographic characterization in order to achieve proposed objectives and to assess water-rock interaction processes occurring at depth. Samples were selected according to characteristics such as level of alteration and depth, they were collected using sterilized cups and bags. AC2 borehole has continuous sampling until 124 meters depth, and some rock fragments up to 127.90 meters. It is important to note that serpentinites represent a thick portion of the drill core AC2, between depths of 30 and 120 meters (Ribeiro da Costa & Barriga, 2022), and it can be confirmed by the color of the samples: lighter on lower depths from the carbonate domain and darker as the drill core goes deeper into the serpentinite domain.

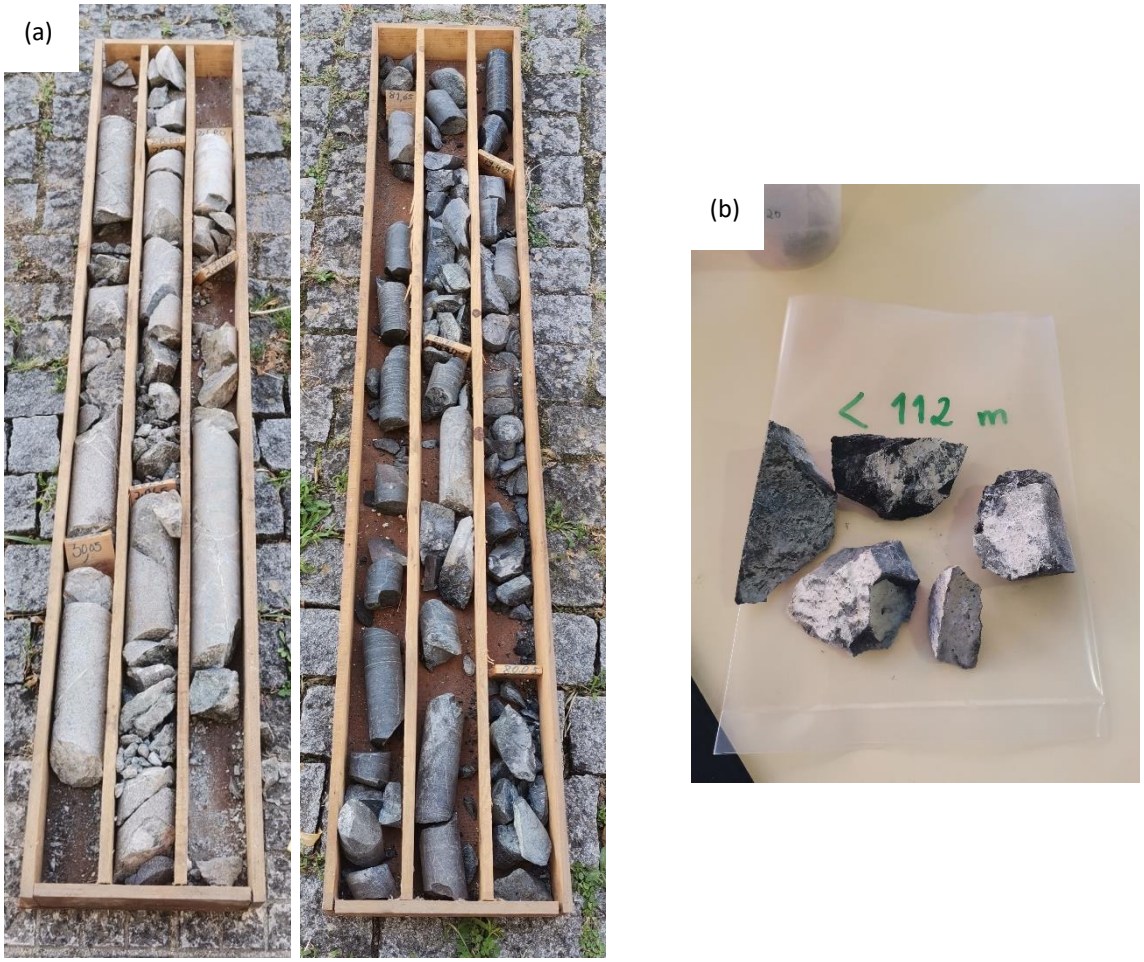

Figure 18: (a) Rock samples used in their core drawers; (b) sample after being broken shows a white layer that represents a fracture vein, that when scratched, turns into a fine dust.

Water samples were collected from streams, springs, and boreholes present in CdV spa park and used in treatments and also used by population, using sterilized bottles with 1L capacity (1st campaign) and falcon tubes with 50 ml capacity (2nd campaign). A map was created in order to visualize where the samples are located, how distant they are from each other (Figure 20), and their coordinates are represented in Table 2. These samples include AC5 and AC3, two boreholes pumping hyperalkaline mineral water from depths of 126 m and 119 m, respectively; Ribeira, a sample collected from CdV stream; Ermida, a hyperalkaline water spring; and Borbologão (Fonte), a non-alkaline normal spring, and these samples were labeled according to the names mentioned previously (Figure 19).

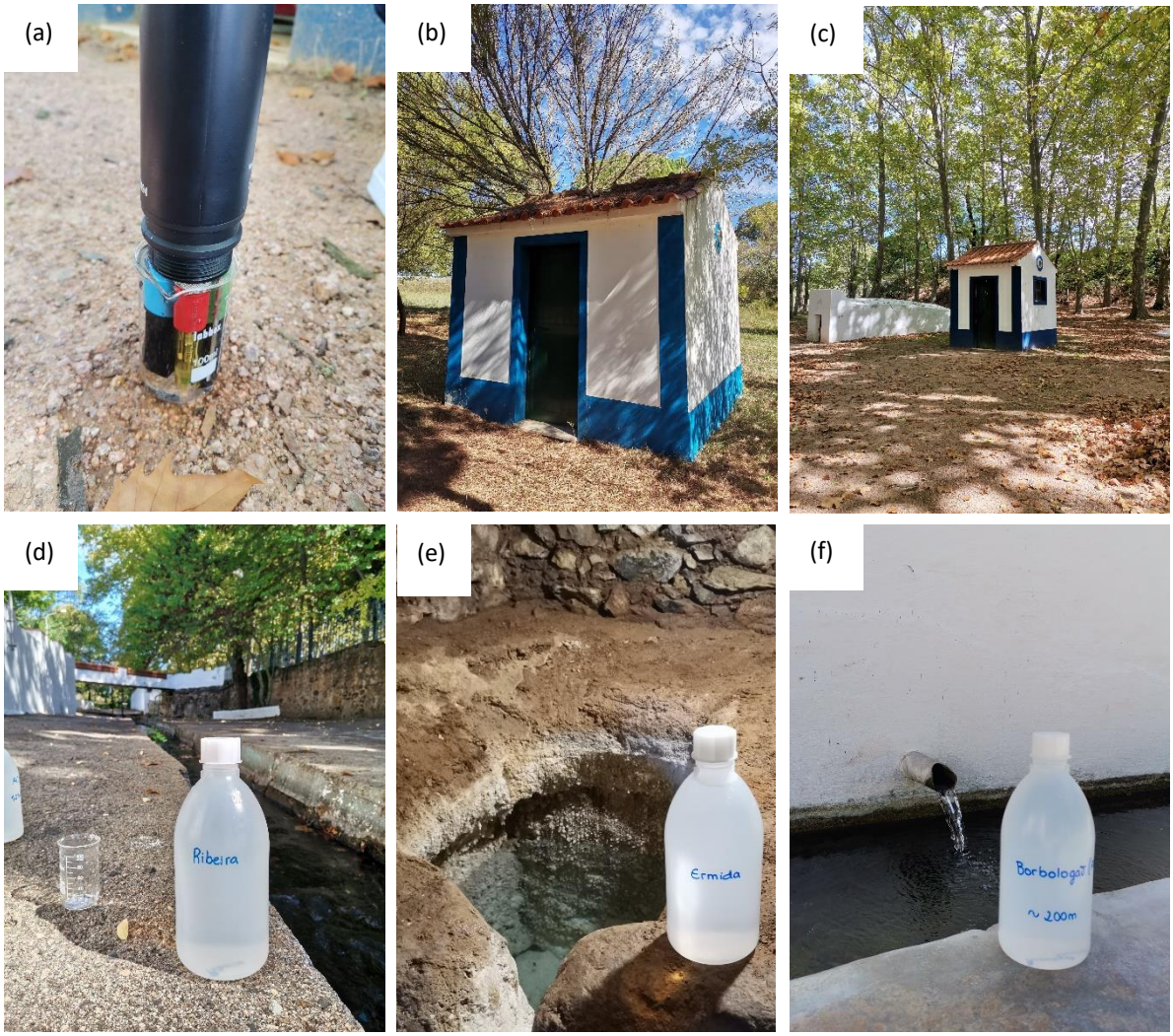

Figure 19: (a) Multiparameter used; water samples location and respective bottles in the study area: (b) AC5 borehole; (c) AC3 borehole; (d) Ribeira or CdV stream; (e) Ermida spring; (f) Borbologão (Fonte) spring.

Figure 20: Map of the CdV spa area with water sample location, with coordinates in ED50 system for zone 29N, representative of mainland Portugal.

Table 2: CdV Water samples coordinates (in WGS84 standard coordinate system).

Sample Reference	Coordinates
AC5	39’08'0”.0"N 7’34'4”.3"W
AC3	39’08'0”.0"N 7’34'4”.2"W
Ribeira	39’08'0”.0"N 7’34'4”.0"W
Ermida	39’08'0”.0"N 7’34'4”.5"W
Borbologão (Fonte)	39’08'0”.9"N 7’34'4”.1"W

4.2. Sample Preparation

In order to achieve stipulated objectives in what concerns a detailed mineralogic, petrographic and geochemical description of the interest samples (whole rock), these same samples had to be meticulously prepared in laboratory, following a series of steps and protocols to prevent any possible contamination and so that the correct part of the sample is extracted.

Initially, a tray covered in special aluminum foil (UHV Foil, All-Foils Inc.) was prepared, including single pieces of the alumina foil to store samples. These samples were scratched using Dremel (model 3000), with a diamond wheel point with a round head (2 mm diameter), while hanging from a heavy steel support, like shown in Figure 21. The speed modes used were 4 and 5, corresponding respectively to 19000 and 20000 rotations per minute (RPM). Before the treatment of each sample, the alumina foil in the tray was sterilized (ashed at 550°C/3 hrs), in addition to every tool used during this process. This method showed great results, as the diamond wheel point is effective in removing the interest part of the sample from the initial fragment, as shown in Figure 22.

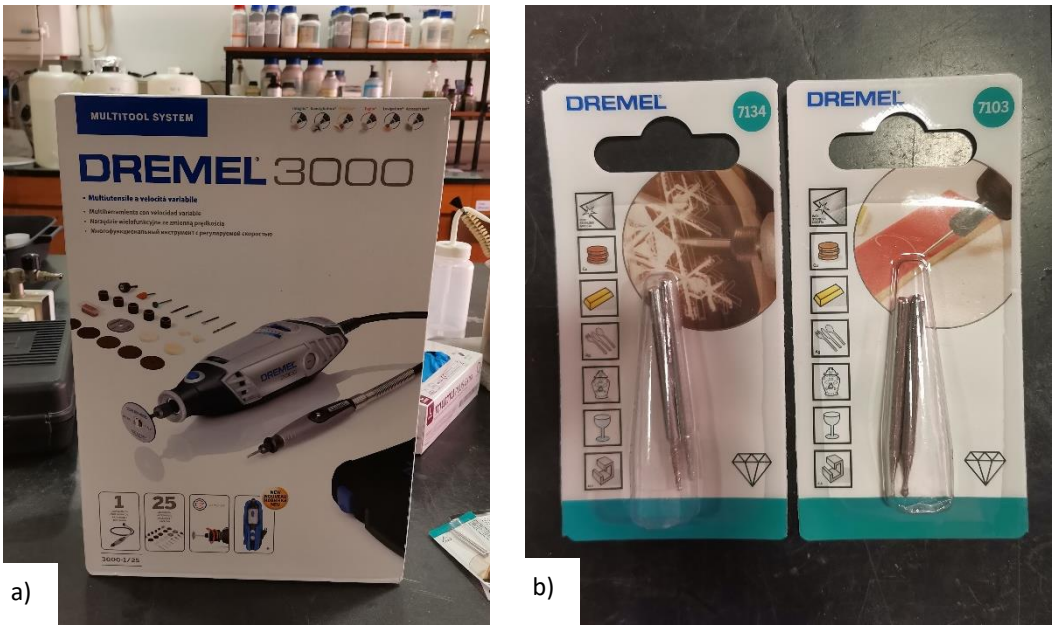

Figure 21: a) Dremel 3000; b) Diamond wheel points used (Flat and round head).

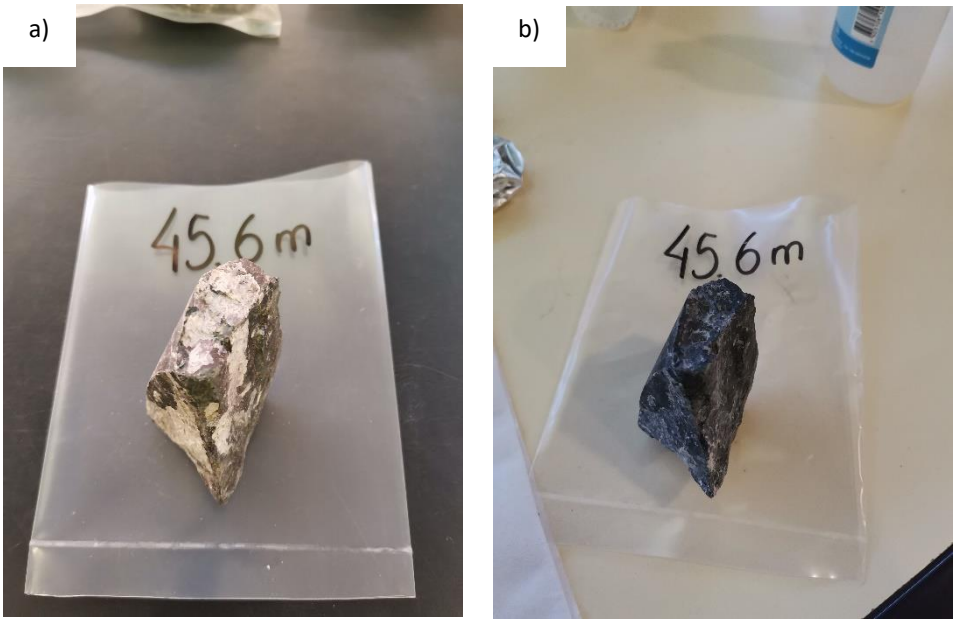

Figure 22: Sample CdV45.60 a) Before and b) After being scratched with Dremel to make CdV45.60W sample.

In order to help with the petrographic and mineralogical description of the samples, three thin sections were made from the same core sample, in different orientations, labeled from 1 to 3, according to depth 125,20 meters. This sample stands out due to a noticeable carbonate layer that crossed the whole core sample that is important to achieve some objectives of this thesis (Figure 23). The thin sections made and their orientation are shown by the lines in Figure 24.

Figure 23: Core sample used to make thin sections for analysis. CdV125.20_1 to 3 label the different thin sections and A-A' represent the orientation of the thin sections.

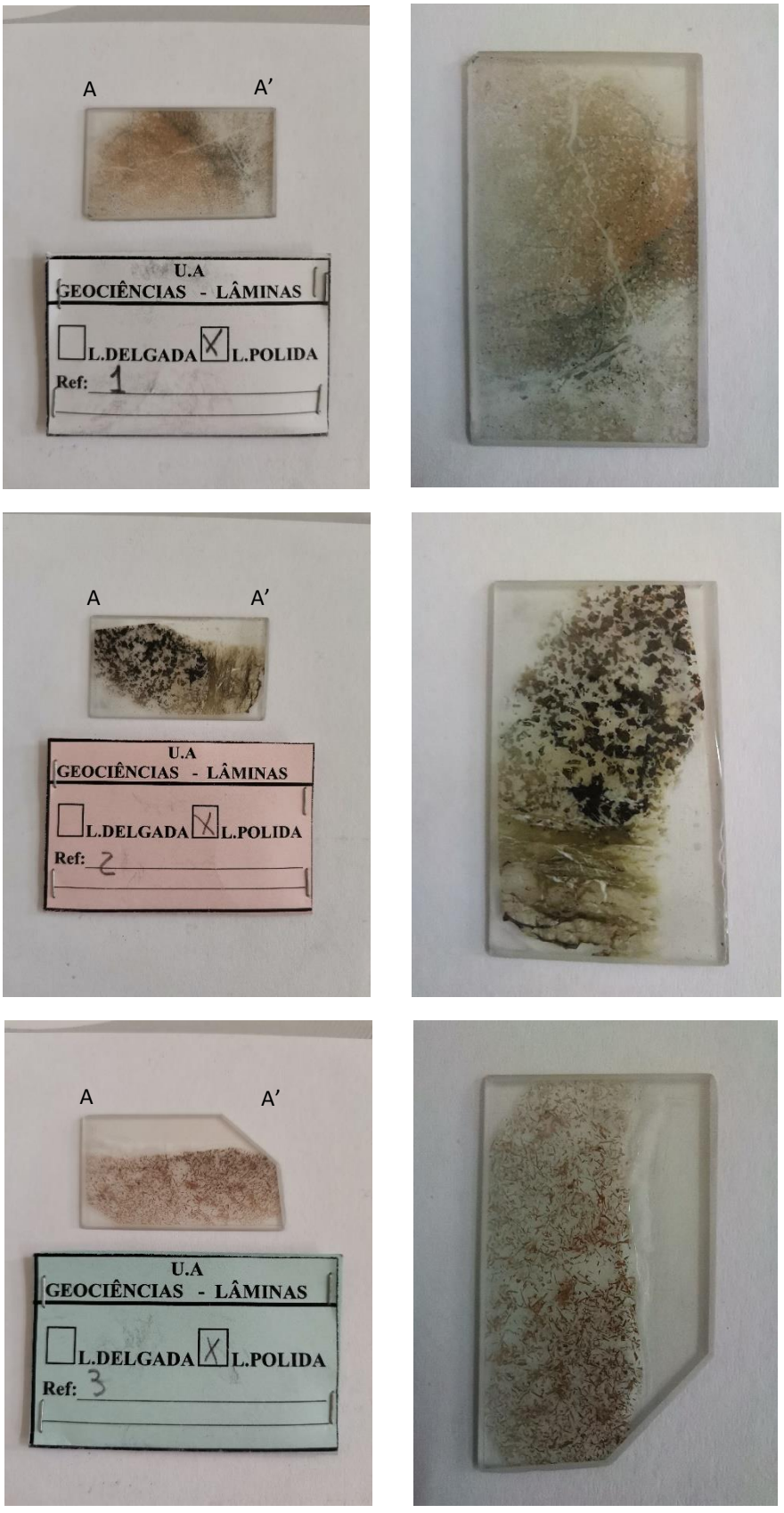

Figure 24: Thin sections CdV125.20_1 to 3. A-A' represent the orientation, as seen in Figure 23.

Finally, the samples were labeled according to depth (whole samples, like CdV26.80, that labels the representative whole sample from 26.80m depth for example) and layer (partial samples): the letter W represents the fractures present in the samples, or the white part, and B represents the black part, representative of the matrix of the samples. CdV125.20_1 to CdV125.20_3 are not whole or partial samples, as they represent samples used from the same core sample to make the thin sections previously mentioned, so they're represented in Table 3 with *. CdVR1 and CdVR2 express each calcite precipitation sample collected from the Ermida spring, where R1 corresponds to the sample that was emersed in water and R2 was submerged. All this information is summarized in Table 3.

Table 3: Sample references according to their depth, layer and contact with hyperalkaline water (for R1 and R2).

Bulk Sample	Partial Sample	Depth (m)
CdV26.80	CdV26.80W	26.80
	CdV26.80B	
CdV27.00	CdV27.00W	27.00
	CdV27.00B	
CdV28.00	CdV28.00W	28.00
	CdV28.00B	
CdV42.85	CdV42.85W	42.85
	CdV42.85B	
CdV45.60	CdV45.60W	45.60
	CdV45.60B	
CdV80.25	CdV80.25W	80.25
	CdV80.25B	
CdV80.80	CdV80.80W	80.80
	CdV80.80B	
CdV112.00	CdV112.00W	112.00
	CdV112.00B	
CdV113.15	CdV113.15W	113.15
	CdV113.15B	
CdV116.00	CdV116.00W	116.00
	CdV116.00B	
	CdV125.20_1*	125.20
	CdV125.20_2*	
	CdV125.20_3*	
	CdVR1	Emersed
	CdVR2	Submerged

4.3. Laboratorial Characterization

To achieve the main goal of this document in the detailed petrographic and geochemical description of the Cabeço de Vide ultramafic rocks, laboratory studies were made. These studies are very important to identify textural, mineralogical, physico-chemical, crystallochemical and biological features that are crucial to the study of the serpentinization process, providing a detailed database concerning the compositional features of our samples and their serpentinized derivatives exhibiting variable degrees of serpentinization.

Mineralogical experiments include X-Ray Diffraction (XRD), in order to determine the mineralogical composition of the samples, combined with a petrographic description through the detailed analysis of three thin sections of a collected core sample, as well as Scanning Electron Microscopy (SEM). Whole-rock geochemical data and physico-chemical properties were obtained by X-Ray Fluorescence (XRF), Attenuated Total Reflectance Fourier-transform infrared spectroscopy (ATR-FTIR). Four samples were also sent for Mössbauer Spectroscopy studies, as the data analyses and discussion from this method is still ongoing work.

To determine the astrobiological potential related to serpentinization, DNA extraction was made using methods frequently used in Biology Department of University of Aveiro (DBio-UA) and using PureLink's Microbiome DNA Purification Kit for Soil Samples.

4.3.1. Water Characterization (Filtration, in-situ data and ICP-MS)

After the first field campaign, on the day after collection, water samples were filtered with 0.45 µm filters (Millipore) in low pressure, shown in Figure 25. All the data from the filtration is mentioned in Table 4, where ΔF refers to the difference in weight from the filters, after spending 14 days on a greenhouse in 40°C temperature and 19 days with ambient temperature and humidity conditions, or in other words, the amount of material present in the filters in the end of the filtration process. All water samples were then stored at 4°C.

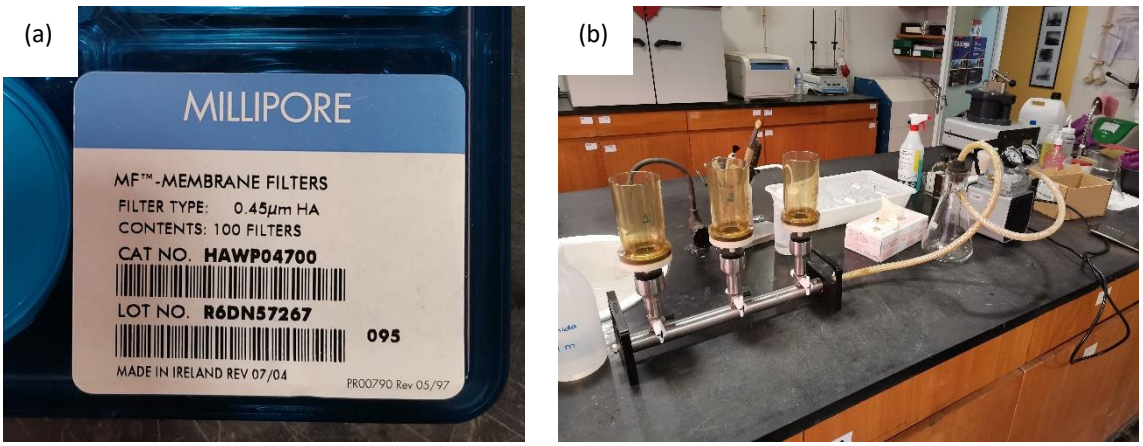

Figure 25: Millipore filters used during the filtration of water samples (a) and equipment used during this experiment (b).

Table 4: CdV Water filtration data from the first field campaign samples.

Filtragem			
##	F (inicial) (g)	F (final) (g)	ΔF (g)
AC3	0.0823	0.0823	0.0000
	0.0835	0.0836	0.0001
	0.0793	0.0794	0.0001
AC5	0.0835	0.0836	0.0001
	0.0795	0.0797	0.0002
	0.0814	0.0817	0.0003
Ermida	0.083	0.0838	0.0008
	0.079	0.0832	0.0042
	0.0802	0.0804	0.0002
Fonte	0.0787	0.0796	0.0009
	0.0793	0.0793	0.0000
	0.0805	0.0817	0.0012
Ribeira	0.0802	0.082	0.0018
	0.0775	0.0805	0.0030
	0.0815	0.0835	0.0020

During the second campaign, the same water samples were collected, and were filtered in-situ, using a portable filter unit with the previously used Millipore 0.45 µm filters, attachable to a 50mL syringe, as seen in Figure 26. Water physico-chemical parameters, including pH, conductivity, oxidation/reduction potential and temperature, were measured *in situ* using digital multiparameters shown in Figure 27. All water samples were analyzed using ICP-MS for cations, in HNO_3 acidified samples, and ionic chromatography for fluoride, chloride, sulfate, bromide, nitrate and phosphate, in non-acidified samples, in DGeo, UA.

Figure 26: Portable filter unit used during in-situ filtration of CdV water samples.

Figure 27: Multi parameters used to measure pH, conductivity, temperature and ORP in-situ.

For the study of chemical elements present in the chemical composition of waters from CdV stream, springs and boreholes, these were analyzed with Inductively Coupled Plasma Mass Spectrometry in Geochemistry Laboratory of DGeo, UA, and it is a highly sensitive elemental analysis technology capable of detecting most of the elements from the periodic table at milligram or even nanogram levels per liter, as each element has its specific detection limit value. This technique works on the basis of the decomposition of samples to neutral elements in high temperature argon plasma and these samples are then analyzed based on their mass to charge ratios (Fernandez-Turiel et al., 2000). For this analysis, samples were acidified (1% v/v HNO_3) (Figure 28) and stored at 4°C. The analysis of bigger anions, like fluoride (F^-), chloride (Cl^-), sulfate (SO_4^{2-}), bromide (Br^-), nitrate (NO_3^-) and phosphate (PO_4^{3-}) was made with ionic chromatography in Hydrochemistry Laboratory of DGeo, UA.

Figure 28: 1% volume HNO_3 used and CdV water samples ready to be analyzed.

The full chemical composition of CdV waters studied is present in Attachments 1, where they are separated in 1st campaign data and 2nd campaign data, with respective analytical and unit symbol, as well as the respective quantification limits for each chemical element studied.

4.3.2. Mineral Characterization by X-Ray Diffraction (XRD)

X-ray diffraction (XRD) is an important, non-destructive and widely used material characterization technique. X-rays have wavelengths comparable to atomic size, and therefore, intensities of X-ray diffraction technique or diffraction patterns are used to harness information about minerals' atomic structures. XRD is a non-destructive testing technique, which can be employed for examining a wide range of materials, including minerals, ceramics, polymers, and others. When the X-rays hit solid materials, they become dispersed by the electrons orbiting around the nucleus of atoms. These dispersed waves, emitted in various directions, interact with each other. Diffraction is the constructive interference of scattered X-rays, since the orderly arrangement of atomic structures in solids causes constructive interactions, also considering the fact that these interferences can be destructive or constructive (Ali, 2022).

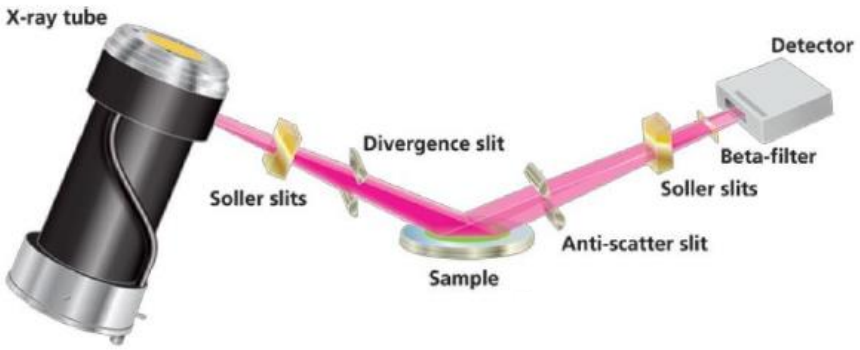

Figure 29: Figurative example of how XRD works (Source: Ali, 2022).

Since every mineral species has a specific crystalline structure, each mineral species has a specific diffraction model, when exposed to a direct beam of X-ray with certain wavelength, depending on the nature of the X-ray anti-cathode tube used. Following Bragg's equation, diffraction occurs when a monochromatic beam of X-rays with wavelength λ hits the crystalline network planes under a certain angle θ and the distance traveled by the reflected rays on successive planes differs by an integer number of n wavelengths (Ali, 2022).

$$\text{Bragg's equation: } n\lambda = 2d \sin\theta$$

During this thesis, two types of analysis were performed: Non-oriented aggregates and oriented aggregates. Non-oriented aggregates are designated due to the fact that the sample preparation is made in dry environment, so the crystals don't have time to become orientated. Oriented aggregates, however, are made in liquid environment, so the particles have time to settle according to their preferential orientation, where the clay fraction is separated from the bulk sample, allowing the X-Ray beam to directly hit the z axis of the minerals. Oriented aggregates analysis is made by making glass slides with the <2µm fraction of the sample, running the program from 2° to 20° θ (Figure 30).

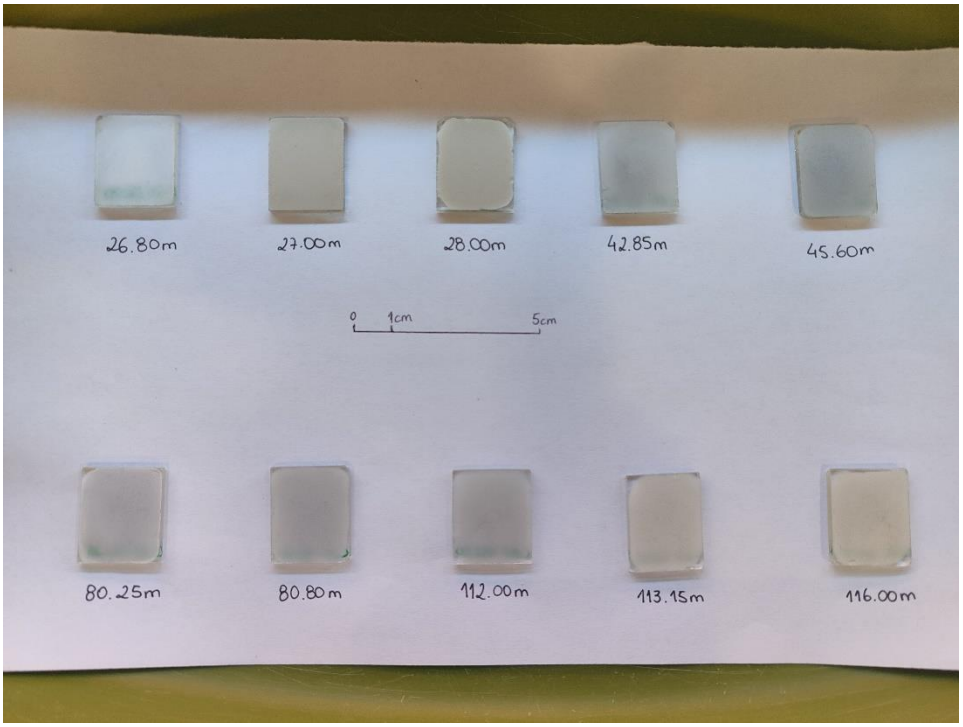

Figure 30: Glass slides with <2µm fraction of CdV whole samples.

XRD measurements were performed using model X'Pert Pro from Panalytical diffractometer (Figure 30) using Cu Kα radiation (I=1,5405 Å) and scans were run between 2° and 65° θ, on a long run program. Semi-qualitative mineralogical analysis of the samples was performed using the HighScore Plus 4.9 program (Malvern Panalytical) with respective mineralogical database, assisting the interpretation of the diffractograms and then correlating them with Brindley & Brown charts.

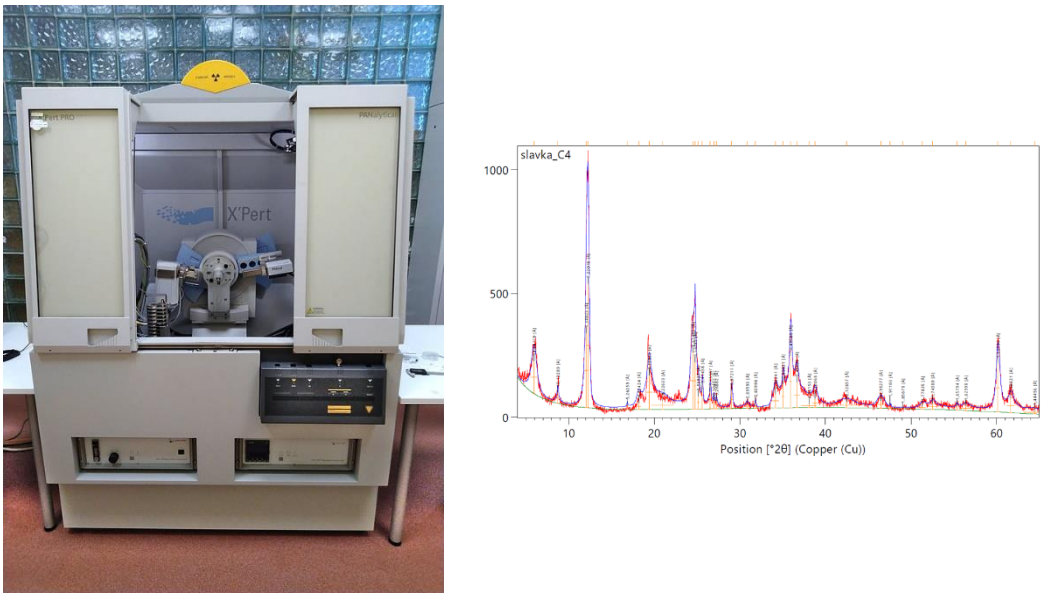

Figure 31: Diffractometer and an example of diffractogram.

Semi-quantitative analysis was also performed exclusively in whole samples, that are representative of their respective depths. This method consists of calculating the areas of the respective maximum intensity peak for each mineral, correcting the same area with a correction factor, with reflective power, specific for each mineral, according to the capability each mineral has of diffracting incident X-Ray beams. Every corrected areas are added, and every relative mineral percentage is finally recalculated to 100%. The table below shows the reflective powers of minerals present in CdV whole samples.

Table 5: Reflective Power of the Minerals found in CdV samples.

Mineral	Reflective Power
Serpentines	0.5
Amphiboles	0.75
Calcite	1
Chlorite	0.75
K-Feldspar	1
Magnetite-Maghemite	1.3
Phlogopite	0.5
Smectite	4
Talc	0.8

It is also important to note that every mineral symbol used during this thesis, mentioned in the List of Acronyms, are symbols approved by the International Mineralogical Association (IMA) Commission on New Minerals, Nomenclature and Classification (CNMNC), referenced by Warr (2021).

4.3.3. X-Ray Fluorescence Spectrometry (XRF)

X-Ray Fluorescence Spectrometry (XRF) is a technique used to analyze major, minor and trace chemical elements that have an atomic number bigger than nine (Z > 9), with concentration values either in percentage or ppm. This type of chemical analysis is based on the photoelectric absorption effect, where all the chemical elements present in a sample are excited by a polychromatic beam of primary X-Rays with certain energy, emitting secondary radiation or fluorescence (Figure 32).

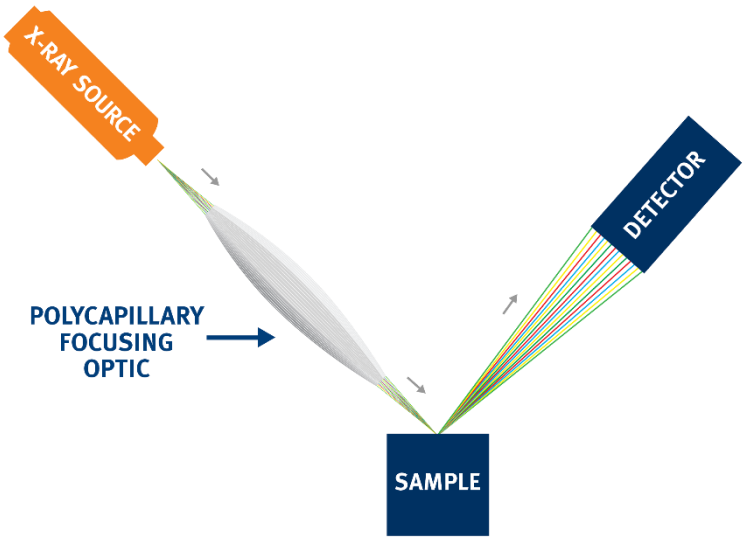

Figure 32: XRF Spectrometry example (Source: https://www.xos.com/XRF).

This radiation is dispersed by analyzing crystals or dispersers in a way that allows the elements' secondary radiations to be resolved and then captured by proportional detectors or flickering. Finally, it is necessary to establish a correlation between the measured intensities and the concentration of the chemical elements measured. This method is relatively fast and accurate, and it is the main method of chemical analysis in clays and clay minerals (Gomes, 1988).

Summarizing, 10g of sample were weighted to a plastic cup and 6 to 8 drops of a binding agent (Mowiol Polyvinyl Alcohol 2%) were added. Sample was homogenized and put in a press inside a specific mold, where it was subjected to compressive strength up to 15 t. The final sample (Figure 33) was then analyzed by XRF.

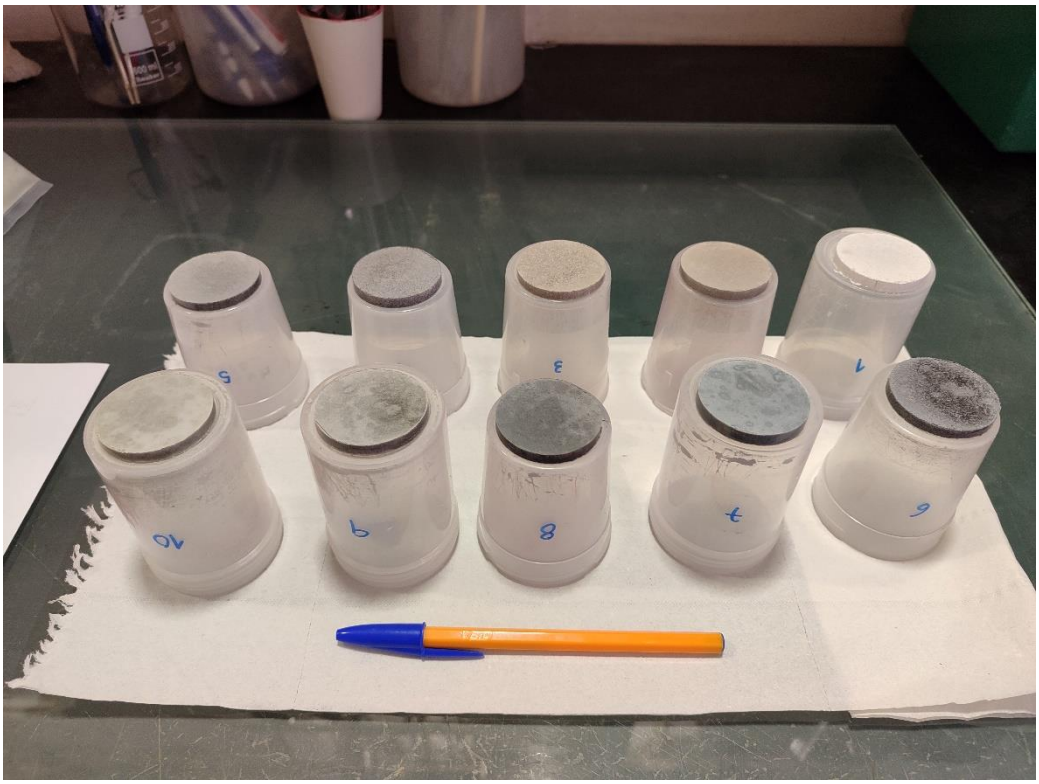

Figure 33: Sample tablet ready for XRF analysis.

Partial samples are put into a small cylindrical sampler, due to the lower quantities of sample available, in order to allow the X-Ray beam to pass through the sample (Figure 34).

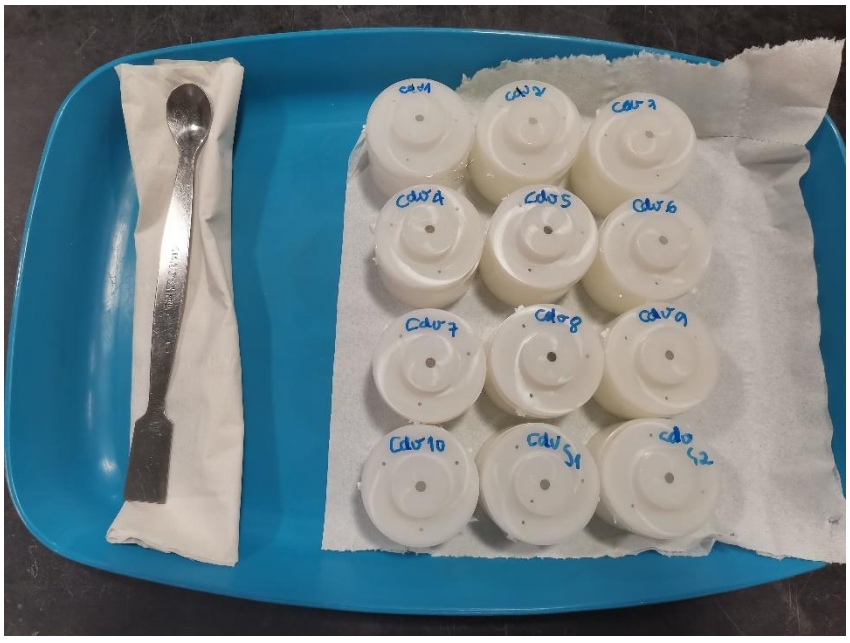

Figure 34: Cylindrical samplers where partial sample was stored, for XRF analysis.

4.3.4. Attenuated Total Reflectance Fourier-transform infrared spectroscopy (ATR - FTIR)

Fourier-transform infrared spectroscopy (FTIR) can provide fundamental information on the molecular structure of organic and inorganic components and has been used extensively for chemical characterization of geological samples in the past few decades. FTIR is one of the most versatile analytical techniques for the non-destructive, chemical characterization of geological samples, such as minerals, shale, coal, and others. The basic fundamental mechanism of this technique is related to the transitions between quantized vibrational energy states. In FTIR analysis, absorption of infrared radiation results when a photon transfers to a molecule and excites it to a higher energy state (Chen et al., 2015).

FTIR was performed in a Bruker Alpha II Platinum ATR compact spectrometer, available in the Chemistry Department of Universidade de Aveiro (DQ-UA).

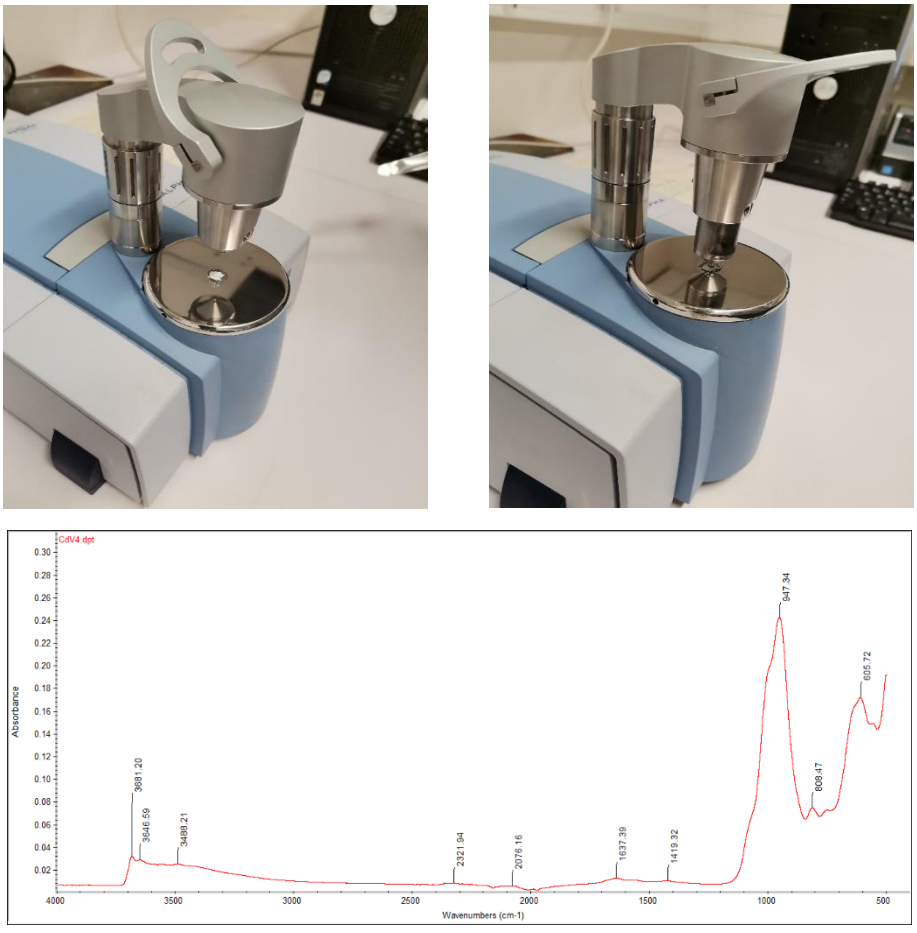

Figure 35: FTIR Spectrometer (on top) and resulting graph (bottom).

4.3.5. Mössbauer Spectroscopy

Mössbauer spectroscopy (MS) is a spectroscopic technique based on the Mössbauer effect, discovered in 1957 by Rudolf Mössbauer, who received the Nobel Prize in Physics in 1961 for his work. The Mössbauer effect consists of recoilless gamma ray emission and absorption due to conservation of momentum. This technique is widely used in mineralogy to examine the valence state of iron: Fe^0 (metal), Fe^{2+} and Fe^{3+}, as well as type of coordination polyhedron occupied by iron atoms, that can be trigonal, tetrahedral, octahedral, etc.). The inclusion of Mössbauer spectrometers on the Mars Exploration Rovers has added visibility and importance to this technique for processing and interpretation of data from Mars, due to the molecular hydrogen produced through iron oxidation during formation of serpentine and magnetite (Darby Dyar et al., 2006; Greenberger et al., 2015).

When considering iron in serpentine, it is usually assumed to be ferrous (Fe^{2+}), however it has been demonstrated that a significant amount of ferric iron (Fe^{3+}) can be incorporated into the serpentine structure. Trivalent cation is incorporated into the trioctahedral serpentine structure by a ferri-Tschermak's substitution or by an octahedral-vacancy model (Evans, 2008). So, in any case, serpentine can play an important role in Fe^{3+} storage that was once disregarded when estimating H_2 production (Andreani et al., 2013).

Majority of Fe^{3+} is present in serpentines in rocks that have been up to 75% serpentinized, after which serpentine becomes more Mg-rich with more Fe^{3+} in magnetite. Andreani et al., (2013) estimated that Fe oxidation within serpentine accounts for 80% of the total H_2 produced in 50% serpentinized rocks and 22-40% of the total H_2 produced in 90% serpentinized rocks, with the remaining H_2 from Fe^{2+} oxidation that goes into magnetite.

With this information in mind, identification of tetrahedral Fe^{3+} in serpentine indicates maximum H_2 production during serpentinization and the highest astrobiological potential. Understanding the serpentinization dynamics at natural sites requires the knowledge of iron content and redox state in natural serpentine minerals, and its relationship with both magnetite abundance, serpentinization degree, and the regional setting (Greenberger et al., 2015).

For this procedure, four samples were sent to the Mössbauer Spectroscopy Laboratory in Campus Tecnológico e Nuclear of Instituto Superior Técnico de Lisboa.

4.3.6. Scanning Electron Microscopy (SEM)

Scanning Electron Microscopy (SEM) is a versatile advanced instrument which is largely employed to observe the surface phenomena of the materials. The sample is shot in a SEM using high-energy electron and the outcoming electrons/X-rays are analysed. These outcoming electrons or X-rays can give information about morphology, composition, orientation of grains, crystallographic information of a material, and other features. This multipurpose instrument is also able to examine and analyse the materials with high resolution (Mohammed & Abdullah, 2019).

The SEM instrument is based on the principle that the primary electrons released from the source provide energy to the atomic electrons of the sample which can then release as the secondary electrons and an image can be formed, as these secondary electrons from each point of the sample are collected by detectors and treated to create high resolution images, pixel by pixel. The primary electrons produced and emitted from the electron gun are accelerated by heating or by applying high energy and are scanned across the sample surface by scanning coils in a raster pattern (Figure 36, left). Energy Dispersive X-Ray Spectroscopy (EDS) works together with SEM to provide qualitative and semi-qualitative results. These two techniques combined have the potential to introduce fundamental information that can't be provided by the common laboratory tests (Akhtar et al., 2018).

This analysis was performed in a 4th generation TESCAN VEGA Scanning Electron Microscope (SEM) with tungsten filament electron source, present in DGeo, UA (Figure 36, right).

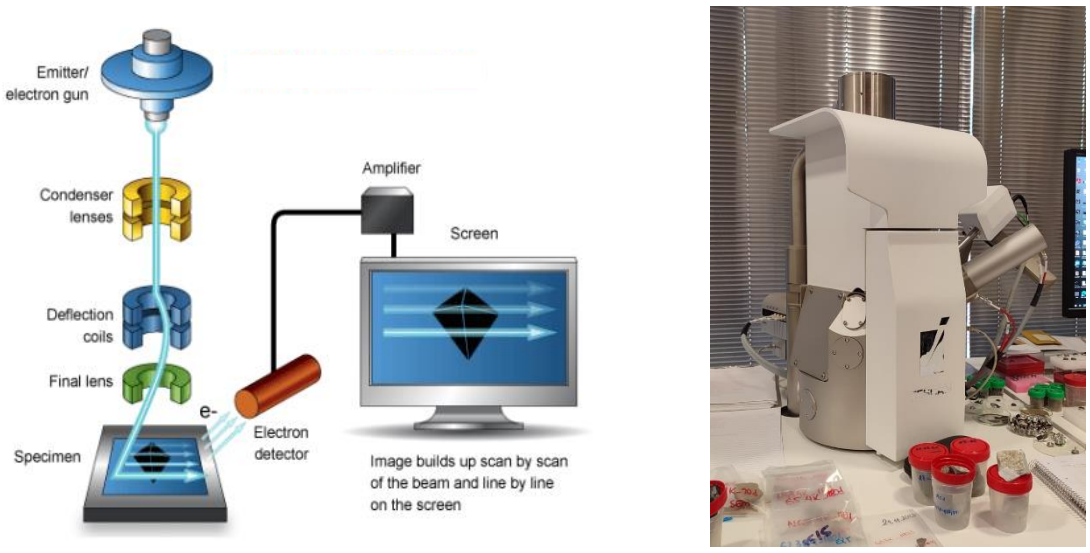

Figure 36: Schematic of a Scanning Electron Microscope (Adapted from http://www.ammrf.orf.au/) (left), and TESCAN VEGA SEM used to analyze CdV samples (right).

4.3.7. Thin section petrography

Thin-section petrography is polarized light microscopy of rocks and other mineral-containing materials, using samples ground to a standard thickness of 30 µm. This standard thickness gives known colors between crossed polarizers, facilitating the use of reference tables of mineral optics for identifying minerals and thus simplify the comparison of different samples between them. This method is regularly used in Geology to describe and classify rocks, soils and sand. It is also used in other specialties such as archaeology, to study many inorganic materials used during the production of certain cultural objects, including material identification and manufacturing technologies, and art, studying material, structural and mineralogical changes in surfaces and to study the effects of conservation treatments on those materials. One advantage of thin-section petrography is that the equipment necessary is relatively inexpensive in relation to the other types of equipment used. This type of analysis is a very efficient method to obtain important information, as it is often the most useful starting point for the study of inorganic materials (Reedy, 1994).

Thin sections are prepared through a number of steps, starting with cutting the core sample, mounting the desired side of the sample to the special glass used for thin sections using an epoxy resin with a refractive index similar to quartz, followed by a number of polishing procedures, with different powders, each with unique characteristics for a smooth finish on our interest sample, in order to achieve a uniform thickness of 30 µm.

Figure 37: Thin section made (CdV125.20_1) and a polarizing microscope.

4.3.8. DNA Extraction

Successful and efficient extraction of high quality, high molecular weight genomic DNA from the environmental samples is an essential primary step to understand the genetic, metabolic and evolutionary characteristics of the microbial communities.

Extraction will follow a number of specific steps that are represented in Figure 38.

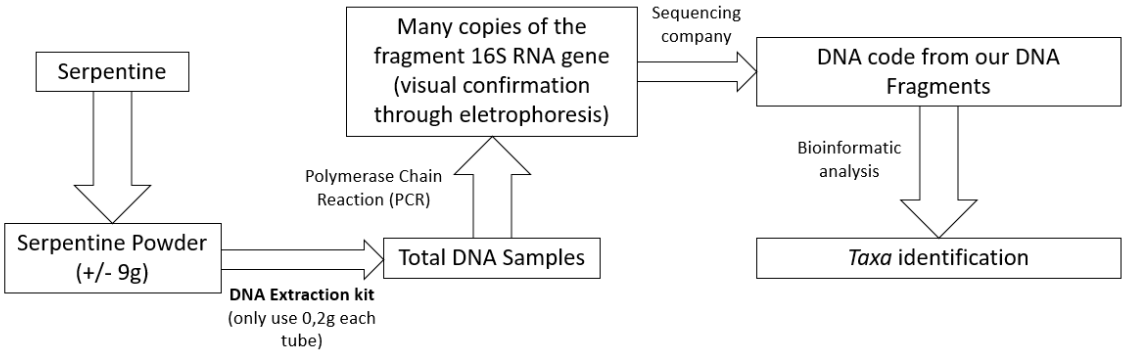

Figure 38: Workflow of the DNA Extraction made.

To gather samples for DNA analysis, it is required to have special attention to avoid any type of contamination of the sample core used. For this process, almost every step of the extraction of sample needs to be done inside a Laminar Flow Chamber (Figure 39), where everything inside of it has to be disinfected and there are protocols to follow. The process starts with the sterilization of the sample, where first we sanitize the core and all materials used with ethanol, including drill points, petri cases, spatulas and tweezers, and expose everything to UV light for fifteen (15) minutes each side. It is important to mention that every time some operation outside of the chamber needs to be done, it is necessary to sanitize what goes back inside with ethanol (hands, drill points, drill itself, etc.). The core is wrapped in thick layers of UHV aluminum foil to bring outside of the chamber to be hit with a hammer, in order to later access the inside of the core and allow extraction of untouched serpentine sample. Once more inside of the chamber, the extraction of sample can be started, using a diamond wheel point with a round head (2 mm diameter) for Dremel often used, per example, for carving, as shown previously in Figure 21. This machine cannot be used during long periods of time, because the increase in temperature in the diamond wheel point while in contact with the sample can put the whole operation in danger, since high temperature can permanently damage any DNA possibly present in our sample.

Figure 39: Sample core inside flow chamber ready to be sterilized with UV light and whole equipment used.

To further prevent any possible contamination or a posterior DNA analysis of contaminated sample, only the inside part of the serpentine present in this core is scratched and used furthermore in this process, as shown in Figure 40 (a). The interest sample was stored in small sterile plastic tubes in a special cooler with a temperature of -20°C.

(a)

(b)

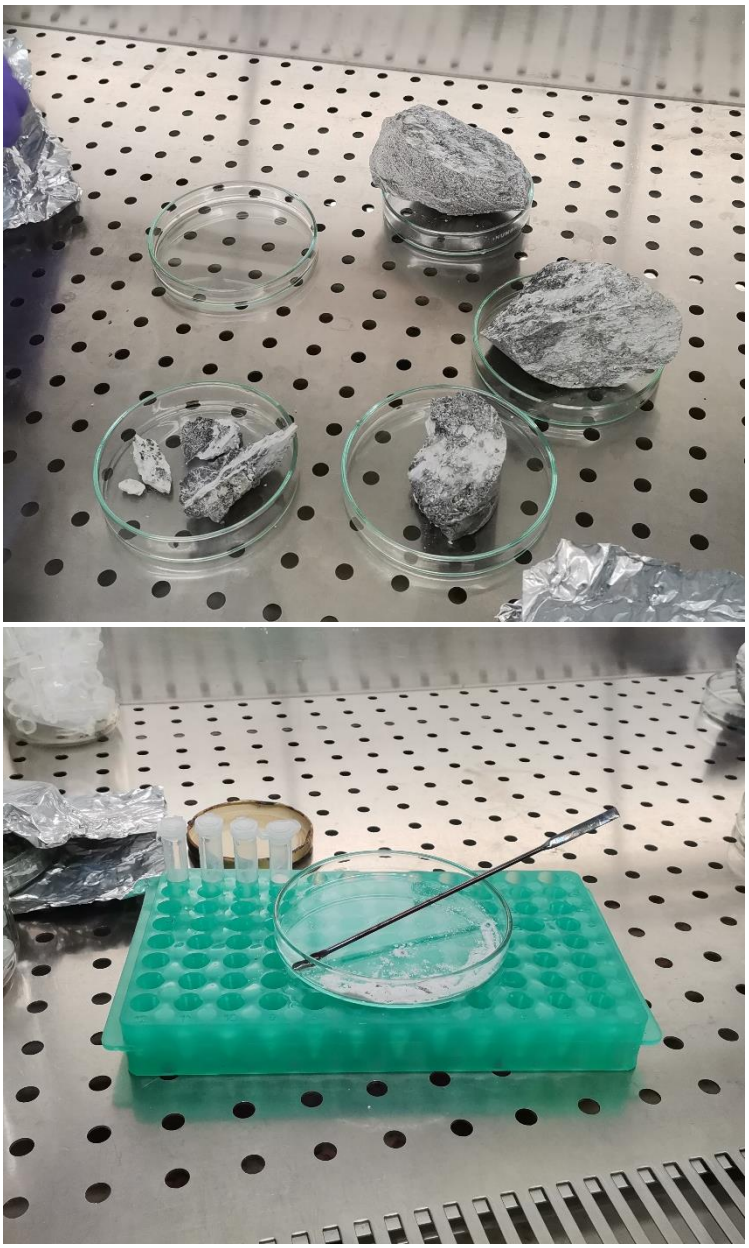

Figure 40: Inside parts of the core used to gather sample for further analysis (a) and interest sample and respective plastic points for storage (b).

DNA extraction from the samples collected was made in DBio (UA) using PureLink Microbiome DNA Purification Kit for Soil Samples. This means the extraction itself had to be made following a certain protocol present in this kit. This protocol can be found in the *Methods* chapter of the kits User Guide, and it is separated into three main steps, repeated for every sample: 1) Preparing the lysate; 2) Binding the DNA to the column; and 3) Washing and eluting the DNA.

1) Preparation of the lysate:
    a. Add 600µL of–S1 - Lysis Buffer to the Bead Tube.
    b. Add 0.2±0.05 g of sample (Figure 41 (a)), previously dipped in liquid nitrogen and cap securely, then vortex (b).

(a) 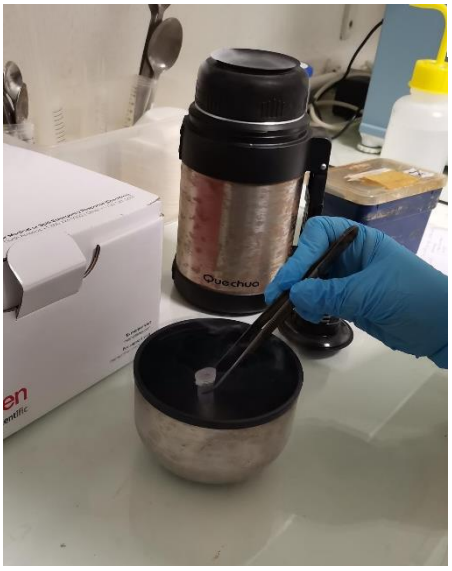 (b) 

Figure 41: Sample dipped in liquid Nitrogen (a) and put in Vortex to facilitate the mixture between sample and reagent.

    c. Add 100µL of S2 – Lysis Enhancer, cap securely, and vortex briefly.
    d. Incubate at 65°C for 10 minutes, in a heating bed (Figure 42).

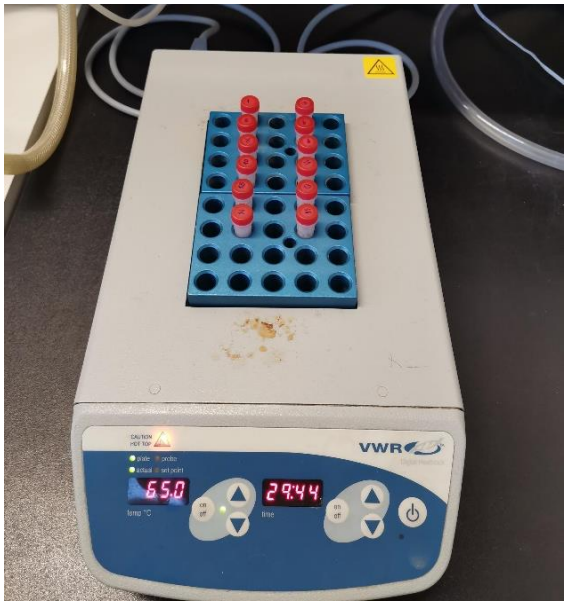

Figure 42: Heating bed used with samples, at 65°C.

e. Homogenize by bead beating for 10 minutes at maximum speed on the vortex mixer. Use the hands-free adapter and horizontal agitation.
f. Centrifuge at 14,000 * g for 5 minutes.
g. Transfer up to 400 µL of the supernatant to a clean microcentrifuge tube. A layer of debris may be present on top of the bead pellet. Avoid transfer of this debris with the supernatant.
h. Add 250 µL of S3 – Cleanup Buffer, and vortex immediately to ensure even dispersion of this reagent and uniform precipitation of inhibitors.
i. Incubate on ice for 10 minutes.
j. Centrifuge at 14,000 * g for 1 minute.
k. Transfer up to 500 µL of the supernatant to a clean microcentrifuge tube, avoiding the pellet.

2) Binding the DNA to the column:
   a. Add 900 µL of S4 – Binding Buffer, and vortex briefly.
   b. Load 700 µL of the sample mixture onto a spin column-tube assembly, and centrifuge at 14,000 * g for 1 minute.
   c. Discard the flow-through and repeat step 2b with the remaining sample mixture. Ensure that the entire sample mixture has passed into the collection tube by inspecting the column. If sample remains in the column, centrifuge again at 14,000 * g for 1 minute.
3) Washing and eluting the DNA:
   a. Place the spin column in a clean collection tube, add 500 µL of S5 – Wash Buffer, and centrifuge the spin column-tube assembly at 14,000 * g for 1 minute.

b. Discard the flow through, then centrifuge the spin column-tube assembly at 14,000 * g for 30 seconds. The second centrifugation optimized removal of S5 – Wash Buffer, which could interfere with downstream applications.
c. Place the spin column in a clean tube, add 100 µL of S6 – Elution Buffer, then incubate at room temperature for 1 minute.
d. Centrifuge the spin column-tube assembly at 14,000 * g for 1 minute, then discard the column. The purified DNA is in the tube.

Finally, the DNA is ready for immediate use. Alternatively, store the purified DNA at 4°C for up to 1 week or at -20°C for long-term storage.

Polymerase Chain Reaction (PCR)

Following the extraction protocol, we proceed to do PCR (polymerase chain reaction), which is technique widely used to amplify DNA, rapidly making millions or billions of copies of specific DNA samples, which can then be studied in greater detail. PCR involves using short synthetic DNA fragments called primers (27F and 1492R) to select a segment of the genome to be amplified (16S ribosomal RNA, also known as 16S rRNA), and then multiple rounds of DNA synthesis to amplify that segment. Figure 43 shows the whole process that the PCR machine specifically does for this samples, where we can distinguish different cycles.

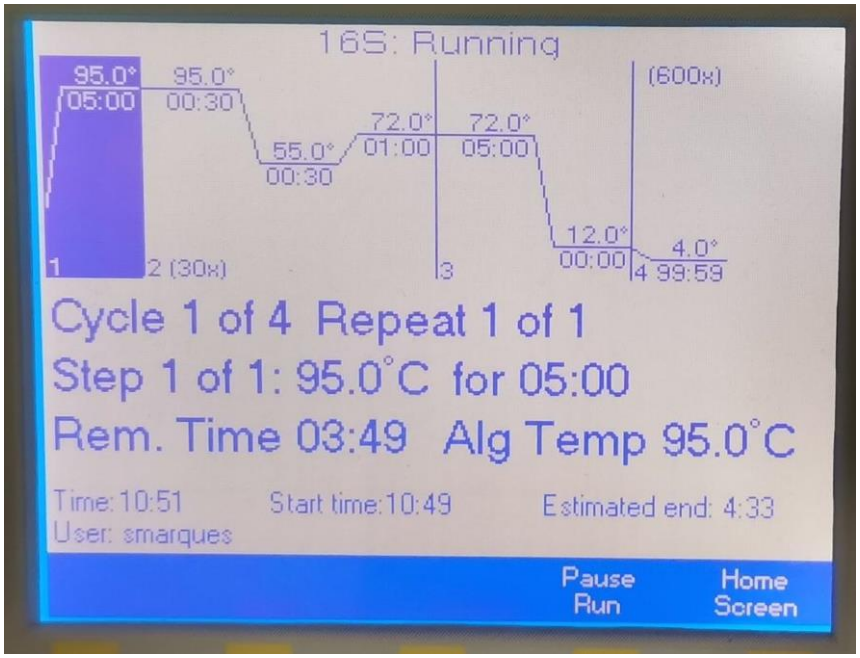

Figure 43: PCR Process with different cycles.

Cycle 1 increases the temperature inside to 95°C in 5 minutes, preparing the samples for the following cycles. Cycle 2 includes 2 changes in temperature, repeating itself 30 times, and this cycle replicates the DNA part that contains the information, creating multiple amounts of replicas. Cycle 3 stabilizes the DNA present in the sample and finally, Cycle 4 maintains a temperature of 4°C, keeping a stable low temperature on our samples while we can't take them from the PCR machine for storage at the conditions mentioned previously in the end of the extraction protocol.

Electrophoresis

Fundamentally, electrophoresis is a technique that uses electrical current to separate DNA, RNA or proteins based on their physical properties such as size and charge. This technique is used in laboratories to separate macromolecules based on size. It applies a negative charge, so proteins move towards a positive charge, and is extensively used in DNA studies to identify, for example, the presence of DNA in a sample and the amount of DNA present. In this experiment, we used Agarose Gel Electrophoresis, where negatively charged DNA migrates through the pores of an agarose gel towards the positively charged end of the gel when an electrical current is applied. The resulting bands can then be visualized using ultraviolet (UV) light.

DNA samples were prepared by mixing 1 µL of loading dye with 3 µL of each PCR product corresponding to each sample and 1 µL of clean distilled water, while markers (M1 and M2) were prepared by mixing 1 µL of the loading dye with 1 µL of the marker and 3 µL of distilled water. Positive (CP1, CP2) and negative controls (CN1, CN2) were prepared the same way as samples were, using respective controls instead of sample. CP1 and CN1 were made with samples 1, 3 and 5, while CP2 and CN2 were made with the rest of the samples (Figure 44).

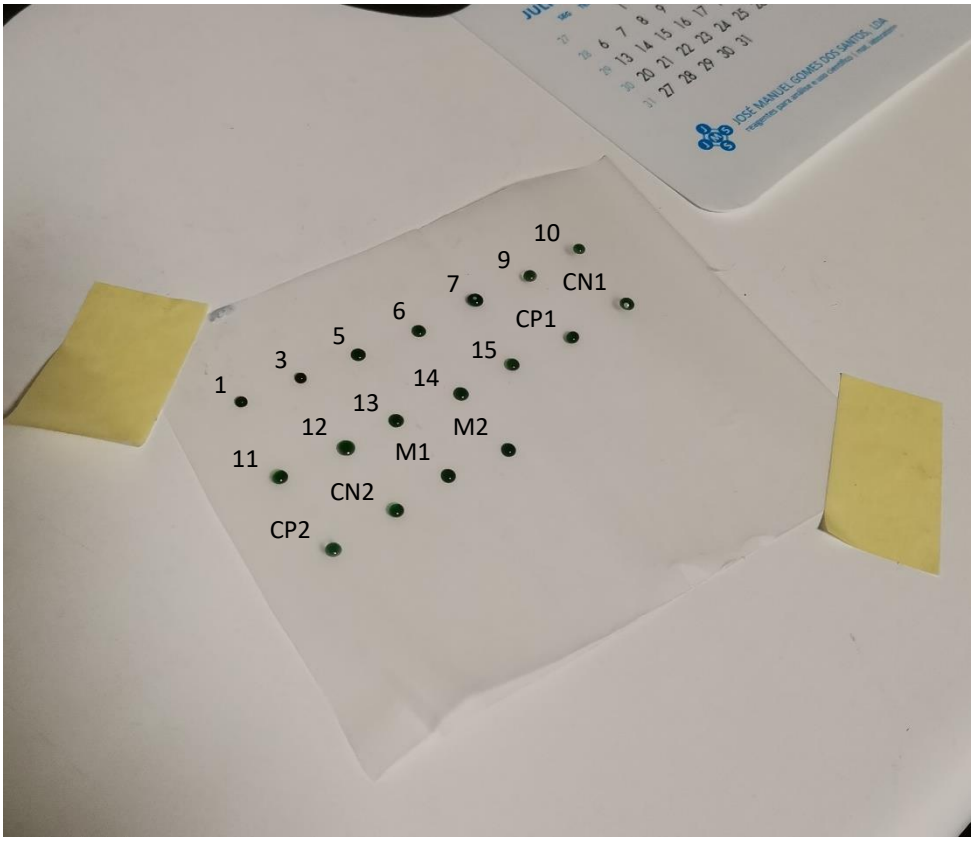

Figure 44: Samples prepared and labeled, before being introduced into the agarose gel mixture.

This experiment begins with the preparation of 50mL of an agarose gel solution by combining 0,5g of agarose with 50mL of TAE buffer, which is a buffer solution containing a mixture of Tris base, acetic acid and EDTA. This solution was heated until it is completely clear, and no small floating particles are visible. After letting the solution cool down, 2 µL of SYBR Green solution are added to the gel solution. The final solution was mixed gently and casted into the tray, where combs were used to create pits to deposit the DNA sample after everything was ready (Figure 45).

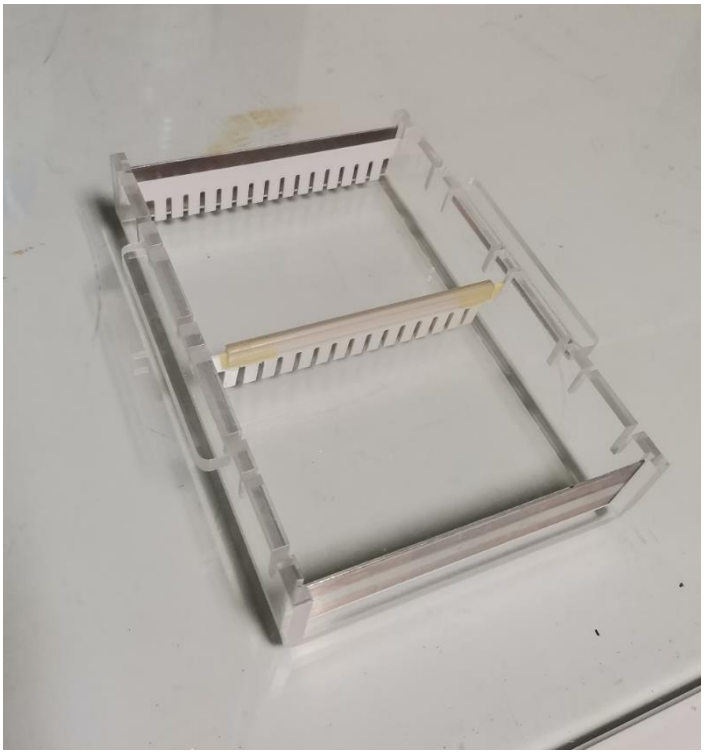

Figure 45: Agarose gel mixture in the tray with combs to create pits.

When the gel became solid, the samples were loaded, and electrophoresis was performed for 50 minutes at 90 V (Figure 46).

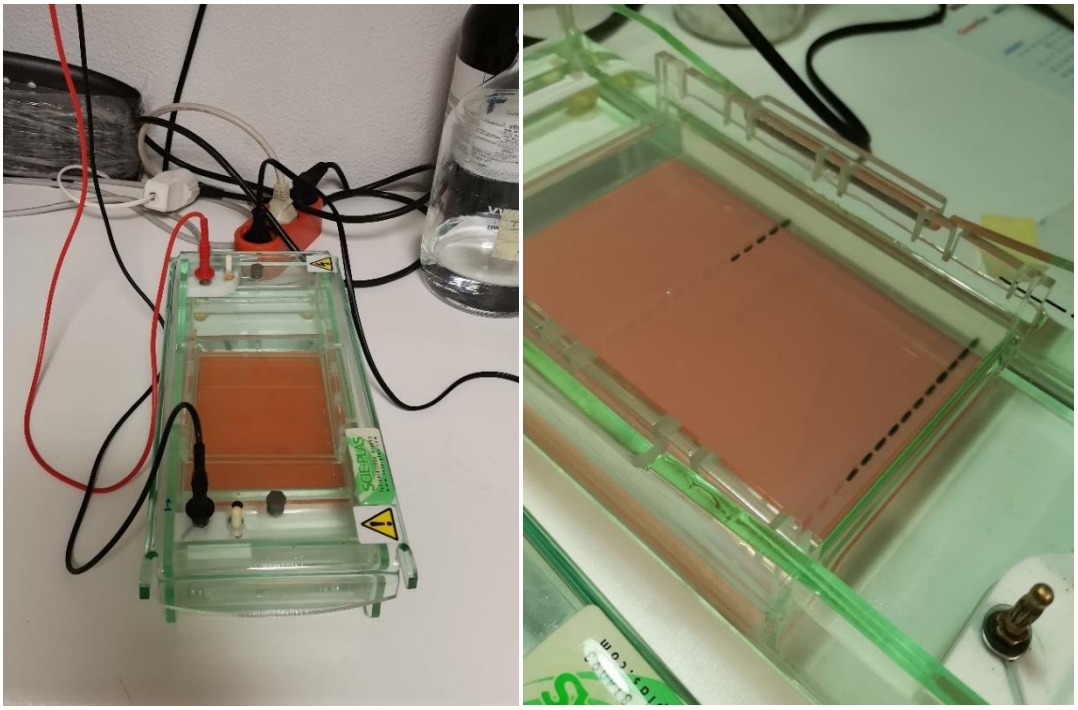

Figure 46: Tray with positive and negative electrodes (left) and agarose gel with samples loaded ready to start the experiment (right).

As mentioned before, the DNA migrates through the pores or pits created towards the positive charge, as it is possible to observe in Figure 47 with the different colors during the experiment (green, purple and yellow), showing the DNA migration.

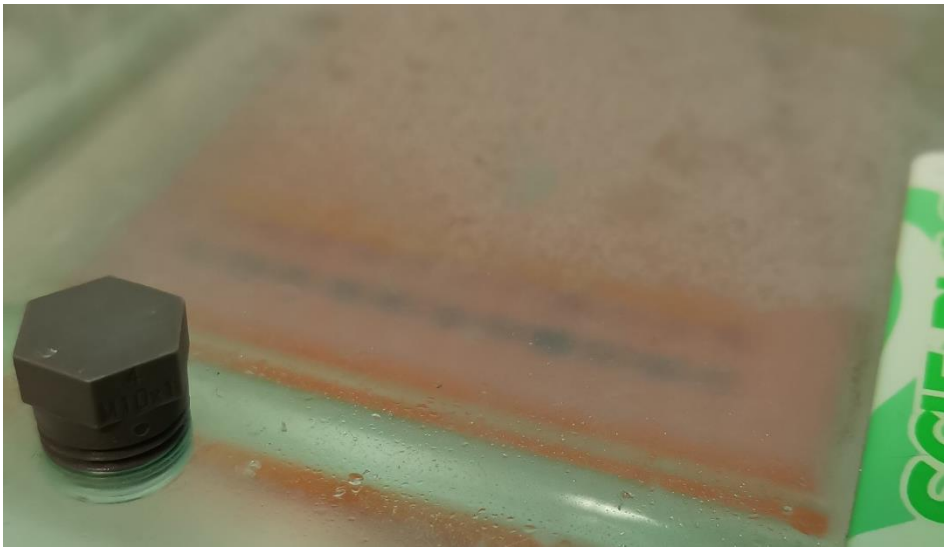

Figure 47: DNA Migration showed by the different colors during electrophoresis.

Since the resulting bands can be visualized using ultraviolet light, the final gel with samples was put into a molecular imager, specifically the Bio Rad ChemiDoc™ XRS+ with Image Lab™ Software, shown in Figure 48.

Figure 48: Molecular Imager (left) and final Agarose Gel loaded into the imager (right).

5. Results and Discussion

To have a better perception of the types of analyses made during this thesis, Tables 6 and 7 were made. This allows an easier and simpler visualization of what methods were used to analyze each sample, according to location, for water samples, and depth, for rock samples.

Table 6: CdV Water analysis methods used, per sample, summarized.

	Water Analysis Methods per Sample			
	Sample Reference	Liters	FILTRATION	ICP-MS
1st campaign 06/09/2021	AC5	1.0	X	X
	AC3	1.0	X	X
	Ribeira	1.0	X	X
	Borbologão	1.0	X	X
	Ermida	1.0	X	X
2nd campaign 28/09/2023	AC5	0.05	X	X
	AC3	0.05	X	X
	Ribeira	0.05	X	X
	Borbologão	0.05	X	X
	Ermida	0.05	X	X

*Table 7: CdV Rock sample analysis used, per sample, summarized. * indicates that CdV125.20_1 to 3 are neither whole nor partial samples.*

Rock Sample Analysis Methods per Sample									
DEPTH (m)	**Sample Reference**	**XRD Total**	**XRD Partial**	**XRF Total**	**XRF Partial**	**PM**	**ATR-FTIR Partial**	**SEM**	**Mössbauer**
26.80	**CdV 26.80**	X	X	X	X	-	X	X	-
27.00	**CdV 27.00**	X	X	X	X	-	X	-	X
28.00	**CdV 28.00**	X	X	X	X	-	X	-	-
42.85	**CdV 42.85**	X	X	X	X	-	X	X	X
45.60	**CdV 45.60**	X	X	X	X	-	X	-	-
80.25	**CdV 80.25**	X	X	X	X	-	X	-	X
80.80	**CdV 80.80**	X	X	X	X	-	X	X	-
112.00	**CdV 112.00**	X	X	X	X	-	X	-	X
113.15	**CdV 113.15**	X	X	X	X	-	X	X	-
116.00	**CdV 116.00**	X	X	X	X	-	X	-	X
125.20	**CdV 125.20**	-	X*	-	X*	X	-	-	-

5.1. Water Data Interpretation

Environmental isotopes (^{18}O and ^{2}H) were measured in Centro de Ciências e Tecnologias Nucleares ($C^{2}TN$), in Instituto Superior Técnico, Universidade de Lisboa, Portugal. ^{18}O and ^{2}H determinations were made by laser spectroscopic analysis (LGR 24d), and they were used to estimate the relative importance of locally infiltrated meteoric waters to the recharge of Cabeço de Vide mineral waters. The interpretation of environmental isotopes is a widely used tool associated with hydrogeological and hydrogeochemical data to determine potential recharge areas. These can be compared to determine the connection between surface and ground waters of rivers and lakes, in addition to the residence time and the presence of zones favorable to percolation (Salameh, 2004)

Cabeço de Vide mineral waters, the local Mg-HCO_3 waters (issuing from the serpentinized dunites) and stream waters have similar $\delta^{2}H$ and $\delta^{18}O$ values (around -27‰ and -4.5‰, respectively), indicating a possible common meteoric origin (Table 8).

Table 8: Environmental isotope composition of the CdV water samples collected.

Sample	δ18O (‰)	δ2H (‰)	Type
AC5	-4.79	-29.7	Water
AC3	-4.69	-28.7	Water
Ribeira	-4.64	-26.8	Water
Fonte	-4.56	-27.8	Water
Ermida	-4.95	-30.5	Water

According to the graph (Figure 49) that correlates the concentration of these environmental stable isotopes in all our water samples (AC5, AC3, Ribeira, Fonte and Ermida), the relationship between these concentrations shows some similarities to the relationship in the Global Meteoric Water Line (GMWL: $\delta^{2}H = 8\ \delta^{18}O + 10$) defined by Craig (1961), later improved by Terzer et al. (2013). This indicates that i) they are meteoric waters which have not been subjected to surface evaporation (being directly infiltrated to the ground), and ii) that there is no evidence of water/rock interaction at high temperatures, consistent with the low issue temperature (~19.5°C) of the CdV mineral waters (Marques et al., 2008).

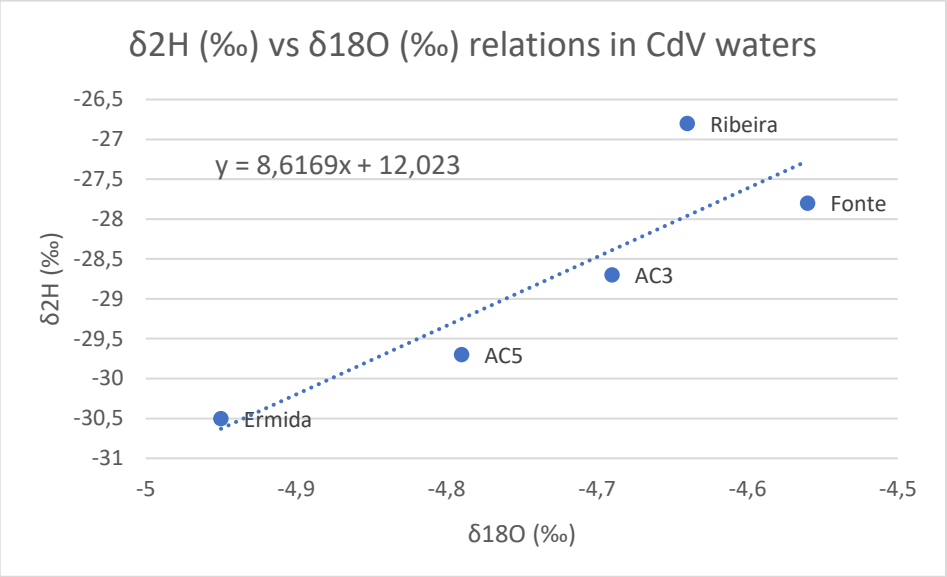

Figure 49: Graph correlating the concentrations of the environmental stable isotopes 18O and 2H in CdV water samples.

The shift observed between the GMWL and the isotopic composition of Cabeço de Vide mineral water could be due to the formation of hydrous minerals (e.g., clay minerals) and calcite precipitation, like the one seen in Ermida, leading to the depletion in the water isotopic composition. These types of minerals are enriched in ^{18}O but depleted in ^{2}H compared to the water from which they precipitate at isotopic equilibrium (Chacko et al., 2001). Therefore, the residual Cabeço de Vide mineral waters should become progressively depleted in ^{18}O and enriched in ^{2}H, during the precipitation of hydrous minerals (Marques et al., 2008).

Through analysis of the water in-situ data (Table 9), the pH values can be highlighted, as they show that waters from CdV boreholes (AC3 and AC5) have values of 11.66/11.28 and 11.58/11.19, respectively, representative of very alkaline pH values (bigger than 11). These two water samples also show rather low mineralization, with conductivity values of 641/631 and 527/573 µS/cm, respectively, both between 400 and 650 µS/cm (Marques et al., 2008). These electrical conductivity values can be a distinctive indication of active serpentinization.

Table 9: In-Situ parameters measured in the two campaigns in Cabeço de Vide.

Sample Ref.	Date	Conductivity (µS/cm)	Temperature (°C)	pH	ORP (Eh/mV)
AC5	06/09/2021	527	20.68	11.58	-184.1
AC5	28/09/2023	573	20.60	11.19	-230.6
AC3	06/09/2021	641	20.33	11.66	-172.3
AC3	28/09/2023	631	20.20	11.28	-236.7
Ribeira	06/09/2021	729	17.53	8.28	17.0
Ribeira	28/09/2023	868	20.20	8.10	-52.1
Fonte	06/09/2021	852	19.94	7.76	112.0
Fonte	28/09/2023	988	20.60	7.61	-24.1
Ermida	06/09/2021	339	19.14	10.53	6.5
Ermida	28/09/2023	470	20.20	9.13	-111.3

Stream water sample (Ribeira) discharging from the serpentinites show a high quantity of Mg, 80.4 mg/L in the first campaign and 94.9 mg/L, that can be explain by serpentine dissolution. CdV mineral waters (AC3 and AC5), however, show extremely low values of Mg, (0.23 and 0.08) mg/L in the first campaign, and less than the quantification limit, in the second, respectively. Barnes et al., (1967) suggests that serpentinization of the ultramafic rocks can contribute to the mineral water chemistry, which can explain this low concentration of Mg in CdV mineral waters. This fact suggests that water chemistry is strongly host rock dependent. The full chemical composition of CdV waters is present in Attachments 1.

Table 10: Some elements from the chemical composition of CdV waters (ICP-MS).

Analyte Symbol		B (µg/L)	Na (mg/L)	Mg (mg/L)	Al (µg/L)	K (mg/L)	Ca (mg/L)
1st Campaign	AC5	196.8	39.45	0.08	139.2	3.89	21.68
	AC3	230.0	49.99	0.23	183.5	4.50	22.84
	Ribeira	13.5	10.76	80.4	<2.5	0.64	35.83
	Fonte	16.2	10.96	94.4	2.63	0.83	38.98
	Ermida	209.8	58.63	0.24	82.6	5.07	3.53
2nd Campaign	AC5	218.7	40.87	<0.05	152.64	4.12	22.95
	AC3	250.1	52.00	<0.05	212.73	5.71	24.82
	Ribeira	19.1	11.94	94.9	6.69	0.83	38.58
	Fonte	17.8	11.77	107.2	5.35	0.90	44.66
	Ermida	152.7	77.51	7.7	26.42	8.87	10.12

CdV thermomineral water springs, due to their hyperalkaline pH values and high Ca^{2+} concentrations, are often surrounded by calcite ($CaCO_3$) precipitation, as shown in Figure 50, as carbon dioxide (CO_2) from the atmosphere is absorbed into the alkaline fluids. Due to the high calcium levels under such deep and closed conditions, CO_2 exsolves from the water. In addition, CO_2 is likely consumed by hydrogenation to form CH_4. Methane produced by CO_2 hydrogenation in deep serpentinized rocks enters the thermomineral waters and it is transported to the surface, meaning that the rocks present contain favourable conditions for gas synthesis (presence of H_2, CO_2 and suitable metal catalysts) and accumulation, such as fractures, present in CdV samples (Etiope et al., 2013). This calcite precipitation was confirmed by XRD analysis of samples R1 and R2, removed from areas highlighted with a red circle in Figure 50, right), that shows only calcite ($CaCO_3$) in their composition.

Figure 50: Calcite precipitation (highlighted with red circles) in AC5 borehole (left) and Ermida spring (right).

The higher boron (B) concentration observed in samples AC5 and AC3, CdV mineral waters, can be associated with leaching from metamorphic and igneous rocks or to the dissolution of carbonates, as B has a strong affinity with OH^- and the aqueous speciation is mainly controlled by water pH (Marques et al., 2008). These hyperalkaline waters are also characterized by high Ca^{2+}, Na^+ and K^+ and chloride concentrations, presenting a Na-Cl/Ca-OH facies (Marques et al., 2018).

Ermida spring chemical composition and data measured *in-situ* shows some evidence of a possible mixing process occurring with the local shallow groundwaters. This is observed by an increase in Mg^{2+} and electrical conductivity, along with a decrease in pH. In this likely mixing process, mineral water from Ermida spring approaches the chemical composition of the local shallow Mg-HCO_3-type groundwaters (Marques et al., 2018).

5.2. X-Ray Diffraction (XRD)

As mentioned previously, samples were labeled according to depth, in whole samples, and layers, in partial samples. Whole rock samples are representative of the respective depth, for example, CdV26.80 whole sample corresponds to a sample that is representative of 26.80 meters depth. Partial samples represent two domains of the sample: W represents the white layer and symbolizes the minerals that fill the fracture veins, while B represents the black layer, the matrix of CdV rock samples. Mineralogical compositions of all samples were analyzed. Since the whole samples are the only ones that are representative of determined depths, semiquantitative analysis was performed using peak areas and reflective powers of minerals present in the samples. All diffractograms are presented in Attachments 2. Mineral acronyms are present in the List of Acronyms.

Non-Oriented Aggregates

Mineralogically (<63 µm fraction), two main domains can be identified in AC2 core, and the characteristics of these domains are in accord with bibliography of CdV whole rock samples previously mentioned: shallower samples, between 20 and 30 meters, are close to the contact between serpentinized peridotites and carbonate host-rocks, and serpentinites represent a major section of this drill core, between depths of 30 and 120m (Maurício et al., 2017; Rocha et al., 2017; Ribeiro da Costa & Barriga, 2022). These conclusions were made preliminarily by semi-quantitative analysis of CdV whole rock samples.

Table 11: Serpentine percentages in CdV AC2 whole rock samples (in < 63 µm fraction).

CdV Samples	Serpentine (%)
26.80	0
27.00	0
28.00	19
42.85	81
45.60	91
80.25	88
80.80	83
112.00	90
113.15	97
116.00	60

Table 12: CdV AC2 whole rock samples mineralogical composition, in wt.%.

Samples / Minerals	26.80 (%)	27.00 (%)	28.00 (%)	42.85 (%)	45.60 (%)	80.25 (%)	80.80 (%)	112.00 (%)	113.15 (%)	116.00 (%)
Serpentine			19	81	91	88	83	90	97	60
Amphibole		8								
Calcite	77	5	14				10			14
Chlorite	4			3	1	5		5	3	5
K-Feldspar		11	7							
Magnetite-Maghemite				16	8	7	7	5		
Phlogopite	16	69	46							
Smectite		7	12							
Talc	3		2							21
Total	100	100	100	100	100	100	100	100	100	100

Whole sample analysis shows that shallower samples have mineralogical compositions containing mostly calcite and phlogopite, a type of mica that typically is present in peridotites and it is difficult to suffer alteration. This domain does not show any presence of serpentines except sample CdV28.00 (that shows small quantities of serpentine), possibly due to the lack of presence of fractures, that does not allow water to flow, and water is fundamental for serpentinization processes to occur. Amphiboles, chlorites, K-feldspar, smectites and talc are also present in this domain in lower quantities.

Starting in depths of 30 meters, evidence of serpentinization process starts to show in the mineralogical composition of the samples. Serpentinized samples are predominantly composed of lizardite, magnetite-maghemite and chlorites. The presence of lizardite as predominant mineral is extremely important, as this serpentine group mineral is characterized for forming in specific conditions, in low temperatures, below 300°C. The absence of higher temperature serpentine minerals like chrysotile and antigorite, combined with the fact that brucite is not present in any of the CdV samples, is indicative of a high evolutive state of the alteration process occurring at depth. Brucite is found in serpentinized ultramafic rocks that contain significant amounts of olivine, so the absence of olivine on every sample studied also tells us that brucite cannot be found in these samples. The presence of chlorite can be explained by the fact that this mineral is a product of the alteration of pyroxenes. Magnetite-maghemite is a product of the oxidation of the ferrous iron present in serpentinized ultramafic minerals. Its formation (magnetitization) is an extremely important reaction, as it can be associated with the generation of reduced volatile species such as H_2 and CH_4, and alteration of the magnetic properties of ultramafic rocks (Costa et al., 1993; Iyer, 2007).

CdV80.80 also shows the presence of calcite, also present in CdV116.00, with talc, as accessory minerals. Talc is commonly associated with the alteration of orthopyroxene in the presence of water (Mével, 2003).

Table 13: Mineralogical composition of CdV AC2 whole samples.

		Serpentine Minerals										
CdV AC2		Atg	Crl	Lz	Amp	Cal	Chl	K-Fs	Mag-Mgh	Phl	Sme	Tlc
Whole Sample	26.80				X	X	X			X		X
	27.00				X	X		X		X	X	
	28.00			X		X		X		X	X	X
	42.85			X			X		X			
	45.60			X			X		X			
	80.25			X			X		X			
	80.80			X		X			X			
	112.00			X			X		X			
	113.15			X			X					
	116.00			X	X	X	X					X

In partial samples, W samples, representative of the fractures present in the samples, show a simpler mineralogical composition, where calcite is the main mineral present in almost all samples except for a few exceptions. The presence of calcite in the fracture zone is important due to the precipitation of calcium in the hydrothermal fluid. Amphiboles, chlorite, smectite, talc and phlogopite are accessory minerals found in some samples in lower depths, between 26.80 and 30 meters. Deeper samples show a mineral composition mainly composed of lizardite and calcite and chlorites, magnetite-maghemite and phlogopite are also found in two of these samples, separately, as secondary minerals, and amphiboles and talc in sample CdV116.00W.

In the matrix of the samples, labeled B samples, a wider range of mineralogical compositions can be found, but the main minerals present are still calcite and lizardite, with the serpentine mineral being present in samples deeper than 30 meters depth. Chlorites and magnetite-maghemite are the main secondary minerals in the matrix of CdV samples. Amphiboles, K-feldspar, phlogopite, smectites and talc are also present in some samples. It is relevant to note that the majority of samples don't show the existence of mafic minerals, like pyroxenes, and only some relics of amphiboles, showing an advanced state of serpentinization in these samples.

Table 14: Mineralogical composition of CdV AC2 partial samples (W and B).

		Serpentine Minerals										
CdV AC2		Atg	Crl	Lz	Amp	Cal	Chl	K-Fs	Mag-Mgh	Phl	Sme	Tlc
Partial Sample	26.80W					X	X			X		X
	27.00W				X	X					X	
	28.00W					X				X	X	X
	42.85W			X			X			X		
	45.60W			X		X	X					
	80.25W			X		X						
	80.80W			X		X						
	112.00W			X		X	X		X			
	113.15W			X		X	X					
	116.00W			X		X	X					
	26.80B				X	X	X			X		X
	27.00B				X	X	X	X	X	X	X	
	28.00B						X	X		X	X	X
	42.85B			X		X	X		X	X		
	45.60B			X		X	X		X			
	80.25B			X		X			X			
	80.80B			X		X	X					
	112.00B			X			X		X			
	113.15B			X			X					
	116.00B			X	X	X	X					X

Samples from depths of 27.00 and 28.00 meters show the presence of smectite in their mineralogical composition. This fact is also validated by the simultaneous presence of this mineral in their partial samples. Section 060 allows to verify if the structure of the clay minerals present in the sample is dioctahedral or trioctahedral. Both these samples show the presence of a bigger intensity peak at 1.54 (Å) in relation to the 1.50 (Å) peak in these samples, indicative of a trioctahedral structure in the clay minerals.

Oriented Aggregates

XRD analysis of oriented aggregates is the most adequate technique for the identification of the clay fraction present in the samples. For this purpose, samples were analyzed in their natural form, labeled "nat", with glycerol treatment ("gly") and after being heated to 500°C ("500"). These three distinct treatments allow to distinguish between the type of clay minerals, considering the fact that these minerals show different behaviors in response to the different treatments. The identification of the clay minerals present in CdV samples was made according to the position of the peaks in < 2µm fraction, in relation with reference values present in Table 15 and respective diffractograms are present in Attachments 2.

Table 15: Reference values for main peaks (001) of clay minerals in natural conditions, and after glycerol and thermal treatment to 500°C (Source: Albers et al., 2002).

Mineral	Natural	Glycolated	Heated 500°C
Kaolinite	7	7	-
Illite	10	10	10
Chlorite	14	14	14
Smectite	14	17	10
Vermiculite	14	15	10

Considering the analysis of CdV samples, the identification of chlorite in all samples can be explained by the fact that this mineral has an octahedral sheet as interlayer, combining layers of two tetrahedral and one octahedral sheet, so the main peak does not change when treated with glycerol, unlike vermiculite, that gains volumes due to having H_2O molecules, Mg^{2+} and other ions in its interlayer, allowing some "swelling" of the space between layers when treated. The identification of the secondary peaks of chlorite (7.0 and 4.7 Å) in all samples also corroborates the fact mentioned previously. The simultaneous presence of chlorite and serpentine in samples from 45.60 to 116.00 meters is concordant with samples mineral composition analyzed by <63 µm fraction. The presence of a strong 10 (Å) peak in samples CdV27.00 and CdV28.00 determined the identification of illite. In sample CdV27.00, the presence of a peak around 15/16 (Å) after glycerol and thermal treatment determined the identification of smectite, also identified in CdV27.00 whole sample mineralogical composition with XRD. All this information is summarized in Table 16.

Table 16: Mineral composition of the clay fraction (<2 µm) of CdV AC2 whole samples.

Minerals \ Samples	26.80	27.00	28.00	42.85	45.60	80.25	80.80	112.00	113.15	116.00
Chl	X	X	X	X	X	X	X	X	X	X
Ilt		X	X							X
Sme		X								
Srp					X	X	X	X	X	X

5.3. X-Ray Fluorescence (XRF)

The chemical analysis of major elements in CdV whole samples (Figure 51) shows that samples from the serpentinized domain contain bigger percentages of magnesium, in relation with shallower samples (deeper than 30 meters), with values on average around 35 wt.% MgO. CdV26.80 has 37 wt.% of LOI that can be justified by the fact that this sample is the most representative of the carbonate domain (43.75 wt.% CaO), and due to the volatile materials present in its composition in the form of "combined water" and carbon dioxide from the carbonates.

(%)	MgO	Al2O3	SiO2	P2O5	K2O	CaO	TiO2	MnO	Fe2O3	Ni	Na2O	Cl	SO3	LOI
CdV26.80	7.221	1.711	7.576	0.017	0.601	43.75	0.062	0.123	1.004	0.003	0.064	0.01	0.184	37.12
CdV27.00	10.187	11.626	45.861	0.869	6.59	7.271	1.01	0.075	8.787	0.012	1.216	0.227	0.666	5.01
CdV28.00	13.919	8.951	39.796	0.533	4.149	11.876	0.845	0.065	7.355	0.005	0.345	0.116	0.036	11.68
CdV42.85	36.869	2.224	36.506	0.037	0.044	1.204	0.188	0.131	10.565	0.191	0.084	0.05	0.185	11.5
CdV45.60	36.383	3.936	36.28	0.168	N.d.	0.903	0.383	0.228	8.863	0.194	N.d.	0.057	0.117	12.25
CdV80.25	41.396	1.488	35.004	0.032	N.d.	0.11	0.115	0.137	8.165	0.223	0.064	0.052	0.28	12.64
CdV80.80	37.555	1.185	34.703	0.011	0.005	4.062	0.071	0.179	6.588	0.122	N.d.	0.031	0.2	14.95
CdV112.00	38.715	1.98	37.361	0.023	N.d.	0.385	0.092	0.104	10.612	0.236	0.084	0.066	0.149	9.93
CdV113.15	34.495	7.361	35.443	0.015	0.048	0.767	0.237	0.281	8.219	0.116	0.089	0.081	0.125	12.61
CdV116.00	27.247	4.8	34.036	0.016	0.06	8.178	0.185	0.226	9.51	0.143	0.093	0.059	0.162	14.97

Figure 51: Chemical composition of CdV AC2 whole samples, according to depth, in percentage (N.d. – not detected).

Every sample from the serpentinized domain shows high percentages of LOI (around 12/13 wt.%). This can be explained mainly by the presence of serpentine in the mineralogical composition of these samples. Samples from shallower depths show calcite as the main and one of the main minerals of their mineralogical composition, and this can be confirmed with the analysis of the chemical composition of those samples, mainly CdV26.80 and CdV28.00, with 43.75 and 11.88 wt.% Ca, respectively. The presence of phlogopite in samples CdV27.00 and CdV28.00 justifies high concentrations of potassium found in chemical analysis of these samples, since phlogopite is a mica with chemical composition $KMg_3(AlSi_3O_{10})(OH)_2$, and typically appears in peridotites. The higher relative percentages of iron and sodium in CdV27.00 and CdV28.00 are also associated with the presence of phlogopite, especially in sample CdV27.00. Serpentinized samples show higher percentages of nickel, manganese and chromium, as they can be products of alteration in the octahedral sheets of serpentine. The presence of magnetite and chlorite in the serpentinized samples can explain the relative high percentages of iron in these samples.

SPSS software was used as an auxiliary method for interpretation of chemical data from CdV AC2 whole samples by principal component analysis. This is a method of data reduction and is based on the correlation matrix of the variables involved. The first step in this analysis is the interpretation of the correlation matrix between the chemical elements (Table 17).

Table 17: Correlation Matrix coefficients of chemical elements in CdV AC2 whole sample.

Correlation Matrix

		Na2O	MgO	Al2O3	SiO2	Fe2O3	K2O	CaO
Correlation	Na2O	1,000	-,595	,803	,450	,105	,936	,016
	MgO	-,595	1,000	-,559	,310	,581	-,712	-,758
	Al2O3	,803	-,559	1,000	,513	,162	,843	-,076
	SiO2	,450	,310	,513	1,000	,836	,403	-,849
	Fe2O3	,105	,581	,162	,836	1,000	-,019	-,894
	K2O	,936	-,712	,843	,403	-,019	1,000	,123
	CaO	,016	-,758	-,076	-,849	-,894	,123	1,000
	TiO2	,845	-,582	,907	,548	,147	,940	-,058
	P2O5	,926	-,623	,850	,497	,082	,981	,008
	MnO	-,506	,474	-,164	-,079	,104	-,614	-,265
	SO3	,837	-,321	,423	,294	,066	,632	-,027
	Ni	-,546	,927	-,601	,242	,627	-,697	-,671
	LOI	-,407	-,390	-,449	-,991	-,882	-,330	,890

		TiO2	P2O5	MnO	SO3	Ni	LOI
Correlation	Na2O	,845	,926	-,506	,837	-,546	-,407
	MgO	-,582	-,623	,474	-,321	,927	-,390
	Al2O3	,907	,850	-,164	,423	-,601	-,449
	SiO2	,548	,497	-,079	,294	,242	-,991
	Fe2O3	,147	,082	,104	,066	,627	-,882
	K2O	,940	,981	-,614	,632	-,697	-,330
	CaO	-,058	,008	-,265	-,027	-,671	,890
	TiO2	1,000	,972	-,449	,466	-,585	-,473
	P2O5	,972	1,000	-,557	,626	-,601	-,429
	MnO	-,449	-,557	1,000	-,350	,342	,049
	SO3	,466	,626	-,350	1,000	-,254	-,293
	Ni	-,585	-,601	,342	-,254	1,000	-,342
	LOI	-,473	-,429	,049	-,293	-,342	1,000

The first strong positive correlation that can be highlighted is between sodium and phosphorus, and can be attributed by the presence of phlogopite in some samples, since they are simultaneously part of the composition of this mineral. The strong correlation between potassium, aluminum, phosphorus, sodium and titanium, all between them, can be attributed to the primary mineralogy of the samples, or the protolith.

Magnesium and nickel show a very strong correlation due to the fact that the majority of the CdV samples studied are mainly composed of serpentine and these two elements can exist in the octahedral sheets of this mineral. Calcium and LOI show a strong positive correlation, attributed to carbonates.

This analysis distinguished two main components, 1 and 2, that represent 50.4 and 34.7%, respectively. The component matrix of these two components is shown in Table 18. To simplify the visualization of these components, their composition and their interpretation, SPSS also gives a graphical representation of them (Figure 52).

Table 18: Component analysis of CdV AC2 whole samples.

	Component	
	1	2
Na2O	,958	
MgO	-,673	,709
Al2O3	,877	,114
SiO2	,460	,872
Fe2O3		,947
K2O	,994	
CaO		-,988
TiO2	,950	,105
P2O5	,986	
MnO	-,551	,203
SO3	,665	
Ni	-,654	,671
LOI	-,392	-,916

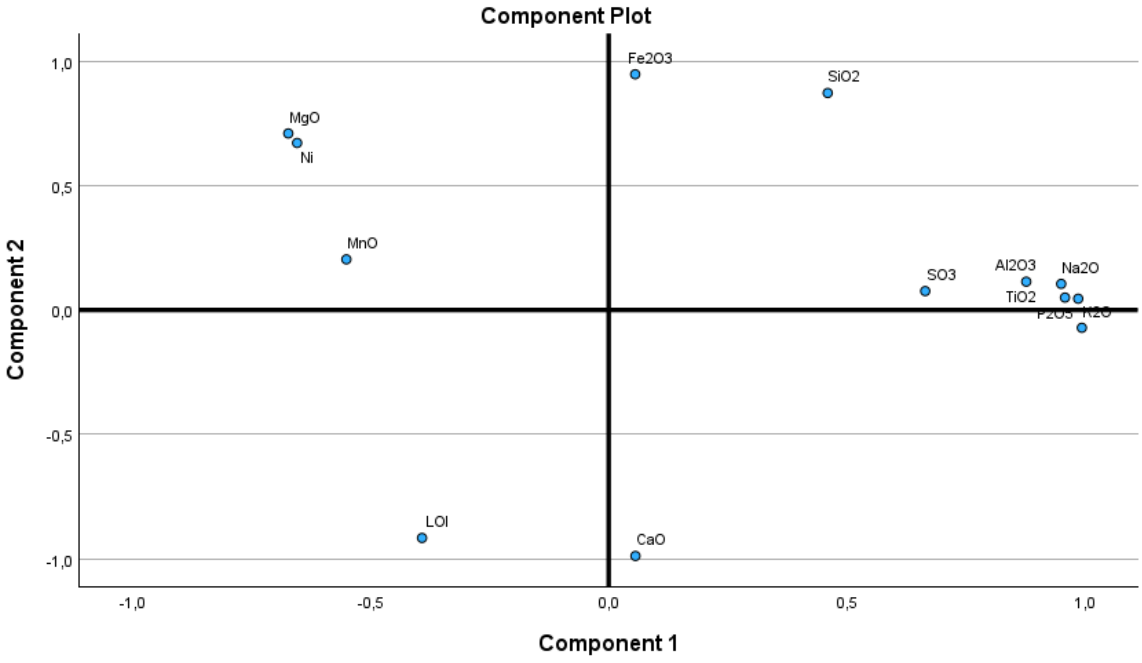

Figure 52: Graph that opposes the two components from CdV AC2 whole samples.

The analysis of the correlation graph between the two main components distinguishes some main characteristics observed previously in CdV AC2 samples. Component 2 clearly shows a strong negative correlation with calcium and LOI, separating the samples that contain carbonates from the ones that do not. As mentioned previously, calcium and LOI are strongly associated, and this graph confirms this fact. On the other hand, samples on the positive side of the axis of Component 2 can correspond to non-carbonated ones. Analyzing the elements present in the graph, we can distinguish second quadrant (top left) elements as being correspondent to serpentines and the first quadrant (top right) ones to compositions closer to the primary mineralization of these samples, with aluminum and potassium, as mentioned previously with the correlation matrix, as well as the presence of higher quantities of phlogopite present in some samples. Silica was expected, in theory, to be correlated with magnesium, due to the predominance of serpentines in the CdV samples, but it is present in the first quadrant because these samples show the presence of other silicates in their mineral composition, especially phyllosilicates like phlogopite, smectite and chlorite, that contain elements not commonly found in serpentines, like aluminum.

Projecting the two main components that resulted from this analysis in accordance with the references of the samples, it is easy to visualize three different domains (Figure 53), confirming the data from XRD semi-quantitative analysis made previously. Sample CdV26.80 is the only one predominantly composed of calcite (77 wt.%), so it is separated from all the other samples, with strong negative correlation with both components, especially with Component 2. Samples CdV27.00 and CdV28.00 show a predominance of a phlogopite in their mineralogical composition, 69 and 46 wt.% respectively, thus they display a strong positive correlation with Component 1, as this component showed strong positive correlations with elements like aluminum and potassium. Finally, samples from CdV42.85 to CdV116.00 represent the serpentinized domain, as they also show similar whole sample chemical compositions. This fact confirms the observations made regarding the second quadrant of the correlation matrix between components, that indicated that this section of the graph corresponded to serpentines.

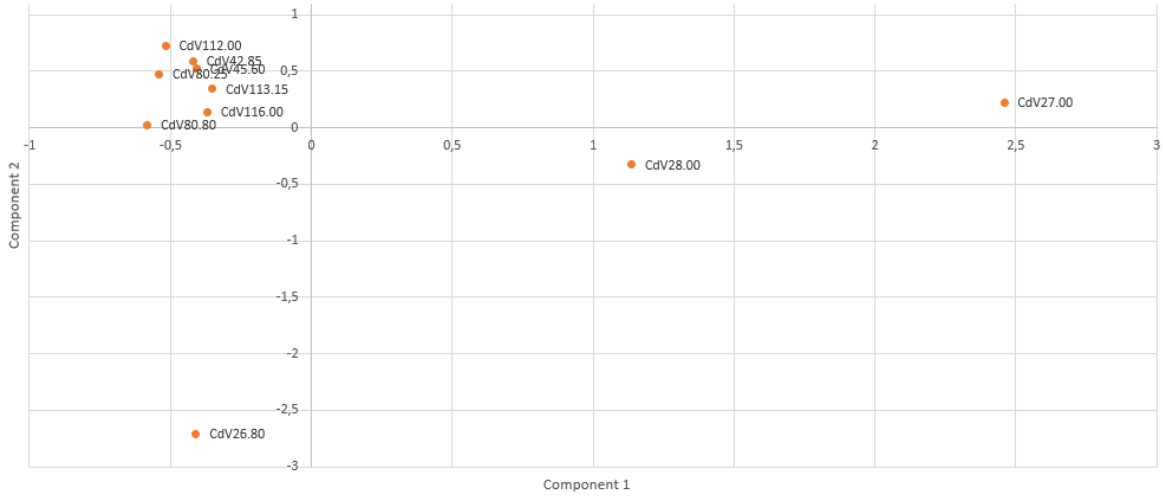

Figure 53: Graph that represents the correlation between CdV AC2 samples and the two main components that resulted from SPSS analysis.

Minor and trace elements from CdV AC2 whole samples are present in Attachments 2, together with the chemical compositions of CdV partial samples and samples CdV125.20_1 to 3.

In the analysis of minor and trace elements from CdV whole samples, chromium concentrations in serpentinized samples can be highlighted. This chromium can be associated with the mineral chromite, that can be responsible for the formation of magnetite, during serpentinization, due to chromite oxidation. This fact is also identified in CdV partial samples, especially in the partial samples that correspond to the matrix of the CdV sample, labeled with the letter B. Chromite was not identified in the mineralogical composition of CdV samples, however in subchapter 5.5 a few rare grains of chromite were analyzed with SEM and EDS. Wolfram also shows higher concentration values in the samples from the serpentinized samples. Elements like fluorine, barium, and strontium, as well as scandium, samarium, cerium and thorium, show higher concentration values in the non-serpentinized samples. The highest concentration of barium is present in sample CdV27.00 and can possibly be attributed to the predominance of phlogopite in the mineralogical composition of this sample. This fact is also observed in the case of rubidium, that shows higher concentration in the samples that contain mostly phlogopite, as these two elements can be present as impurities in this mineral.

5.4. Attenuated Total Reflectance Fourier-transform Infrared Spectroscopy (ATR-FTIR)

FTIR spectroscopy analysis is extremely important to correctly identify the predominant serpentine mineral phase present and is complementary to another technique used in this thesis, X-Ray Diffraction (XRD), as details of their physiochemical properties such as crystal structure are not easy to identify by traditional petrographic methods. This technique was performed using methodology described previously in chapter 4 (4.3.4) and allowed the analysis of resulting spectrograms according to interpretations made by Farmer and Russel (1964), Russel and Fraser (1994), Post (2000), Madejová (2001, 2003 & 2017), Bishop et al. (2002), Crespo et al. (2019) and Fritsch et al. (2021). Spectrogram graphs are presented in Attachments 4 chapter.

When analysing FTIR spectra, especially in clay minerals, it is important to consider the interval of absorptions corresponding to the OH stretching, between 3800 and 3300 cm^{-1}. The geometric behaviour of the absorbance curve can determine what type of mineral is present in the samples studied. This is crucial for the determination of the predominant serpentine mineral phase in Cabeço de Vide samples. Comparing Madejová (2003) and Madejová et al. (2017) IR spectra results from clay minerals and serpentine minerals specifically, with spectra from CdV samples, it is clear that samples studied show absorbance geometries corresponding to serpentine minerals, specifically lizardite, as shown by Figures 54 and 55. In comparison with lizardite, IR spectra of chrysotile displays a strong absorption band at 1023 cm^{-1} associated with an out-of-plane (perpendicular to the layers) Si-O vibration, however this absorption band is not present in any of CdV samples.

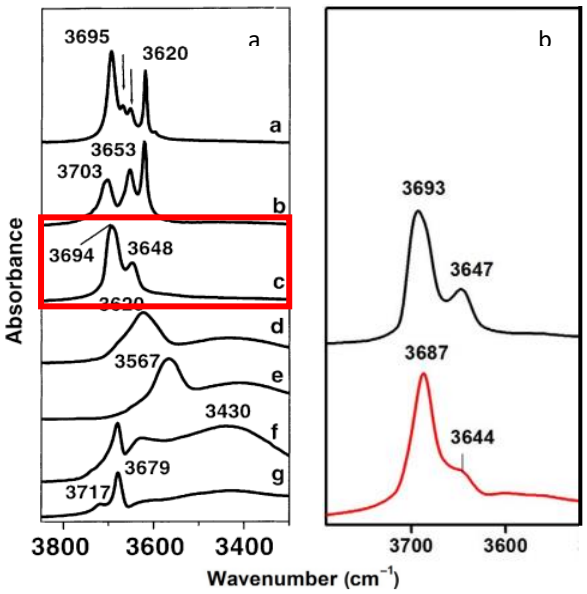

Figure 54: MIR spectra of a) clay minerals, where mineral c (chrysotile) is highlighted; and b) chrysotile (black) and lizardite (red) (Adapted from Madejová (2003 and 2017)).

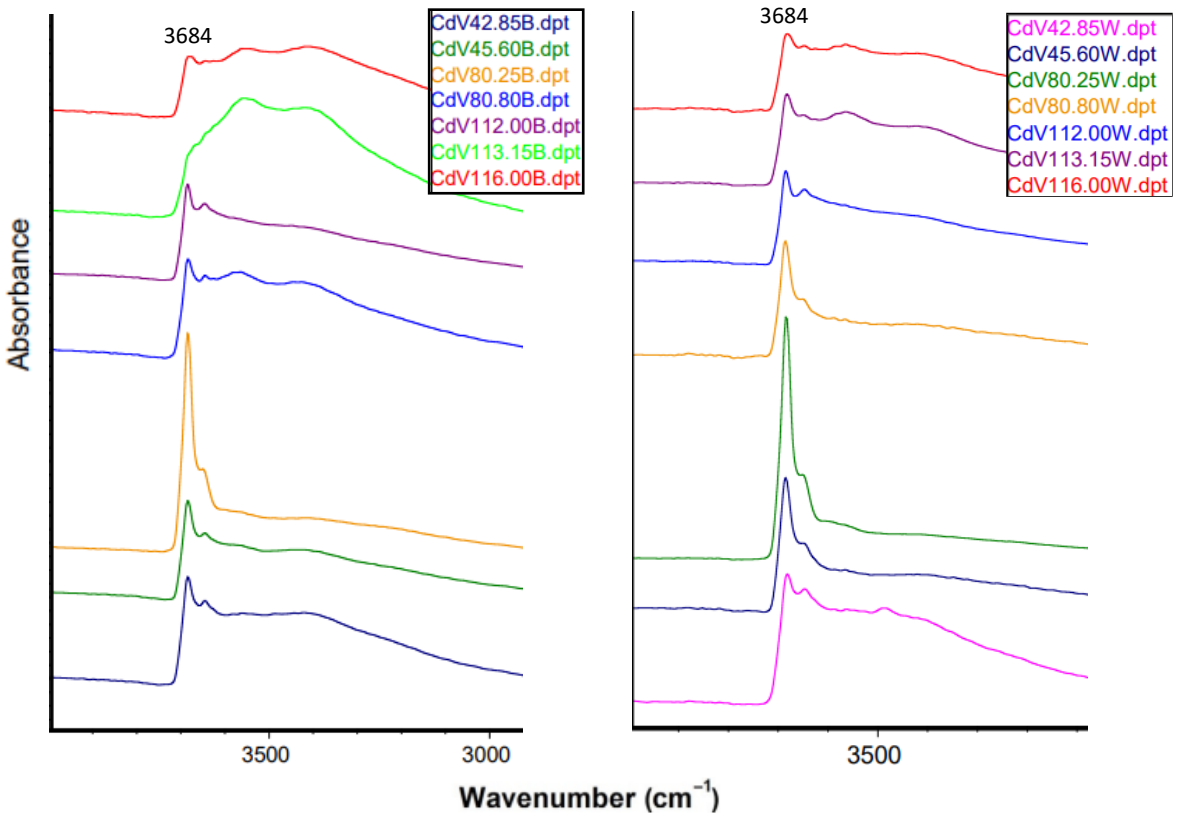

Figure 55: MIR spectra of CdV Partial B (left) and W (right) samples from the serpentinized domain, showing lizardite-like geometries, with some exceptions.

The first band of absorption in samples from the serpentinized domain in B samples is around 3684 cm^{-1}, assigned to the in-phase stretching of the three inner-surface OH groups. This is related to the Mg_3OH stretching vibration in the trioctahedral 2:1 layer, in all these samples. Samples CdV42.85B to CdV112.00B show a shoulder near 3645 cm^{-1} associated with the two degenerate out-of-phase stretching modes of the inner surface OH groups (Balan et al., 2002). Between samples CdV80.25B and CdV80.80B it is easy to distinguish two different types of geometries and peak values. This can be explained by the fact that 80.80B has another phyllosilicate in its composition, chlorite, so the FTIR spectra will show this "mixture" in its geometry, as the spectrum of clinochlore (chlorite) shows a broad OH stretching band at around 3628 cm^{-1}. The band at 3584 cm^{-1} in CdV80.80B is related to the minor amounts of Fe^{2+} substituting for Mg^{2+} at octahedral sites. As a result of a higher octahedral iron content, the bands associated with the inner-layer oxy-hydroxyl sheets are shifted to lower positions, that is, to around 3570 and 3429 cm^{-1} (Figure 56). CdV80.80B higher iron content is also shown in the chemical analysis of the samples (80.25: 29,0% and 80.80: 36,2%).

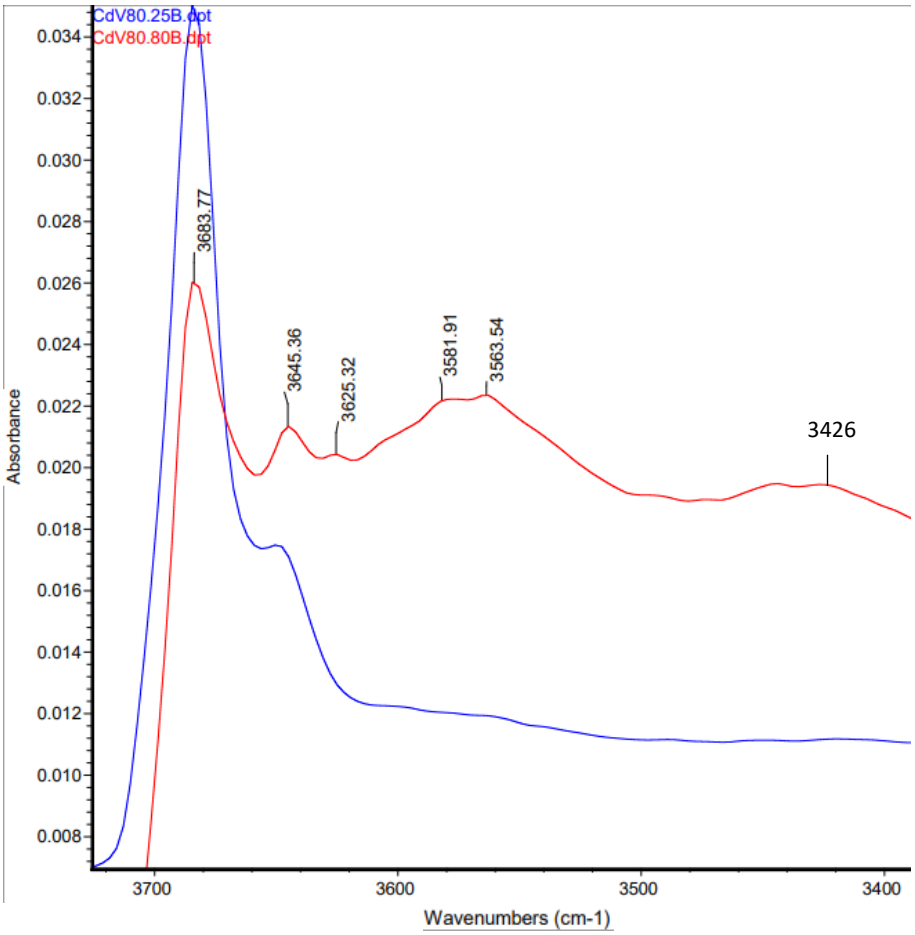

Figure 56: MIR spectra of partial samples CdV80.25B and CdV80.80B.

3406 cm^{-1} is representative of deformation of water, also present in CdV42.85B, CdV45.60B, CdV80.80B and CdV116.00B. Partial samples W show predominantly well-defined lizardite-type geometry, with samples CdV42.85W, CdV113.15W and CdV116.00W also showing peaks around 3406 cm^{-1} of water deformation, as this fact can justify the relative high values of LOI (around 13 and 15%, respectively). All the information mentioned previously validates what was concluded through XRD analysis.

Samples 26.80, 27.00 and 28.00, from both the fracture and the matrix parts of these samples, do not show the absorbance geometry representative of serpentine minerals, confirming XRD analysis that allowed to distinguish the two different domains present in Cabeço de Vide samples. However, they show different geometries that correspond to different clay minerals (Figure 57).

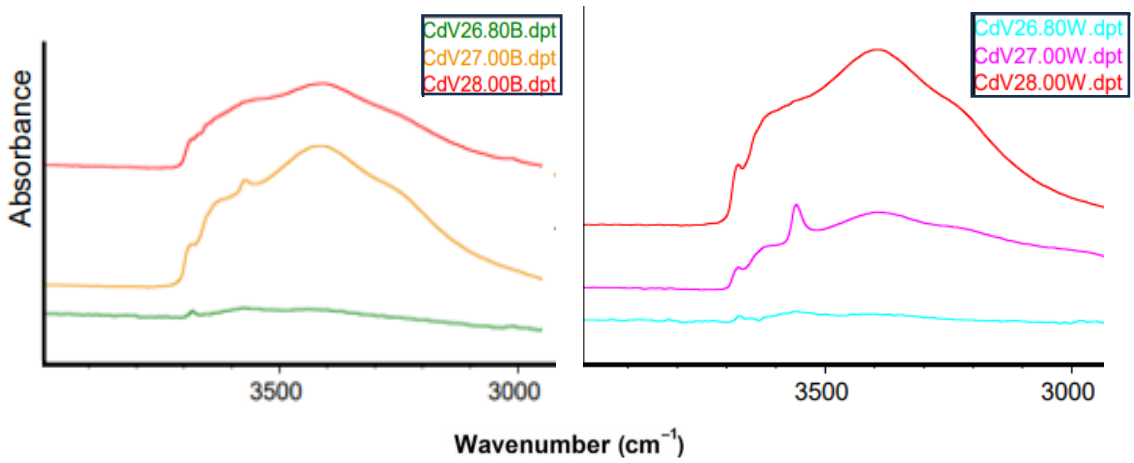

Figure 57: MIR spectra of CdV Partial B (left) and W (right) samples from the carbonate domain.

The geometries of the MIR spectra (between 3800 and 3000 cm^{-1}) of partial samples 27.00 and 28.00 show a possible mixture between saponite, highlighted by a weak (Mg_3OH) band near 3680 cm^{-1} and a very subtle one near 3625 cm^{-1}, and phlogopite (~3400 cm^{-1} curvature). Sample CdV27.00 shows a bigger percentage of phlogopite in whole sample analysis in relation to CdV28.00, but only partial sample CdV27.00B show the presence of this mineral in its mineral composition, explaining the geometry of the spectra near 3400 cm^{-1}. This area of the spectra corresponds to stretching vibration of water molecules, so the existence of a curvature in both partial samples from CdV28.00 in relation to CdV27.00 can be explained by a higher value of LOI (11.68 wt.% and 5.01 wt.%, respectively). The correspondence with these two minerals corroborates with data from XRD analysis.

As seen previously in XRD and other ATR-FTIR data, samples representative from the vein domain (W) and the matrix domain (B) show similar behaviours, with lizardite being present in both domains. Additionally, calcite is present in all W samples, observed by an absorption band around 1410 cm^{-1}, while B samples also show these values except for one sample, from the serpentinized domain. Since sample 26.80 is the only sample predominantly composed of calcite, FTIR spectra from samples 26.80B and 26.80W confirms the observations made with XRD data analysis since the main FTIR peak observed in these samples is correspondent of calcite (1440 cm^{-1}). Samples CdV27.00B and CdV28.00B also show a weaker peak at the same wavelength, while samples 42.85B to CdV80.80B, and CdV116.00B show a strong peak associated with calcite at the same wavelength mentioned for 26.80 partial samples. This is also observed in samples CdV28.00W, CdV45.60W, CdV80.80W and CdV116.00W.

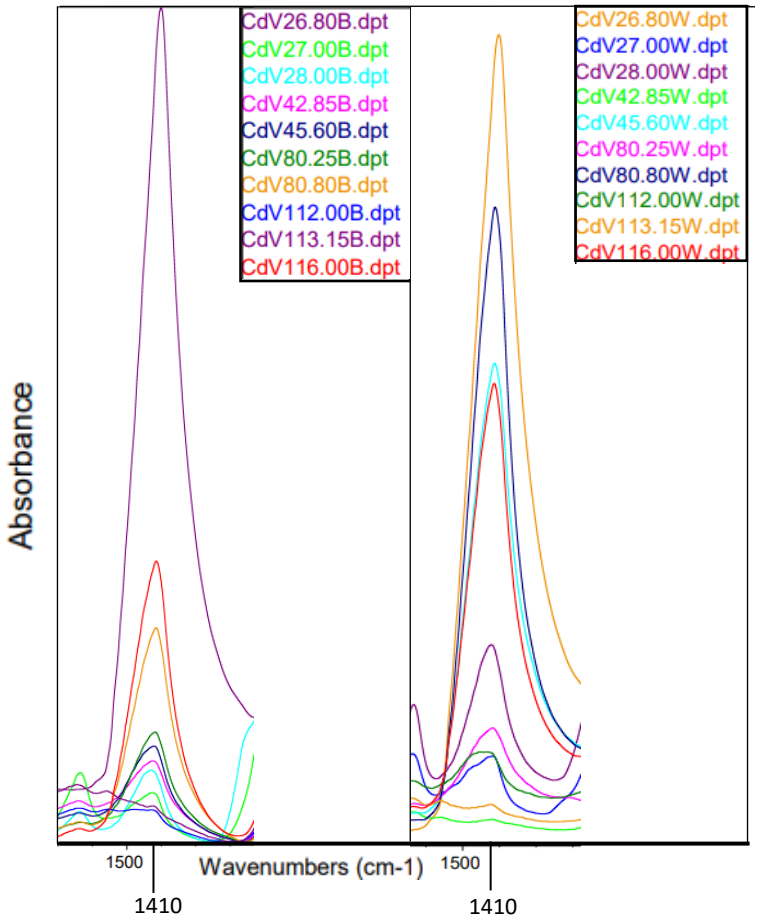

Figure 58: MIR spectra of CdV Partial samples for CO_3 stretching region.

A slight lower position observed for talc was also identified at 666 cm^{-1} in samples CdV26.80B and CdV26.80W, reflecting the greater octahedral Fe^{2+} content in these samples, and it is broadened due to the absorptions of $Mg_2Fe^{2+}OH$, $MgFe^{2+}{}_2OH$ and $Fe^{2+}{}_3OH$ groups. All this information is congruent with XRD data, as calcite and talc were identified in all the samples mentioned beforehand.

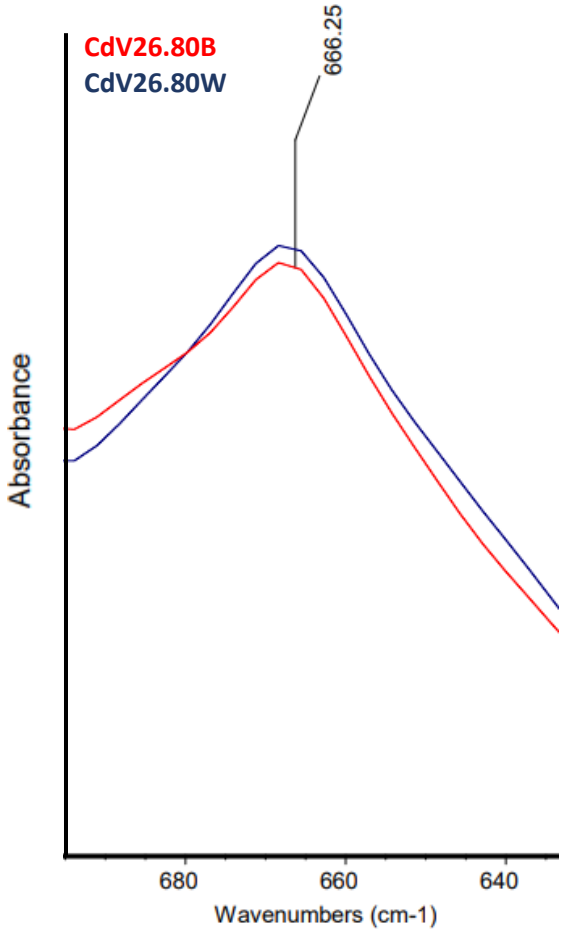

Figure 59: MIR spectra of CdV Partial samples 26.80B and 26.80W in 666 cm^{-1} region.

5.5. Scanning Electron Microscope (SEM) analysis

The analysis of specific areas and points with SEM allows the identification of chemical elements associated with specific and distinct mineral species with EDS elementary chemical analysis. In some cases, this analysis also allows the identification of mineral species that cannot be identified with other techniques, like X-Ray Diffraction, as they are present in the samples in very low quantities. SEM also allows the creation of chemical maps of certain regions of the sample, allowing the analysis of the spatial distribution of the elements present in the samples. Samples CdV26.80, CdV42.85, CdV80.80 and CdV113.15 were chosen for SEM analysis due to interesting characteristics found in them and they can be representative of intervals of depths.

Figure 60: Fragment of sample CdV26.80 analyzed with SEM.

Sample CdV26.80 (Figure 60) was analyzed due to its unique mineral composition, since it is mainly composed of calcite (77%). The analysis of this sample with EDS allowed the confirmation of a matrix mainly composed of calcite. However, some relics of other minerals were found. The quantitative analysis of point 1 and area A1 is shown in Figure 62. A1 is representative of all areas with similar aspects, as they show similar chemical compositions, and it confirms calcite as the main mineral present in this sample, corroborating with XRD, XRF and ATR-FTIR data. With detailed analysis, point 1 confirmed some small fragments of pyrite (FeS_2), as demonstrated by Figure 61 and their chemical analysis, showing 24 wt.% in iron and 30 wt.% sulfur in this case, but this is not completely correct, as EDS can pick up chemical composition from the lower layer. For this case, a specific mineral was targeted with more detail and magnification, in order to get a better representation of the chemical composition of this mineral (Figure 63).

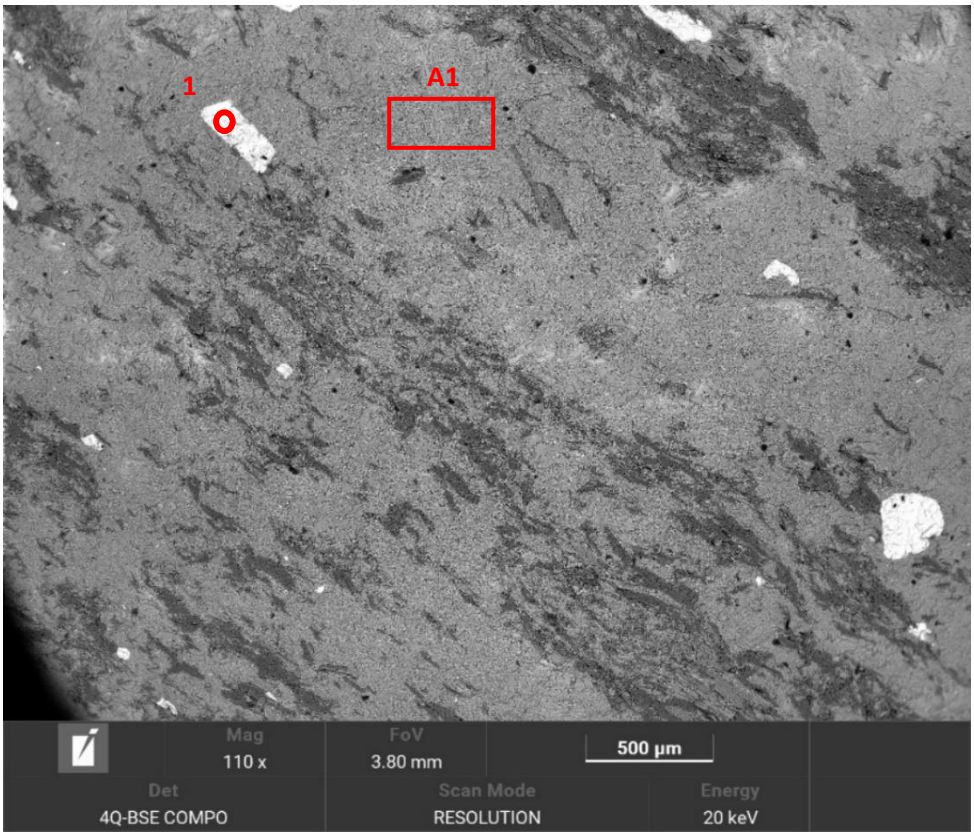

Figure 61: SEM image of a representative section of sample 26.80 (Mag. 110x).

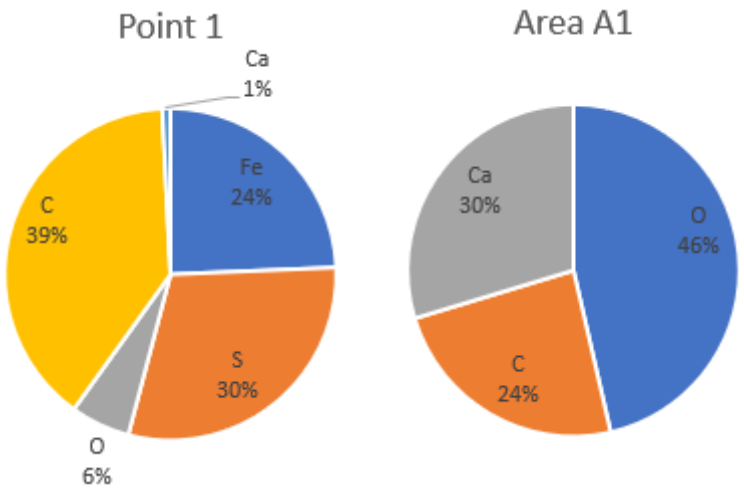

Figure 62: Quantitative analysis of point 1 and area A1 in sample CdV26.80, in wt.%.

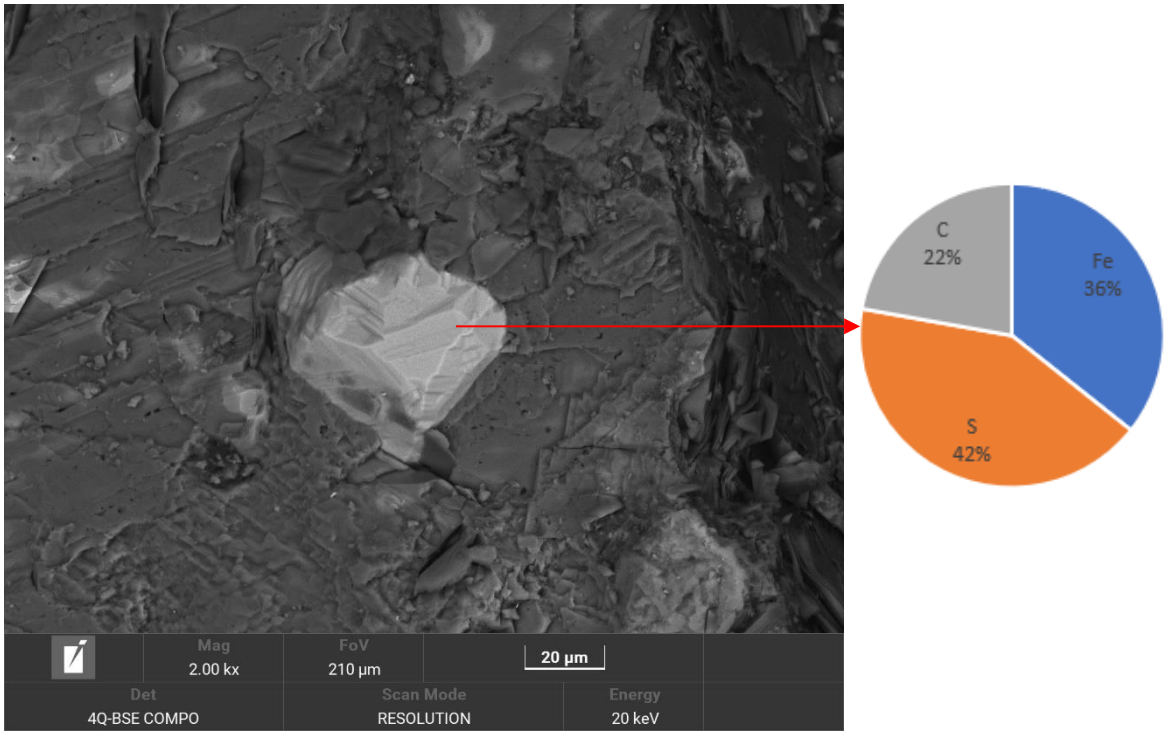

Figure 63: SEM image of a pyrite (FeS_2) grain present in sample 26.80 (Mag. 2000x). Quantitative analysis (wt.%) of main grain in SEM image shows very high quantities of sulfur and iron, indicative of pyrite.

Sample CdV42.85 (Figure 64) was chosen because it is one of the first samples from the serpentinized domain, with serpentine (81 wt.%) as the main mineral in its mineralogical composition, with considerable quantities of magnetite (16 wt.%). Figure 65 shows a section of this sample containing an area with magnetite grains, demonstrated by a chemical composition very rich in iron (68 wt.%), including some common impurities of this mineral, like titanium (1 wt.%) and magnesium (1.51 wt.%).

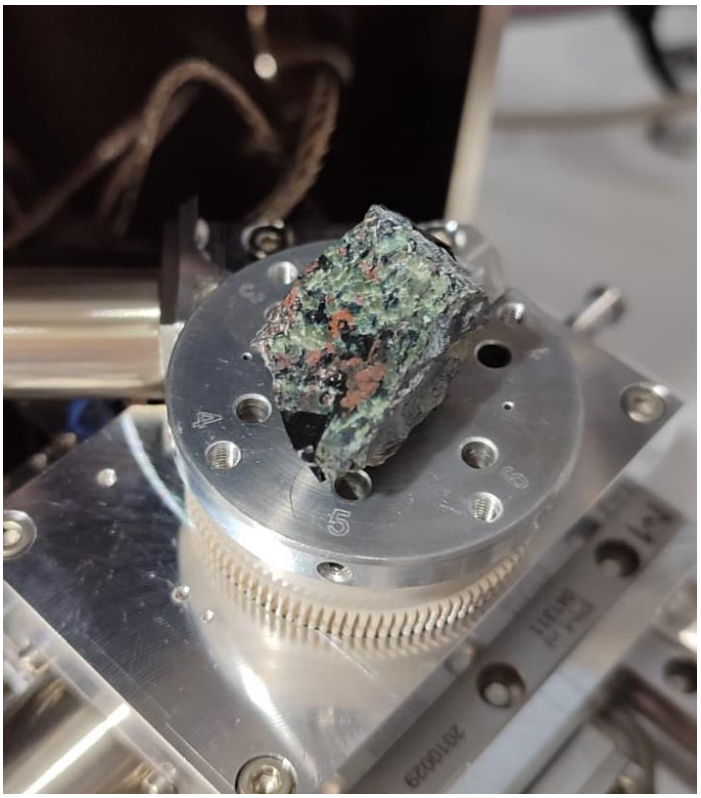

Figure 64: Fragment of sample CdV42.85 analyzed with SEM.

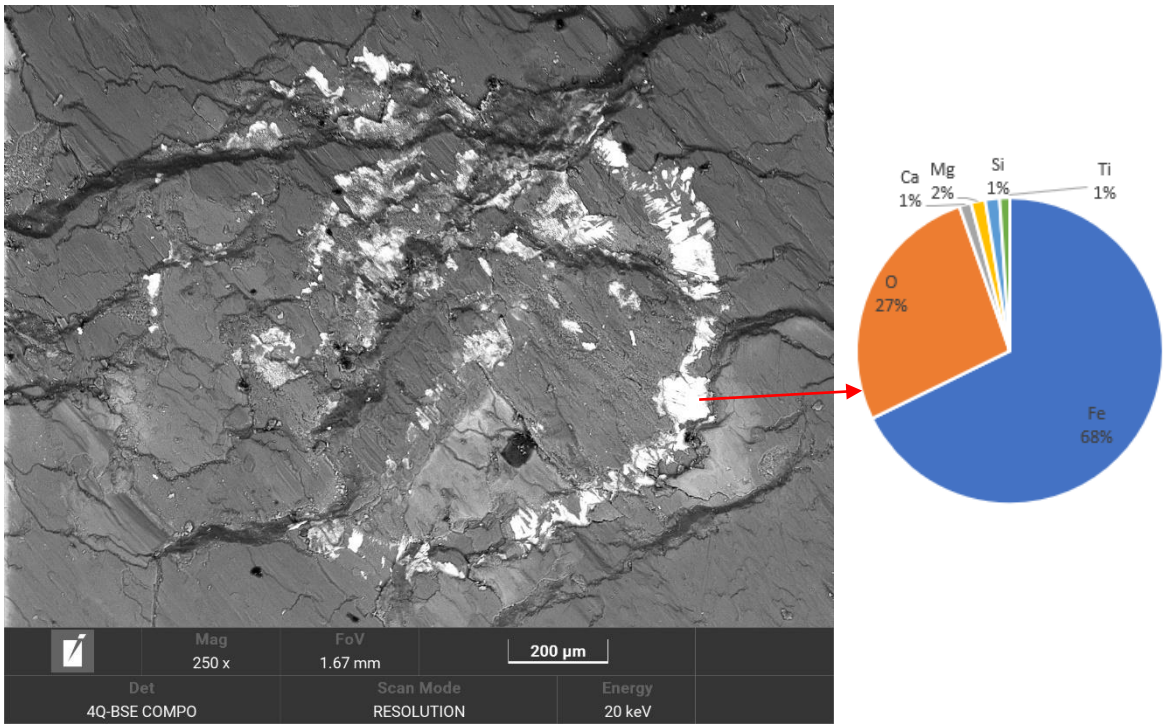

Figure 65: SEM image of a section of sample CdV42.85 containing some magnetite (Mag. 250x). Quantitative analysis (wt.%) of the white part confirms this mineral (Fe: 68 wt.%).

Considering the fact that EDS analysis can sometimes show quantitative percentages of the layers underneath the point/mineral analyzed, this section is not appropriate for the identification of serpentine in the matrix (darker area of previous Figure), since EDS data possibly show a mixture between serpentines and chlorites, also found in this sample with other techniques (Mg 21 wt.%; Si 22 wt.%; Fe 17 wt.%).

Serpentines were detected in another area of this sample, shown in Figure 66, with needle-like structures, characteristic of this mineral. Additionally, an area with an interesting quantity of serpentines was chemically analyzed in order to quantify the elements found, as well as their elemental distribution. In this map (Figure 67), magnesium, silicon and oxygen are strongly associated, as shown by their elemental images, confirming that serpentine is the dominant mineral in this sample and supporting the analysis made previously with XRD, XRF and ATR-FTIR. The presence of iron in this sample (10 wt.%) is mostly identified in the white grains present in the section studied, a fact shown by the elemental image of Fe.

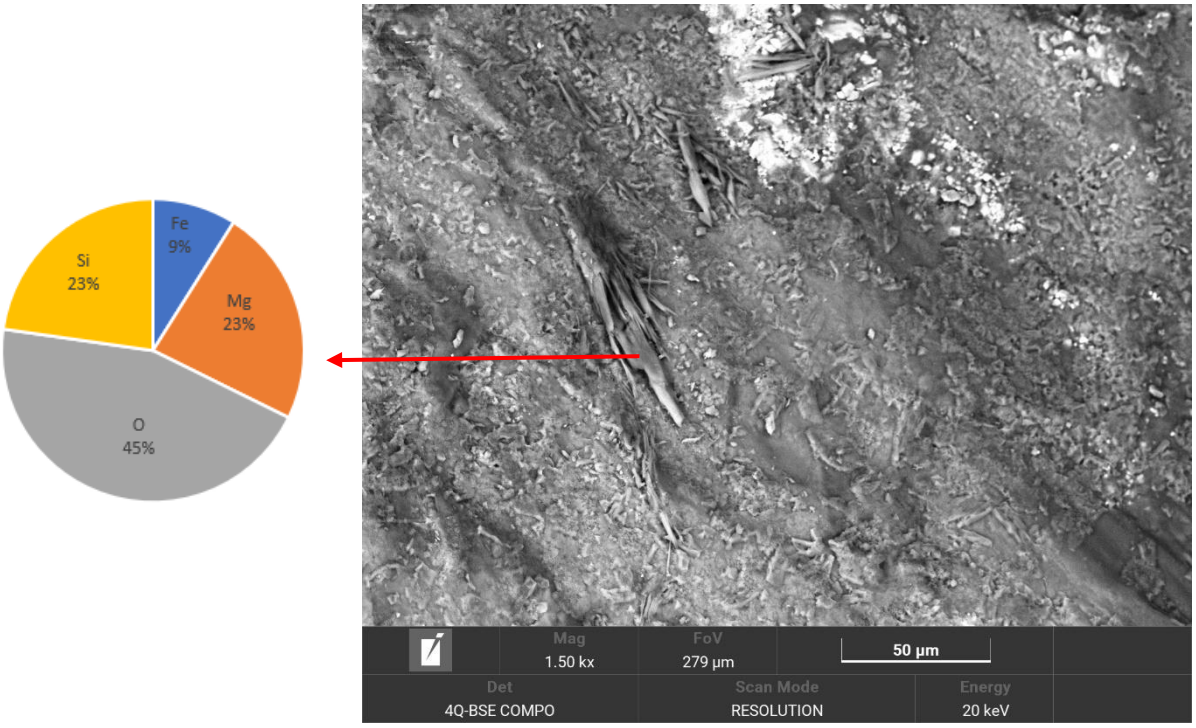

Figure 66: SEM image of a section of sample CdV42.85 containing serpentine (Mag. 1500x) and quantity analysis (in wt.%).

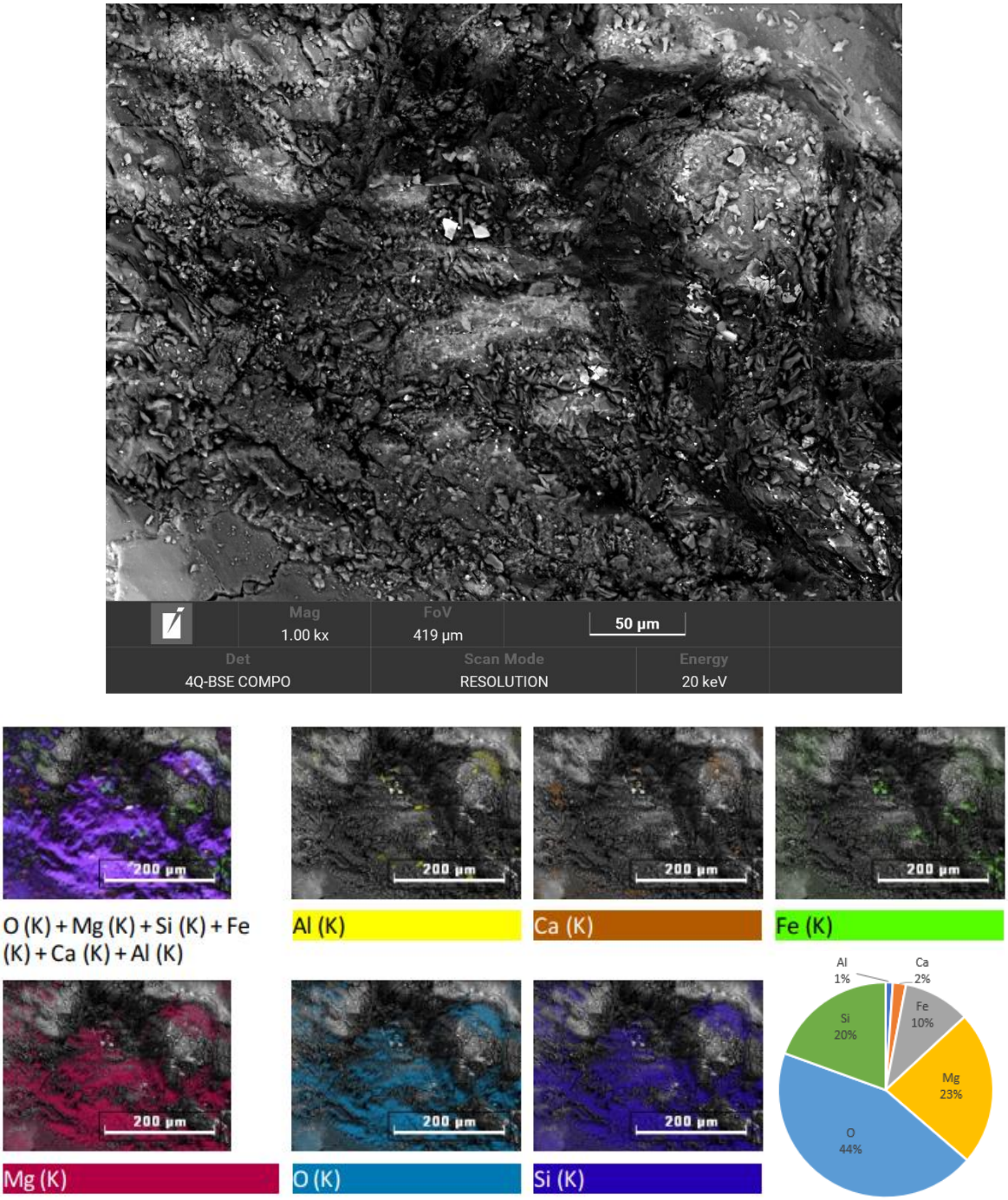

Figure 67: SEM image of mapped section of sample CdV42.85 (Mag. 1000x), respective elemental images from the section studied and quantity analysis (wt.%).

Samples CdV80.25 and CdV80.80 show similar mineralogical compositions, the first contains chlorite and the second one calcite, so sample CdV80.80 (Figure 68) was chosen for SEM analysis due to the fact that it showed some different circular grains, observed macroscopically, that can be of interest for analysis. This sample is predominantly composed of serpentine (83 wt.%) and this fact is supported by EDS analysis of the main mineralogy present in the sample, supporting what was concluded by XRD, XRF and FTIR analyses.

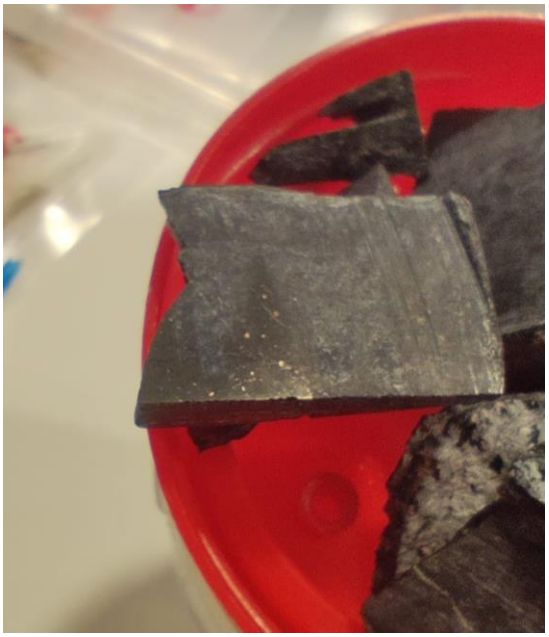

Figure 68: Fragment of sample CdV80.80 analyzed with SEM.

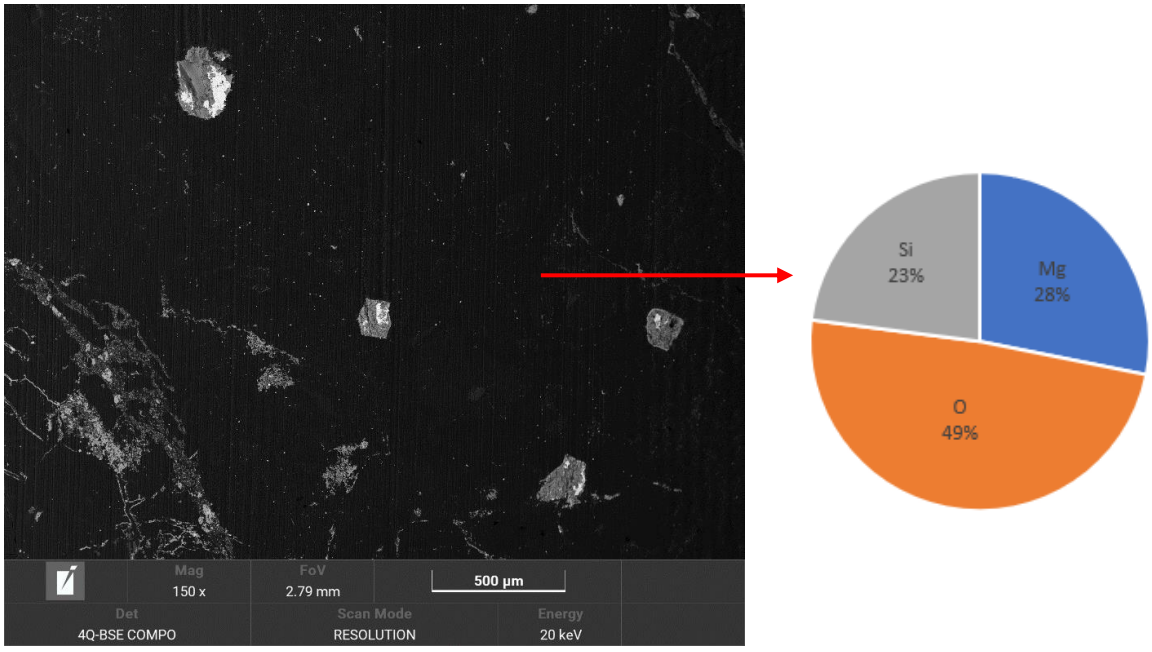

Figure 69: SEM image of a section of sample CdV80.80 (Mag. 150x). Serpentine in the matrix is confirmed by quantity analysis, showing a strong association of magnesium, silicon and oxygen (wt.%).

When zoomed and analyzed, EDS analysis of the section shown in Figure 70 identifies the grain observed previously as chromite, possibly ferritchromit, due to the iron percentage, highlighting the importance of studying this area of this specific sample. This sample showed the presence of a different mineral, with a completely distinct chemical composition, shown in white in Figure 70, with more than 75 wt.% copper. This is a rare occurrence in this sample, present only inside some grains, as copper was found in low quantities in chemical analysis of whole sample CdV80.80 (7.7 ppm). Cu-bearing mineral assemblages can form through desulfurization of primary sulfides (CdV80.80: SO_3=0.2 wt.%) due to highly reducing and sulfur-depleted conditions during serpentinization, as highly reducing conditions are produced by serpentinization processes (Schwarzenbach et al., 2014). Figure 71 shows a chemical element map of a section with a grain of chromite that was studied in order to determine the behavior of the elements present.

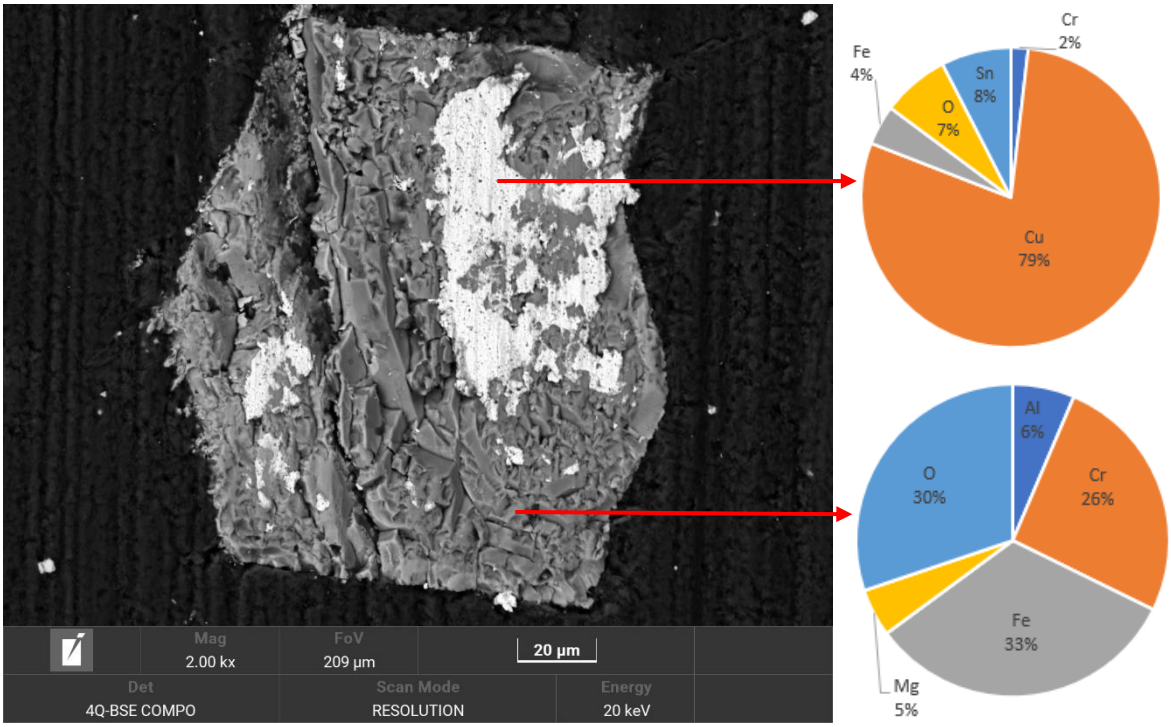

Figure 70: SEM image of a grain of chromite in sample CdV80.80. Quantity analysis (wt.%) proves the presence of this mineral, as well as the presence of another mineral, copper rich, in the white parts of the chromite grain.

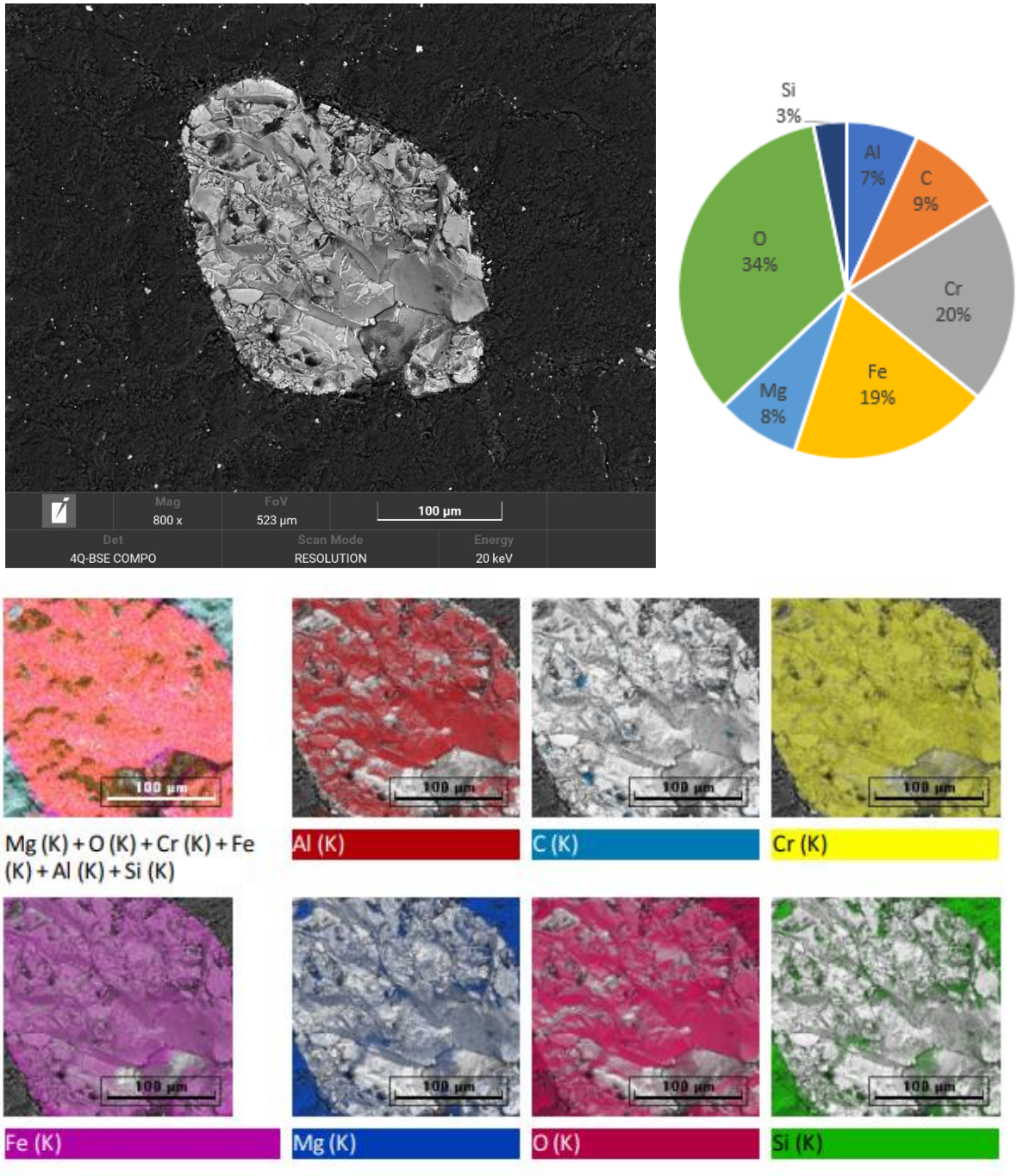

Figure 71: SEM image of a chromite grain mapped in sample CdV80.80 with EDS (Mag. 800x) with elemental analysis and quantity analysis (in wt.%).

Another grain detected in the sample was analyzed in order to conclude if all the grains observed macroscopically are chromite or mainly composed of chromium. This different grain was mainly composed of iron, indicative of magnetite, identified in this sample by other methods (Figures 72 and 73). This section also showed an area containing an intermediate zone between the matrix, serpentine-rich, and the magnetite grain.

Chromites are common accessories in peridotitic rocks, and their oxidation during serpentinization of host peridotites, with formation of ferritchromit ± magnetite rims, due to gradual oxidation of Fe^{2+} to Fe^{3+} and intense Mg, Al and eventually, Cr, depletion, has been extensively documented, with studies of the Cabeço de Vide serpentinized peridotites being made. Chromite oxidation patterns during peridotite serpentinization are dependent on the specific composition of the interacting fluid (pH), namely fluid-rock ratios and interactions (Ribeiro da Costa & Barriga, 2022).

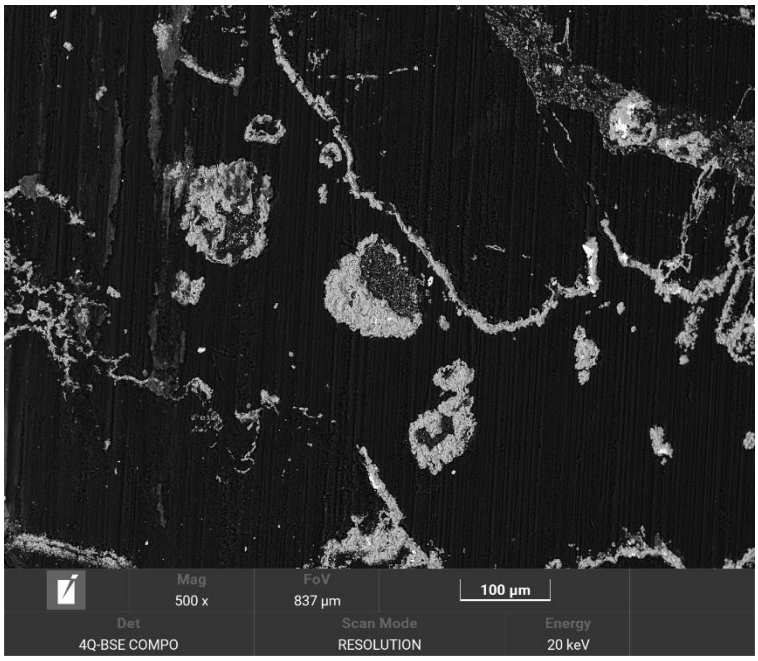

Figure 72: SEM image of a section of the sample CdV80.80 containing a grain of magnetite (Mag. 500x).

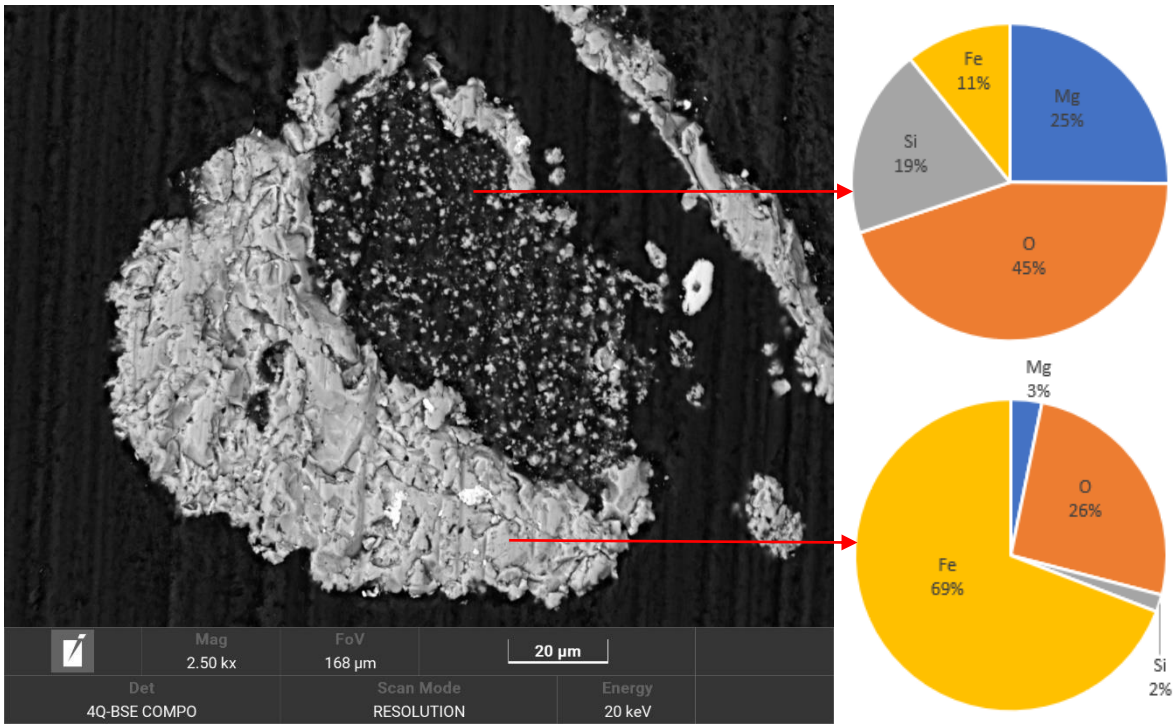

Figure 73: SEM image of a section of sample CdV80.80 containing a magnetite grain and serpentine (Mag. 2500x).

Sample CdV113.15 (Figure 74) was chosen for SEM analysis due to the fact that it is the sample that contains the highest percentage of serpentine in its mineral composition (97 wt.%) confirmed with data from XRD, XRF and ATR-FTIR. This is also confirmed by EDS analysis of different sections of the samples, where the chemical composition of the matrix shows a strong association between magnesium, silicon and oxygen.

Figure 74: Fragment of sample CdV113.15 analyzed with SEM.

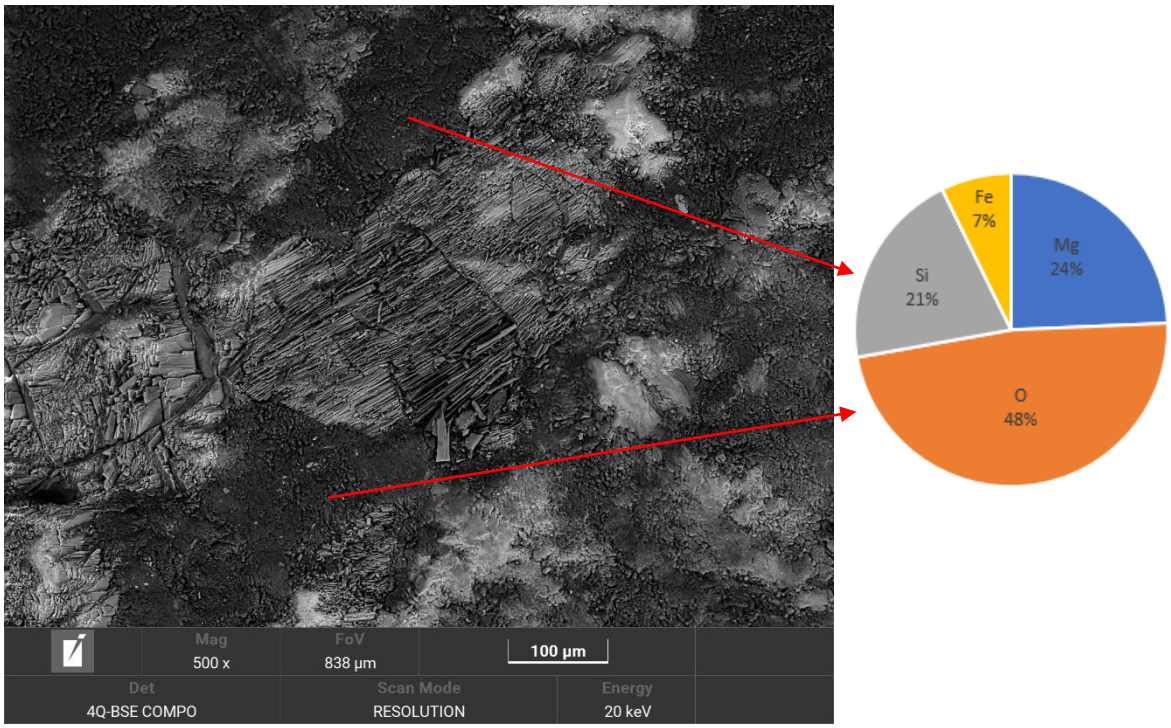

Figure 75: SEM image of a section of the sample CdV113.15 (Mag. 500x). Quantity analysis shows serpentine in the matrix of the sample (wt.%).

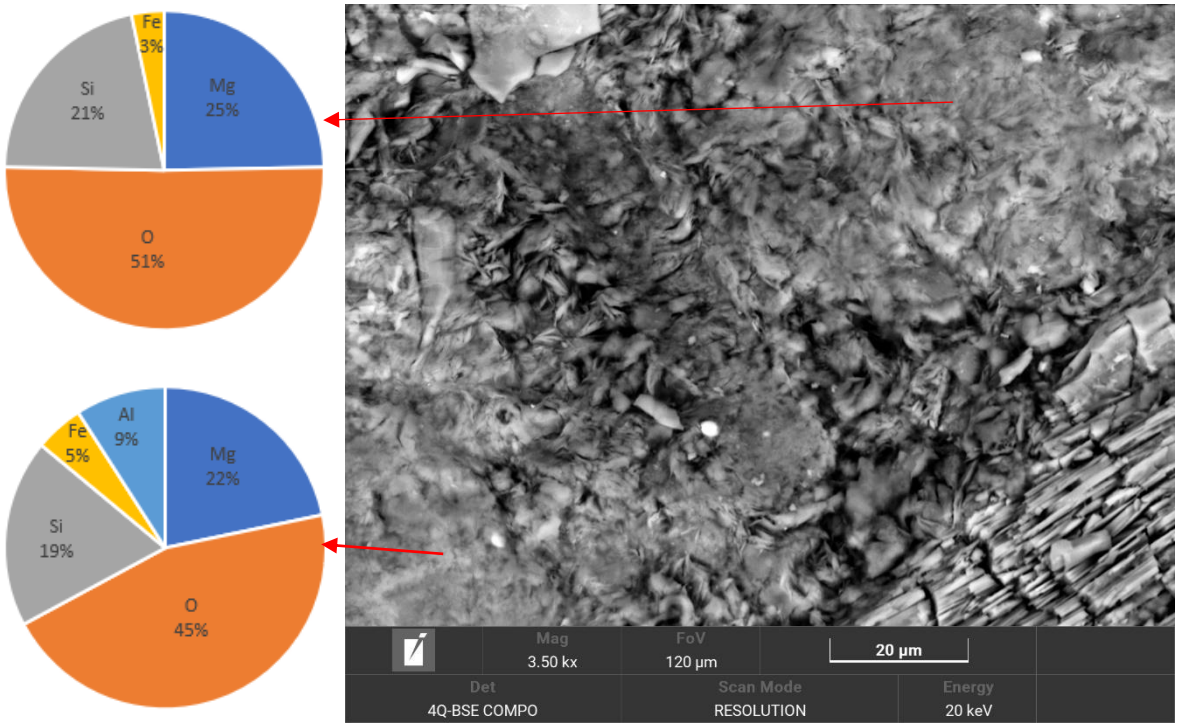

Figure 76: SEM image of a section of the sample 113.15 showing serpentines (Mag. 3500x).

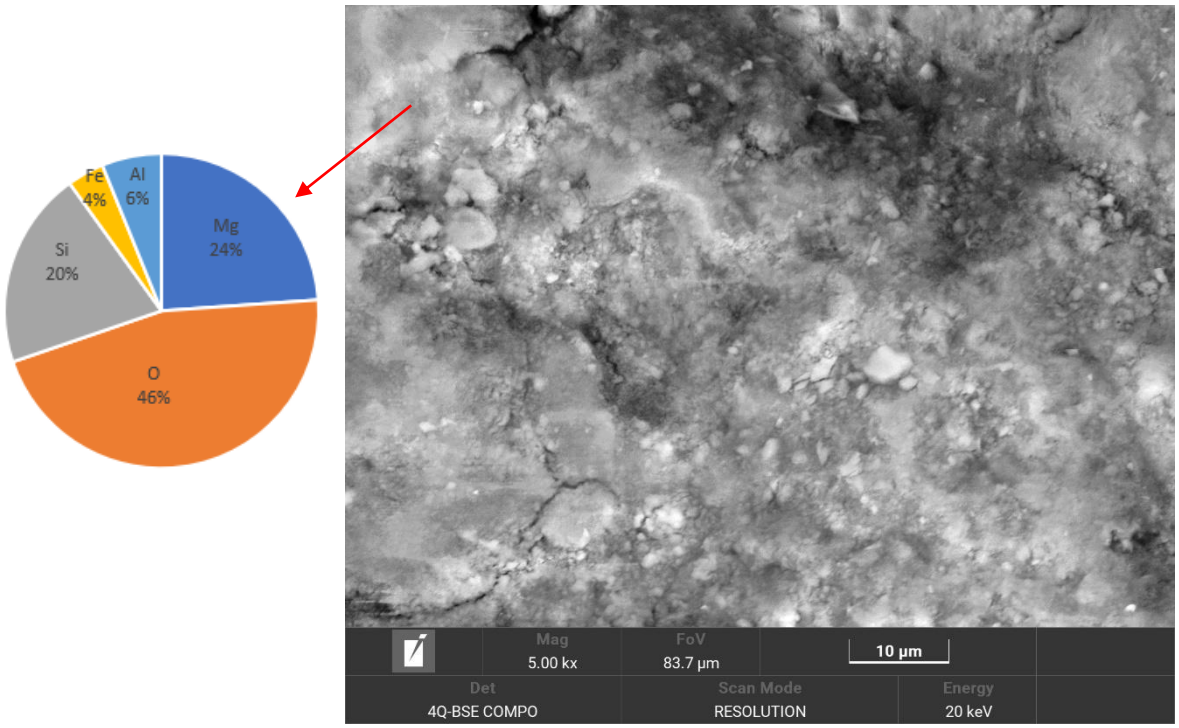

Figure 77: SEM image of a section of sample CdV113.15 showing a predominance of serpentines, indicated by quantity analysis by EDS (wt.%) (Mag. 5000x).

5.6. Analysis of samples CdV125.20_1 to 3

5.6.1. Petrographic Microscope Analysis

Macroscopically, it is easy to identify two different sections inside thin section from sample CdV125.20_1: one rich in serpentine $[Mg,Fe,Ni,Al,Zn,Mn)_{2\text{-}3}(Si,Al,Fe)_2O_5(OH)_4]$ and a larger one with amphibole and carbonates. In the first section, serpentine and phlogopite $[KMg_3AlSi_3O_{10}(F, OH)_2]$, magnesium-rich mica, are the most abundant minerals, represented in Figure 78. Also actinolite-tremolite amphibole $[Ca_2(Mg_{4.5\text{-}2.5}Fe^{2+}_{0.5\text{-}2.5})\ Si_8O_{22}(OH)_2]$, rich in calcium, is showed by the presence of needles in certain areas of the thin section, along with prehnite $[Ca_2Al(AlSi_3O_{10})(OH)_2]$, a hydrated calcium silicate that forms at low temperature and commonly present in veins, confirmed by its biaxial positive interference figure. This section also shows the existence of titanite $[CaTiSiO_5]$, titanium and calcium oxide, relics of clinopyroxene $[Ca(Mg,Fe)Si_2O_6]$, and opaque minerals like magnetite and ilmenite, that can be identified using a reflected light microscope. The second section also shows the presence of relics of hornblende, and carbonates associated with the hornblende (Figure 79).

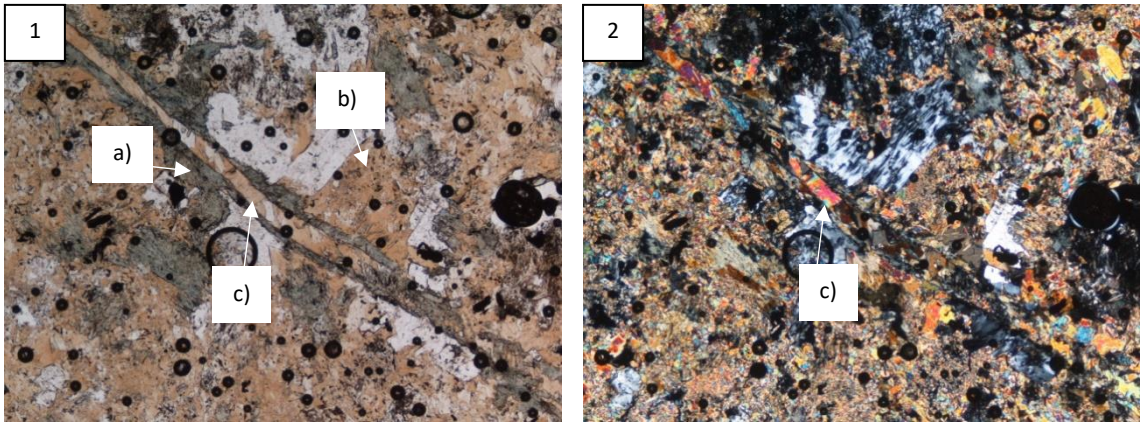

Figure 78: Optical microscopy in parallel (1) and crossed (2) polars showing the most abundant minerals in this section: a) serpentine, b) phlogopite, and c) relics of clinopyroxene inside the main vein of this section. 40x zoom.

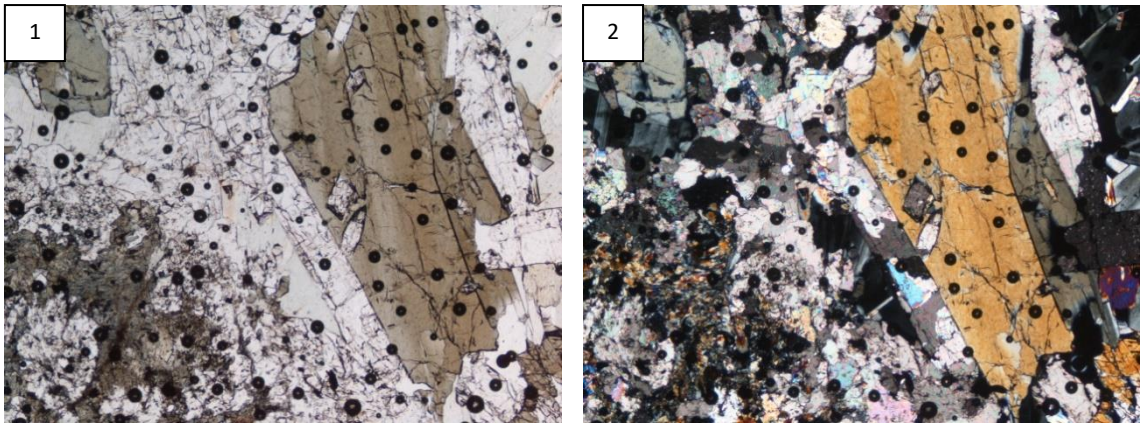

Figure 79: Optical microscopy in parallel (1) and crossed (2) polars showing the second section of the thin section L1 and showing hornblende (a). 40x zoom.

Without any visual assistance, it is possible to identify three different sections in CdV125.20_2: one closer to the bedrock, one corresponding to veins and the third showing the darker part of the sample (Figure 79). The first section, possibly closer to the composition of the bedrock, shows feldspar [$AlNaO_8Si_3$], corresponding to a sericitic alteration of plagioclase, a process that indicates hydration of the mineral phases. The zone with veins appears to have a non-desired thickness, which can induce error during interpretation, but it seems to show the presence of relics of olivine [$(Mg,Fe)_2SiO_4$] and a lot of alteration, that can correspond to serpentinization and oxidation (Figure 80). Serpentine forms at the mesh rims surrounding the relict cores of olivine, resulting in a pseudomorphic mesh texture of serpentines. In the third section, the main mineral that can be identified is blue amphibole, important because it represents an alkaline environment, and it can be identified as riebeckite [$Na_2(Fe^{2+}_3Fe^{3+}_2)Si_8O_{22}(OH)_2$]. This amphibole is surrounded by a different type of amphibole, rich in titanium, that can possibly be kaersutite [$NaCa_2(Mg_3AlTi^{4+})(Si_6Al_2)O_{22}O_2$], a calcic titanium bearing amphibole mineral. In this section, you can also identify a reddish mineral. After confirmation of a uniaxial negative interference figure, it can be described as a titanium-rich biotite, that sometimes appears as a red mineral in cross polars. There is also evidence of a reddish-brown mineral that shows a mixture between iron hydroxides and serpentine, is called iddingsite [$MgFe^{2+}_2Si_3O_{10}$. $4(H_2O)$], which forms in the presence of liquid water (Figure 81).

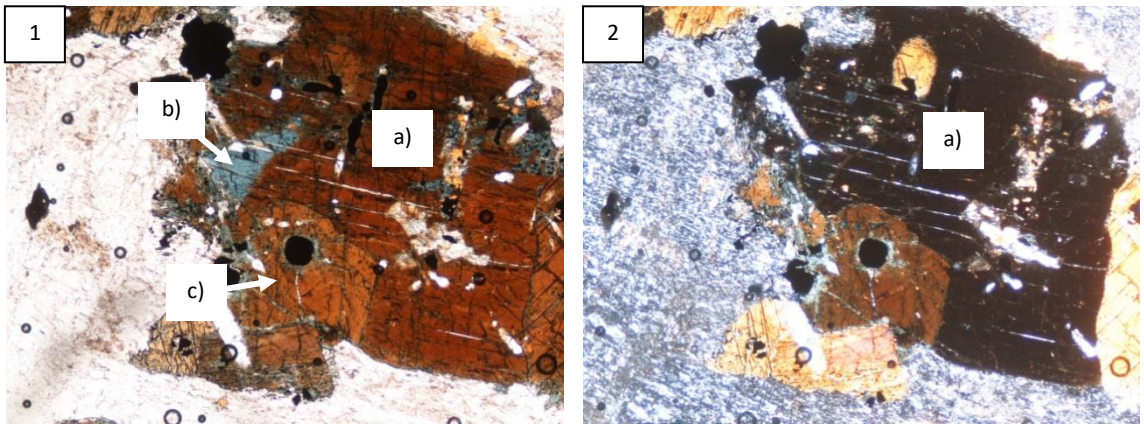

Figure 80: Optical microscopy in parallel (1) and crossed (2) polars showing the main minerals of the third section of L2: kaersutite (a) surrounding riebeckite, blue amphibole (b), and iddingsite (c). 40x zoom.

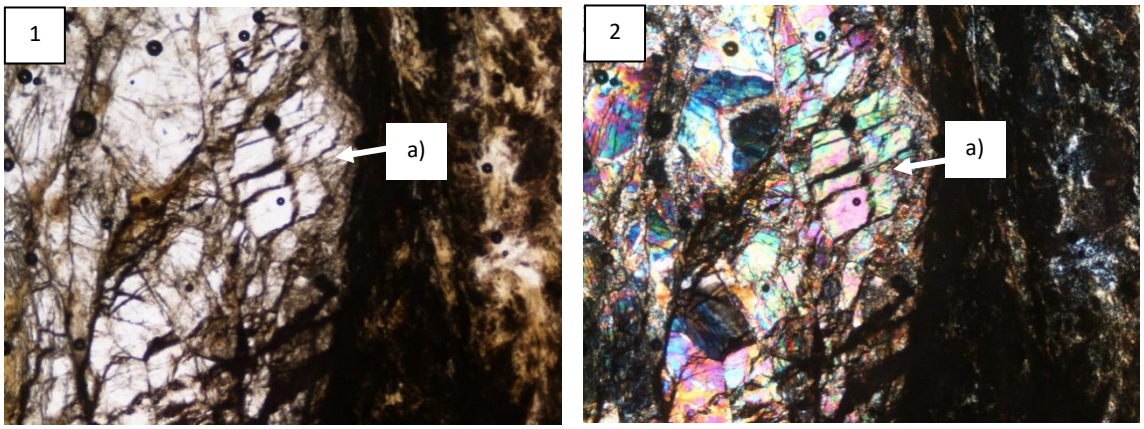

Figure 81: Optical microscopy in parallel (1) and crossed (2) polars showing pseudomorphic mesh texture with relict mesh cores of olivine (a) surrounded by serpentine, with a lot of alteration overall. 40x zoom.

In CdV125.20_3, it is possible to identify variably altered feldspar, indicative of processes of sericitization and caulinitization, showed colorless or white with a dirty aspect in parallel polars and grey in crossed polars. There are also some grains of microcline [$KAlSi_3O_8$] and quartz [SiO_2] in some areas of the thin section. Biotite can also be identified, possibly altered in sphene or leucoxene. The presence of some needle-like structures induces the possibility of the existence of rutile [TiO_2], that is confirmed through the identification of alteration of biotite, described by the possibility of titanium leaving from biotite and originating the needles, confirming the presence of rutile. This thin section also has carbonates present in veins and surrounding areas adjacent to veins (Figure 82). There is also a large carbonate area, also related to veins, that is rich in calcite [$CaCO_3$] (Figure 83).

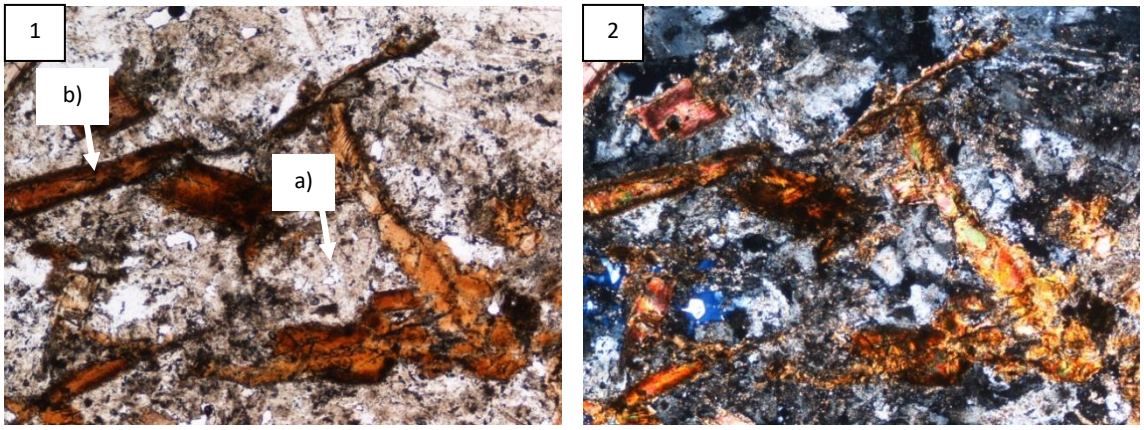

Figure 82: Optical microscopy in parallel (1) and crossed (2) polars showing feldspar (a) and rutile needles (b). 40x zoom.

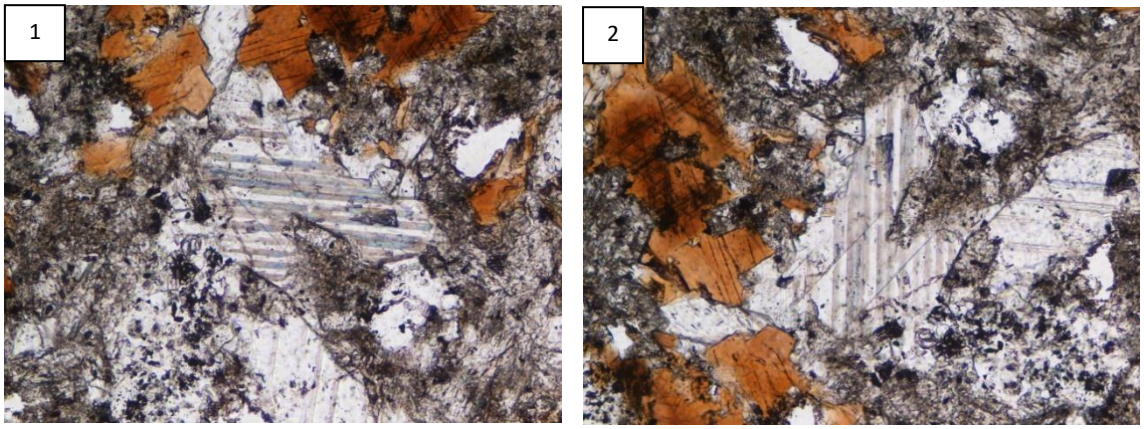

Figure 83: Optical microscopy in parallel polars of the carbonate area of L3 showing calcite in the center of the picture, in vertical (1) and horizontal (2) orientation. 100x zoom.

5.6.2. XRD Analysis

Considering the fact that samples CdV125.20_1 to CdV125.20_3 show different domains inside the same samples, fact showed in petrographic microscope analysis, it is complicated to achieve a complete correlation between thin section and XRD analysis in terms of mineralogical composition. However, XRD analysis allowed the identification of most of the minerals identified by petrographic microscopy, as demonstrated by Table 19.

Table 19: Mineralogical composition of CdV AC2 samples from 125.20m depth.

CdV AC2	Amp	Cal	Chl	Fsp	Mca	Prh	Rt	Srp
125.20_1	X	X	X		X	X	X	X
125.20_2	X		X	X	X	X	X	
125.20_3		X	X	X	X		X	X

Sample CdV125.20_1 shows predominantly the presence of phlogopite (mica) and amphibole, along with smaller quantities of calcite, chlorite, prehnite and serpentine. Even though pyroxene is the most resistant mineral to the serpentinization process, eventually it is partly replaced by hornblende, highlighting the importance of the presence of the relics of hornblende and carbonates associated with hornblende in this sample. This amphibole was identified by petrographic microscope as actinolite-tremolite amphibole, and this fact is very important because the presence of tremolite in serpentinites is due to breakdown of pyroxenes in the presence of water. CdV125.20_2 is primarily composed of feldspar, prehnite, riebeckite (blue amphibole) surrounded by another amphibole (kaersutite). Kaersutite may indicate a more initial stage of alteration, at temperatures around 500°C and low water/rock ratio, preceding the serpentinization of the ultramafics (Costa et al., 1993). This sample also shows some evidence of serpentine, chlorite, and biotite (mica). CdV125.20_3 shows feldspar, biotite (mica) and chlorite as main minerals present in this sample, as well as some minor quantities of calcite and rutile. Samples CdV125.20_2 and 3 show evidence of sericitic alteration of plagioclase with the presence of altered feldspar.

5.7. DNA confirmation and sequencing

Finally, the final image taken by the molecular imager and seen in this machine's specific software (Figure 84) allows us to make a major conclusion, that has massive implications for this thesis: there is DNA in our serpentine samples. We can say this because, for the thousands of DNA bands present in the markers used, these samples show a white stripe, confirming the presence of DNA in these samples. Positive controls are well defined and negative control shows no DNA, which are indicative of a successful execution of the protocols, and these allow us to affirm the presence of DNA in the samples.

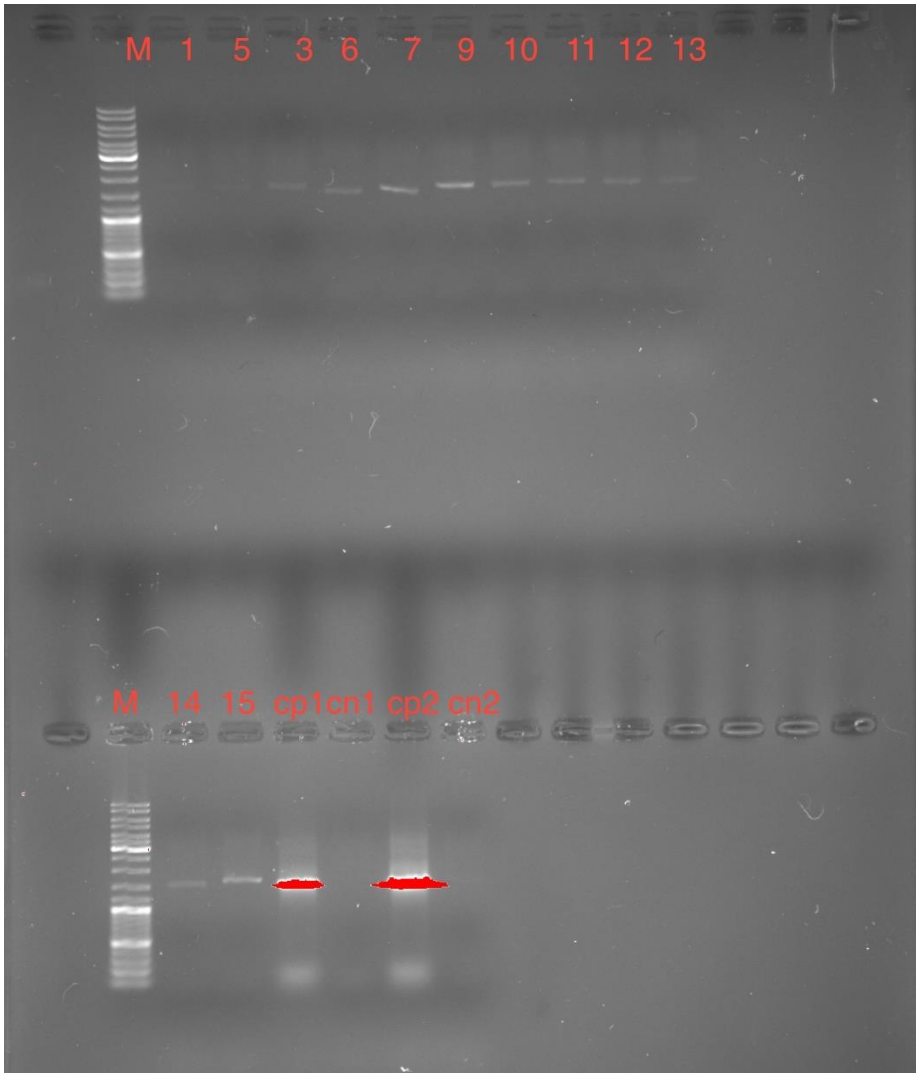

Figure 84: UV light image of the final agarose gel with samples, markers and controls labeled.

Following all the previous DNA procedures, the next step involved sending DNA samples for sequencing for two specific domains: Bacteria and Archaea, the most representative domains of microbial life. They're capable of adapting and surviving in extreme conditions, like temperature, salinity and nutrient scarcity, as they are capable of producing resistance and dormant structures. They have simple shapes and metabolism diversity, since they can have multiple sources of energy, like hydrogen, sulfur and carbon. The best example related to this thesis is methanogens, who have hydrogen as a source of energy and who curiously produce methane themselves. Unfortunately, these samples did not contain sufficient DNA to achieve detailed sequencing results. This fact also has implications for the final step of interpretation of biological data, made through bioinformatic analysis.

6. Conclusions

The two fundamental objectives within this document are a more detailed study of the CdV ultramafic rocks, specifically from drill core AC2, in what concerns both textural and mineralogical features, and the characterization of waters collected from streams, springs and boreholes in the study area, to fully understand the water-rock interaction process occurring at depth. This will provide a detailed database concerning the main compositional features of the minerals that make up the ultramafic rocks and their serpentinized derivatives exhibiting variable degrees of serpentinization. Processes related to serpentinization have a paramount astrobiological potential and for this reason, this thesis also focuses on the biosignature preservation potential in minerals of CdV samples, as serpentinization process is one of the possible sources of energy for life to emerge in the early Earth. Furthermore, all this information can be exceptionally valuable to serve as inventory or library of data for a future Mars Sample Return Mission.

Studies that establish a relation between Mars and the study area focus mainly on the characteristics of the water of the spa and boreholes. The unique features of these waters are produced due to the weathering of serpentinized and gabbroic rocks. Such types of groundwaters can infiltrate at depth, along major faults and fractures, and evolve to hyperalkaline thermomineral waters, resulting from hydration of olivine and pyroxene, from fissured/fractured dunite rocks, in a deeper and closed system.

There is no evidence of water/rock interaction at high temperatures, consistent with the low issue temperature (~19.5°C) of mineral waters from Cabeço de Vide, highlighted by the projection of their environmental isotopic values above the GMWL line. Stream water sample Ribeira showed high quantities of magnesium, that can be explained by serpentine dissolution. The fact that serpentinization of ultramafic rocks can contribute to the mineral water chemistry explains the low values of magnesium present in CdV mineral waters (AC5 and AC3). Calcite precipitation associated with CdV boreholes and springs is explained by the interaction between high calcium values in the alkaline fluids (pH>11 in CdV mineral waters) with the carbon dioxide from the atmosphere. Considering this information, the Cabeço de Vide mineral waters can be responsible for serpentinization at low temperature conditions of the ultramafic rocks present at depth.

The mineralogical composition of the CdV AC2 samples showed a predominant quantity of serpentine, indicative of a high evolutive state, starting at sample CdV42.85 until CdV116.00. The identification of lizardite as the main serpentine mineral present in these samples is indicative of the high evolution state, since lizardite is the most stable serpentine mineral at normal conditions. Since brucite is associated with chrysotile, the absence of this mineral is also indicative of a higher evolutive state of serpentinization. Iron oxides like magnetite, one of the main accessory minerals in these samples, are important, as they are a secondary product of the serpentinization process, as seen in Equation (2). Samples from shallower depths showed predominantly calcite (CdV26.80), originated from precipitation of calcite in the hydrothermal fluid, and

phlogopite (CdV27.00 and CdV28.00), indicative of an area that can show mineralogical compositions closer to the primary mineralogy, as main minerals. Partial sample analysis showed that the fractures present in CdV samples are mainly composed of calcite. Thin section analysis allowed the identification of a pseudomorphic mesh texture with serpentine surrounding relict mesh cores of olivine (CdV125.20_2).

Chemically, the distinct domains present in CdV samples facilitated the visualization of chemical composition data with SPSS, as high values of calcium corresponded to samples that contained calcite in their mineralogical composition, and this also showed a very high value of Loss on Ignition (LOI), originated from the presence of carbonates, particularly in sample CdV26.80 (37 wt.% of LOI). Magnesium is directly associated with the presence of serpentine minerals, while the presence of magnetite can be indicative of the high percentages of iron in the samples from the serpentinized domain. This information corroborates with previous studies by Rocha et al. (2017) and models proposed by Marques et al. (2018).

Attenuated Total Reflectance Fourier-transform Infra-Red Spectroscopy (ATR-FTIR) and Scanning Electron Microscope (SEM) analyses allowed the confirmation of the analyses made with previous techniques. ATR-FTIR analysis was extremely important for the achievement of good results, since it successfully validated the observations made through XRD, also confirming the fact that these techniques are complementary and allow relevant information that can miss if only XRD analysis is made. SEM analysis was crucial for the corroboration of all the information studied with other methods, as it allowed the identification of the minerals by their microscale chemical analysis. This method also allowed the identification of mineralogical occurrences that were not possible to make by techniques like XRD, for example in sample CdV80.80, emphasizing the importance of complementary studies to all the techniques used.

The confirmation of DNA in the Cabeço de Vide sample studied for this purpose was extremely important for the achievement of one of the objectives of the thesis. Even considering the fact that the sample did not contain sufficient DNA for detailed sequencing results and resulting interpretation of biological data, this information can be extremely valuable for the scientific community, as this was the first time that DNA was extracted from rock samples originated from continental serpentinization processes occurring at depth.

Considering all the information mentioned above, this thesis confirmed the importance of water/rock interactions occurring at depth in Cabeço de Vide, while corroborating all the information that emphasizes the lithological similarities between the study area and Mars, more specifically Jezero Crater, with the identification of carbonates, smectites, serpentines, iron oxides, and others. The hydrothermally altered mafic-ultramafic complex from CdV truly provides a unique opportunity for the investigation and study of continental serpentinized rocks on Earth. This thesis highlights the fact that CdV is an excellent mineralogical and astrobiological environment to study as a Mars analog.

With the objective of making this thesis more complete and answering some questions that remain unanswered, some elements are recommended for future work. This thesis only analyzed petrographic features from one depth, and it showed the presence of minerals, like olivine and tremolite amphibole, that were not identified by XRD and standard analysis. The production of thin sections of all samples or at least in intervals that can be representative of sections of the drill core can definitely improve the quality of this specific area of study. ATR-FTIR for Near Infrared (7500-4000 cm^{-1}) is important to better distinguish the serpentine minerals, as showed by Balan et al. (2002) and Madejová et al. (2017), as NIR region allows the identification of not only the vibrational modes related to the inner surface OH groups, but also that of inner OH groups, and their geometry and peaks can easily distinguish these minerals. The analysis and discussion of the Mössbauer Spectroscopy data is extremely important for this thesis, as this method allows the identification of all the iron information, like grade of oxidation of the iron present in CdV samples. To obtain a true and complete vision of subsurface environments, water and rock sampling should both be analyzed in order to characterize the microorganisms associated with them, as microbial communities inhabiting rocks show a different composition from those detected in underground water. Finally, if samples from CdV effectively show the presence of Bacteria and Archaea domains, we can confirm serpentines are an amazing starting point in the search of life on the Red Planet, and we can affirm this would have immense implications for Perseverance Mars Mission and possible formation of life on Mars.

7. References

Akhtar, K., Khan, S. A., Khan, S. B., & Asiri, A. M. (2018). Scanning electron microscopy: Principle and applications in nanomaterials characterization. *Handbook of Materials Characterization*, 113–145. https://doi.org/10.1007/978-3-319-92955-2_4/COVER

Albers, A. P. F., Melchiades, F. G., Machado, R., Baldo, J. B., & Boschi, A. O. (2002). Um método simples de caracterização de argilominerais por difração de raios X. *Cerâmica*, *48*(305), 34–37. https://doi.org/10.1590/S0366-69132002000100008

Ali, A., Wai Chiang, Y., & Santos, R. M. (2022). X-ray Diffraction Techniques for Mineral Characterization: A Review for Engineers of the Fundamentals, Applications, and Research Directions. *Minerals*. https://doi.org/10.3390/min12020205

Amador, E. S., Bandfield, J. L., & Thomas, N. H. (2018). A search for minerals associated with serpentinization across Mars using CRISM spectral data. *Icarus*, *311*, 113–134. https://doi.org/10.1016/J.ICARUS.2018.03.021

Andreani, M., Muñoz, M., Marcaillou, C., & Delacour, A. (2013). µXANES study of iron redox state in serpentine during oceanic serpentinization. *Lithos*, *178*, 70–83. https://doi.org/10.1016/J.LITHOS.2013.04.008

Azua-Bustos, A., González-Silva, C., & Fairén, A. G. (2022). The Atacama Desert in Northern Chile as an Analog Model of Mars. *Frontiers in Astronomy and Space Sciences*, *8*, 810426. https://doi.org/10.3389/FSPAS.2021.810426/BIBTEX

Balan, E., Saitta, A. M., Mauri, F., Lemaire, C., & Guyot, F. (2002). First-principles calculation of the infrared spectrum of lizardite. *American Mineralogist*, *87*(10), 1286–1290. https://doi.org/10.2138/AM-2002-1003

Barbato, A. K., Vithanage, M., Barbato, A., Karunatillake, S., Hood, D. R., & Vithanage, M. (2019). Variatons in Serpentine along the HC-VC Suture Zone of Sri-Lanka: An Analogue for Studying Martian Serpentinites. *50th Lunar and Planetary Science Conference*. https://www.researchgate.net/publication/332301136

Barnes, I., Lamarche, V. C., & Himmelberg, G. (1967). Geochemical evidence of present-day serpentinization. *Science (New York, N.Y.)*, *156*(3776), 830–832. https://doi.org/10.1126/SCIENCE.156.3776.830

Bishop, J., Murad, E., & Dyar, M. D. (2002). The influence of octahedral and tetrahedral cation substitution on the structure of smectites and serpentines as observed through infrared spectroscopy. *Clay Minerals*, *37*(4), 617–628. https://doi.org/10.1180/0009855023740064

Breitenfeld, L. B., Rogers, A. D., Glotch, T. D., Kaplan, H. H., Hamilton, V. E., & Christensen, P. R. (2022). Mapping Phyllosilicates on the Asteroid Bennu Using Thermal Emission Spectra and Machine Learning Model Applications. *Geophysical Research Letters*, *49*(20), e2022GL100815. https://doi.org/10.1029/2022GL100815

Brown, A. J., Viviano, C. E., & Goudge, T. A. (2020). Olivine-Carbonate Mineralogy of the Jezero Crater Region. *Journal of Geophysical Research: Planets*, *125*(3), e2019JE006011. https://doi.org/10.1029/2019JE006011

Broz, A., Horgan, B., Kalucha, H., Garczynski, B., Haber, J., Dehouck, E., Hurowitz, J., Johnson, J., Bell, J., & Mastcam-Z team, the. (2023). Diagenetic Alteration of Hogwallow Flats, Jezero Crater, Mars. *54th Lunar and Planetary Science Conference*. https://www.jpl.nasa.gov/images/pia25672-persever-

Chacko, T., Cole, D. R., & Horita, J. (2001). Equilibrium Oxygen, Hydrogen and Carbon Isotope Fractionation Factors Applicable to Geologic Systems. *Reviews in Mineralogy and Geochemistry*, *43*(1), 1–81. https://doi.org/10.2138/GSRMG.43.1.1

Chen, Y., Zou, C., Mastalerz, M., Hu, S., Gasaway, C., & Tao, X. (2015). Applications of Micro-Fourier Transform Infrared Spectroscopy (FTIR) in the Geological Sciences-A Review. *International Journal of Molecular Sciences*. https://doi.org/10.3390/ijms161226227

Comellas, J. M., Sharma, S. K., Gasda, P. J., Cousin, A., Mayhew, L., Brown, A. J., Acosta-Maeda, T. E., Dehouck, E., Veneranda, M., Connell, S., Cloutis, E., Ollila, A., Lanza, N., Clegg, S., Delapp, D., Maurice, S., & Wiens, R. C. (2023). The Identification of Serpentinization on Mars with Mars2020 SUPERCAM Instrument. *54th Lunar and Planetary Science Conference*.

Costa, I., Barriga, F., Mata, J. & Munhá, J.M. (1993). Rodingitization and serpentinization processes in Alter-do-Chão Massif (NE Alentejo). *Actas da IX Semana de Geoquímica [Proc. IX Geochemical Week].* 27–31.

Craig, H., 1961. Isotopic variations in meteoric waters. Science 133, 1703– 1704.

Crespo, M. A. R., Gómez, D. P., García, M. V. V., Amores, J. M. G., & Escribano, V. S. (2019). Characterization of Serpentines from Different Regions by Transmission Electron Microscopy, X-ray Diffraction, BET Specific Surface Area and Vibrational and Electronic Spectroscopy. *Fibers 2019, Vol. 7, Page 47*, *7*(5), 47. https://doi.org/10.3390/FIB7050047

Dallmeyer, R. D., & Quesada, C. (1992). Cadomian vs. Variscan evolution of the Ossa-Morena zone (SW Iberia): field and 40Ar/39Ar mineral age constraints. *Tectonophysics*, *216*(3–4), 339–364. https://doi.org/10.1016/0040-1951(92)90405-U

Darby Dyar, M., Agresti, D. G., Schaefer, M. W., Grant, C. A., & Sklute, E. C. (2006). *Mössbauer Spectroscopy of Earth and Planetary Materials*. https://doi.org/10.1146/annurev.earth.34.031405.125049

Dobrea, E. Z. N., & Clark, R. (2019). Detection of Serpentine at Jezero Crater. *50th Lunar and Planetary Science Conference*.

Ehlmann, B. L., Mustard, J. F., Swayze, G. A., Clark, R. N., Bishop, J. L., Poulet, F., Des Marais, D. J., Roach, L. H., Milliken, R. E., Wray, J. J., Barnouin-Jha, O., & Murchie, S. L. (2009). Identification of hydrated silicate minerals on Mars using MRO-CRISM: Geologic context near Nili Fossae and implications for aqueous alteration. *Journal of Geophysical Research: Planets*, *114*(E2), 0–08. https://doi.org/10.1029/2009JE003339

Ehlmann, B. L., Kelemen, P. B., Pinet, P., Mustard, J. F., Launeau, P., Ceuleneer, G., Ehlmann, B. L., Kelemen, P. B., Pinet, P., Mustard, J. F., Launeau, P., & Ceuleneer, G. (2012). Aqueous Alteration of Ultramafic Rocks in Oman: An Analog for Understanding Carbonate and Serpentine on Mars. *43rd Lunar and Planetary Science Conference*. https://doi.org/10.1126/science/1189667

Eigenbrode, J. L., Summons, R. E., Steele, A., Freissinet, C., Millan, M., Navarro-González, R., Sutter, B., McAdam, A. C., Franz, H. B., Glavin, D. P., Archer, P. D., Mahaffy, P. R., Conrad, P. G., Hurowitz, J. A., Grotzinger, J. P., Gupta, S., Ming, D. W., Sumner, D. Y., Szopa, C., … Coll, P. (2018). Organic matter preserved in 3-billion-year-old mudstones at Gale crater, Mars. *Science*, *360*(6393), 1096–1101. https://doi.org/10.1126/SCIENCE.AAS9185/SUPPL_FILE/AAS9185-EIGENBRODE-SM.PDF

Etiope, G., Vance, S., Christensen, L. E., Marques, J. M., & Ribeiro da Costa, I. (2013). Methane in serpentinized ultramafic rocks in mainland Portugal. *Marine and Petroleum Geology*, *45*, 12–16. https://doi.org/10.1016/J.MARPETGEO.2013.04.009

Evans, B. W. (2008). Control of the Products of Serpentinization by the Fe2+Mg−1 Exchange Potential of Olivine and Orthopyroxene. *Journal of Petrology*, *49*(10), 1873–1887. https://doi.org/10.1093/PETROLOGY/EGN050

Farmer, V. C., & Russell, J. D. (1964). The infra-red spectra of layer silicates. *Spectrochimica Acta*, *20*(7), 1149–1173. https://doi.org/10.1016/0371-1951(64)80165-X

Fassett, C. I., & Head, J. W. (2005). Fluvial sedimentary deposits on Mars: Ancient deltas in a crater lake in the Nili Fossae region. *Geophysical Research Letters*, *32*(14), 1–5. https://doi.org/10.1029/2005GL023456

Fernandes, J., & Francés, A. P. (2010). Sistema Aquífero Monforte - Alter do Chão. Resultados obtidos no âmbito do Estudo dos Recursos Hídricos Subterrâneos do Alentejo (Projecto ERHSA). In *Os Aquíferos das Bacias Hidrográficas do Rio Tejo e das Ribeiras do Oeste* (Colecção Tágides, Vol. 7, pp. 145–155). https://www.researchgate.net/publication/279921867_Sistema_Aquifero_Monforte_-_Alter_do_Chao_Resultados_obtidos_no_ambito_do_Estudo_dos_Recursos_Hidricos_Subterraneos_do_Alentejo_Projecto_ERHSA

Fernández-Turiel, J. L., Llorens, J. F., López-Vera, F., Gómez-Artola, C., Morell, I., & Gimeno, D. (2000). Strategy for water analysis using ICP-MS. *Fresenius' Journal of Analytical Chemistry*, *368*(6), 601–606. https://doi.org/10.1007/S002160000552

Ferreira, M. P., & Mendonça, J. J. L. (1990). Enquadramento Geológico e Hidrogeológico das Nascentes de Água Minero-Medicinal de Cabeço de Vide. In *Livro de Homenagem a Carlos Romariz* (pp. 151–173). https://www.researchgate.net/publication/307940939_Enquadramento_Geologico_e_Hidrogeologico_das_Nascentes_de_Agua_Minero-Medicinal_de_Cabeco_de_Vide

Fritsch, E., Balan, E., Petit, S., & Juillot, F. (2021). Structural, textural, and chemical controls on the OH stretching vibrations in serpentine-group minerals. *European Journal of Mineralogy*, *33*(4), 447–462. https://doi.org/10.5194/EJM-33-447-2021

Früh-Green, G. L., Connolly, J. A. D., Plas, A., Kelley, D. S., & Grobéty, B. (2004). Serpentinization of Oceanic Peridotites: Implications for Geochemical Cycles and Biological Activity. *Geophysical Monograph Series*, *144*, 119–136. https://doi.org/10.1029/144GM08

Gomes, C. F. (1988). *Argilas: O que são e para que servem*. Fundação Calouste Gulbenkian. Serviço de Educação. https://books.google.com/books/about/Argilas.html?hl=pt-BR&id=bztfNQAACAAJ

Gonçalves, F. (1973). *Carta Geológica de Portugal na Escala de 1/50 000 Notícia Explicativa da Folha 32-B Portalegre*.

Goudge, T. A., Mustard, J. F., Head, J. W., Fassett, C. I., & Wiseman, S. M. (2015). Assessing the mineralogy of the watershed and fan deposits of the Jezero crater paleolake system, Mars. *Journal of Geophysical Research: Planets*, *120*(4), 775–808. https://doi.org/10.1002/2014JE004782

Goudge, T. A., Fassett, C. I., & Mohrig, D. (2019). Incision of paleolake outlet canyons on Mars from overflow flooding. *Geology*, *47*(1), 7–10. https://doi.org/10.1130/G45397.1

Greenberger, R. N., Mustard, J. F., Cloutis, E. A., Pratt, L. M., Sauer, P. E., Mann, P., Turner, K., Darby Dyar, M., & Bish, D. L. (2015). Serpentinization, iron oxidation, and aqueous conditions in an ophiolite: Implications for hydrogen production and habitability on Mars. *Earth and Planetary Science Letters*, *416*, 21–34. https://doi.org/10.1016/J.EPSL.2015.02.002

Holm, N. G., Oze, C., Mousis, O., Waite, J. H., & Guilbert-Lepoutre, A. (2015). Serpentinization and the Formation of H2 and CH4 on Celestial Bodies (Planets, Moons, Comets). *Astrobiology*, *15*(7), 587–600. https://doi.org/10.1089/AST.2014.1188/ASSET/IMAGES/LARGE/FIGURE5.JPEG

Horgan, B. H. N., Anderson, R. B., Dromart, G., Amador, E. S., & Rice, M. S. (2020). The mineral diversity of Jezero crater: Evidence for possible lacustrine carbonates on Mars. *Icarus*, *339*, 113526. https://doi.org/10.1016/J.ICARUS.2019.113526

Horneck, G., Walter, N., Westall, F., Grenfell, J. L., Martin, W. F., Gomez, F., Leuko, S., Lee, N., Onofri, S., Tsiganis, K., Saladino, R., Pilat-Lohinger, E., Palomba, E., Harrison, J., Rull, F., Muller, C., Strazzulla, G., Brucato, J. R., Rettberg, P., & Capria, M. T. (2016). AstRoMap European Astrobiology Roadmap. *Astrobiology*, *16*(3), 201–243. https://doi.org/10.1089/AST.2015.1441

Iyer, K. (2007). *Mechanisms of serpentinization and some geochemical effects*.

Karunatillake, S., Hood, D., Barbato, A., Vithanage, M., Chandrajith, R., Perl, S., Lorenzo, J., Oze, C., Williams, A., Malaviarachchi, S. P. K., Dharmapriya, P. L., Karunatillake, S., Hood, D., Barbato, A., Vithanage, M., Chandrajith, R., Perl, S., Lorenzo, J., Oze, C., … Dharmapriya, P. L. (2021). Sri Lanka's Serpentine Zone as a Mars Analog Site. *Terrestrial Analogs*. https://ui.adsabs.harvard.edu/abs/2021LPICo2595.8088K/abstract

Kelley, D. S., Karson, J. A., Blackman, D. K., Früh-Green, G. L., Butterfield, D. A., Lilley, M. D., Olson, E. J., Schrenk, M. O., Roe, K. K., Lebon, G. T., & Rivizzigno, P. (2001). An off-axis hydrothermal vent field near the Mid-Atlantic Ridge at 30 degrees N. *Nature*, *412*(6843), 145–149. https://doi.org/10.1038/35084000

Kim, D. W. (2022). Mars Space Exploration and Astronautical Religion in Human Research History: Psychological Countermeasures of Long-Term Astronauts. *Aerospace 2022, Vol. 9, Page 814*, *9*(12), 814. https://doi.org/10.3390/AEROSPACE9120814

Lang, S. Q., & Brazelton, W. J. (2020). Habitability of the marine serpentinite subsurface: a casestudy of the Lost City hydrothermal field. *Philosophical Transactions of the Royal Society A*, *378*(2165). https://doi.org/10.1098/RSTA.2018.0429

Madejová, J., & Komadel, P. (2001). Baseline studies of the clay minerals society source clays: Infrared methods. *Clays and Clay Minerals*, *49*(5), 410–432. https://doi.org/10.1346/CCMN.2001.0490508/METRICS

Madejová, J. (2003). FTIR techniques in clay mineral studies. *Vibrational Spectroscopy*, *31*(1), 1–10. https://doi.org/10.1016/S0924-2031(02)00065-6

Madejová, J., Gates, W. P., & Petit, S. (2017). IR Spectra of Clay Minerals. *Developments in Clay Science*, *8*, 107–149. https://doi.org/10.1016/B978-0-08-100355-8.00005-9

Mandon, L., Quantin-Nataf, C., Royer, C., Beck, P., Fouchet, T., Johnson, J. R., Dehouck, E., Le Mouélic, S., Poulet, F., Montmessin, F., Pilorget, C., Gasnault, O., Forni, O., Mayhew, L. E., Beyssac, O., Bertrand, T., Clavé, E., Pinet, P., Brown, A. J., … Wiens, R. C. (2023). Reflectance of Jezero Crater Floor: 2. Mineralogical Interpretation. *Journal of Geophysical Research: Planets*, *128*(7), e2022JE007450. https://doi.org/10.1029/2022JE007450

Marcaillou, C., Muñoz, M., Vidal, O., Parra, T., & Harfouche, M. (2011). Mineralogical evidence for H2 degassing during serpentinization at 300 °C/300 bar. *Earth and Planetary Science Letters*, *303*(3–4), 281–290. https://doi.org/10.1016/J.EPSL.2011.01.006

Marques, J. M., Carreira, P. M., Carvalho, M. R., Matias, M. J., Goff, F. E., Basto, M. J., Graça, R. C., Aires-Barros, L., & Rocha, L. (2008). Origins of high pH mineral waters from ultramafic rocks, Central Portugal. *Applied Geochemistry*, *23*(12), 3278–3289. https://doi.org/10.1016/J.APGEOCHEM.2008.06.029

Marques, J. M., Etiope, G., Neves, M. O., Carreira, P. M., Rocha, C., Vance, S. D., Christensen, L., Miller, A. Z., & Suzuki, S. (2018). Linking serpentinization, hyperalkaline mineral waters and abiotic methane production in continental peridotites: an integrated hydrogeological-bio-geochemical model from the Cabeço de Vide CH4-rich aquifer (Portugal). *Applied Geochemistry*, *96*, 287–301. https://doi.org/10.1016/J.APGEOCHEM.2018.07.011

Marques, J. M., Carreira, P. M., Neves, O., Marques, J. E., & Teixeira, J. (2019). Revision of the hydrogeological conceptual models of two Portuguese thermomineral water systems: similarities and differences. *Sustainable Water Resources Management*, *5*(1), 117–133. https://doi.org/10.1007/S40899-018-0218-8/FIGURES/12

Maurício, A., Pereira, M. F., Rocha, C., Figueiredo, C., & Marques, J. M. (2017). X-ray Micro-CT Study of Cabeço de Vide Serpentinites and Carbonate Rock Samples: A Preliminary Approach. *Procedia Earth and Planetary Science*, *17*, 952–955. https://doi.org/10.1016/J.PROEPS.2017.01.034

Mayor, M., & Queloz, D. (1995). A Jupiter-mass companion to a solar-type star. *Nature 1995 378:6555*, *378*(6555), 355–359. https://doi.org/10.1038/378355a0

Mével, C. (2003). Serpentinization of abyssal peridotites at mid-ocean ridges. *Comptes Rendus Geoscience*, *335*(10–11), 825–852. https://doi.org/10.1016/J.CRTE.2003.08.006

Mohammed, A., & Abdullah, A. (2019). Scanning Electron Microscopy (SEM): A Review. *2018 International Conference on Hydraulics and Pneumatics - HERVEX*.

Moody, J. B. (1976). Serpentinization: a review. *Lithos*, *9*(2), 125–138. https://doi.org/10.1016/0024-4937(76)90030-X

Müntener, O. (2010). Serpentine and serpentinization: A link between planet formation and life. *Geology*, *38*(10), 959–960. https://doi.org/10.1130/FOCUS102010.1

Núñez, J. I., Johnson, J. R., Rice, M. S., Horgan, B. N., Vaughan, A., Garczynski, B. J., Duflot, L. E., Million, C. C., St Clair, M., Merusi, M., Kinch, K. M., Hayes, A. G., Tate, C., Gupta, S., Barnes, R., Kah, L., Maki, J., Bell III, J. F., Benison, K. C., … Mastcam-Z Team. (2023). Spectral Diversity Along the Delta Front in Jezero Crater, Mars as seen with Mastcam-Z on the Mars 2020 Perseverance Rover. *54th Lunar and Planetary Science Conference*.

O'Hanley, D. S., & Dyar, M. D. (1993). The composition of lizardite 1T and, the formation of magnetite in serpentinites. *American Mineralogist*, *78*, 391–404.

O'Hanley, D. S. (1996). *Serpentinites: records of tectonic and petrological history*.

Pinto, Z., Pañeda, A., Castelo Branco, J. M. (2003), Área de Campo Maior. Relatório inédito de prospeção e pesquisa (2º semestre de 2003) da Rio Narcea Gold Mines S. A., 26 p.

Pinto, Z. A., Pañeda, A., Castelo Branco, J. M., Leal Gomes, C., & Dias, P. A. (2006). Cartografia Geológica do Complexo básico-ultrabásico de Cabeço de Vide - Ensaio sobre a Geometria e Potencial Metalogénico. *VII Congresso Nacional de Geologia*.

Post, J. L., & Borer, L. (2000). High-resolution infrared spectra, physical properties, and micromorphology of serpentines. *Applied Clay Science*, *16*(1–2), 73–85. https://doi.org/10.1016/S0169-1317(99)00047-2

Reedy, C. L. (1994). Thin-section Petrography in Studies of Cultural Materials. *Journal of the American Institute for Conservation*, *33*(2), 115–129. https://doi.org/10.1179/019713694806124793

Ribeiro da Costa, I., & Barriga, F. J. A. S. (2022). Chromite Oxidation Patterns Associated to Serpentinization: Case Studies from the Mid-Atlantic Ridge, the Alter do Chão Massif (NE Alentejo, Portugal) and the Ronda Massif (Spain). *Minerals*, *12*(10), 1300. https://doi.org/10.3390/MIN12101300/S1

Rocha, F., Costa, C., & Marques, J. M. (2017). Mineralogical Evidence of Hydrothermal Alteration in Cabeço de Vide Mafic – Ultramafic Complex, Central Portugal. *Procedia Earth and Planetary Science*, *17*, 936–939. https://doi.org/10.1016/J.PROEPS.2017.01.025

Russell, J. D., & Fraser, A. R. (1994). Infrared methods. *Clay Mineralogy: Spectroscopic and Chemical Determinative Methods*, 11–67. https://doi.org/10.1007/978-94-011-0727-3_2

Russell, M. J., Hall, A. J., & Martin, W. (2010). Serpentinization as a source of energy at the origin of life. *Geobiology*, *8*(5), 355–371. https://doi.org/10.1111/J.1472-4669.2010.00249.X

Russell, M. J., Barge, L. M., Bhartia, R., Bocanegra, D., Bracher, P. J., Branscomb, E., Kidd, R., McGlynn, S., Meier, D. H., Nitschke, W., Shibuya, T., Vance, S., White, L., & Kanik, I. (2014). The drive to life on wet and Icy Worlds. *Astrobiology*, *14*(4), 308–343. https://doi.org/10.1089/AST.2013.1110

Salameh, E. (2004). Using environmental isotopes in the study of the recharge-discharge mechanisms of the Yarmouk catchment area in Jordan. *Hydrogeology Journal*, *12*(4), 451–463. https://doi.org/10.1007/S10040-004-0357-X

Schwarzenbach, E. M., Gazel, E., & Caddick, M. J. (2014). Hydrothermal processes in partially serpentinized peridotites from Costa Rica: evidence from native copper and complex sulfide assemblages. *Contributions to Mineralogy and Petrology*, *168*(5), 1–21. https://doi.org/10.1007/S00410-014-1079-2/FIGURES/8

Sharma, S., Roppel, R. D., Murphy, A. E., Beegle, L. W., Bhartia, R., Steele, A., Hollis, J. R., Siljeström, S., McCubbin, F. M., Asher, S. A., Abbey, W. J., Allwood, A. C., Berger, E. L., Bleefeld, B. L., Burton, A. S., Bykov, S. V., Cardarelli, E. L., Conrad, P. G., Corpolongo, A., … Yanchilina, A. (2023). Diverse organic-mineral associations in Jezero crater, Mars. *Nature 2023 619:7971*, *619*(7971), 724–732. https://doi.org/10.1038/s41586-023-06143-z

Simon, J. I., Hickman-Lewis, K., Cohen, B. A., Mayhew, L. E., Shuster, D. L., Debaille, V., Hausrath, E. M., Weiss, B. P., Bosak, T., Zorzano, M. P., Amundsen, H. E. F., Beegle, L. W., Bell, J. F., Benison, K. C., Berger, E. L., Beyssac, O., Brown, A. J., Calef, F., Casademont, T. M., … Williford, K. H. (2023). Samples Collected from the Floor of Jezero Crater with the Mars 2020 Perseverance Rover. *Journal of Geophysical Research: Planets*, *128*(6), e2022JE007474. https://doi.org/10.1029/2022JE007474

Steele, A., Benning, L. G., Wirth, R., Schreiber, A., Araki, T., McCubbin, F. M., Fries, M. D., Nittler, L. R., Wang, J., Hallis, L. J., Conrad, P. G., Conley, C., Vitale, S., O'Brien, A. C., Riggi, V., & Rogers, K. (2022). Organic synthesis associated with serpentinization and carbonation on early Mars. *Science*, *375*(6577), 172–177. https://doi.org/10.1126/SCIENCE.ABG7905/SUPPL_FILE/SCIENCE.ABG7905_SM.V1.PDF

Szponar, N., Brazelton, W. J., Schrenk, M. O., Bower, D. M., Steele, A., & Morrill, P. L. (2013). Geochemistry of a continental site of serpentinization, the Tablelands Ophiolite, Gros Morne National Park: A Mars analogue. *Icarus*, *224*(2), 286–296. https://doi.org/10.1016/J.ICARUS.2012.07.004

Terzer, S., Wassenaar, L. I., Araguás-Araguás, L. J., & Aggarwal, P. K. (2013). Global isoscapes for δ18O and δ2H in precipitation: Improved prediction using regionalized climatic regression models. *Hydrology and Earth System Sciences*, *17*(11), 4713–4728. https://doi.org/10.5194/HESS-17-4713-2013

Vance, S. D., & Melwani Daswani, M. (2020). Serpentinite and the search for life beyond Earth. *Philosophical Transactions of the Royal Society A*, *378*(2165). https://doi.org/10.1098/RSTA.2018.0421

Vasavada, A. R. (2022). Mission Overview and Scientific Contributions from the Mars Science Laboratory Curiosity Rover After Eight Years of Surface Operations. *Space Science Reviews 2022 218:3*, *218*(3), 1–65. https://doi.org/10.1007/S11214-022-00882-7

Vithanage, M., Rajapaksha, A. U., Oze, C., Rajakaruna, N., & Dissanayake, C. B. (2014). Metal release from serpentine soils in Sri Lanka. *Environmental Monitoring and Assessment*, *186*(6), 3415–3429. https://doi.org/10.1007/S10661-014-3626-8/TABLES/5

Wang, X. Bin, Ouyang, Z. Y., Zhuo, S. G., Zhang, M. F., Zheng, G. D., & Wang, Y. L. (2014). Serpentinization, abiogenic organic compounds, and deep life. *Science China Earth Sciences*, *57*(5), 878–887. https://doi.org/10.1007/S11430-014-4821-8/METRICS

Warr, L. N. (2021). IMA–CNMNC approved mineral symbols. *Mineralogical Magazine*, *85*(3), 291–320. https://doi.org/10.1180/MGM.2021.43

Webster, C. R., Mahaffy, P. R., Atreya, S. K., Moores, J. E., Flesch, G. J., Malespin, C., McKay, C. P., Martinez, G., Smith, C. L., Martin-Torres, J., Gomez-Elvira, J., Zorzano, M. P., Wong, M. H., Trainer, M. G., Steele, A., Archer, D., Sutter, B., Coll, P. J., Freissinet, C., … Vasavada, A. R. (2018). Background levels of methane in Mars' atmosphere show strong seasonal variations. *Science*, *360*(6393), 1093–1096. https://doi.org/10.1126/SCIENCE.AAQ0131/SUPPL_FILE/AAQ0131-WEBSTER-SM.PDF

Wicks, F. J., & Whittaker, E. J. W. (1977). Serpentine Textures and Serpentinization. *Canadian Mineralogist*, *15*, 459–488.

Zastrow, A. M., & Glotch, T. D. (2021). Distinct Carbonate Lithologies in Jezero Crater, Mars. *Geophysical Research Letters*, *48*(9), e2020GL092365. https://doi.org/10.1029/2020GL092365

8. Attachments

1 – ICP-MS and Ionic Chromatography

1st Campaign												
Analyte Symbol	Li	Be	B	Na	Mg	Al	P	K	Ca	V	Cr	Mn
Unit Symbol	µg/L	µg/L	µg/L	mg/L	mg/L	µg/L	µg/L	mg/L	mg/L	µg/L	µg/L	µg/L
Quantification Limit	0.5	0.5	10	0.05	0.05	2.5	25	0.05	0.05	0.1	0.05	0.1
AC5	1.01	<0.5	196.76	39.45	0.08	139.24	<25	3.89	21.68	<0.10	0.47	0.26
AC3	0.76	<0.5	229.99	49.99	0.23	183.53	<25	4.50	22.84	0.10	1.44	0.70
Ribeira	1.81	<0.5	13.54	10.76	80.35	<2.5	<25	0.64	35.83	4.79	1.35	2.84
Fonte	1.49	<0.5	16.22	10.96	94.41	2.63	29.64	0.83	38.98	4.93	1.98	0.63
Ermida	1.18	<0.5	209.83	58.63	0.24	82.60	<25	5.07	3.53	1.47	0.21	0.27

1st Campaign												
Analyte Symbol	Fe	Co	Ni	Cu	Zn	As	Se	Rb	Sr	Y	Mo	Ag
Unit Symbol	µg/L	µg/L	µg/L	µg/L	µg/L	µg/L	µg/L	µg/L	µg/L	µg/L	µg/L	µg/L
Quantification Limit	1	0.05	0.1	0.1	1	0.25	0.5	0.1	0.25	0.01	0.05	0.05
AC5	6.52	<0.05	0.63	0.71	1.61	<0.25	<0.5	8.58	243	<0.01	0.13	<0.05
AC3	15.53	0.05	4.22	2.02	1.63	<0.25	<0.5	8.84	300	<0.01	0.18	<0.05
Ribeira	7.66	0.13	3.81	1.82	1.55	0.79	<0.5	1.04	161	0.04	0.12	<0.05
Fonte	2.31	0.06	2.34	1.72	1.76	0.85	0.65	1.48	199	0.03	0.13	<0.05
Ermida	3.82	<0.05	0.31	0.91	<1.0	0.50	<0.5	9.83	318	<0.01	0.21	<0.05

1st Campaign												
Analyte Symbol	Cd	Sn	Sb	Ba	La	Ce	Pr	Nd	Sm	Eu	Gd	Tb
Unit Symbol	µg/L	µg/L	µg/L	µg/L	µg/L	µg/L	µg/L	µg/L	µg/L	µg/L	µg/L	µg/L
Quantification Limit	0.1	0.05	0.05	0.25	0.01	0.01	0.01	0.01	0.01	0.01	0.01	0.01
AC5	<0.1	<0.05	<0.05	21.21	<0.01	<0.01	<0.01	<0.01	<0.01	<0.01	<0.01	<0.01
AC3	<0.1	<0.05	<0.05	20.05	0.01	0.02	<0.01	<0.01	<0.01	<0.01	<0.01	<0.01
Ribeira	<0.1	<0.05	<0.05	12.72	<0.01	<0.01	<0.01	0.01	<0.01	<0.01	<0.01	<0.01
Fonte	<0.1	<0.05	<0.05	16.86	<0.01	<0.01	<0.01	<0.01	<0.01	<0.01	<0.01	<0.01
Ermida	<0.1	<0.05	0.31	20.72	<0.01	<0.01	<0.01	<0.01	<0.01	<0.01	<0.01	<0.01

1st Campaign												
Analyte Symbol	Dy	Ho	Er	Tm	Yb	Lu	W	Tl	Pb	Bi	Th	U
Unit Symbol	µg/L	µg/L	µg/L	µg/L	µg/L	µg/L	µg/L	µg/L	µg/L	µg/L	µg/L	µg/L
Quantification Limit	0.01	0.01	0.01	0.01	0.01	0.02	0.05	0.05	0.1	0.5	2.5	0.05
AC5	<0.01	<0.01	<0.01	<0.01	<0.01	<0.02	<0.05	<0.05	<0.1	<0.5	<2.5	<0.05
AC3	<0.01	<0.01	<0.01	<0.01	<0.01	<0.02	<0.05	<0.05	<0.1	<0.5	<2.5	<0.05
Ribeira	<0.01	<0.01	<0.01	<0.01	<0.01	<0.02	<0.05	<0.05	<0.1	<0.5	<2.5	0.19
Fonte	<0.01	<0.01	<0.01	<0.01	<0.01	<0.02	<0.05	<0.05	<0.1	<0.5	<2.5	0.18
Ermida	<0.01	<0.01	<0.01	<0.01	<0.01	<0.02	<0.05	<0.05	<0.1	<0.5	<2.5	<0.05

ICP-MS chemical data of waters from Cabeço de Vide, after the first campaign.

2nd Campaign												
Analyte Symbol	Li	Be	B	Na	Mg	Al	P	K	Ca	V	Cr	Mn
Unit Symbol	µg/L	µg/L	µg/L	mg/L	mg/L	µg/L	µg/L	mg/L	mg/L	µg/L	µg/L	µg/L
Quantification Limit	0.5	0.5	10	0.1	0.05	5.0	25	0.05	0.05	0.1	0.05	0.1
AC5	1.2	<0.5	219	40.87	<0.05	152.64	<25	4.12	23.0	<0.1	<0.05	<0.1
AC3	0.9	<0.5	250	52.00	<0.05	212.73	<25	5.71	24.8	<0.1	<0.05	<0.1
Ribeira	1.8	<0.5	19	11.94	94.9	6.69	27.99	0.83	38.6	5.23	1.32	5.81
Fonte	1.8	<0.5	18	11.77	107.2	5.35	32.20	0.9	44.7	5.33	1.94	0.46
Ermida	5.9	<0.5	153	77.51	7.7	26.42	<25	8.87	10.1	2.29	0.74	0.34

2nd Campaign												
Analyte Symbol	Fe	Co	Ni	Cu	Zn	As	Se	Rb	Sr	Y	Mo	Ag
Unit Symbol	µg/L	µg/L	µg/L	µg/L	µg/L	µg/L	µg/L	µg/L	µg/L	µg/L	µg/L	µg/L
Quantification Limit	2.5	0.05	0.1	0.1	1	0.25	1.0	0.1	0.1	0.02	0.05	0.05
AC5	2.79	<0.5	<0.1	0.34	<1	<0.25	<1	8.30	238	<0.02	0.08	<0.05
AC3	2.72	<0.5	<0.1	0.21	<1	<0.25	<1	8.59	305	<0.02	0.14	<0.05
Ribeira	13.52	0.19	3.82	1.26	3.62	0.88	<1	1.21	170	0.06	0.12	<0.05
Fonte	4.24	0.10	1.82	0.66	4.17	0.86	<1	1.47	204	0.04	0.13	<0.05
Ermida	2.62	<0.5	0.42	0.49	1.63	0.40	<1	17.62	535	0.04	0.40	<0.05

2nd Campaign												
Analyte Symbol	Cd	Sn	Sb	Ba	La	Ce	Pr	Nd	Sm	Eu	Gd	Tb
Unit Symbol	µg/L	µg/L	µg/L	µg/L	µg/L	µg/L	µg/L	µg/L	µg/L	µg/L	µg/L	µg/L
Quantification Limit	0.1	0.05	0.02	0.1	0.01	0.01	0.01	0.01	0.01	0.01	0.01	0.01
AC5	<0.1	<0.05	<0.02	20.72	<0.01	<0.01	<0.01	<0.01	<0.01	0.033	<0.01	<0.01
AC3	<0.1	<0.05	<0.02	20.29	<0.01	<0.01	<0.01	<0.01	<0.01	0.031	<0.01	<0.01
Ribeira	<0.1	<0.05	0.04	15.68	0.015	0.023	<0.01	0.017	<0.01	0.028	<0.01	<0.01
Fonte	<0.1	<0.05	0.04	15.55	<0.01	<0.01	<0.01	<0.01	<0.01	0.025	<0.01	<0.01
Ermida	<0.1	<0.05	0.49	45.77	<0.01	<0.01	<0.01	<0.01	<0.01	0.075	<0.01	<0.01

2nd Campaign												
Analyte Symbol	Dy	Ho	Er	Tm	Yb	Lu	W	Tl	Pb	Bi	Th	U
Unit Symbol	µg/L	µg/L	µg/L	µg/L	µg/L	µg/L	µg/L	µg/L	µg/L	µg/L	µg/L	µg/L
Quantification Limit	0.01	0.01	0.01	0.01	0.01	0.01	0.01	0.05	0.1	0.25	2.5	0.05
AC5	<0.01	<0.01	<0.01	<0.01	<0.01	<0.01	0.036	<0.01	0.16	<0.25	<2.5	<0.05
AC3	<0.01	<0.01	<0.01	<0.01	<0.01	<0.01	0.061	<0.01	0.12	<0.25	<2.5	<0.05
Ribeira	<0.01	<0.01	<0.01	<0.01	<0.01	<0.01	0.029	<0.01	0.25	<0.25	<2.5	0.20
Fonte	<0.01	<0.01	<0.01	<0.01	<0.01	<0.01	0.033	<0.01	0.20	<0.25	<2.5	0.21
Ermida	<0.01	<0.01	<0.01	<0.01	<0.01	<0.01	0.080	<0.01	0.33	<0.25	<2.5	<0.05

ICP-MS chemical data of waters from Cabeço de Vide, after the second campaign.

	fluoride (mg/L)	chloride (mg/L)	sulfate (mg/L)	bromide (mg/L)	nitrate (mg/L)	phosphate (µg/L)
AC5	<QL	43.9	1.7	<QL	<QL	<QL
AC3	<QL	51.7	4.8	<QL	<QL	<QL
RIBEIRA	<QL	16.8	11.4	<QL	3.9	<QL
FONTE	<QL	19.9	13.1	<QL	7.2	<QL
ERMIDA	<QL	57.6	5.8	<QL	<QL	<QL

Ionic Chromatography chemical data of waters from Cabeço de Vide (1st campaign) (QL – Quantification Limit).

2 – X-Ray Diffraction

Whole Sample X-Ray Diffraction

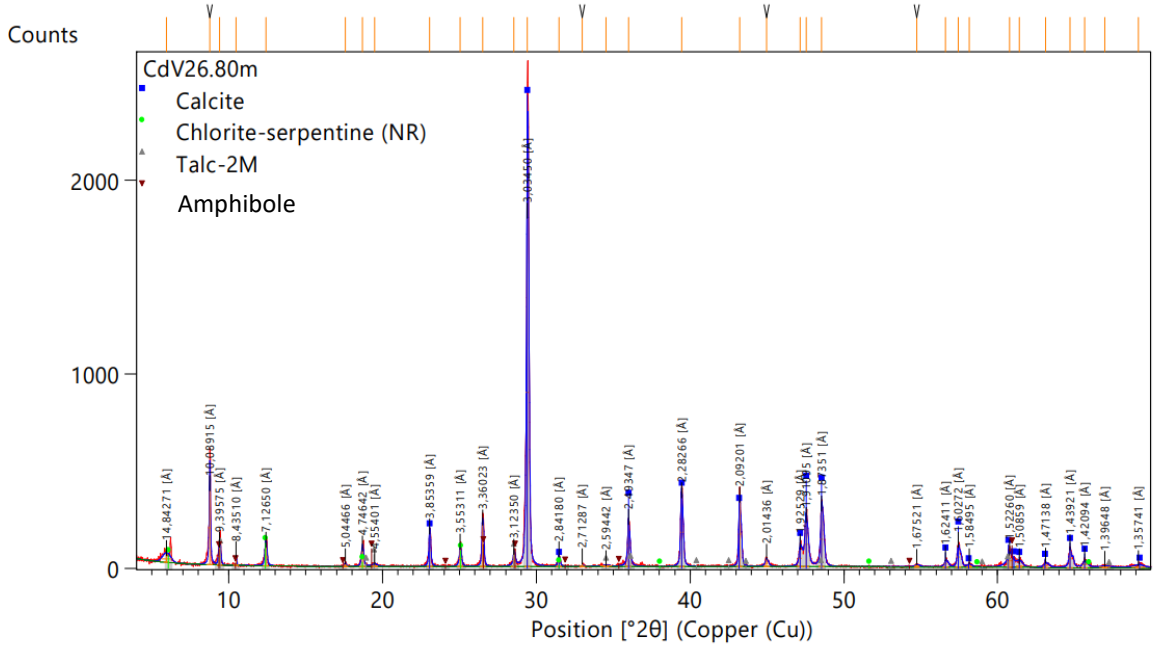

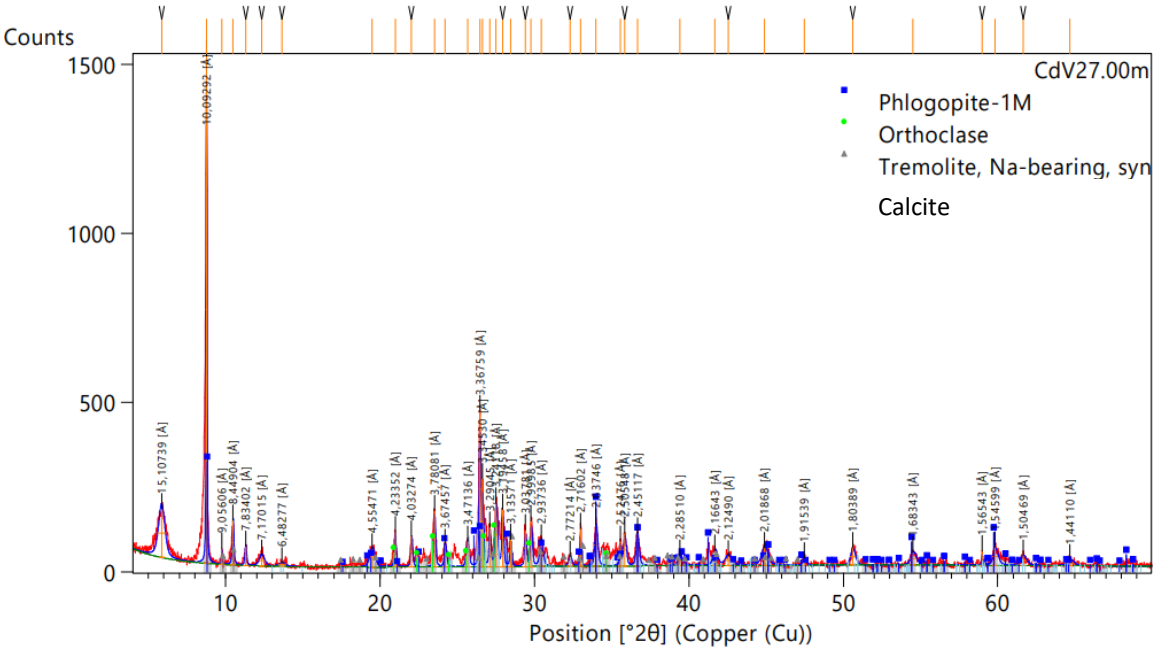

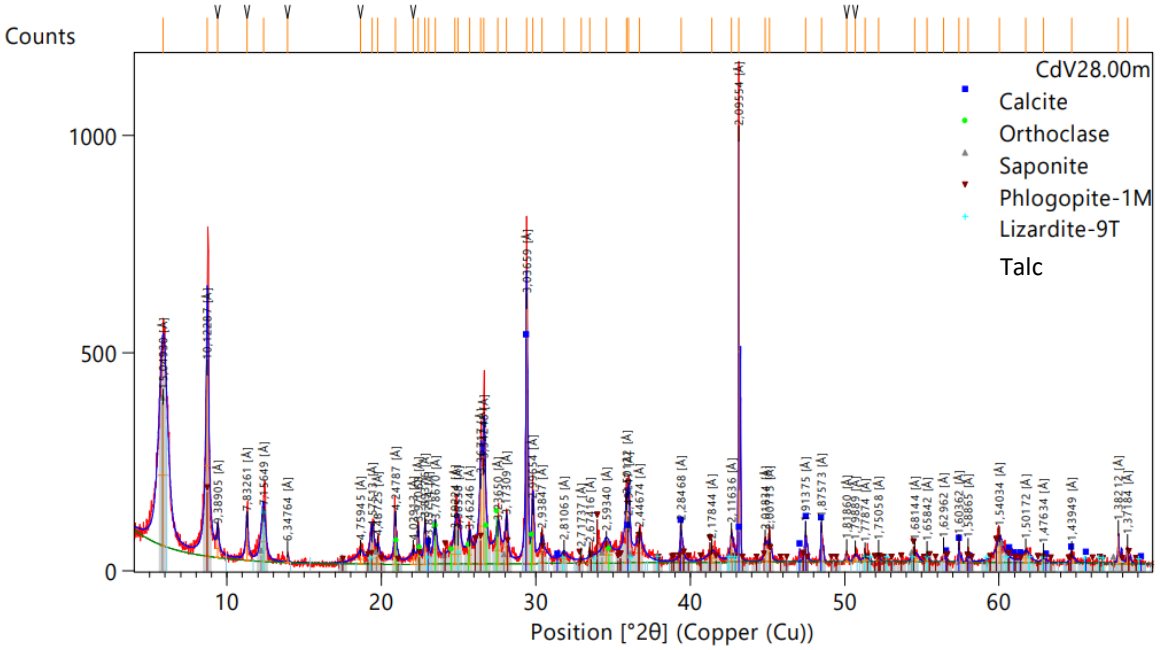
Counts
CdV28.00m
Calcite
Orthoclase
Saponite
Phlogopite-1M
Lizardite-9T
Talc
1000
500
0
10
20
30
40
50
60
Position [°2θ] (Copper (Cu))

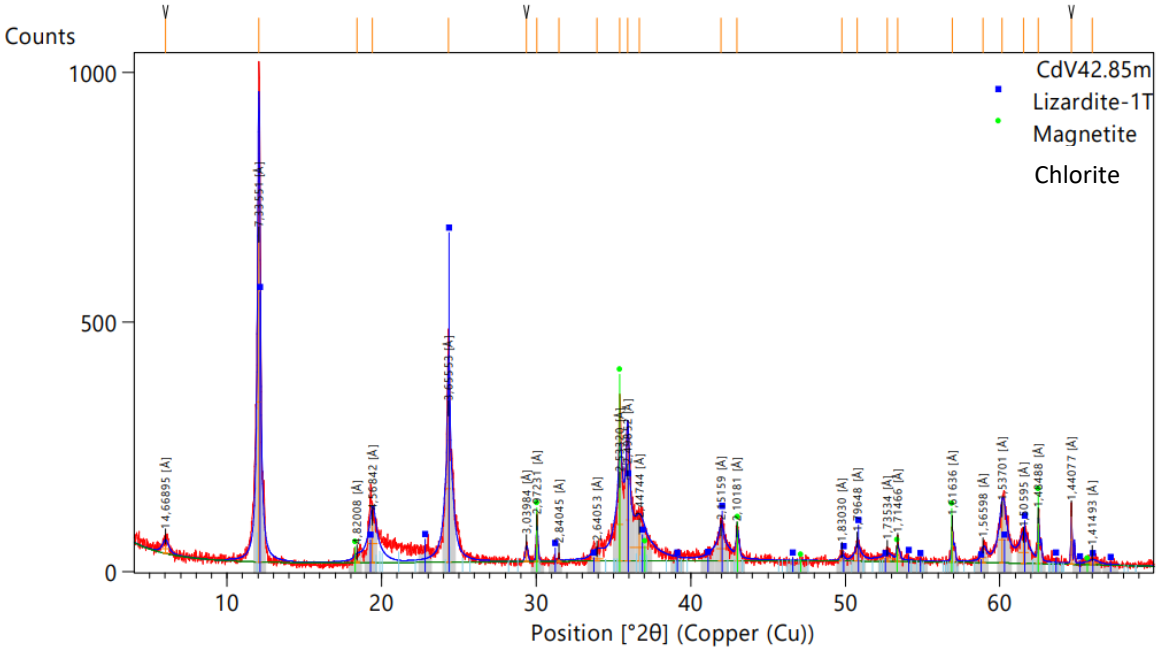
Counts
CdV42.85m
Lizardite-1T
Magnetite
Chlorite
1000
500
0
10
20
30
40
50
60
Position [°2θ] (Copper (Cu))

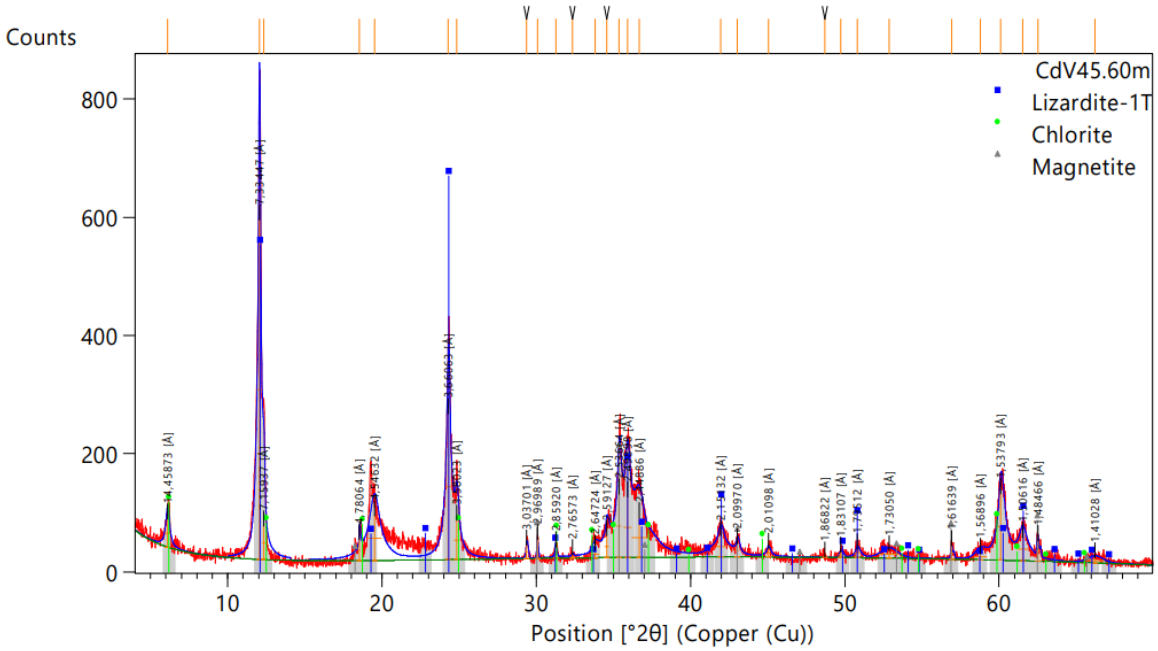
Counts
CdV45.60m
Lizardite-1T
Chlorite
Magnetite
800
600
400
200
0
10
20
30
40
50
60
Position [°2θ] (Copper (Cu))

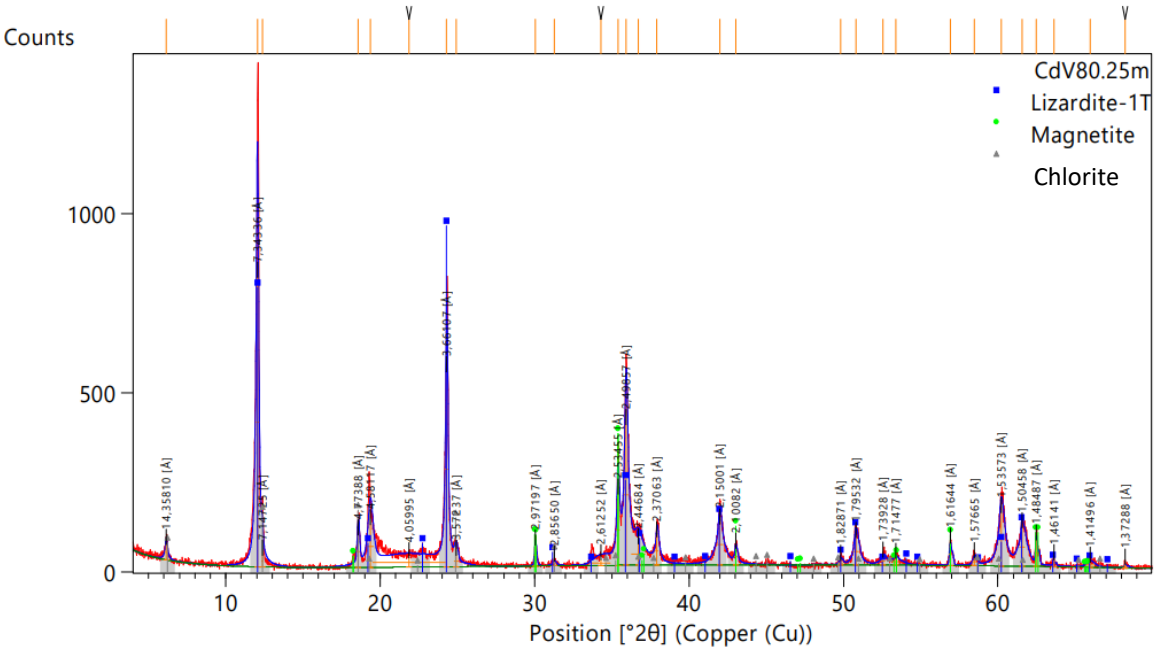
Counts
CdV80.25m
Lizardite-1T
Magnetite
Chlorite
1000
500
0
10
20
30
40
50
60
Position [°2θ] (Copper (Cu))

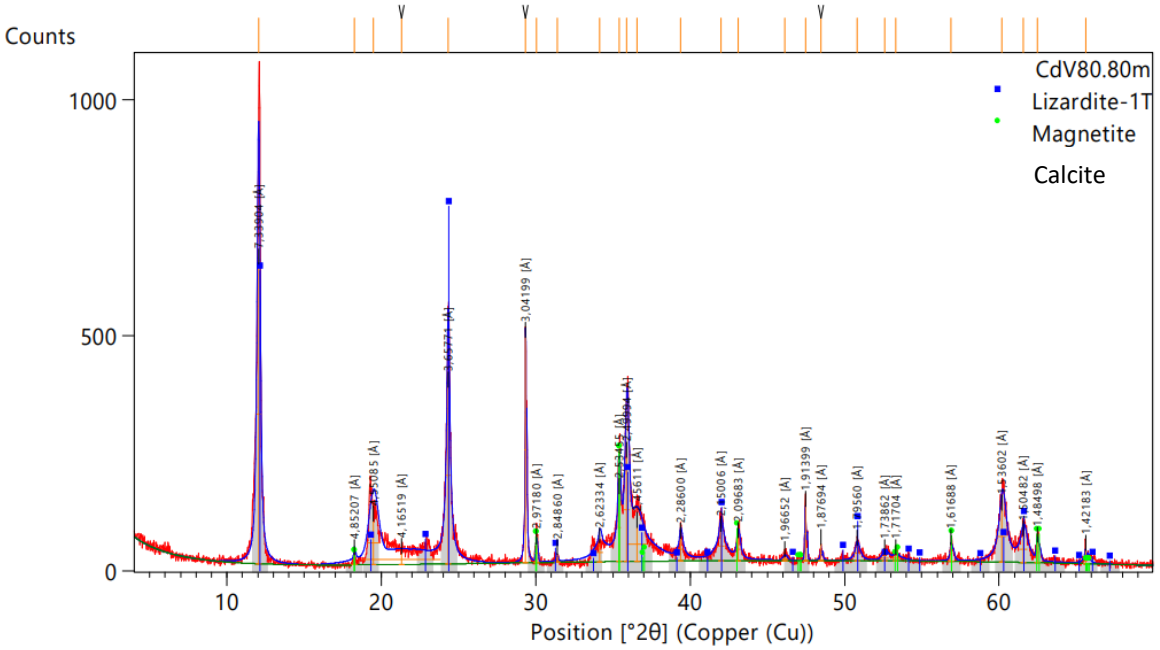
Counts
1000
500
0
CdV80.80m
Lizardite-1T
Magnetite
Calcite
10
20
30
40
50
60
Position [°2θ] (Copper (Cu))

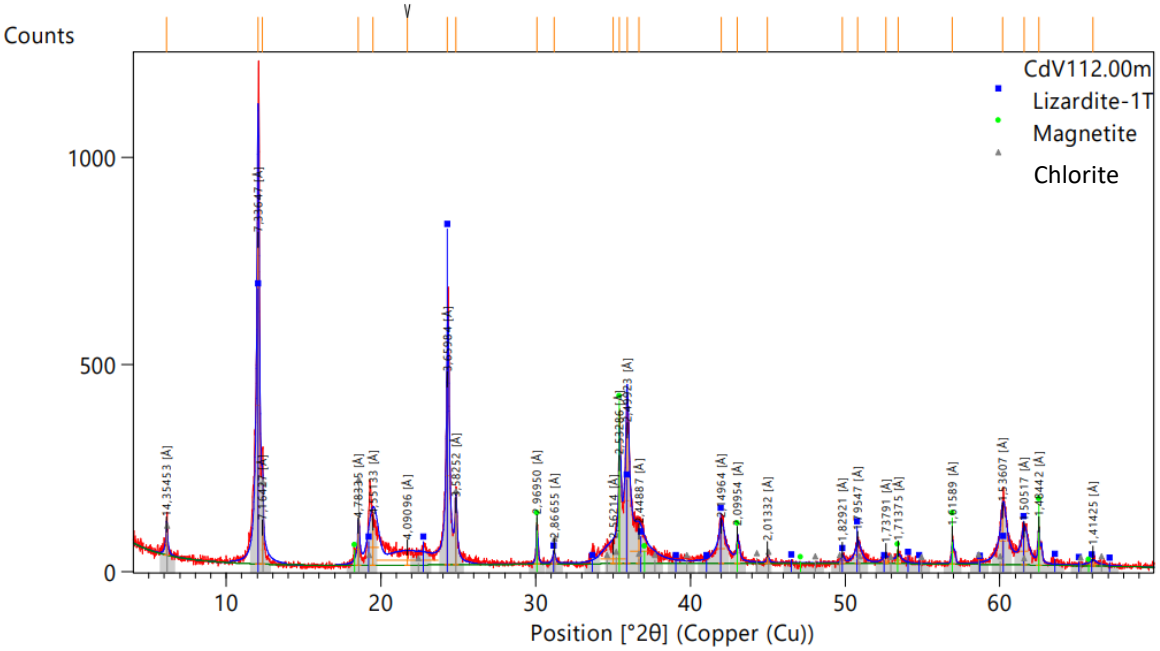
Counts
1000
500
0
CdV112.00m
Lizardite-1T
Magnetite
Chlorite
10
20
30
40
50
60
Position [°2θ] (Copper (Cu))

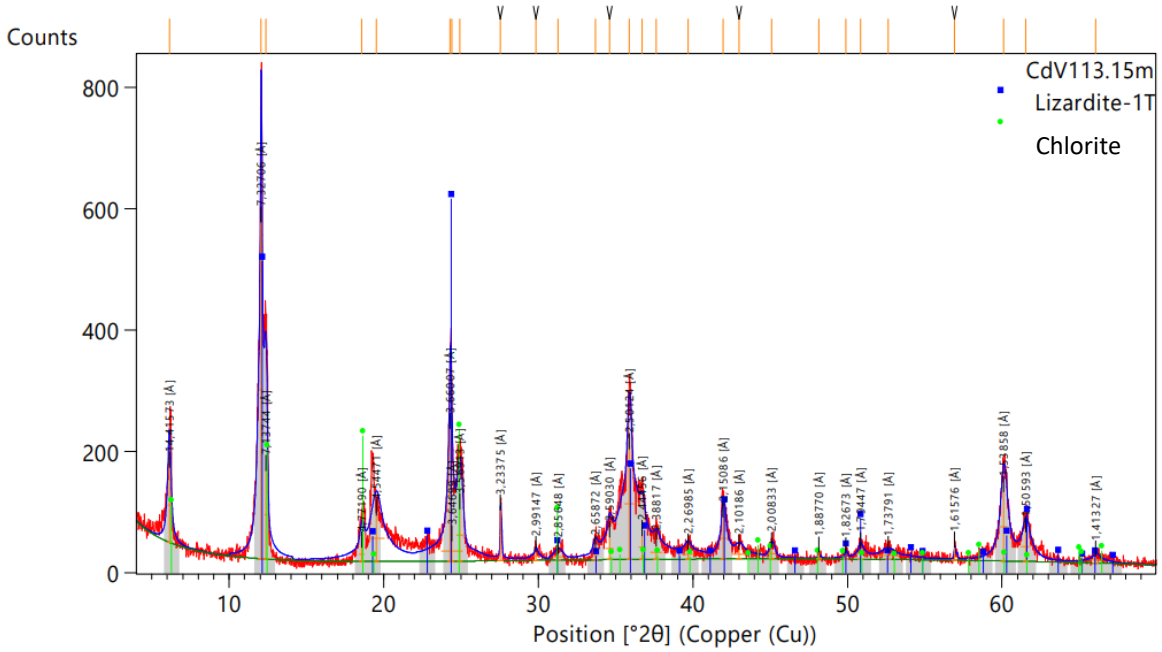
Counts
CdV113.15m
Lizardite-1T
Chlorite
Position [°2θ] (Copper (Cu))

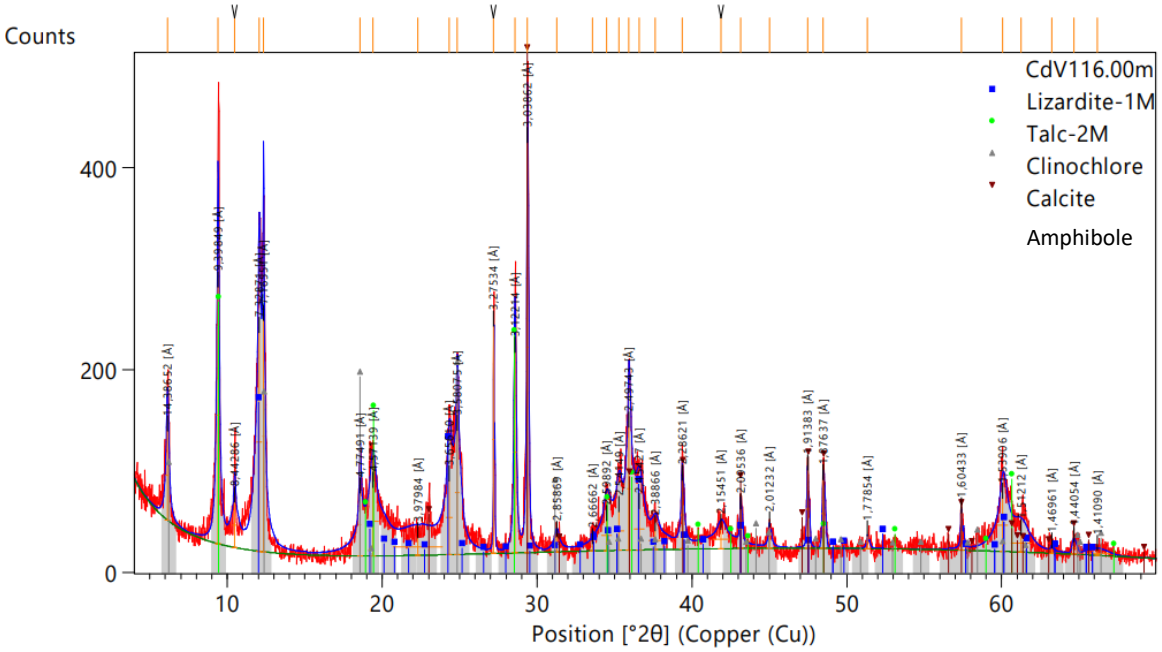
Counts
CdV116.00m
Lizardite-1M
Talc-2M
Clinochlore
Calcite
Amphibole
Position [°2θ] (Copper (Cu))

Partial Sample X-Ray Diffraction (by Depth)

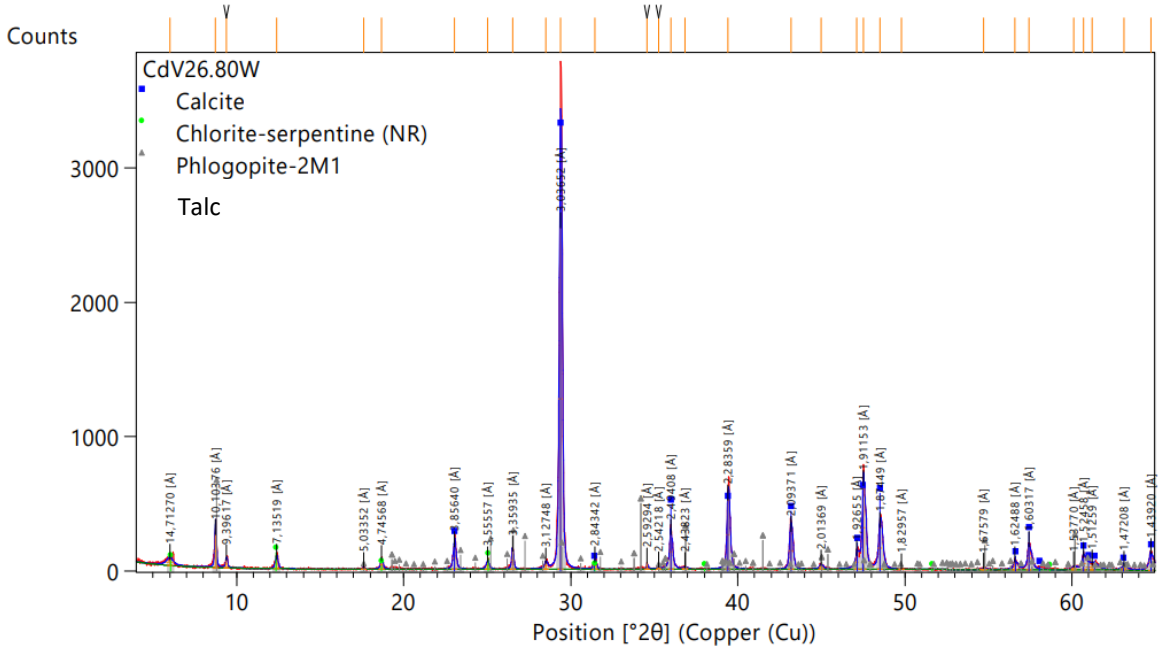

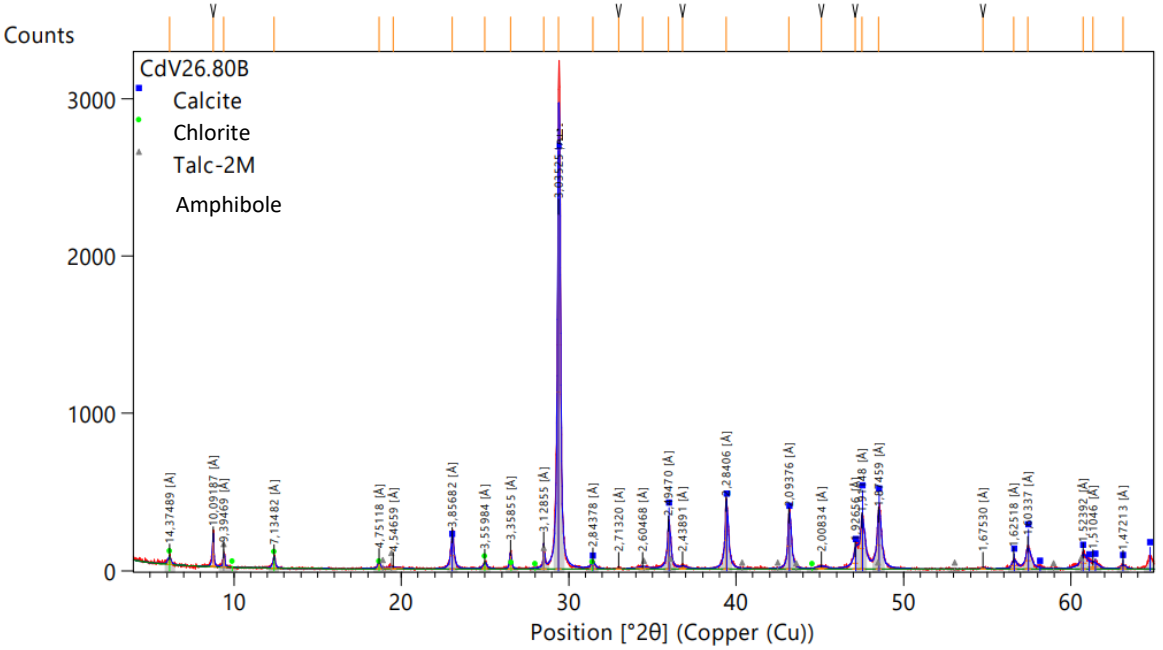

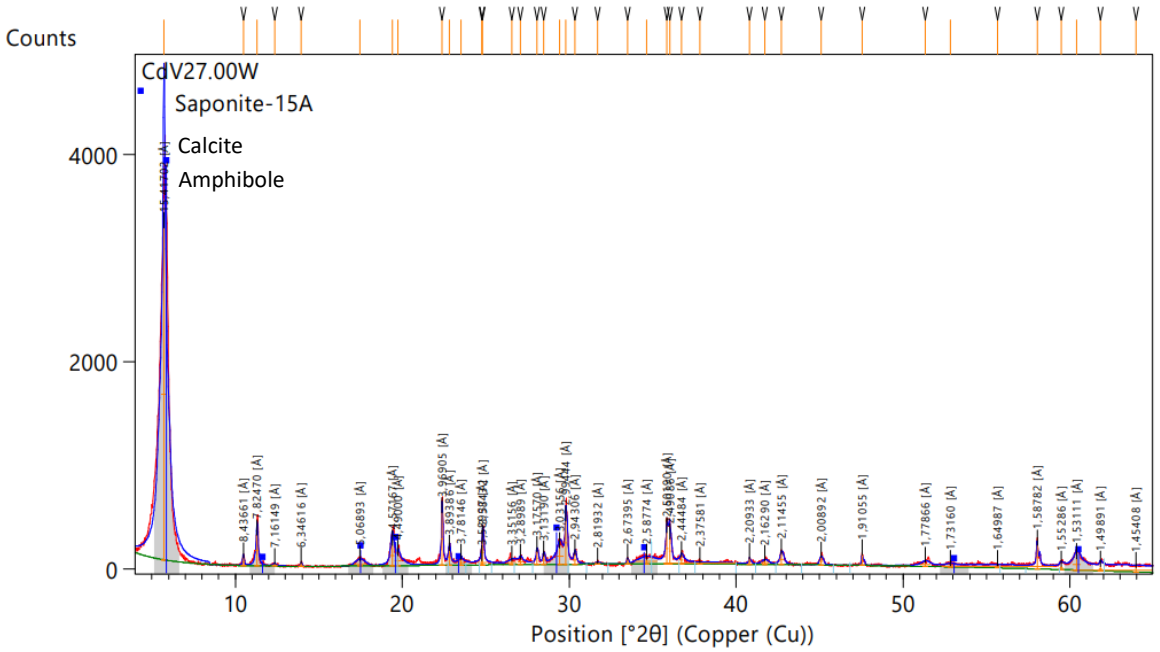
Counts
CdV27.00W
Saponite-15A
Calcite
Amphibole
4000
2000
0
10
20
30
40
50
60
Position [°2θ] (Copper (Cu))

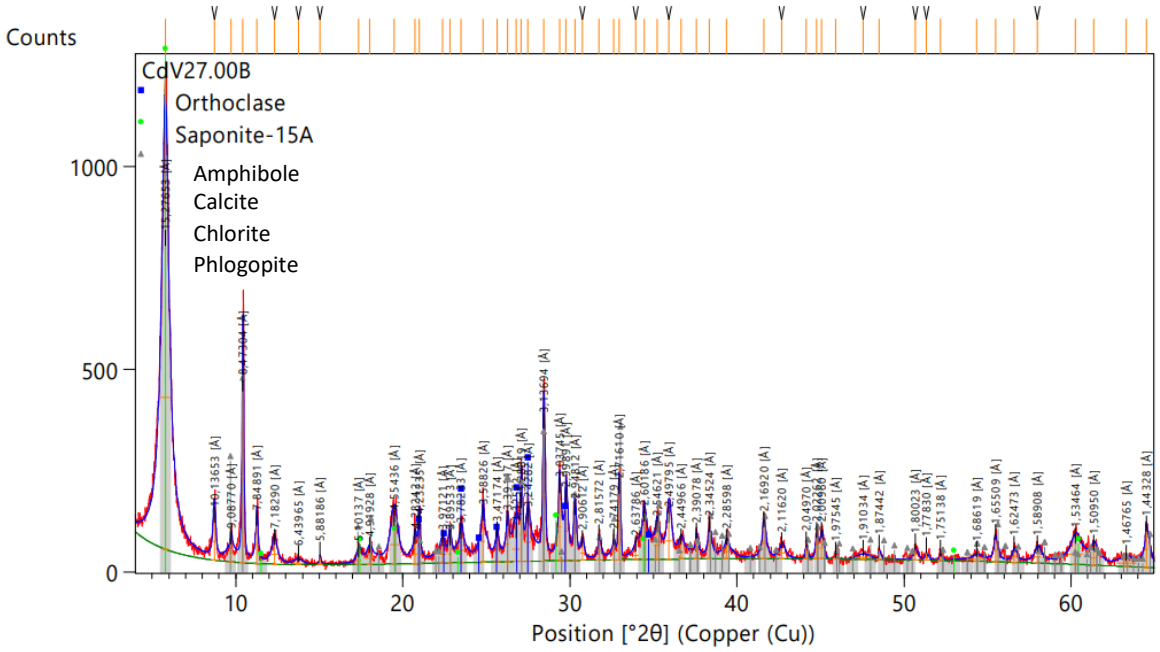
Counts
CdV27.00B
Orthoclase
Saponite-15A
Amphibole
Calcite
Chlorite
Phlogopite
1000
500
0
10
20
30
40
50
60
Position [°2θ] (Copper (Cu))

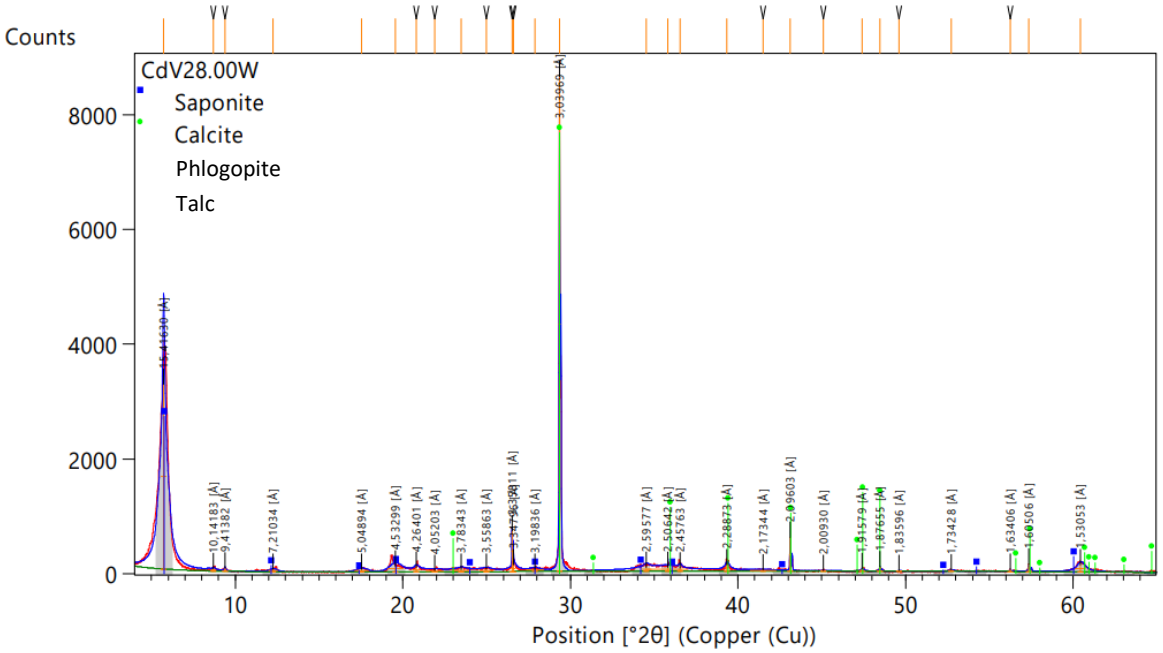
Counts
CdV28.00W
Saponite
Calcite
Phlogopite
Talc
8000
6000
4000
2000
0
10
20
30
40
50
60
Position [°2θ] (Copper (Cu))

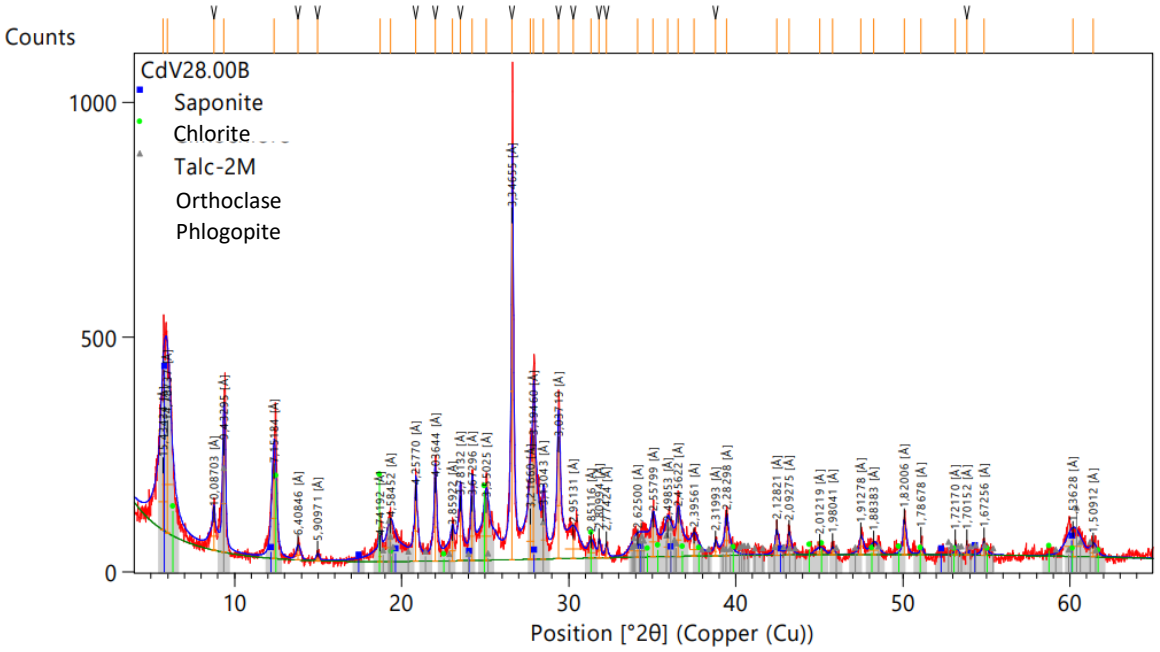
Counts
CdV28.00B
Saponite
Chlorite
Talc-2M
Orthoclase
Phlogopite
1000
500
0
10
20
30
40
50
60
Position [°2θ] (Copper (Cu))

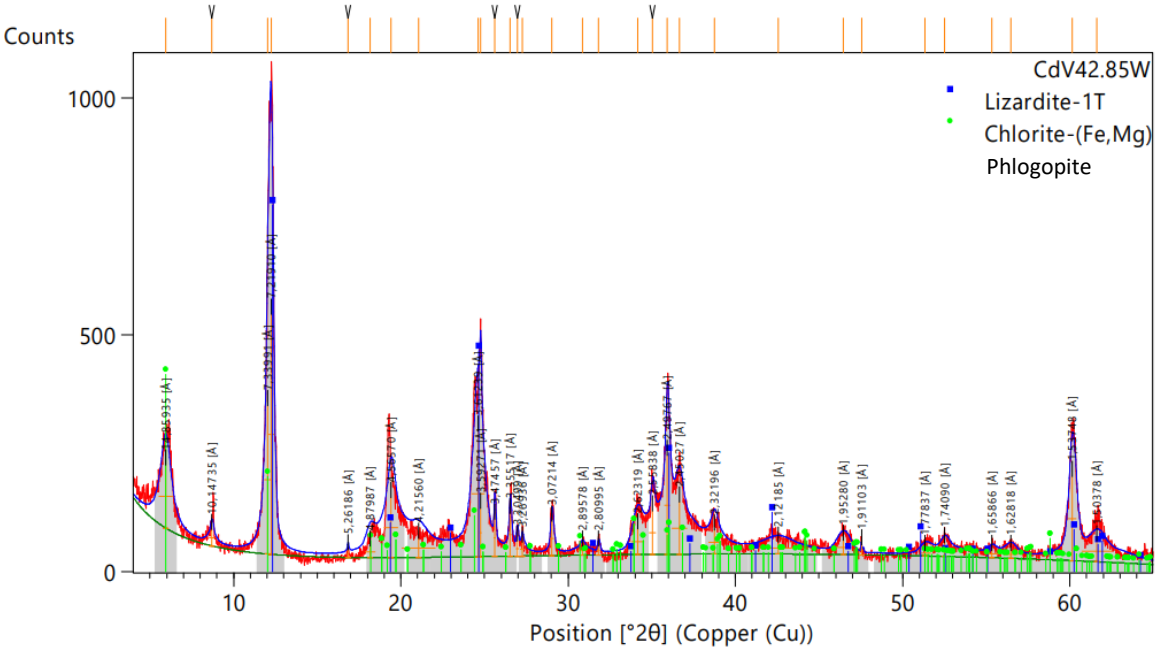
Counts
CdV42.85W
Lizardite-1T
Chlorite-(Fe,Mg)
Phlogopite
1000
500
0
10
20
30
40
50
60
Position [°2θ] (Copper (Cu))

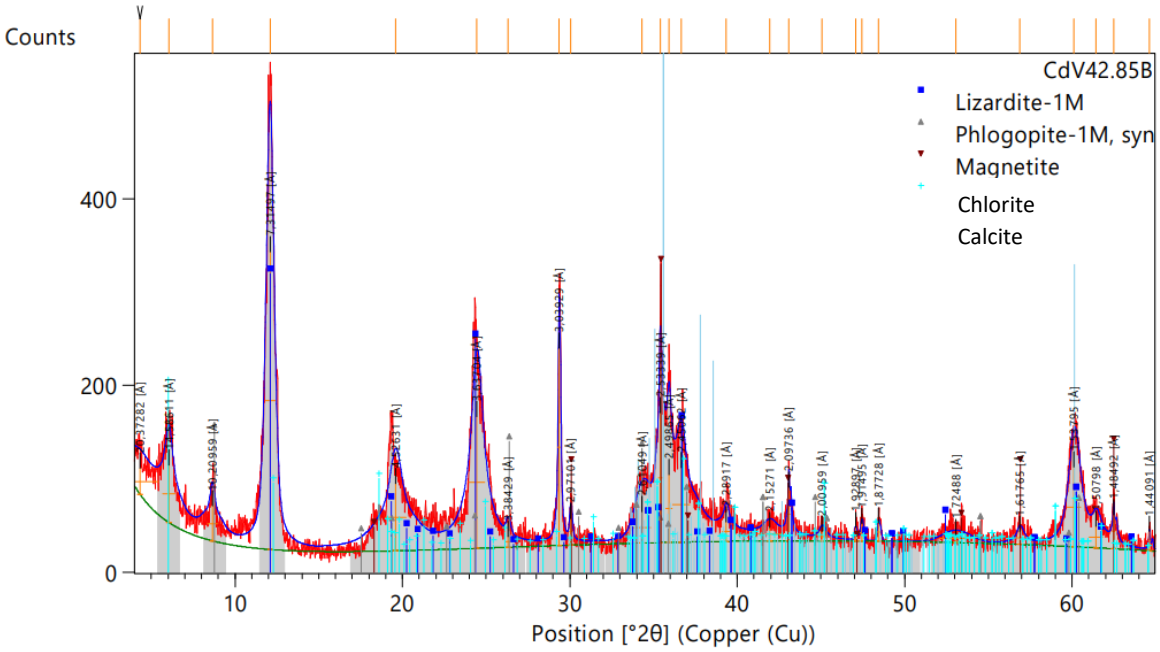
Counts
CdV42.85B
Lizardite-1M
Phlogopite-1M, syn
Magnetite
Chlorite
Calcite
400
200
0
10
20
30
40
50
60
Position [°2θ] (Copper (Cu))

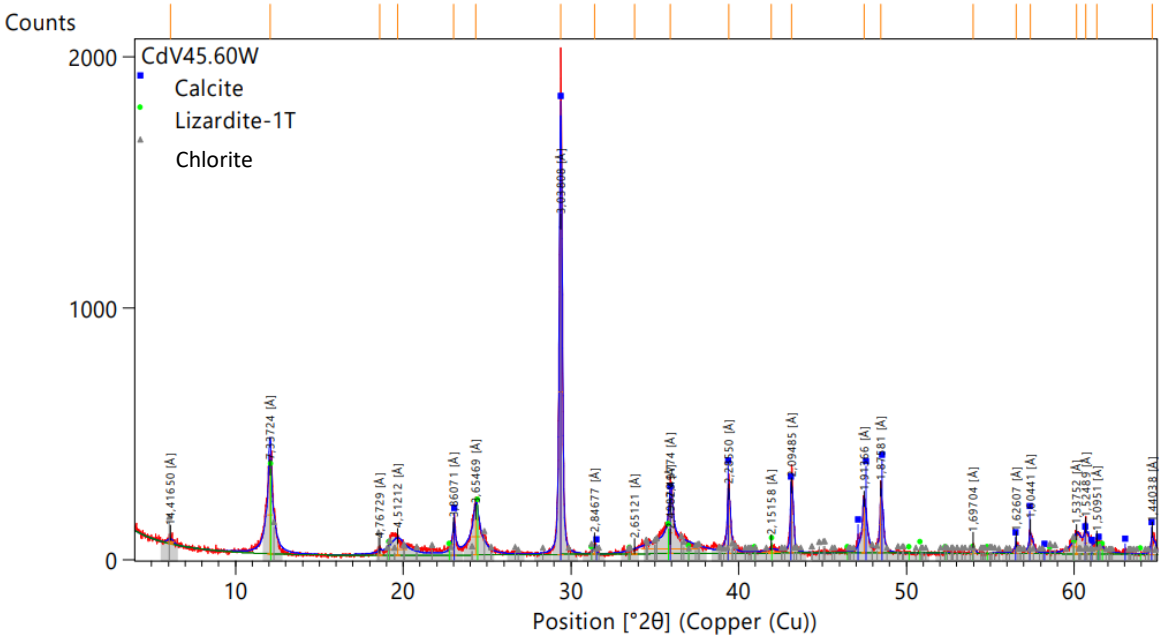
Counts
CdV45.60W
Calcite
Lizardite-1T
Chlorite
2000
1000
0
10
20
30
40
50
60
Position [°2θ] (Copper (Cu))

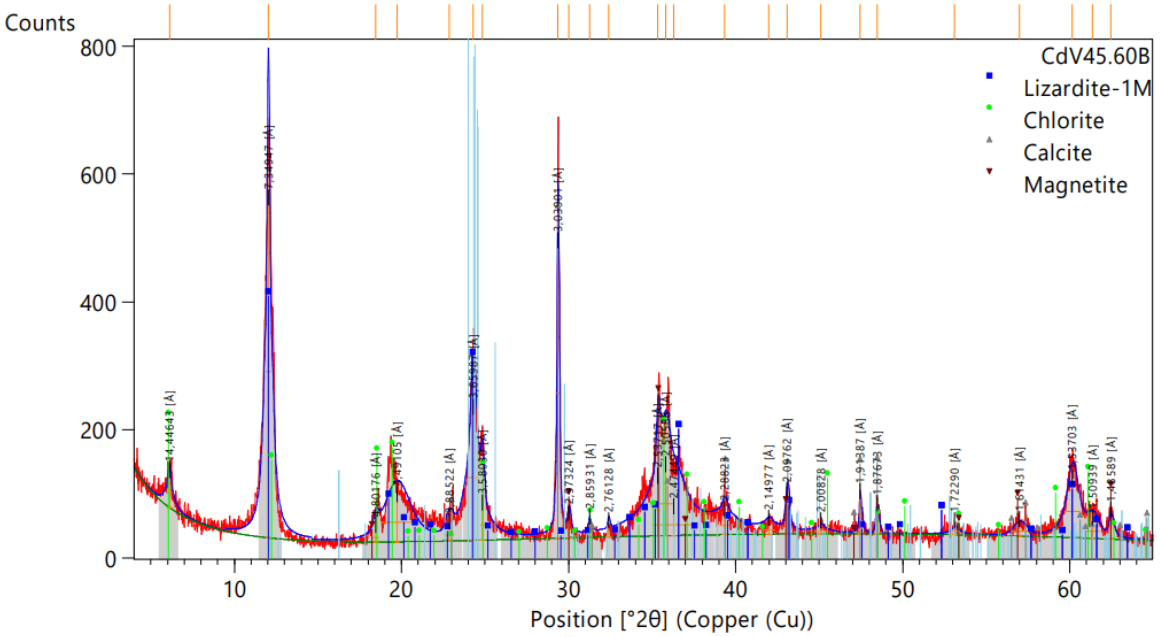
Counts
CdV45.60B
Lizardite-1M
Chlorite
Calcite
Magnetite
800
600
400
200
0
10
20
30
40
50
60
Position [°2θ] (Copper (Cu))

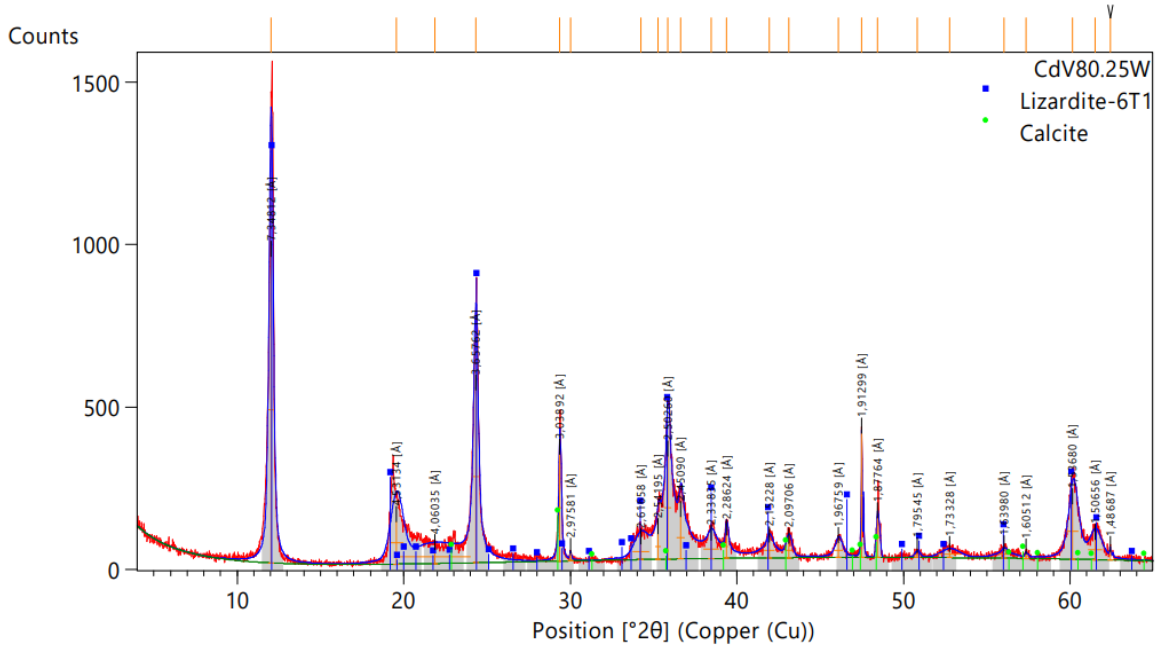
Counts
CdV80.25W
Lizardite-6T1
Calcite
1500
1000
500
0
10
20
30
40
50
60
Position [°2θ] (Copper (Cu))

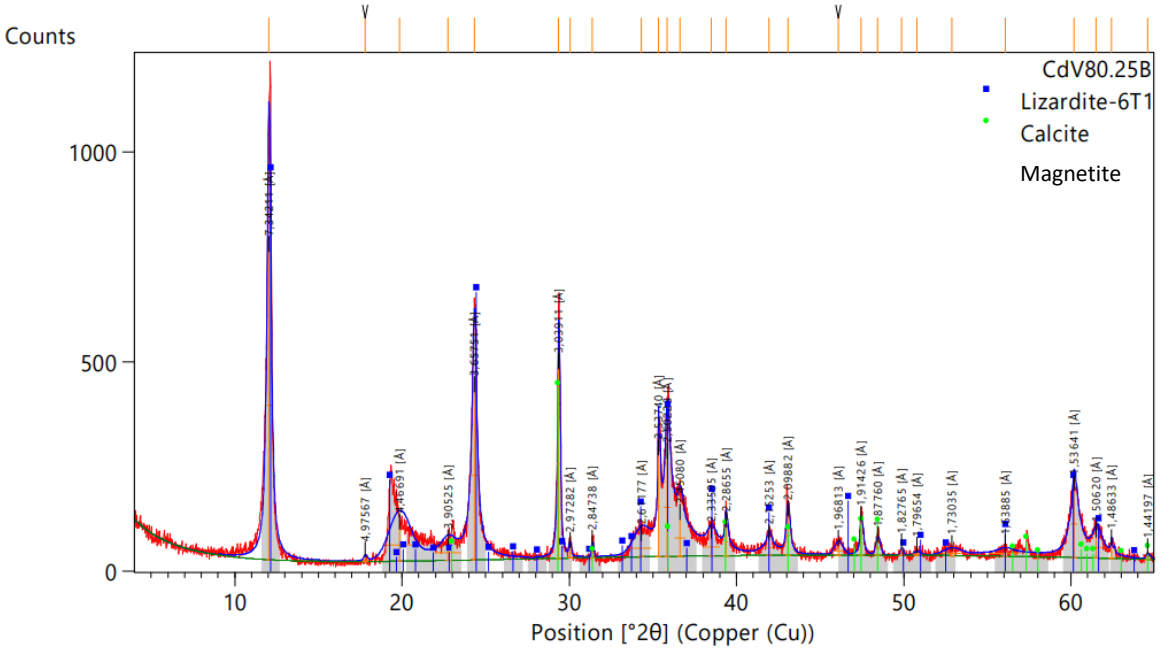
Counts
CdV80.25B
Lizardite-6T1
Calcite
Magnetite
1000
500
0
10
20
30
40
50
60
Position [°2θ] (Copper (Cu))

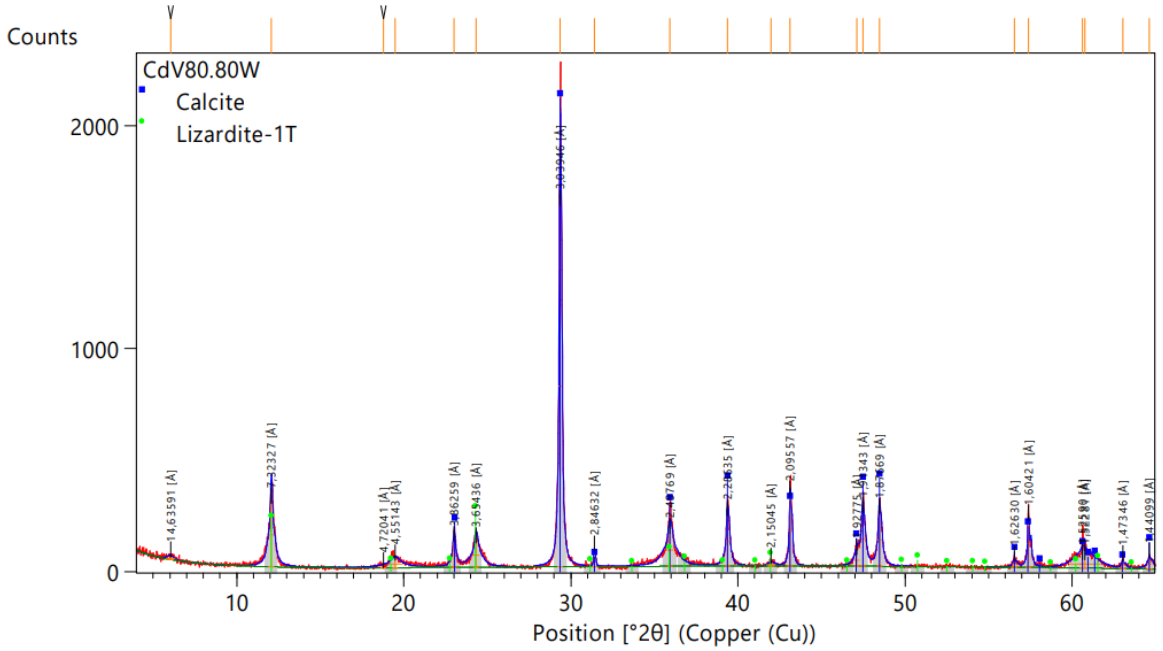
Counts
CdV80.80W
Calcite
Lizardite-1T
2000
1000
0
10
20
30
40
50
60
Position [°2θ] (Copper (Cu))

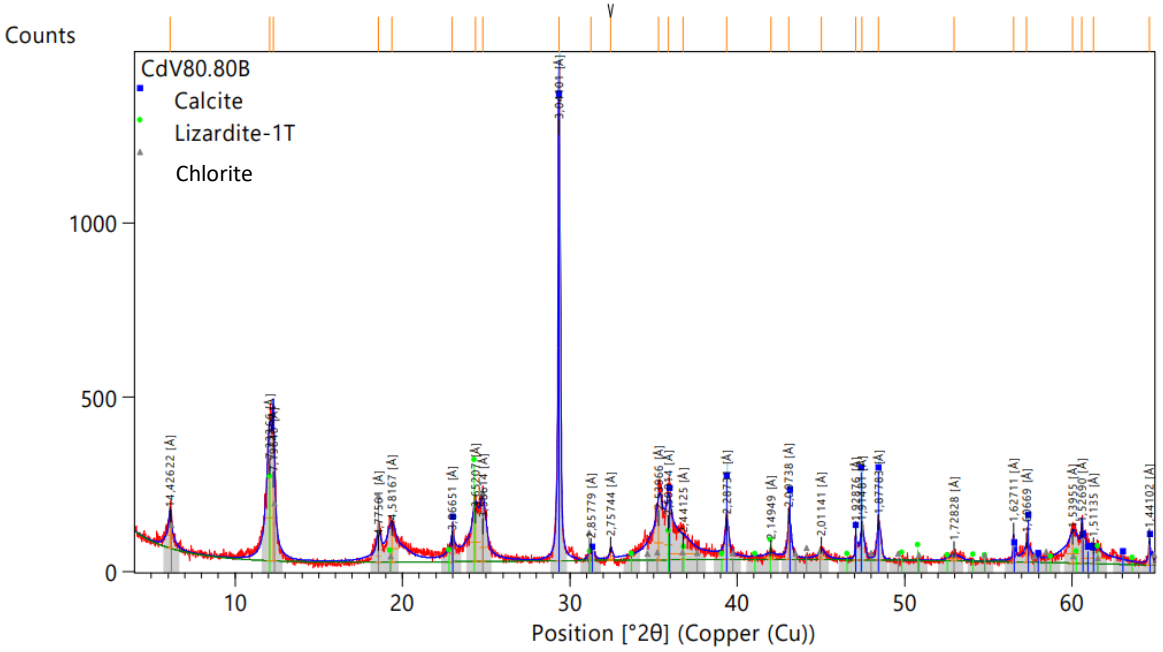
Counts
CdV80.80B
Calcite
Lizardite-1T
Chlorite
1000
500
0
10
20
30
40
50
60
Position [°2θ] (Copper (Cu))

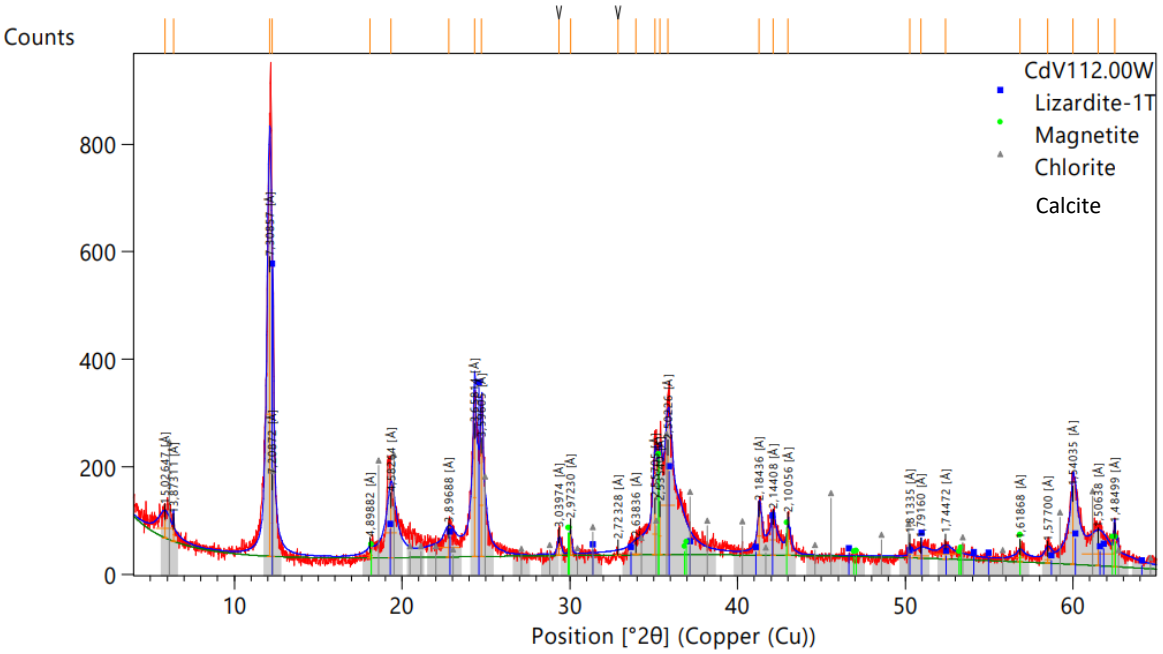
Counts
CdV112.00W
Lizardite-1T
Magnetite
Chlorite
Calcite
800
600
400
200
0
10
20
30
40
50
60
Position [°2θ] (Copper (Cu))

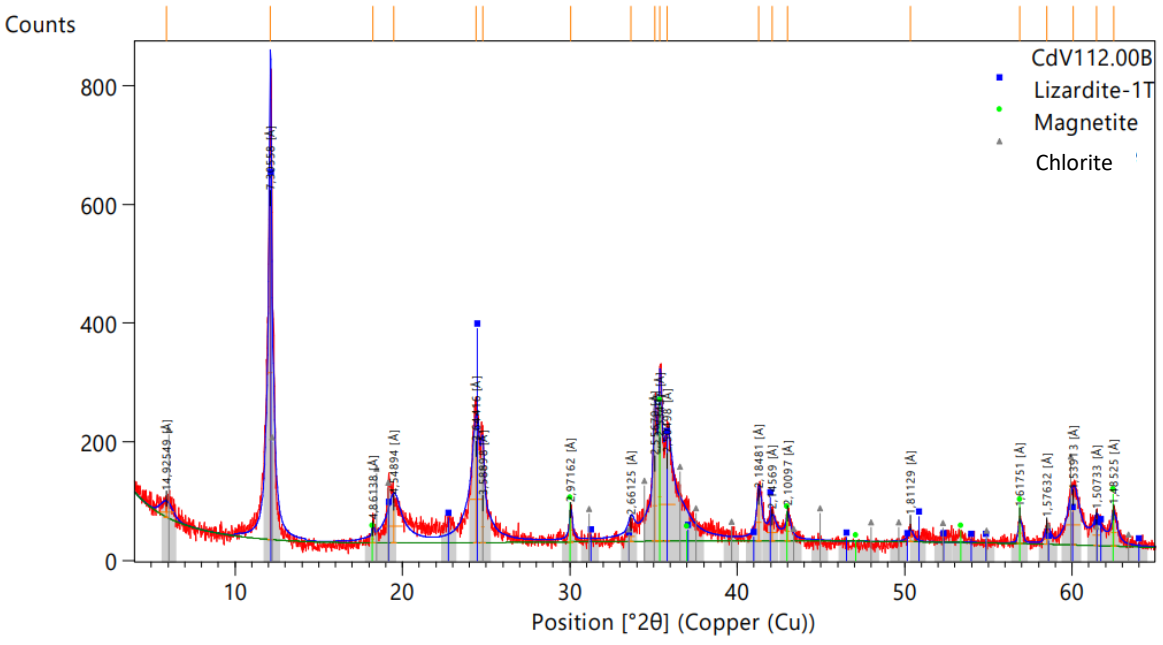
Counts
CdV112.00B
Lizardite-1T
Magnetite
Chlorite
800
600
400
200
0
10
20
30
40
50
60
Position [°2θ] (Copper (Cu))

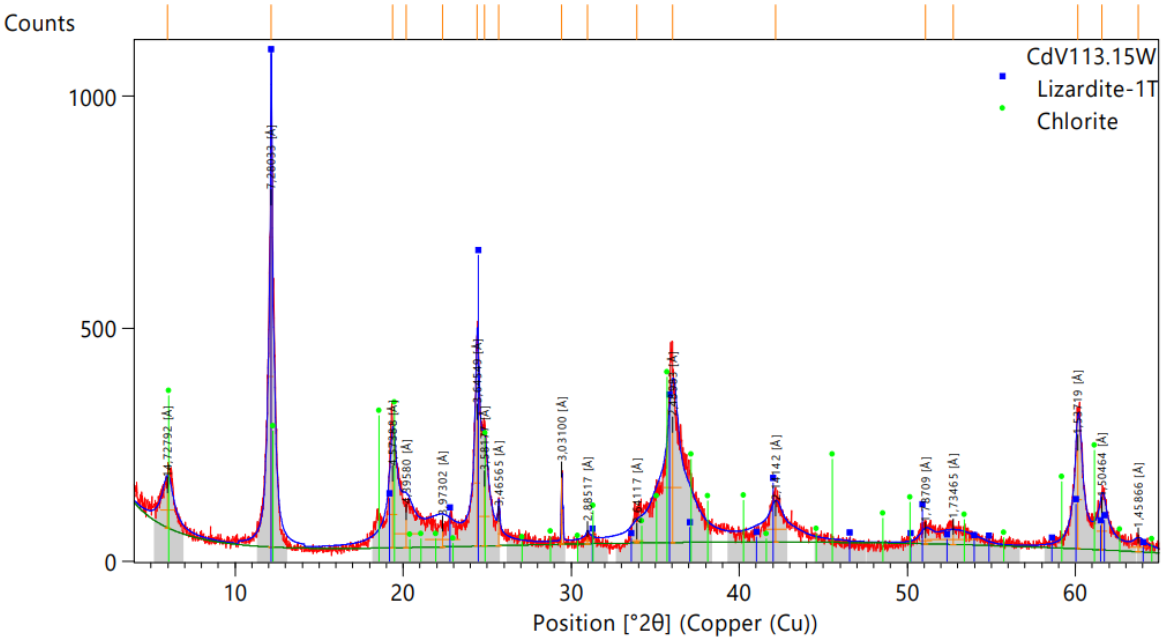
Counts
CdV113.15W
Lizardite-1T
Chlorite
1000
500
0
10
20
30
40
50
60
Position [°2θ] (Copper (Cu))

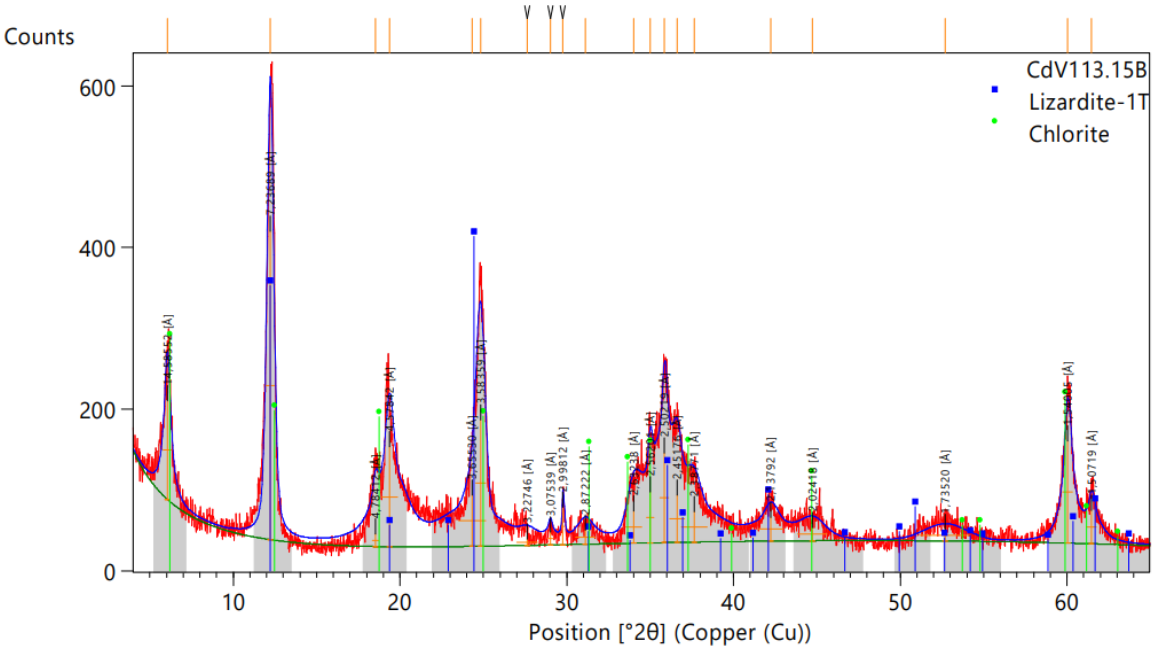
Counts
CdV113.15B
Lizardite-1T
Chlorite
600
400
200
0
10
20
30
40
50
60
Position [°2θ] (Copper (Cu))

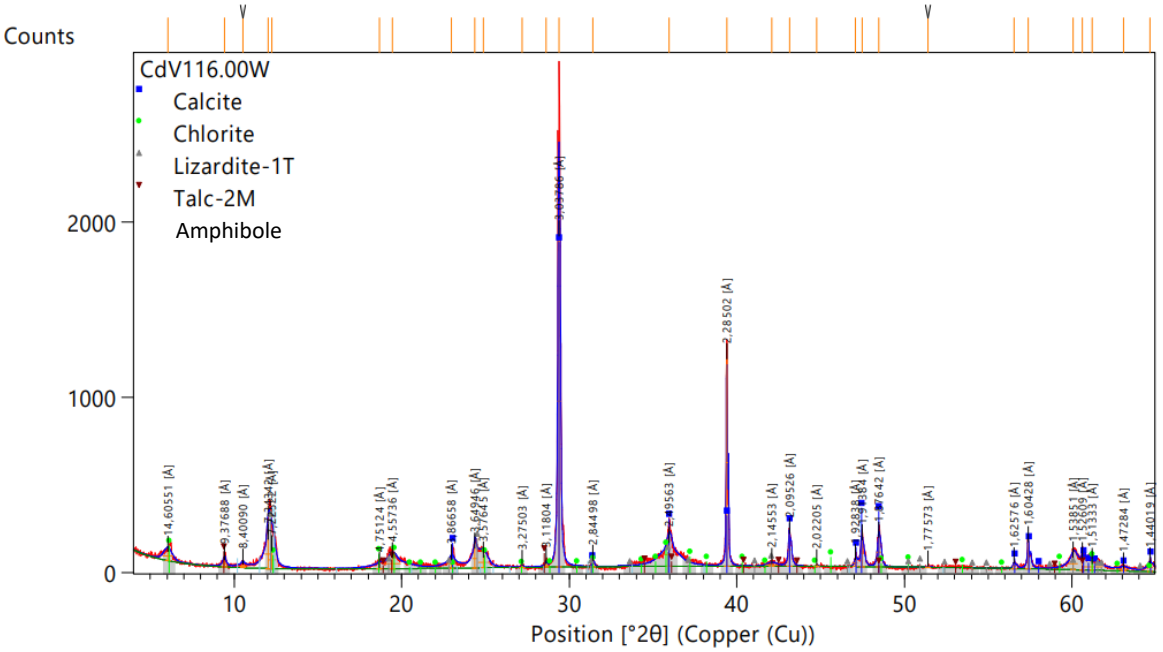
Counts
CdV116.00W
Calcite
Chlorite
Lizardite-1T
Talc-2M
Amphibole
2000
1000
0
10
20
30
40
50
60
Position [°2θ] (Copper (Cu))

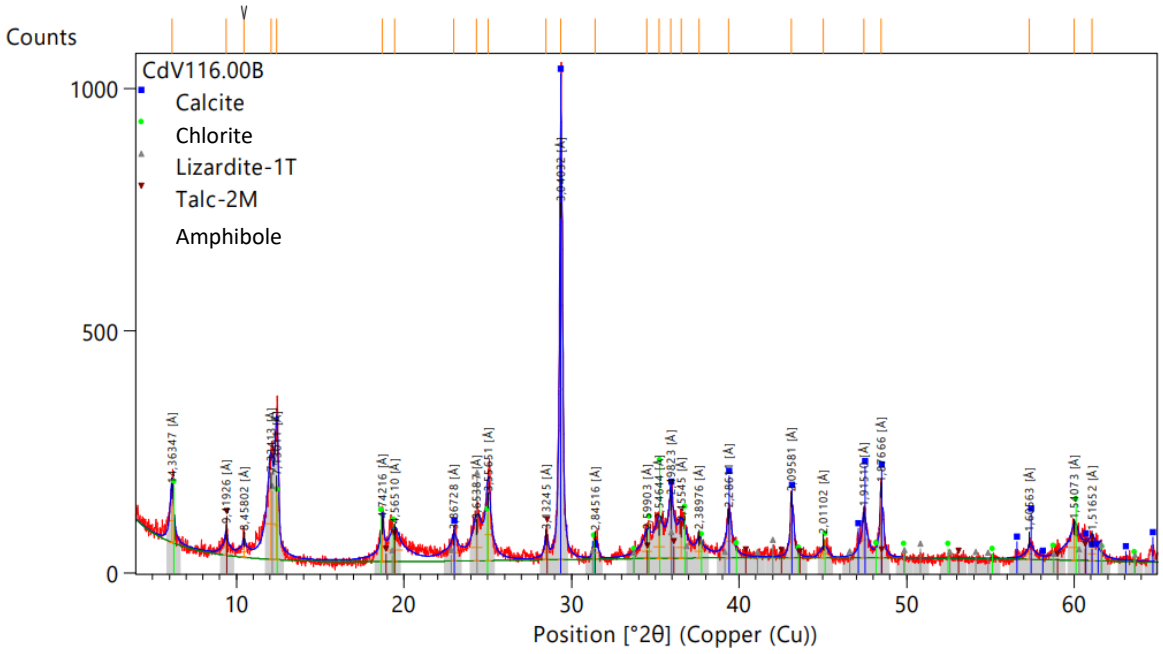
Counts
CdV116.00B
Calcite
Chlorite
Lizardite-1T
Talc-2M
Amphibole
1000
500
0
10
20
30
40
50
60
Position [°2θ] (Copper (Cu))

Oriented aggregates in Whole Samples – by depth

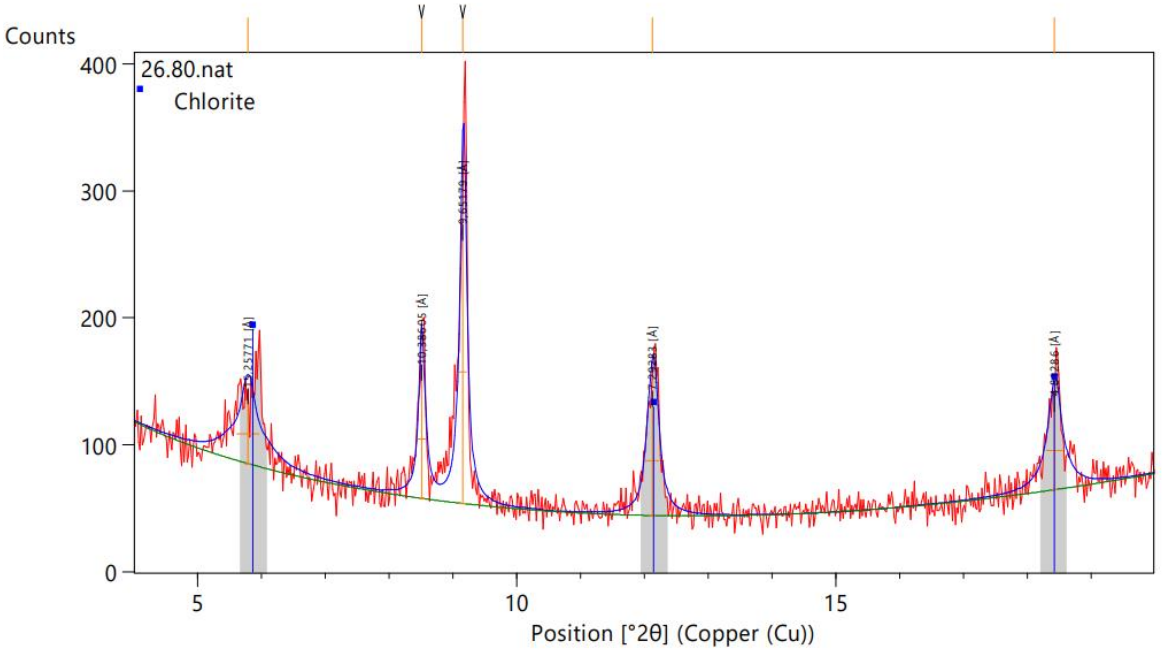

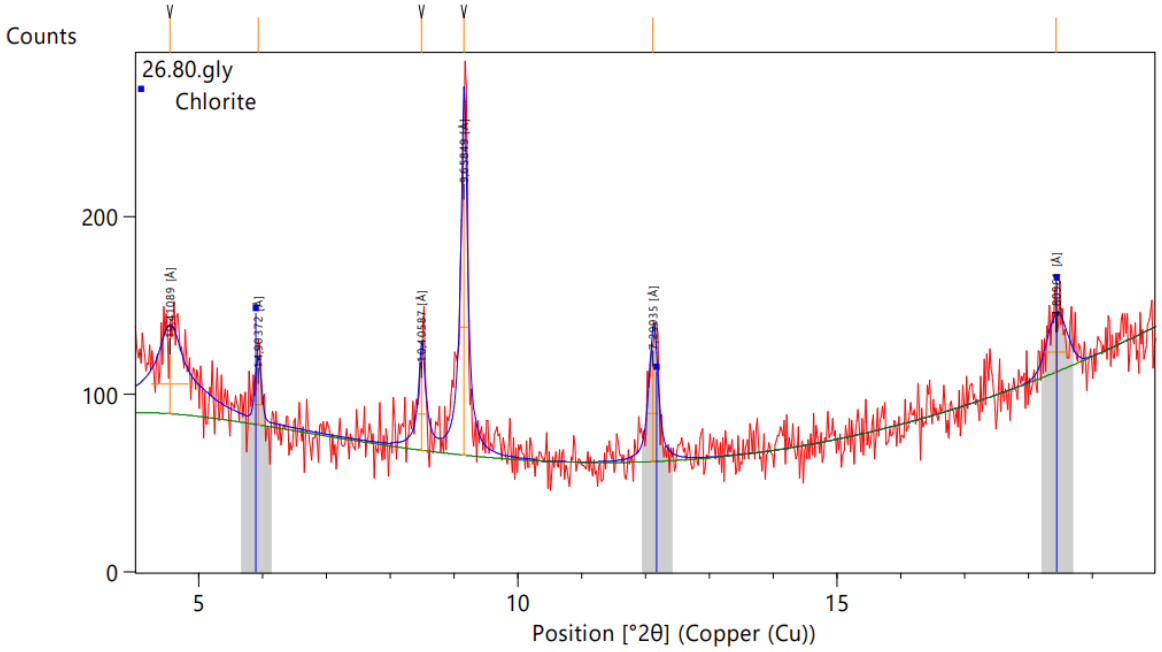

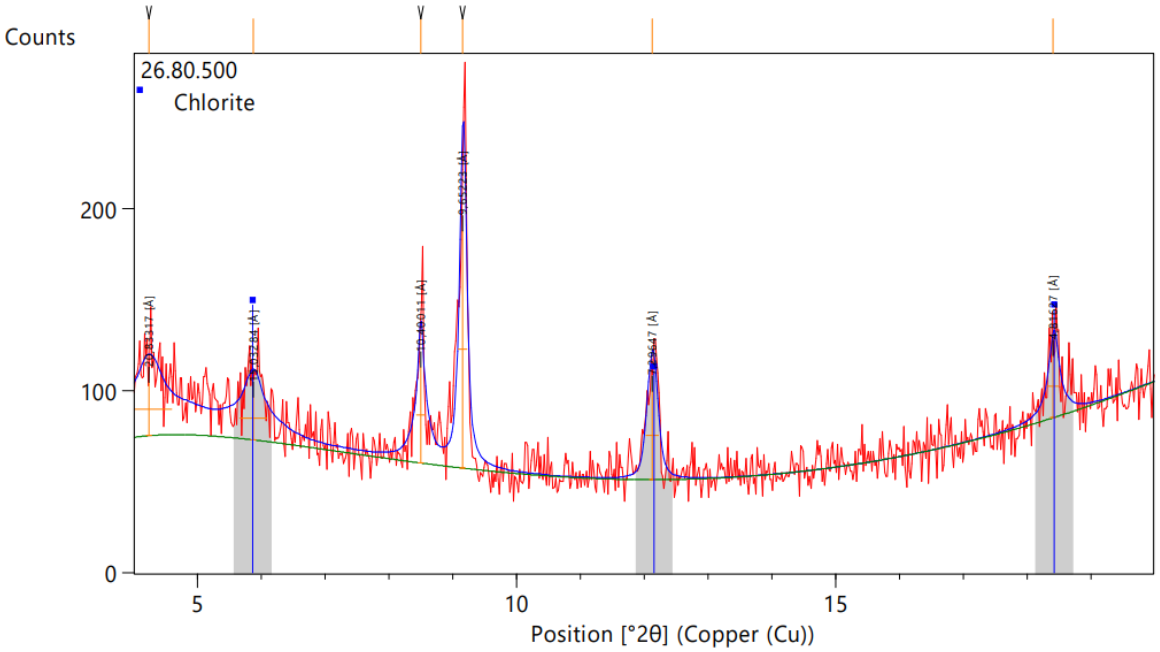
Counts
26.80.500
Chlorite
200
100
0
5
10
15
Position [°2θ] (Copper (Cu))

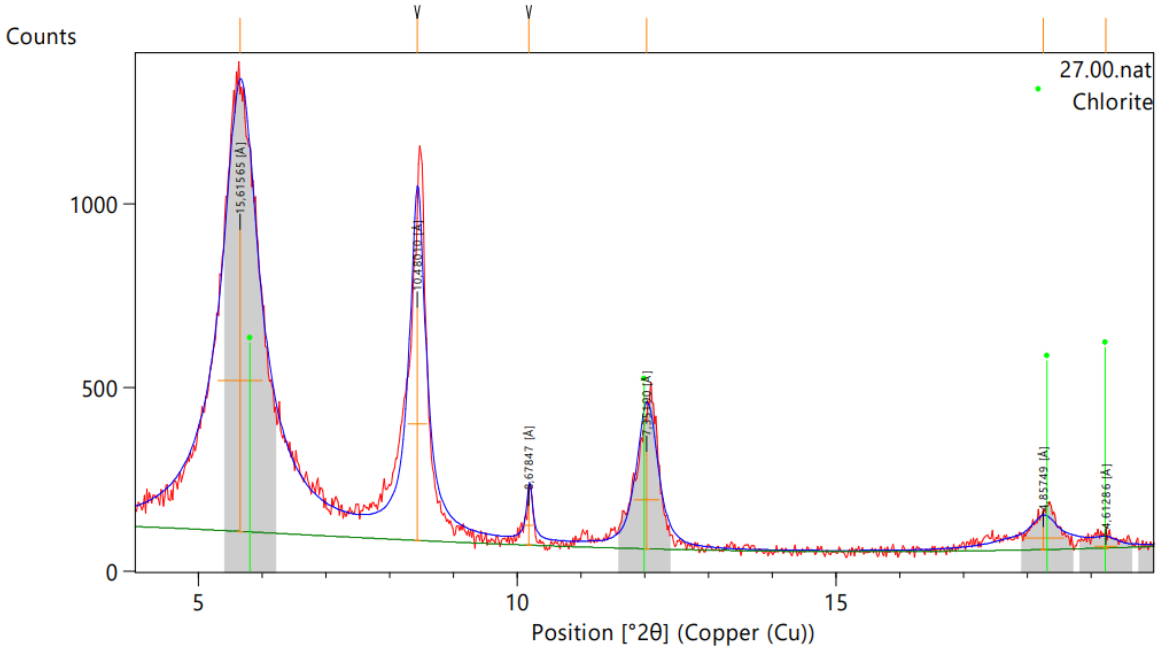
Counts
27.00.nat
Chlorite
1000
500
0
5
10
15
Position [°2θ] (Copper (Cu))

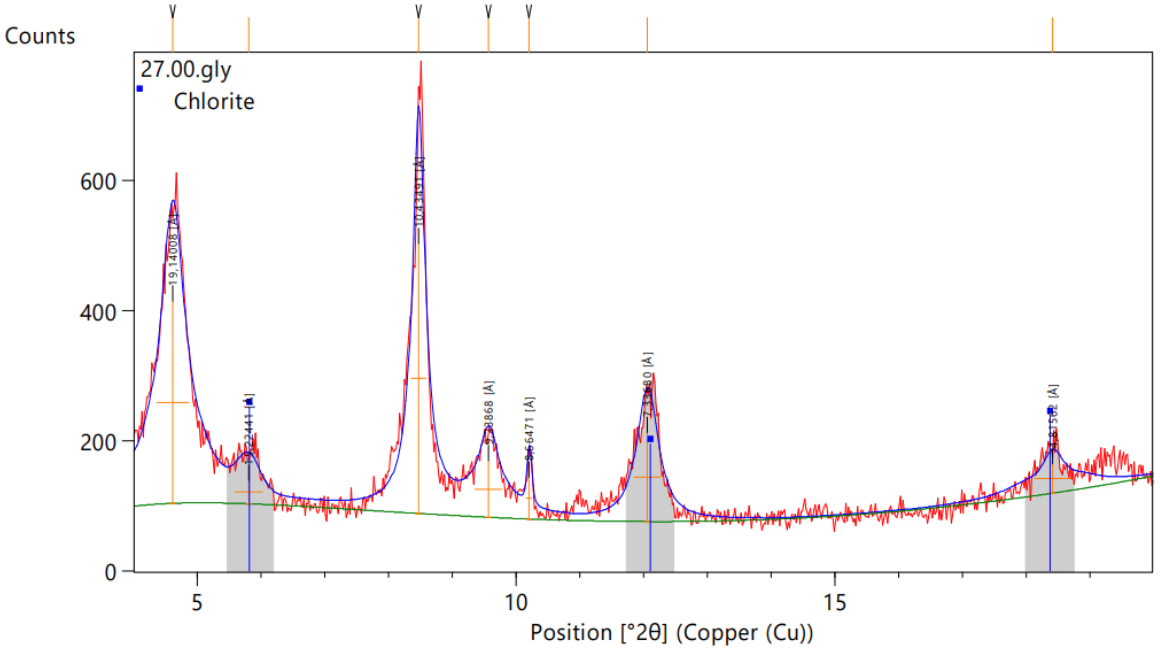
Counts
27.00.gly
Chlorite
600
400
200
0
5
10
15
Position [°2θ] (Copper (Cu))

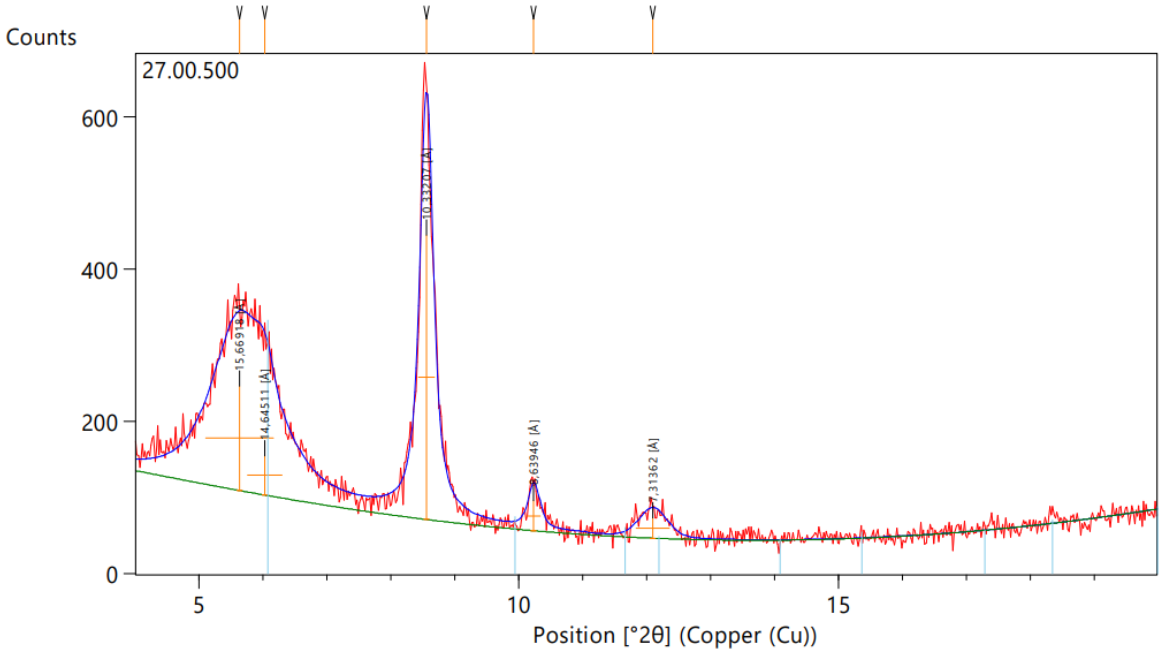
Counts
27.00.500
600
400
200
0
5
10
15
Position [°2θ] (Copper (Cu))

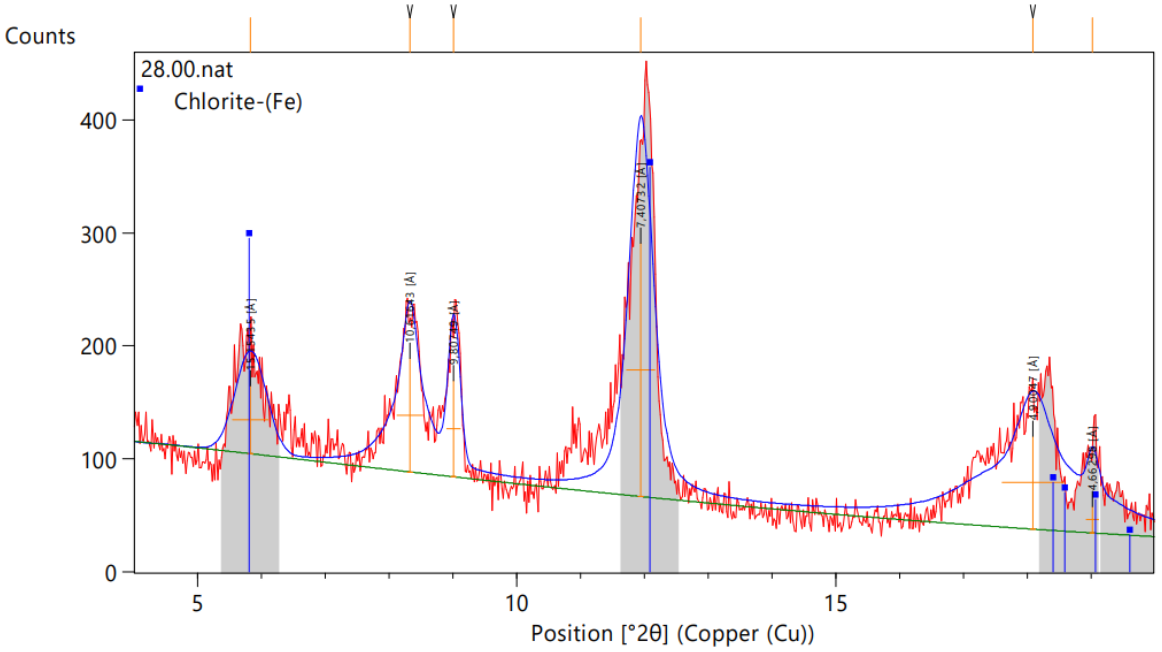
Counts
28.00.nat
Chlorite-(Fe)
400
300
200
100
0
5
10
15
Position [°2θ] (Copper (Cu))

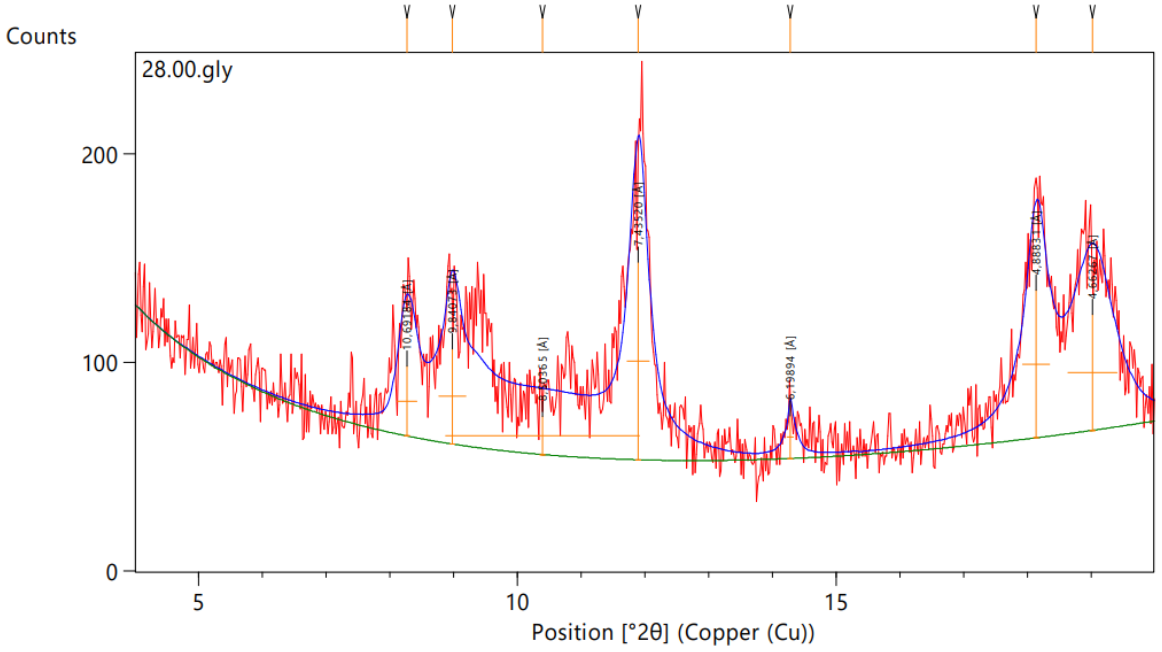
Counts
28.00.gly
200
100
0
5
10
15
Position [°2θ] (Copper (Cu))

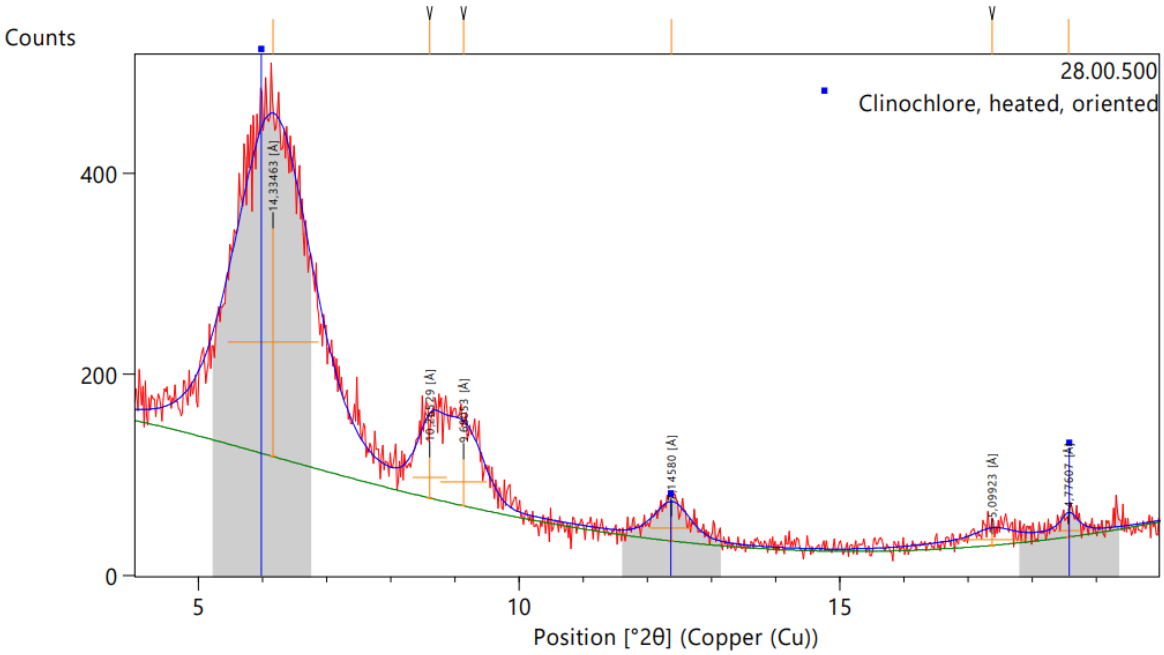
Counts
28.00.500
Clinochlore, heated, oriented
400
200
0
14.33463 [A]
14.4580 [A]
5.09923 [A]
5
10
15
Position [°2θ] (Copper (Cu))

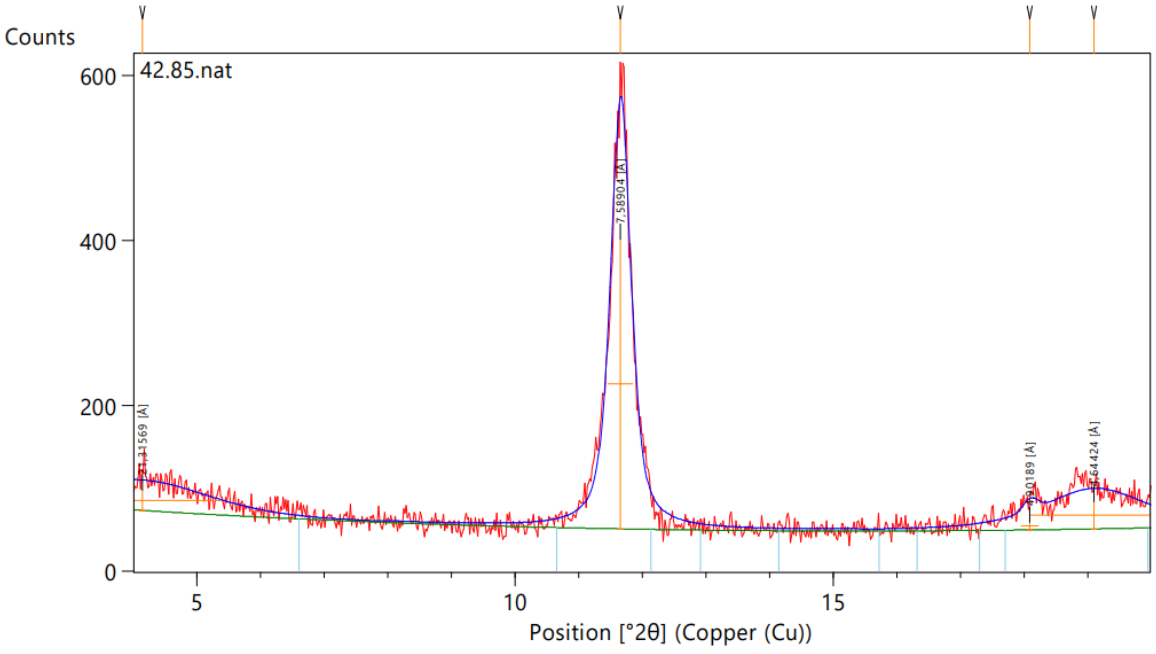
Counts
42.85.nat
600
400
200
0
7.58904 [A]
5
10
15
Position [°2θ] (Copper (Cu))

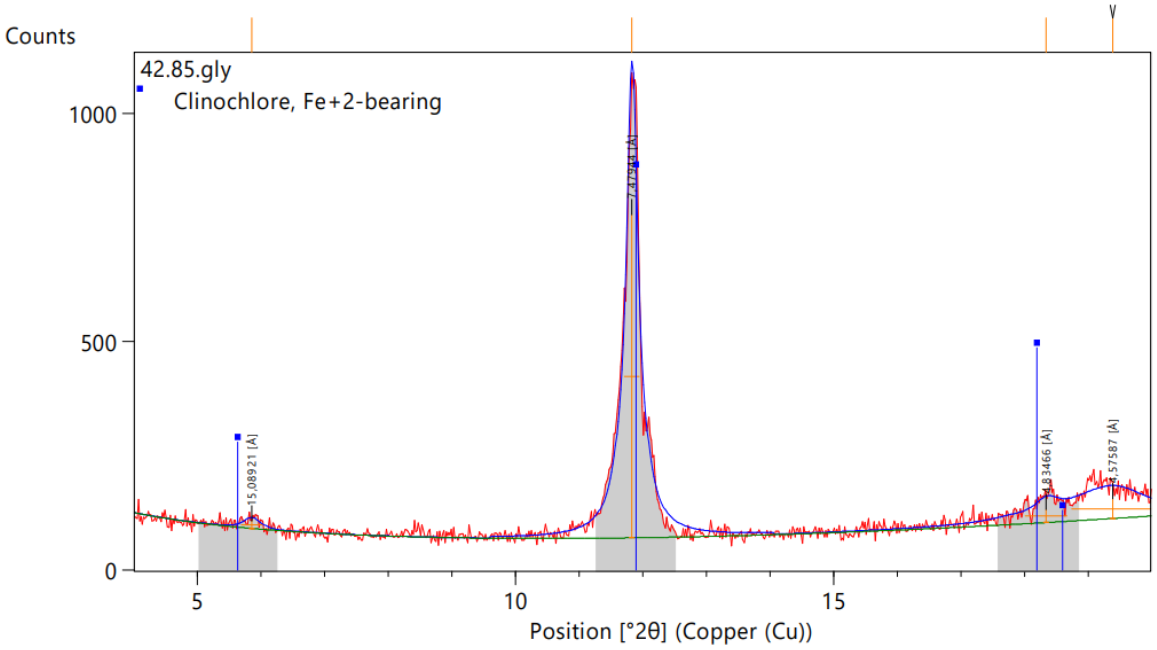
Counts
42.85.gly
Clinochlore, Fe+2-bearing
1000
500
0
5
10
15
Position [°2θ] (Copper (Cu))

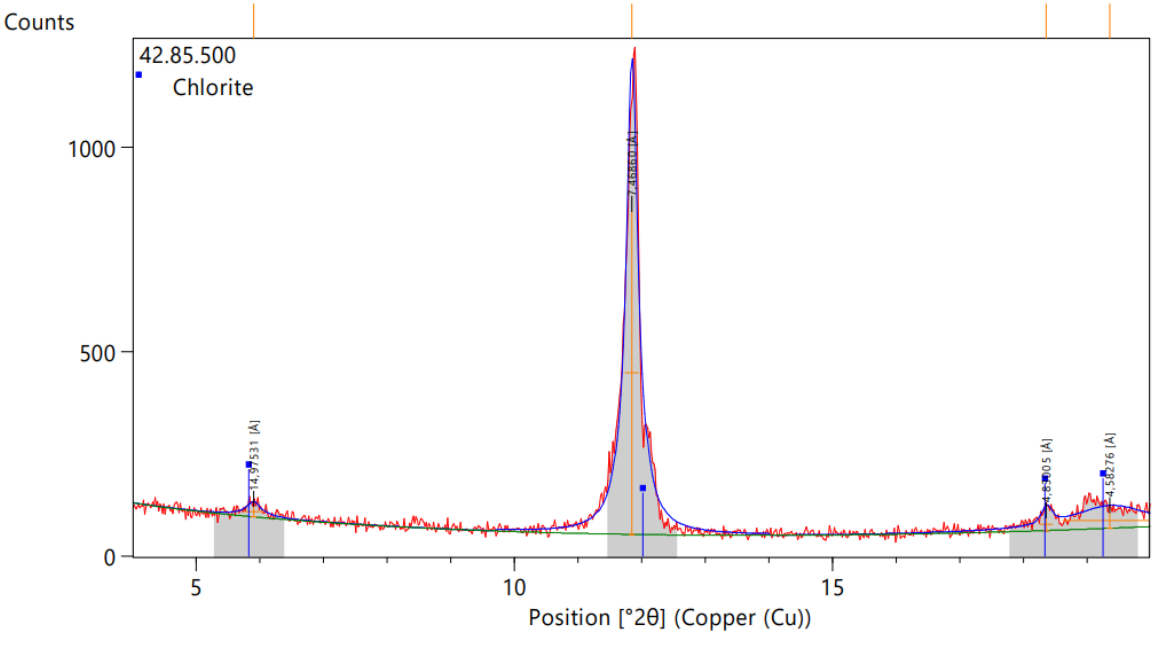
Counts
42.85.500
Chlorite
1000
500
0
5
10
15
Position [°2θ] (Copper (Cu))

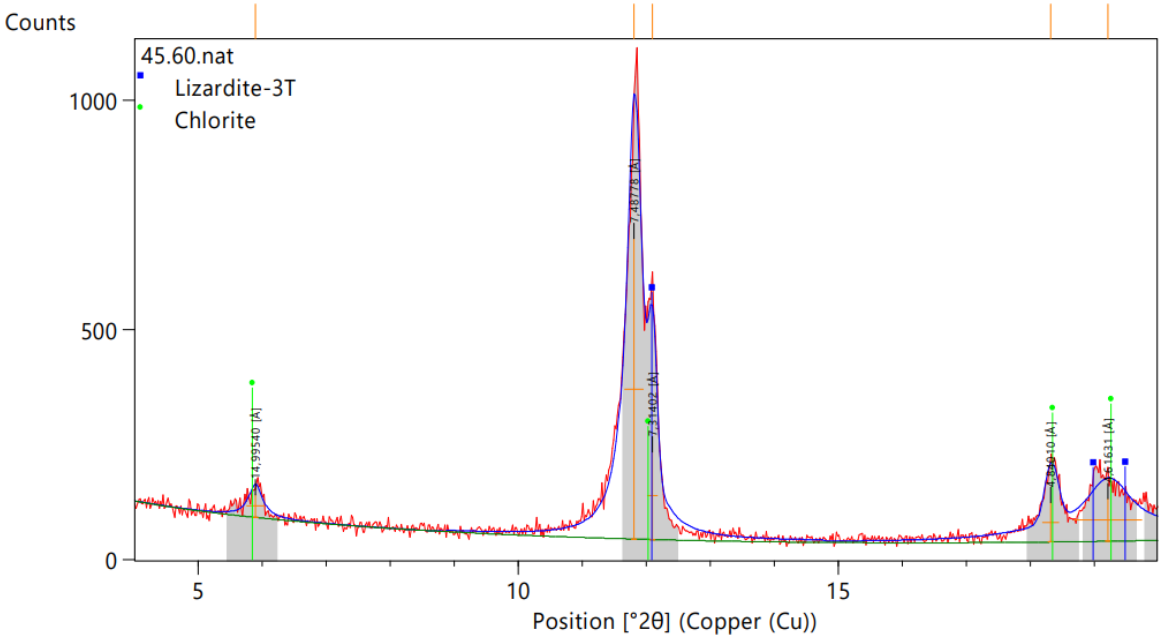
Counts
45.60.nat
Lizardite-3T
Chlorite
1000
500
0
5
10
15
Position [°2θ] (Copper (Cu))

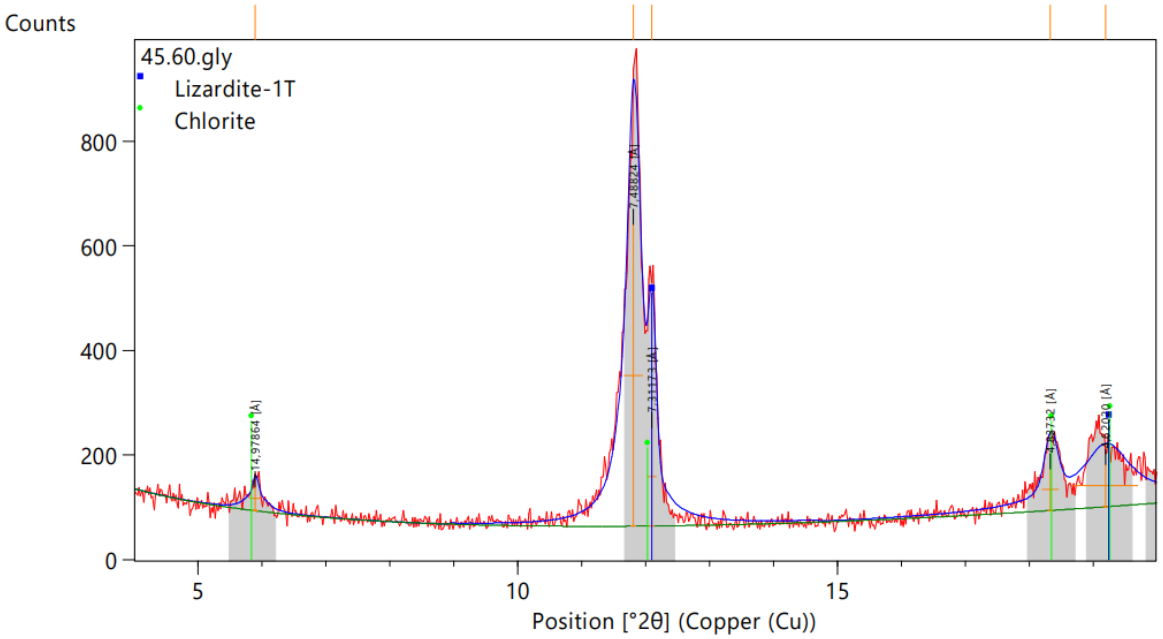
Counts
45.60.gly
Lizardite-1T
Chlorite
800
600
400
200
0
5
10
15
Position [°2θ] (Copper (Cu))

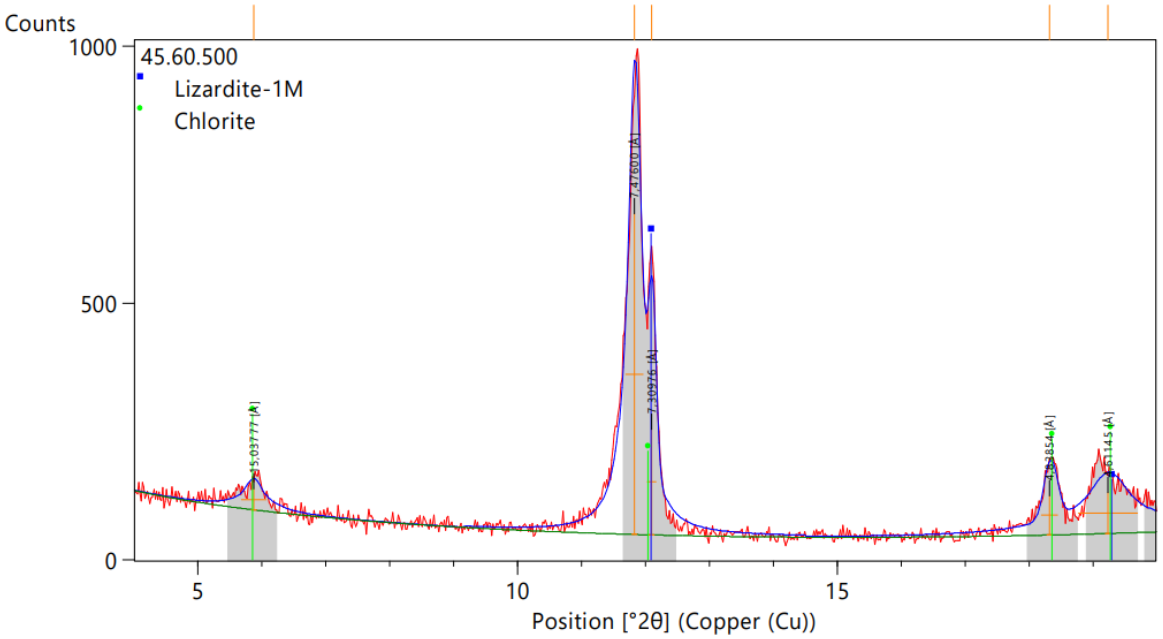
Counts
1000
500
0
45.60.500
Lizardite-1M
Chlorite
5
10
15
Position [°2θ] (Copper (Cu))

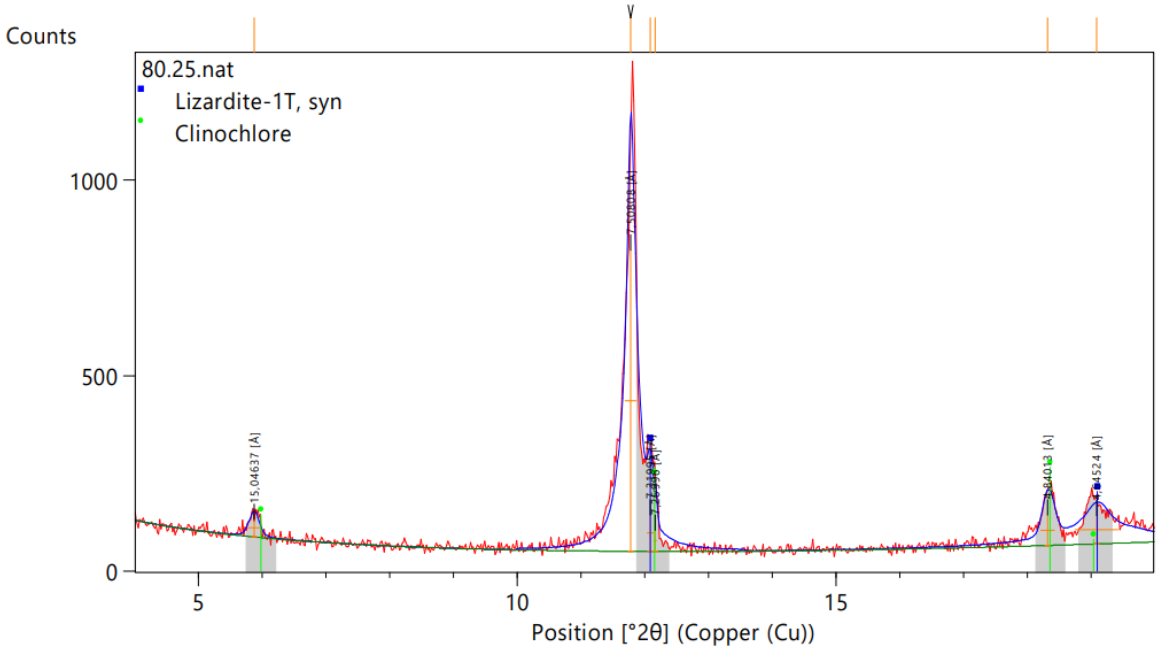
Counts
1000
500
0
80.25.nat
Lizardite-1T, syn
Clinochlore
5
10
15
Position [°2θ] (Copper (Cu))

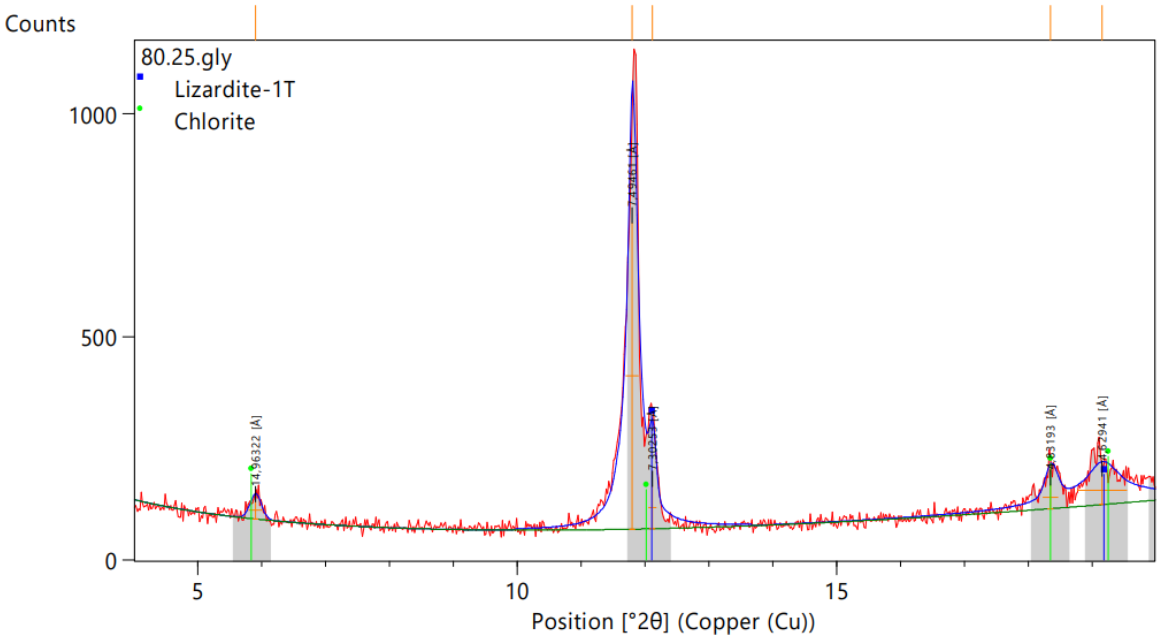
Counts
80.25.gly
Lizardite-1T
Chlorite
1000
500
0
14,96322 [Å]
7,43961 [Å]
4,63193 [Å]
4,47941 [Å]
5
10
15
Position [°2θ] (Copper (Cu))

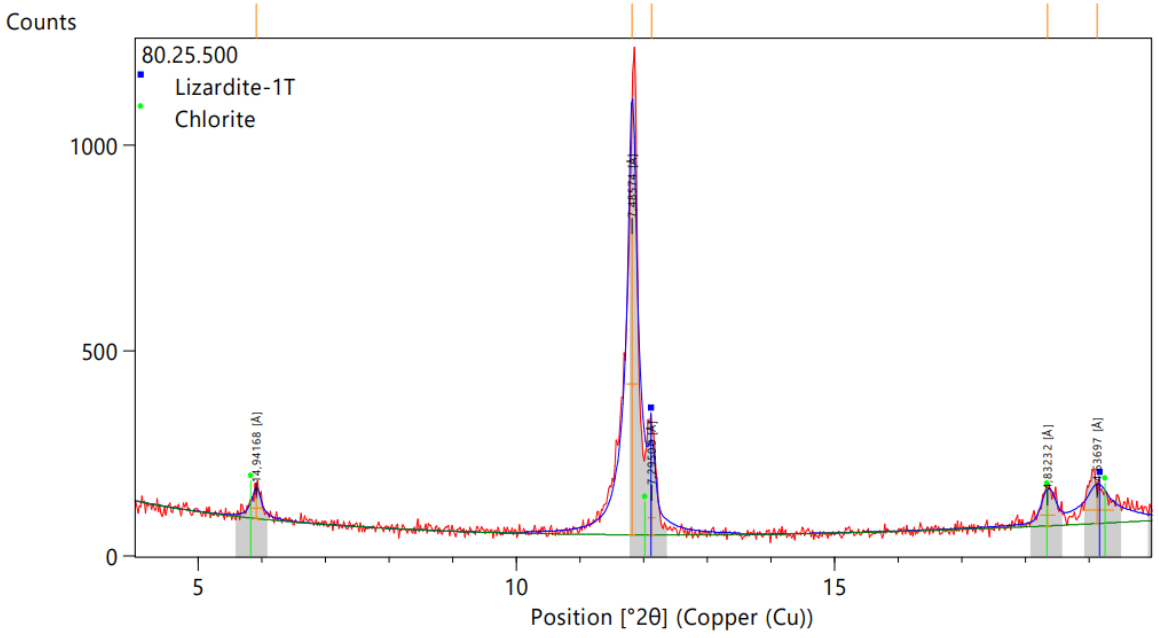
Counts
80.25.500
Lizardite-1T
Chlorite
1000
500
0
14,94168 [Å]
7,43574 [Å]
4,63232 [Å]
4,43697 [Å]
5
10
15
Position [°2θ] (Copper (Cu))

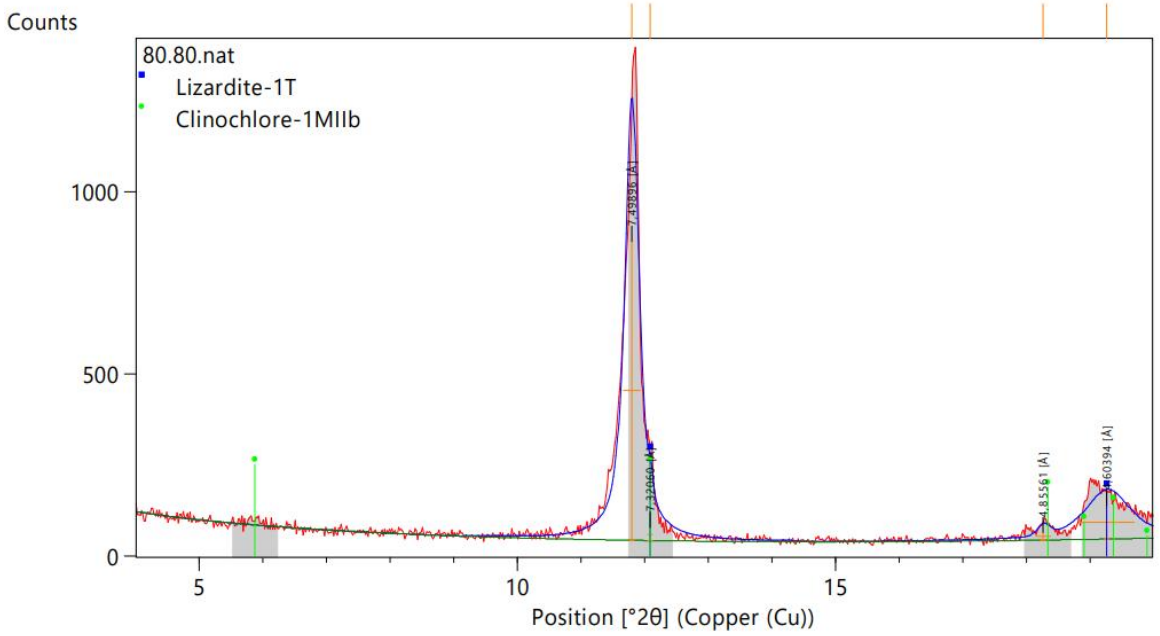
Counts
80.80.nat
Lizardite-1T
Clinochlore-1MIIb
1000
500
0
5
10
15
Position [°2θ] (Copper (Cu))

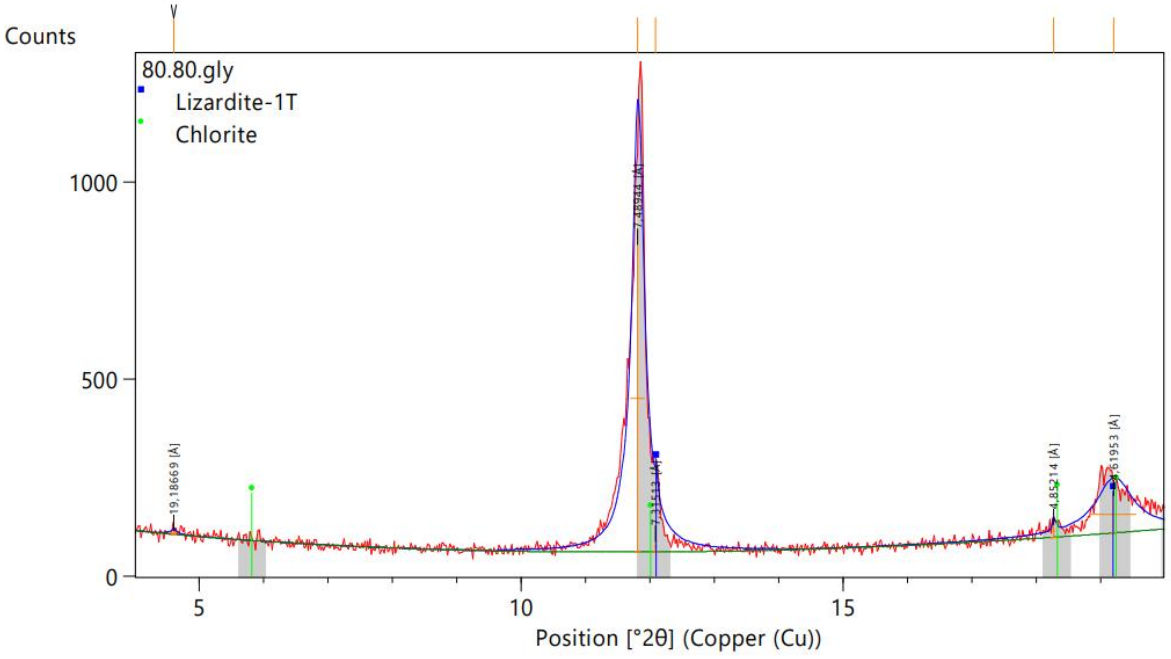
Counts
80.80.gly
Lizardite-1T
Chlorite
1000
500
0
5
10
15
Position [°2θ] (Copper (Cu))

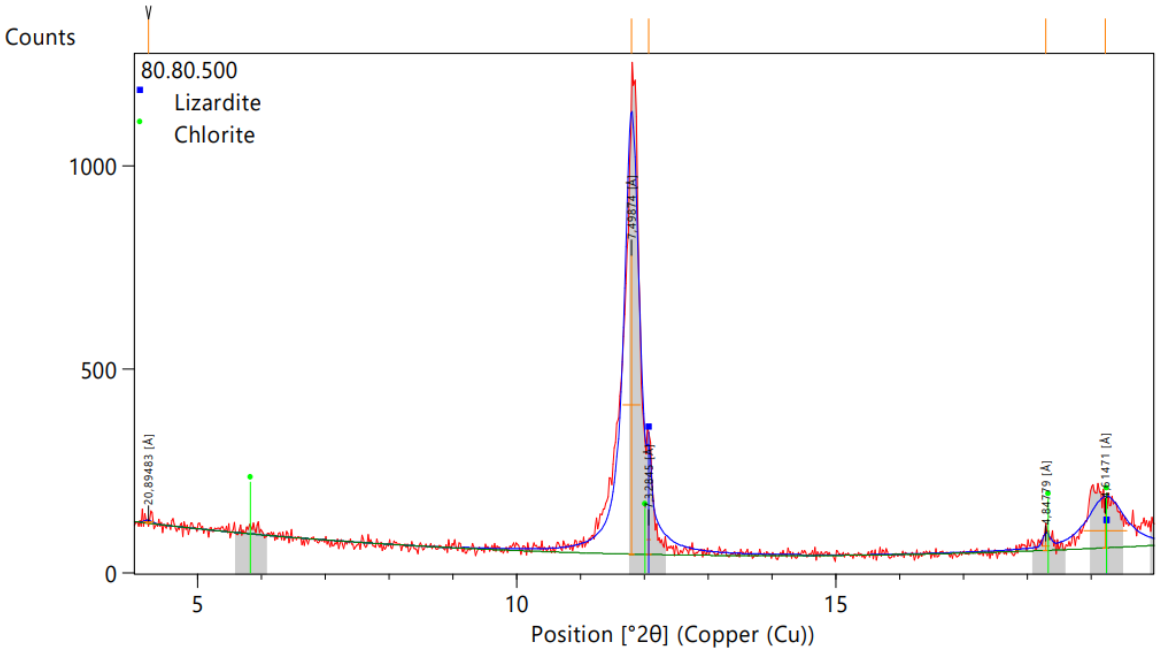
Counts
80.80.500
Lizardite
Chlorite
1000
500
0
7.43874 [Å]
20.89483 [Å]
4.84779 [Å]
3.61471 [Å]
5
10
15
Position [°2θ] (Copper (Cu))

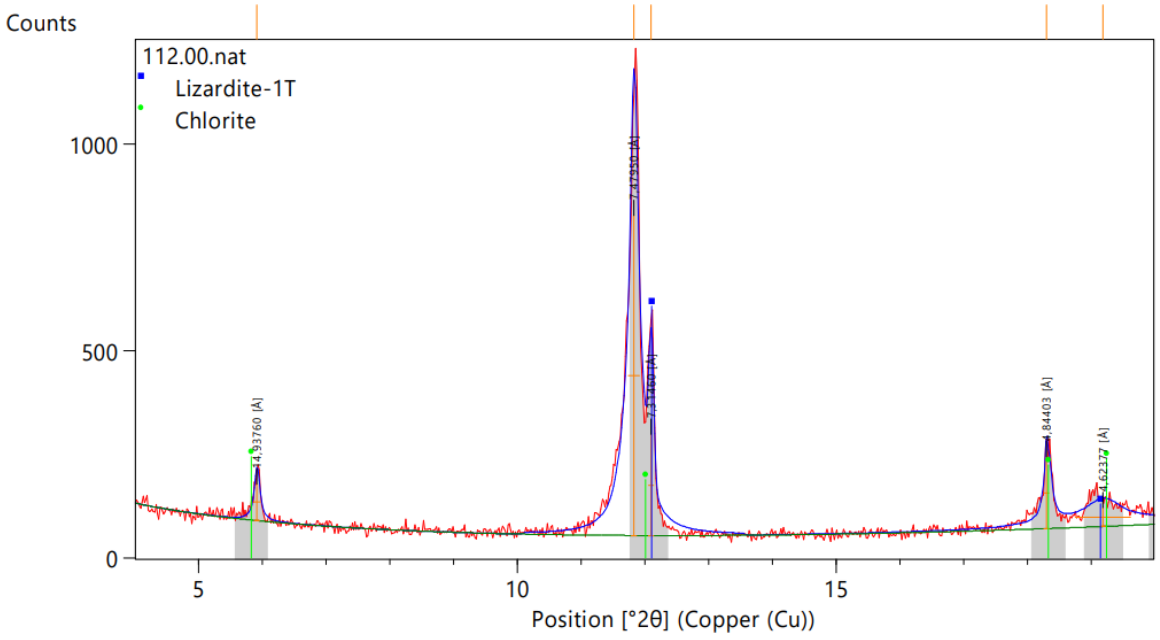
Counts
112.00.nat
Lizardite-1T
Chlorite
1000
500
0
14.93760 [Å]
7.47330 [Å]
4.84403 [Å]
3.62377 [Å]
5
10
15
Position [°2θ] (Copper (Cu))

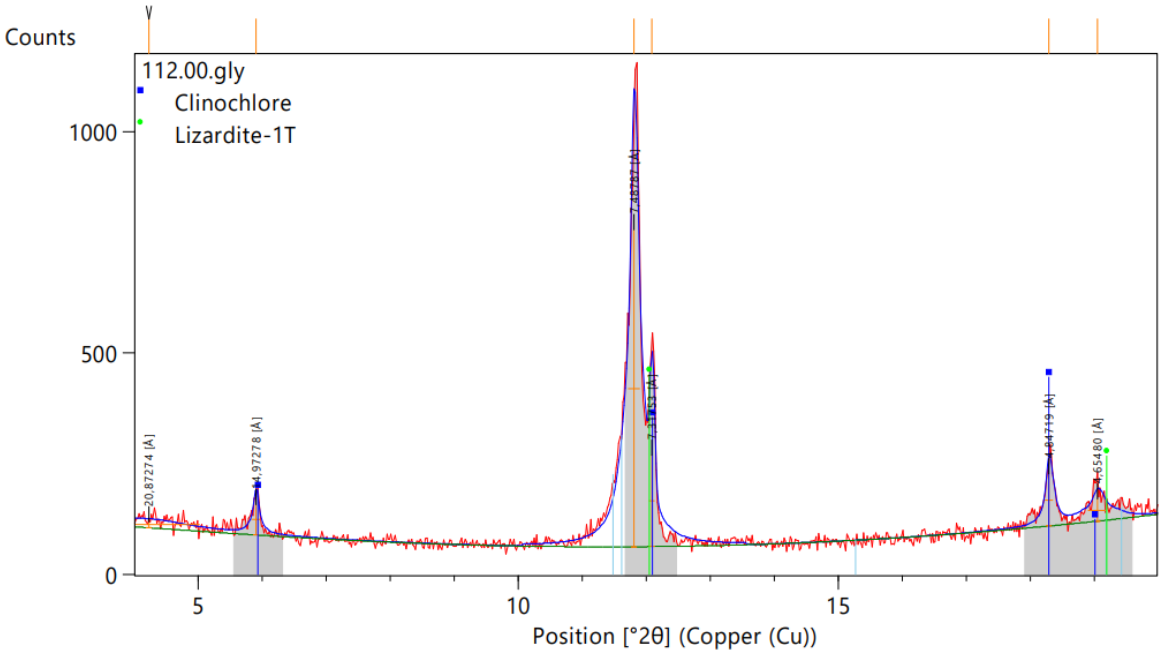
Counts
112.00.gly
Clinochlore
Lizardite-1T
1000
500
0
20.87274 [Å]
14.97278 [Å]
7.46722 [Å]
7.31763 [Å]
4.84719 [Å]
4.65480 [Å]
5
10
15
Position [°2θ] (Copper (Cu))

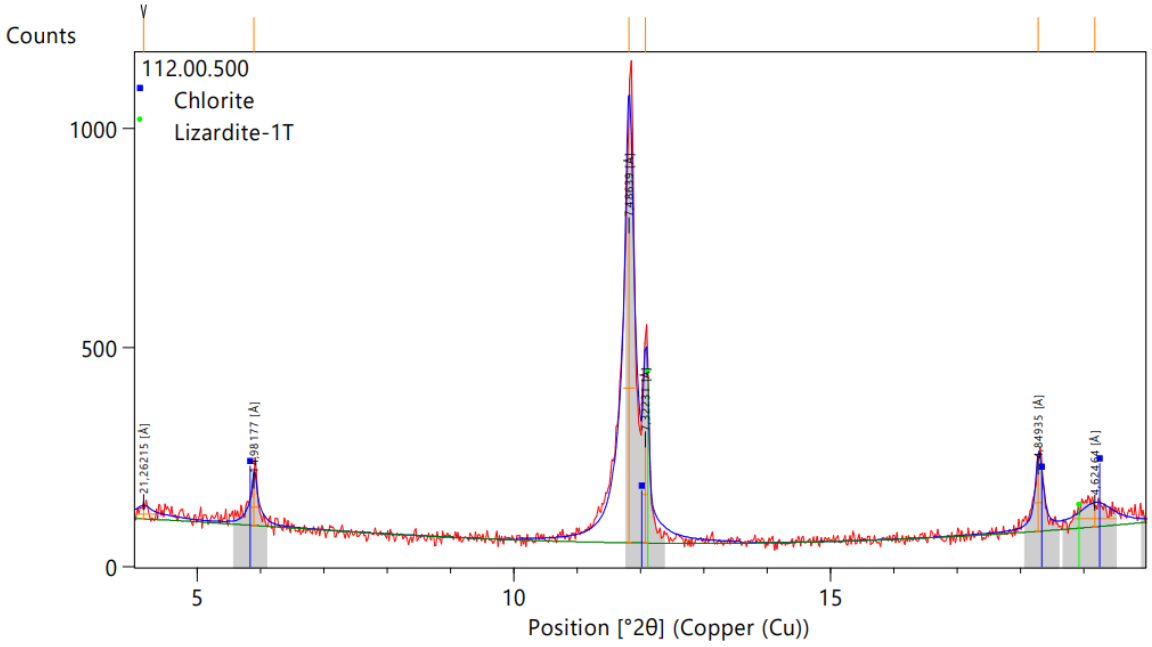
Counts
112.00.500
Chlorite
Lizardite-1T
1000
500
0
21.26215 [Å]
14.98177 [Å]
7.48833 [Å]
7.32231 [Å]
4.84935 [Å]
4.62464 [Å]
5
10
15
Position [°2θ] (Copper (Cu))

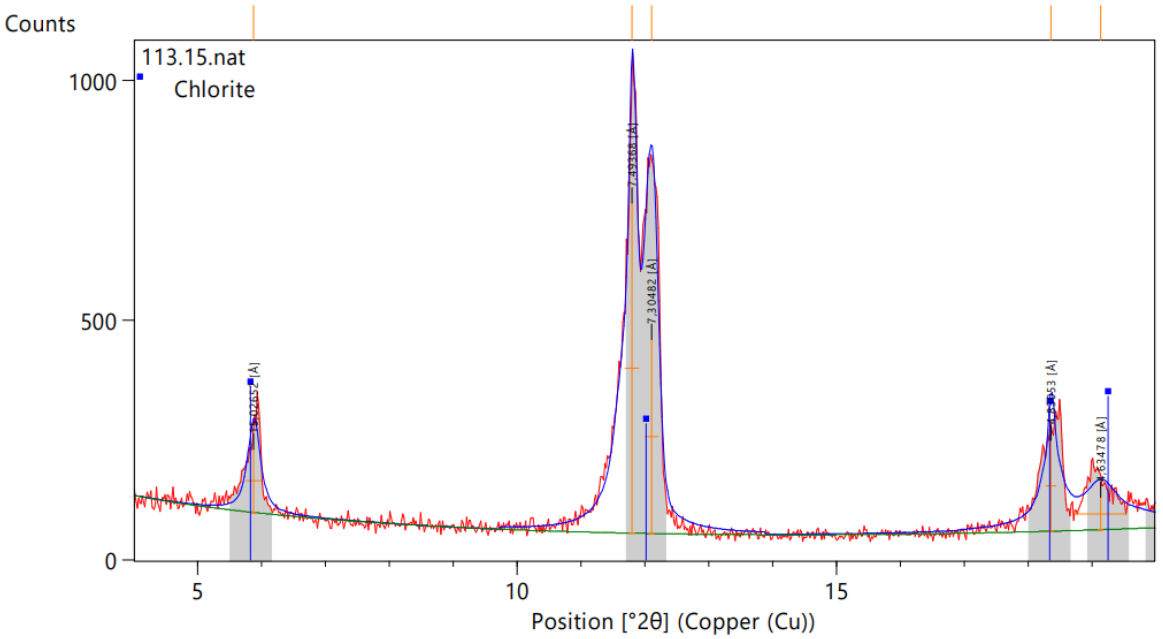
Counts
113.15.nat
Chlorite
1000
500
0
7.49168 [Å]
7.30482 [Å]
14.02652 [Å]
14.13953 [Å]
3.63478 [Å]
5
10
15
Position [°2θ] (Copper (Cu))

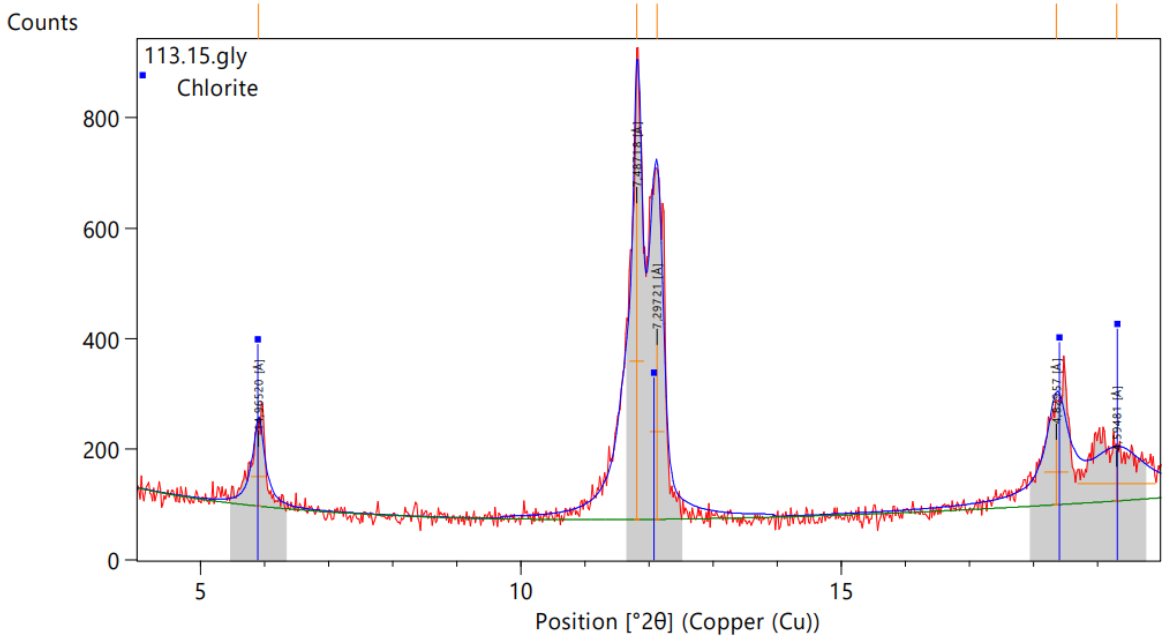
Counts
113.15.gly
Chlorite
800
600
400
200
0
7.48718 [Å]
7.29721 [Å]
14.36926 [Å]
14.36557 [Å]
3.59481 [Å]
5
10
15
Position [°2θ] (Copper (Cu))

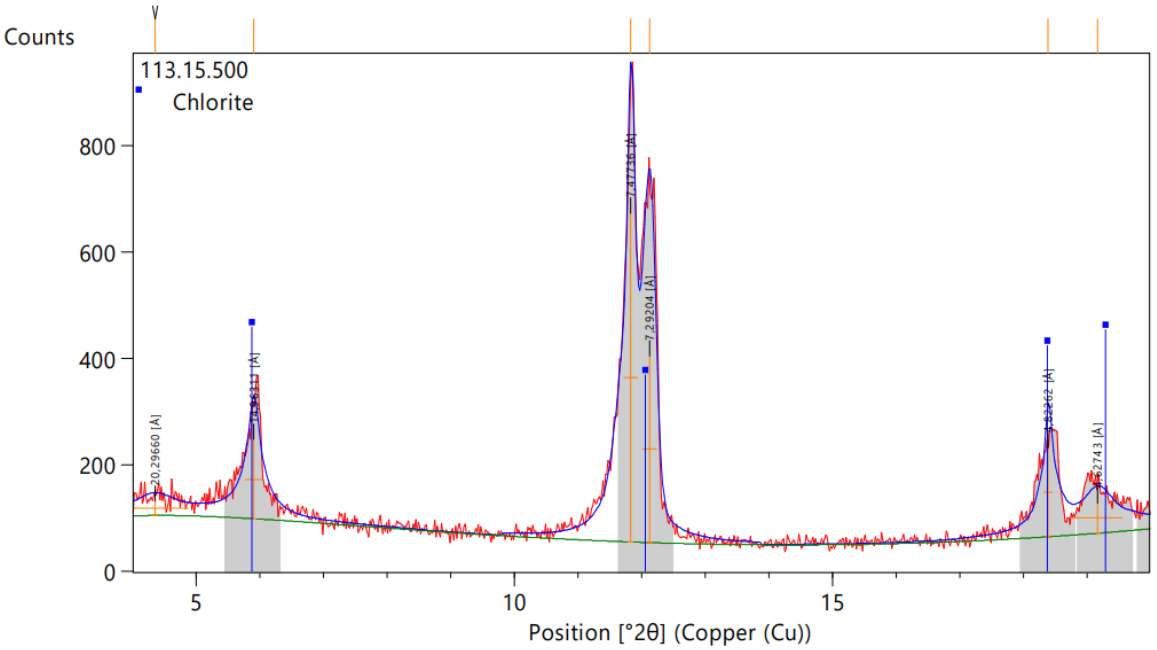
Counts
113.15.500
Chlorite
800
600
400
200
0
5
10
15
Position [°2θ] (Copper (Cu))

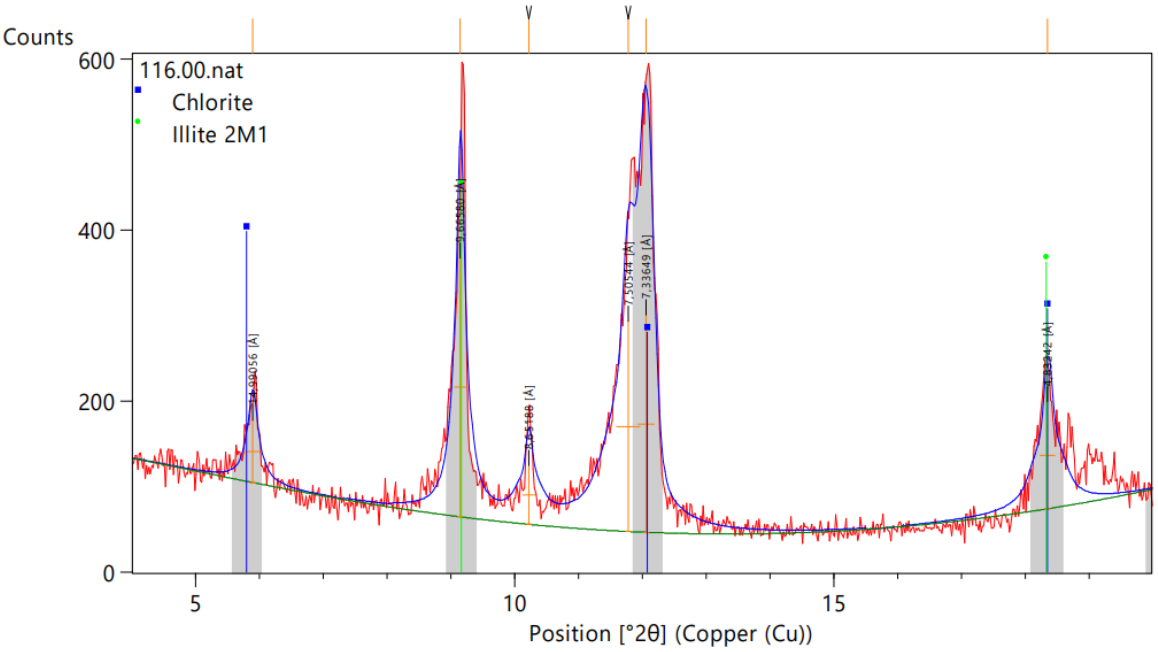
Counts
116.00.nat
Chlorite
Illite 2M1
600
400
200
0
5
10
15
Position [°2θ] (Copper (Cu))

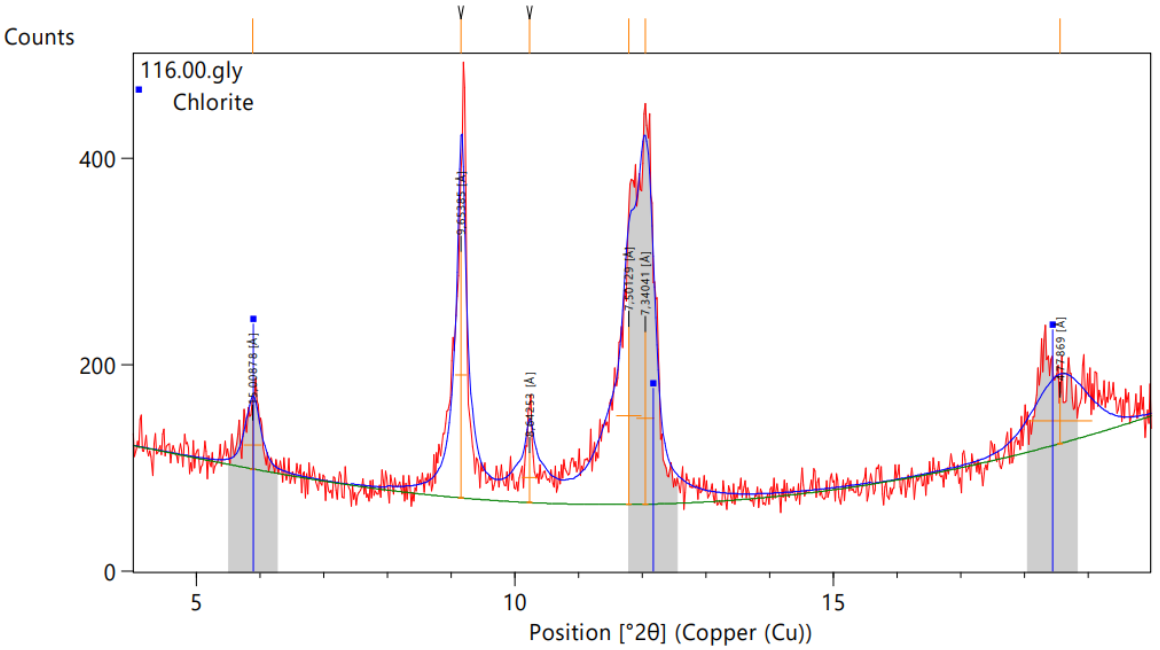
Counts
116.00.gly
Chlorite
400
200
0
5
10
15
Position [°2θ] (Copper (Cu))

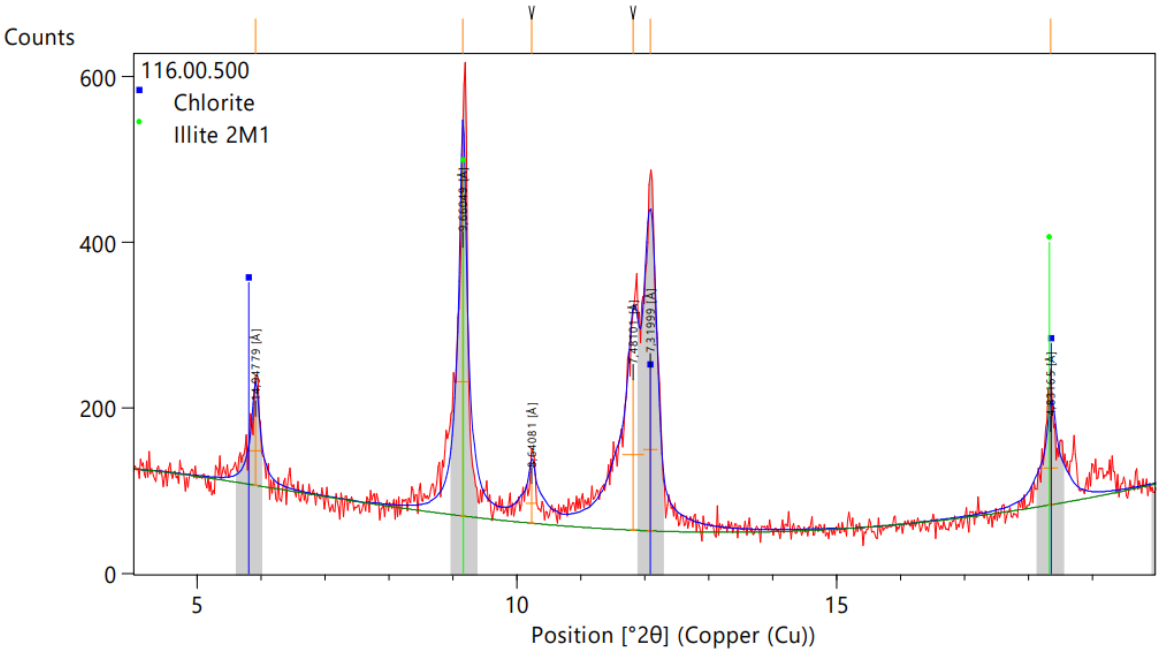
Counts
116.00.500
Chlorite
Illite 2M1
600
400
200
0
5
10
15
Position [°2θ] (Copper (Cu))

Samples CdV: 125.20_1, 125.20_2 and 125.20_3 X-Ray Diffraction

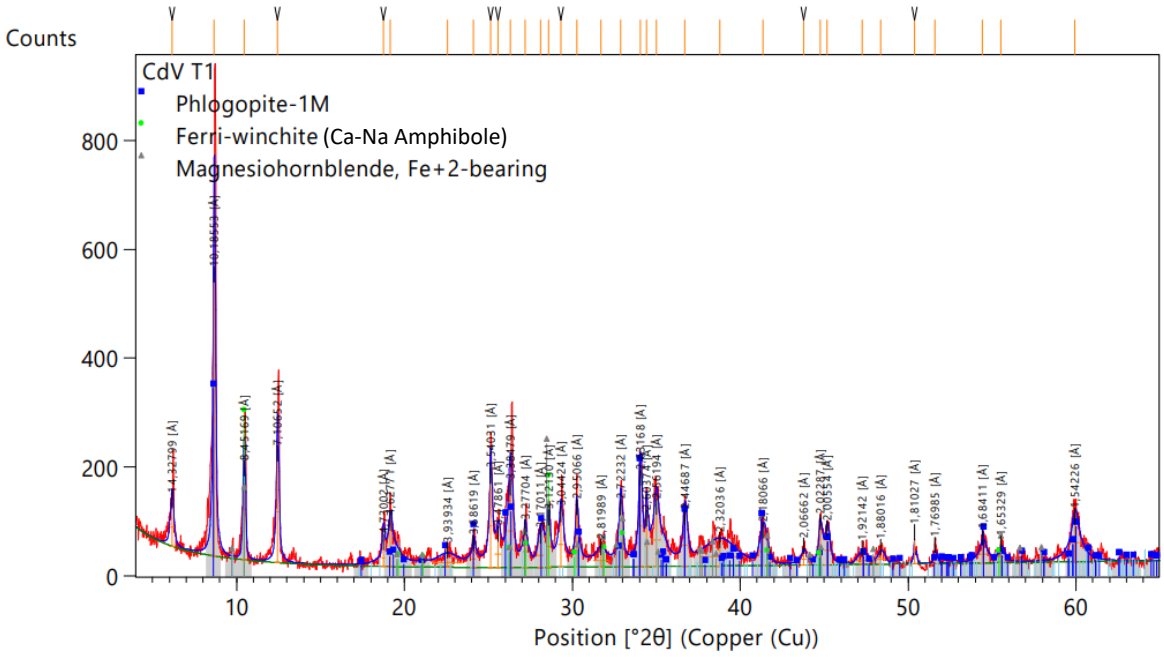

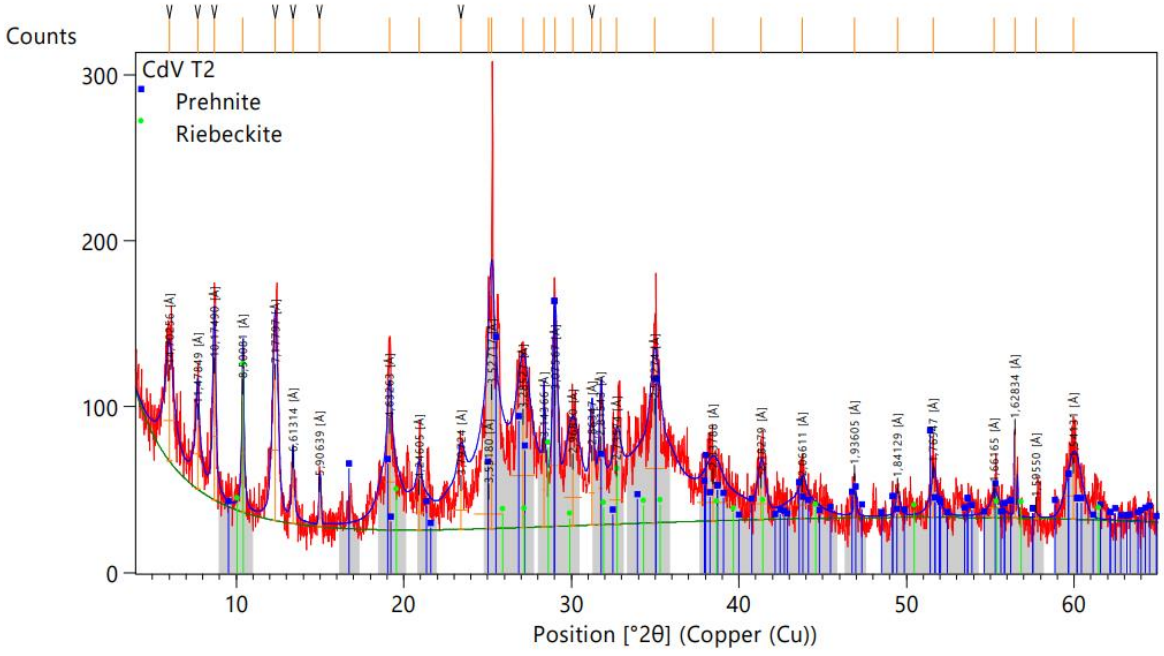

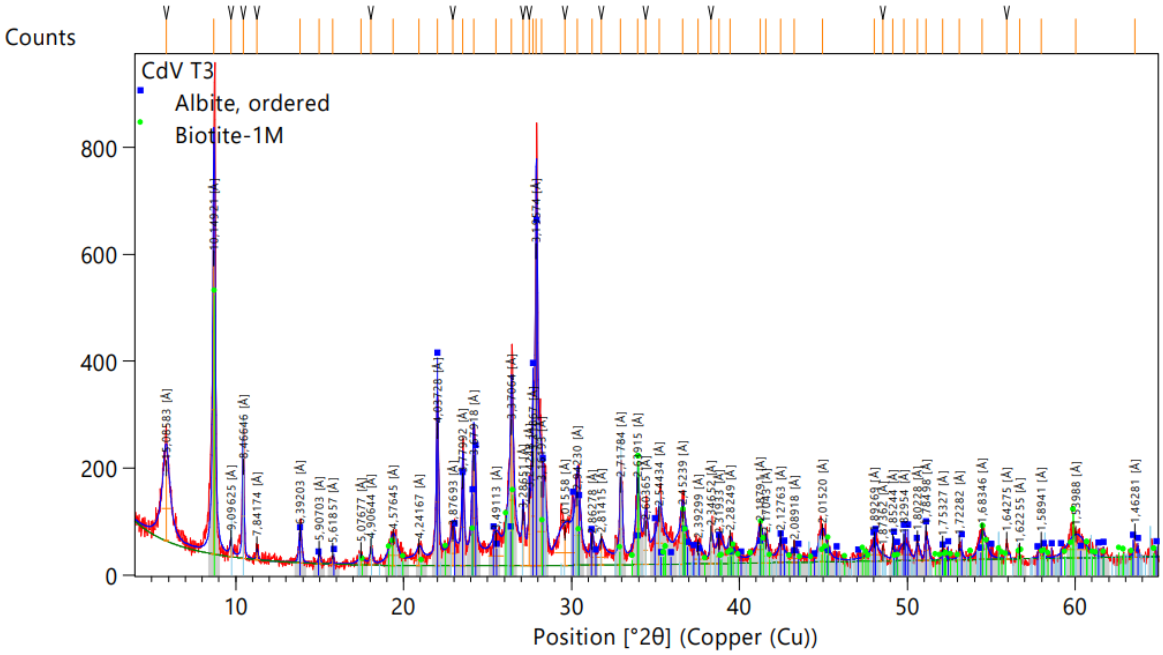
Counts
CdV T3
Albite, ordered
Biotite-1M
800
600
400
200
0
10
20
30
40
50
60
Position [°2θ] (Copper (Cu))

Samples CdV R1 and R2, from Ermida Spring, X-Ray Diffraction

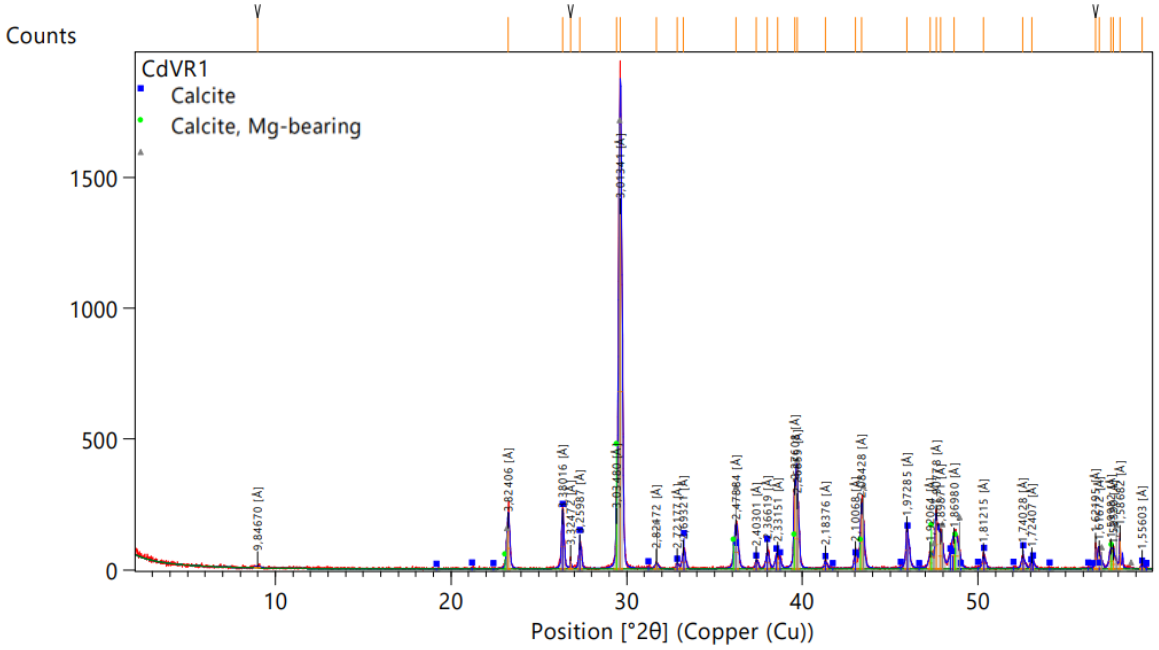

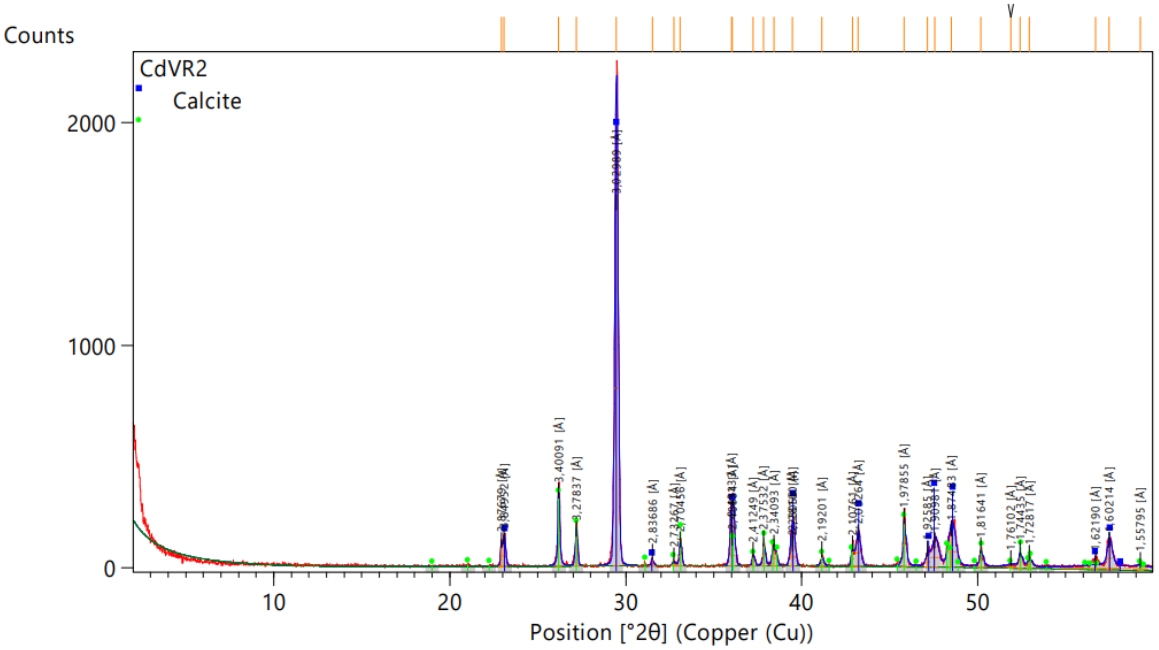

2 - X-Ray Fluorescence – Chemical Analysis

(ppm)	F	Cr	V	Co	Zn	Ba	Sr
CdV26.80	4210	10	30	N.d.	30	190	1270
CdV27.00	1130	590	150	130	80	2820	470
CdV28.00	1370	480	130	20	40	590	260
CdV42.85	N.d.	1910	40	240	30	20	10
CdV45.60	N.d.	2050	80	160	60	10	30
CdV80.25	N.d.	2650	40	200	60	N.d.	10
CdV80.80	N.d.	2970	20	130	260	10	10
CdV112.00	N.d.	2370	30	170	70	10	10
CdV113.15	N.d.	800	60	160	60	20	30
CdV116.00	N.d.	2520	40	230	160	20	50

(ppm)	Sc	Cu	Ga	Ge	As	Se	Br	Rb	Y	Zr	Nb	Mo	Ag	Cd	Sn	Sb	Te	I
CdV26.80	11.9	12.5	2.9	N.d.	N.d.	0.9	N.d.	3.0	2.5	N.d.	N.d.	2.8	N.d.	N.d.	N.d.	N.d.	N.d.	N.d.
CdV27.00	18.9	17.0	11.5	N.d.	19.4	N.d.	N.d.	31.0	17.2	28.8	11.4	1.4	N.d.	4.9	4.7	N.d.	N.d.	N.d.
CdV28.00	20.9	15.3	11.2	N.d.	17.1	N.d.	N.d.	19.0	13.0	20.0	9.3	1.7	N.d.	N.d.	3.3	N.d.	N.d.	N.d.
CdV42.85	N.d.	8.0	2.4	N.d.	N.d.	N.d.	N.d.	2.9	2.6	5.8	1.3	0.9	N.d.	N.d.	N.d.	N.d.	N.d.	N.d.
CdV45.60	4.7	12.3	5.1	N.d.	N.d.	N.d.	1.5	3.8	6.5	17.1	3.3	1.0	N.d.	N.d.	N.d.	N.d.	N.d.	N.d.
CdV80.25	3.9	6.9	3.1	N.d.	N.d.	N.d.	1.4	1.9	1.8	6.6	N.d.	1.3	N.d.	N.d.	N.d.	N.d.	N.d.	N.d.
CdV80.80	N.d.	7.7	3.7	N.d.	N.d.	N.d.	0.9	2.1	1.1	2.6	N.d.	1.3	N.d.	N.d.	N.d.	N.d.	N.d.	N.d.
CdV112.00	N.d.	N.d.	3.0	N.d.	N.d.	N.d.	3.9	2.3	1.9	4.9	N.d.	1.2	N.d.	N.d.	N.d.	N.d.	N.d.	N.d.
CdV113.15	8.8	21.0	5.0	N.d.	N.d.	N.d.	7.3	3.2	4.4	9.6	N.d.	1.3	N.d.	N.d.	N.d.	N.d.	N.d.	N.d.
CdV116.00	8.7	10.1	5.0	N.d.	25.3	N.d.	1.1	3.3	4.6	6.2	0.9	1.4	N.d.	N.d.	N.d.	N.d.	N.d.	N.d.

(ppm)	Cs	Sm	Yb	La	Hf	Ta	Tl	Pb	Bi	Th	U	Ce	Nd	Sm	Yb	Hf	W	Tl
CdV26.80	6.9	N.d.	N.d.	N.d.	N.d.	N.d.	N.d.	4.8	N.d.	22.3	5.1	38.5	18.8	N.d.	N.d.	N.d.	N.d.	N.d.
CdV27.00	N.d.	11.7	N.d.	6.0	5.2	N.d.	2.3	10.7	N.d.	22.8	10.4	114.6	52.0	11.7	N.d.	5.2	4.0	2.3
CdV28.00	6.5	6.8	N.d.	5.0	4.2	N.d.	N.d.	8.1	N.d.	17.0	7.4	84.5	40.7	6.8	N.d.	4.2	N.d.	N.d.
CdV42.85	6.3	N.d.	N.d.	N.d.	N.d.	5.8	N.d.	7.8	N.d.	N.d.	N.d.	20.0	N.d.	N.d.	N.d.	N.d.	28.3	N.d.
CdV45.60	6.2	N.d.	N.d.	N.d.	N.d.	4.9	N.d.	9.0	N.d.	N.d.	N.d.	22.8	N.d.	N.d.	N.d.	N.d.	24.6	N.d.
CdV80.25	N.d.	N.d.	N.d.	N.d.	N.d.	5.7	N.d.	8.3	N.d.	N.d.	N.d.	31.8	N.d.	N.d.	N.d.	N.d.	30.1	N.d.
CdV80.80	6.0	N.d.	N.d.	N.d.	N.d.	N.d.	N.d.	9.8	N.d.	N.d.	N.d.	39.0	N.d.	N.d.	N.d.	N.d.	12.7	N.d.
CdV112.00	N.d.	N.d.	N.d.	N.d.	N.d.	4.2	N.d.	7.0	N.d.	N.d.	N.d.	24.2	N.d.	N.d.	N.d.	N.d.	31.7	N.d.
CdV113.15	6.4	N.d.	N.d.	N.d.	N.d.	N.d.	N.d.	13.0	N.d.	N.d.	N.d.	18.4	N.d.	N.d.	N.d.	N.d.	15.1	N.d.
CdV116.00	N.d.	N.d.	N.d.	N.d.	N.d.	5.0	2.8	14.0	N.d.	N.d.	N.d.	27.8	N.d.	N.d.	N.d.	N.d.	18.7	2.8

Minor and trace elements from chemical analysis of CdV whole samples (in ppm). N.d. – Non detected.

(%)	MgO	Al2O3	SiO2	P2O5	K2O	CaO	TiO2	MnO	Fe2O3	NiO	Na2O	Cl	SO3	ZnO
CdV 26.80B	0.606	0.391	2.877	0.41	0.521	91.293	0.216	0.371	2.692	0.022	N.d.	N.d.	0.209	0.01
CdV 27.00B	2.248	3.006	31.622	1.078	7.044	22.226	1.428	0.355	29.245	0.067	0.022	0.077	0.23	0.049
CdV 28.00B	1.999	4.775	35.657	1.432	3.663	14.263	2.718	0.247	33.451	0.349	0.117	0.048	0.024	0.019
CdV 42.85B	5.945	3.21	23.851	1.497	0.671	11.432	0.541	0.617	50.504	0.643	N.d.	0.126	0.233	0.329
CdV 45.60B	7.827	1.805	24.575	1.02	0.079	15.241	1.088	0.688	45.6	1.306	N.d.	0.093	0.07	0.028
CdV 80.25B	10.322	0.604	31.459	1.37	0,000	23.906	0.11	0.925	28.975	0.418	N.d.	0.069	0.425	0.179
CdV 80.80B	7.33	2.873	20.862	0.932	0.038	26.148	2.678	0.973	36.184	0.506	N.d.	0.092	0.062	0.129
CdV 112.00B	6.997	2.367	24.241	0.858	0.019	1.683	0.075	1.103	61.512	0.511	N.d.	0.035	0.131	0.086
CdV 113.15B	10.311	8.665	35.586	1.634	0.247	6.223	0.851	2.456	33.339	0.173	N.d.	0.131	N.d.	0.06
CdV 116.00B	4.48	3.116	18.268	0.8	0.09	24.026	0.513	0.915	46.417	0.481	N.d.	0.109	0.079	0.04
CdV 26.80W	0.682	0.417	3.145	0.424	0.56	90.648	0.222	0.327	2.958	0.024	N.d.	0.02	0.194	0.009
CdV 27.00W	2.214	1.867	37.959	0.949	7.048	37.979	0.42	0.202	10.23	0.077	N.d.	N.d.	0.116	0.022
CdV 28.00W	3.942	3.723	36.461	1.582	2.847	28.184	1.798	0.359	20.158	0.09	0.063	0.054	0.148	0.018
CdV 42.85W	8.596	7.357	36.922	2.051	0.953	9.741	0.44	0.61	29.827	0.103	N.d.	0.186	0.516	2.202
CdV 45.60W	3.503	0.49	12.398	0.674	0.027	57.521	0.527	0.636	23.373	0.457	N.d.	0.042	0.049	0.035
CdV 80.25W	12.148	0.691	38.27	1.396	0.02	19.146	0.268	1.222	25.769	0.271	N.d.	0.053	0.114	0.101
CdV 80.80W	2.789	0.514	9.667	0.605	0,000	72.305	0.561	0.475	12.586	0.103	N.d.	0.042	0.029	0.036
CdV 112.00W	7.643	3.216	27.681	1.041	0.037	3.59	0.102	1.397	54.155	0.811	N.d.	0.042	0.139	0.113
CdV 113.15W	11.906	6.348	43.814	2.107	0.065	3.888	0.143	1.741	29.411	0.136	N.d.	0.16	0.073	0.09
CdV 116.00W	4.06	1.853	15.411	0.687	0.042	52.136	0.212	0.865	24.036	0.297	N.d.	0.044	0.051	0.036

Major elements from the chemical analysis of CdV Partial samples, in %. N.d. – Not detected.

(%)	Br	SrO	PdO	As2O3	BaO	CeO2	Co3O4	Cr2O3	CuO	Ga2O3	HfO2	La2O3	Nb2O5	Nd2O3	PbO	Rb2O	V2O5	ZrO2
CdV 26.80B	0.004	0.353	0.026	N.d.	N.d.	N.d.	N.d.	N.d.	N.d.	N.d.	N.d.	N.d.	N.d.	N.d.	N.d.	N.d.	N.d.	N.d.
CdV 27.00B	0.004	0.142	N.d.	N.d.	0.191	0.252	0.045	0.138	0.036	0.008	N.d.	0.122	N.d.	0.164	N.d.	0.04	0.087	0.076
CdV 28.00B	0.027	0.291	0.047	0.127	N.d.	0.054	0.066	0.331	0.018	N.d.	N.d.	N.d.	N.d.	N.d.	N.d.	0.024	0.118	0.135
CdV 42.85B	0.013	0.027	N.d.	N.d.	N.d.	N.d.	0.096	0.168	0.054	N.d.	N.d.	N.d.	N.d.	N.d.	N.d.	N.d.	0.042	N.d.
CdV 45.60B	0.013	0.046	0.068	N.d.	N.d.	N.d.	0.13	0.304	N.d.	N.d.	N.d.	N.d.	N.d.	N.d.	N.d.	N.d.	N.d.	0.019
CdV 80.25B	0.01	0.015	0.077	N.d.	N.d.	N.d.	0.068	0.868	0.202	N.d.	N.d.	N.d.	N.d.	N.d.	N.d.	N.d.	N.d.	N.d.
CdV 80.80B	0.016	0.017	0.051	0.032	N.d.	N.d.	0.083	0.849	0.038	N.d.	N.d.	N.d.	N.d.	N.d.	0.017	N.d.	0.075	0.016
CdV 112.00B	0.012	0.018	0.053	N.d.	N.d.	N.d.	0.099	0.201	N.d.	N.d.	N.d.	N.d.	N.d.	N.d.	N.d.	N.d.	N.d.	N.d.
CdV 113.15B	0.005	0.018	0.057	N.d.	N.d.	N.d.	0.067	0.071	0.068	N.d.	N.d.	N.d.	N.d.	N.d.	N.d.	N.d.	0.038	N.d.
CdV 116.00B	0.007	0.023	0.043	N.d.	N.d.	N.d.	0.09	0.412	N.d.	N.d.	N.d.	N.d.	N.d.	N.d.	0.04	N.d.	0.05	N.d.
CdV 26.80W	N.d.	0.345	N.d.	N.d.	N.d.	N.d.	N.d.	N.d.	0.018	N.d.	N.d.	N.d.	N.d.	N.d.	N.d.	0.006	N.d.	N.d.
CdV 27.00W	N.d.	0.094	N.d.	N.d.	0.042	0.429	N.d.	0.066	N.d.	N.d.	N.d.	0.192	N.d.	0.207	N.d.	0.018	N.d.	N.d.
CdV 28.00W	N.d.	0.187	N.d.	N.d.	N.d.	N.d.	N.d.	0.219	N.d.	N.d.	N.d.	N.d.	N.d.	N.d.	N.d.	0.018	N.d.	0.078
CdV 42.85W	0.032	0.05	N.d.	N.d.	N.d.	0.135	N.d.	N.d.	0.42	N.d.	N.d.	N.d.	N.d.	N.d.	N.d.	N.d.	N.d.	N.d.
CdV 45.60W	N.d.	0.075	N.d.	N.d.	N.d.	N.d.	0.097	0.159	0.035	N.d.	N.d.	N.d.	N.d.	N.d.	N.d.	N.d.	N.d.	N.d.
CdV 80.25W	0.067	0.02	N.d.	N.d.	N.d.	N.d.	N.d.	0.569	0.065	0.013	N.d.	N.d.	N.d.	N.d.	N.d.	N.d.	N.d.	N.d.
CdV 80.80W	0.025	0.045	N.d.	N.d.	N.d.	N.d.	N.d.	0.192	N.d.	N.d.	N.d.	N.d.	N.d.	N.d.	N.d.	N.d.	N.d.	N.d.
CdV 112.00W	0.036	0.024	N.d.	N.d.	N.d.	N.d.	0.129	0.192	N.d.	N.d.	N.d.	N.d.	N.d.	N.d.	N.d.	N.d.	N.d.	N.d.
CdV 113.15W	N.d.	0.031	N.d.	N.d.	N.d.	N.d.	N.d.	0.037	0.114	0.029	N.d.	N.d.	N.d.	N.d.	N.d.	N.d.	N.d.	N.d.
CdV 116.00W	N.d.	0.024	N.d.	N.d.	N.d.	N.d.	0.04	0.225	N.d.	N.d.	N.d.	N.d.	N.d.	N.d.	N.d.	N.d.	N.d.	N.d.

Minor elements present in the chemical analysis of CdV Partial samples, in %. N.d. - Not detected.

(%)	MgO	Al2O3	SiO2	P2O5	K2O	CaO	TiO2	MnO	Fe2O3	NiO	Na2O	Cl	SO3
CdV 125.20_1	1.731	7.69	17.988	0.92	5.592	16.193	2.42	0.454	45.264	0.099	0.031	0.451	N.d.
CdV 125.20_2	1.177	6.298	22.085	1.735	3.281	26.089	5.454	0.256	32.392	0.142	0.029	0.233	N.d.
CdV 125.20_3	1.448	5.742	35.471	1.7	6.224	15.865	2.46	0.198	29.204	0.202	0.151	0.195	0.044

Major elements form the chemical analysis of CdV125.20_1 to 3 samples, in %. N.d. - Not detected.

(%)	Br	SrO	PdO	As2O3	BaO	CeO2	Co3O4	Cr2O3	CuO	Ga2O3	HfO2	La2O3	Nb2O5	Nd2O3	PbO	Rb2O	V2O5	ZrO2	ZnO
CdV 125.20_1	0.009	0.378	0.086	N.d.	0.084	0.185	0.074	0.113	0.031	0.017	N.d.	N.d.	N.d.	N.d.	N.d.	0.027	0.125	N.d.	0.038
CdV 125.20_2	0.01	0.375	0.073	N.d.	0.153	N.d.	N.d.	N.d.	0.036	0.011	N.d.	N.d.	0.016	N.d.	N.d.	0.017	N.d.	0.117	0.019
CdV 125.20_3	N.d.	0.279	0.043	N.d.	0.093	0.115	N.d.	0.188	N.d.	0.01	0.05	N.d.	N.d.	N.d.	N.d.	0.067	0.124	0.099	0.031

Minor elements present in the chemical analysis of CdV125.20_1 to 3 samples, in %. N.d. - Not detected.

3 – Attenuated Total Reflectance Fourier-transform Infrared Spectroscopy (ATR - FTIR)

Partial Samples B – Representative of the matrix of the samples

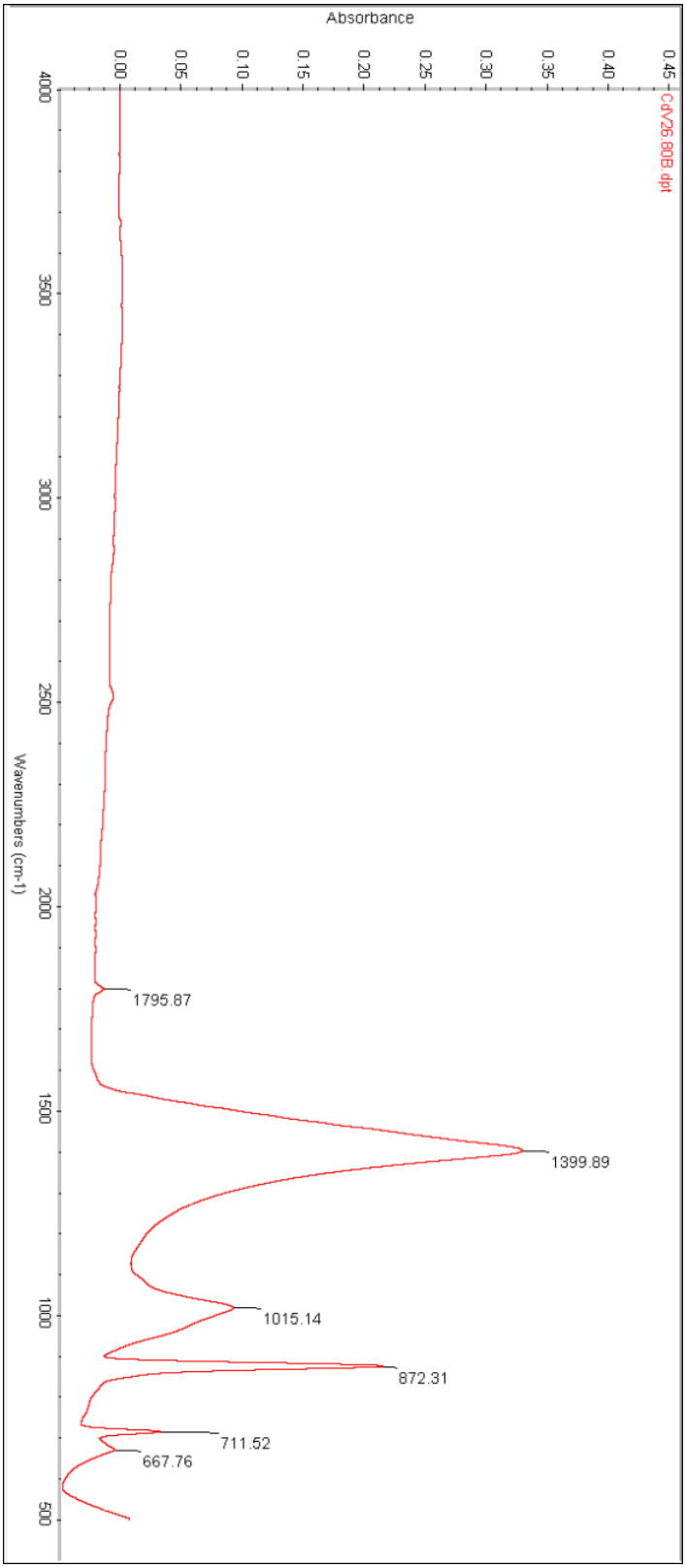

FTIR spectra of partial sample CdV26.80B.

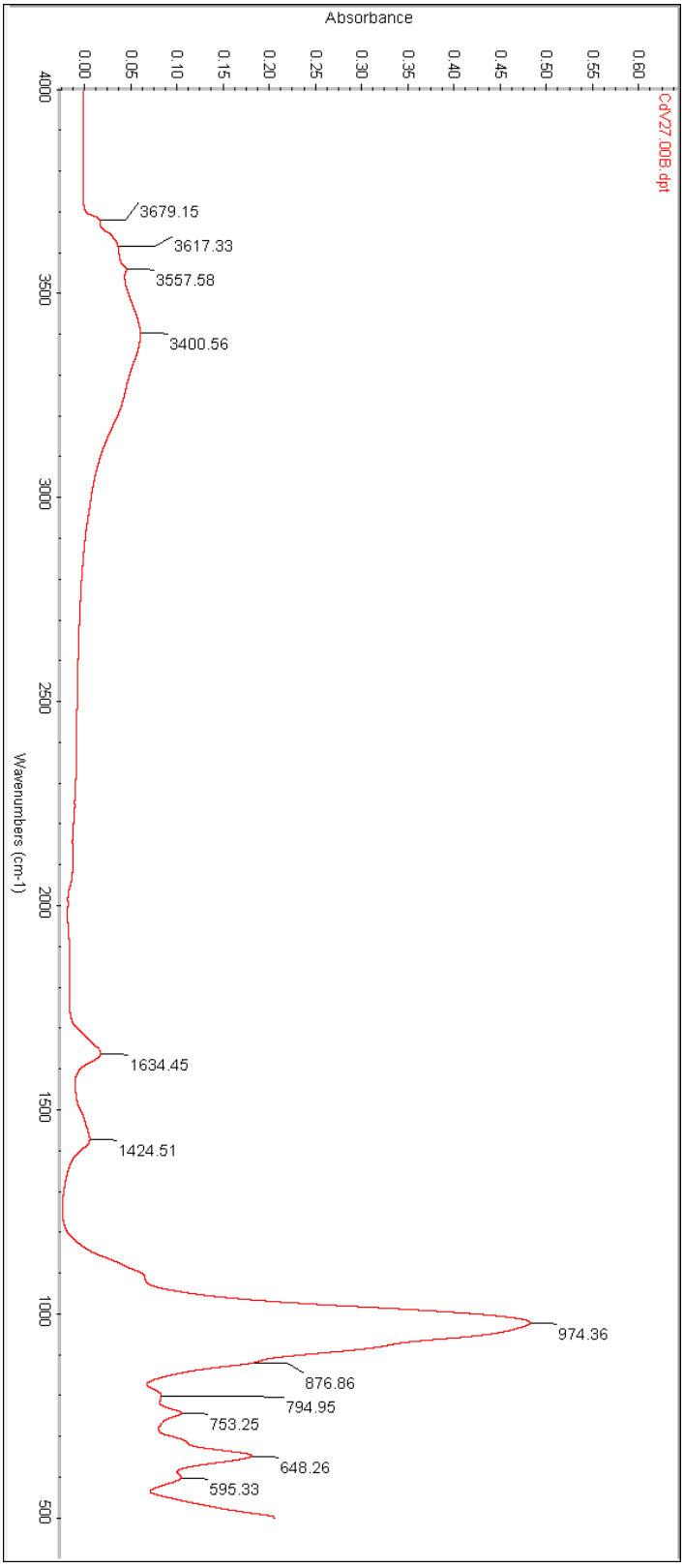

FTIR spectra of partial sample CdV27.00B.

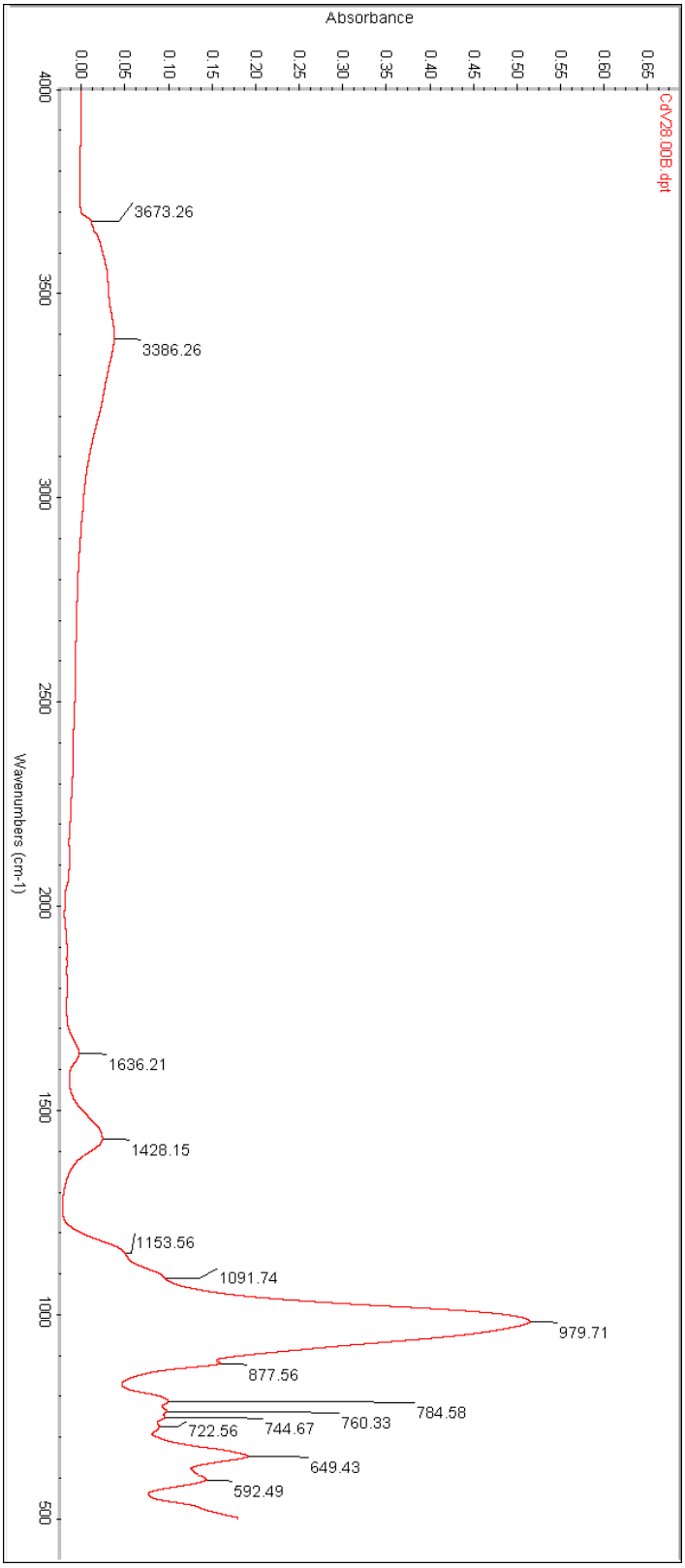

FTIR spectra of partial sample CdV28.00B.

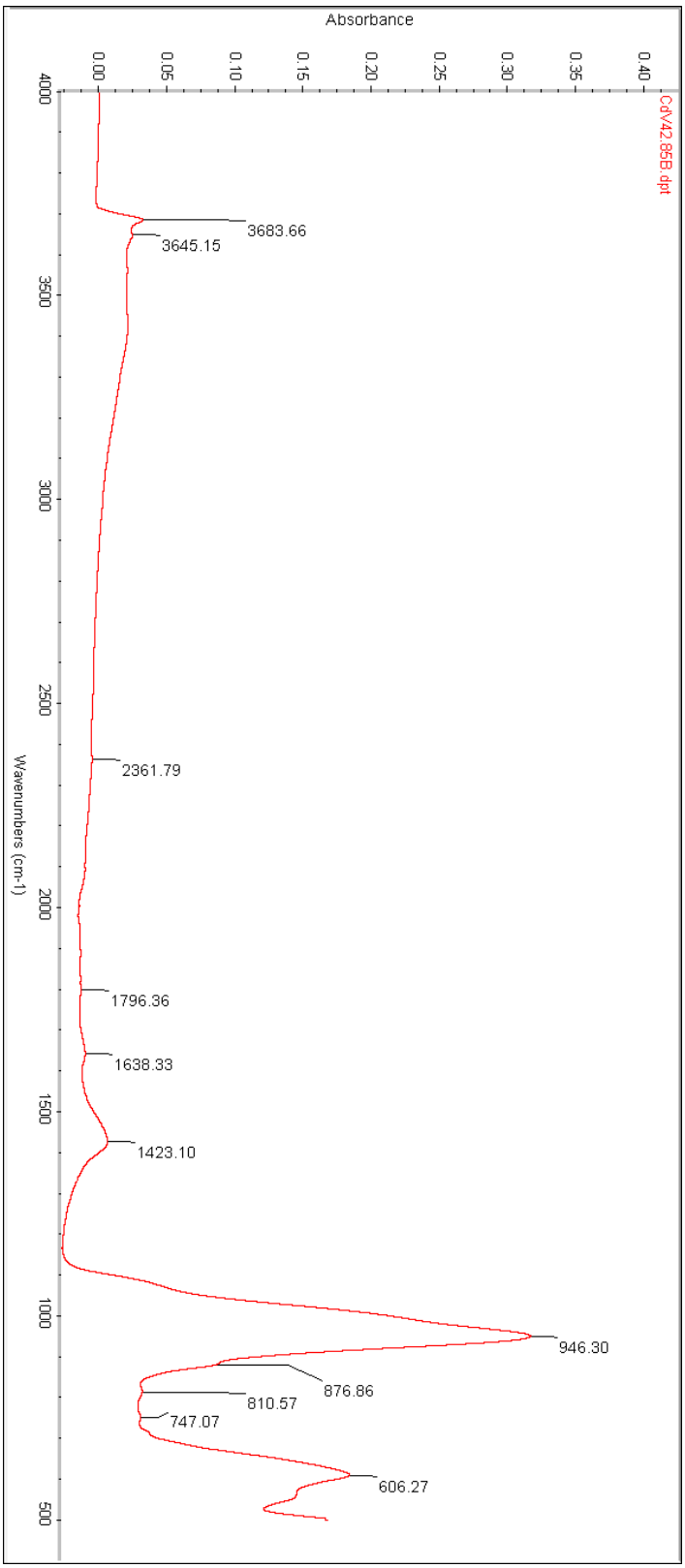

FTIR spectra of partial sample CdV42.85B.

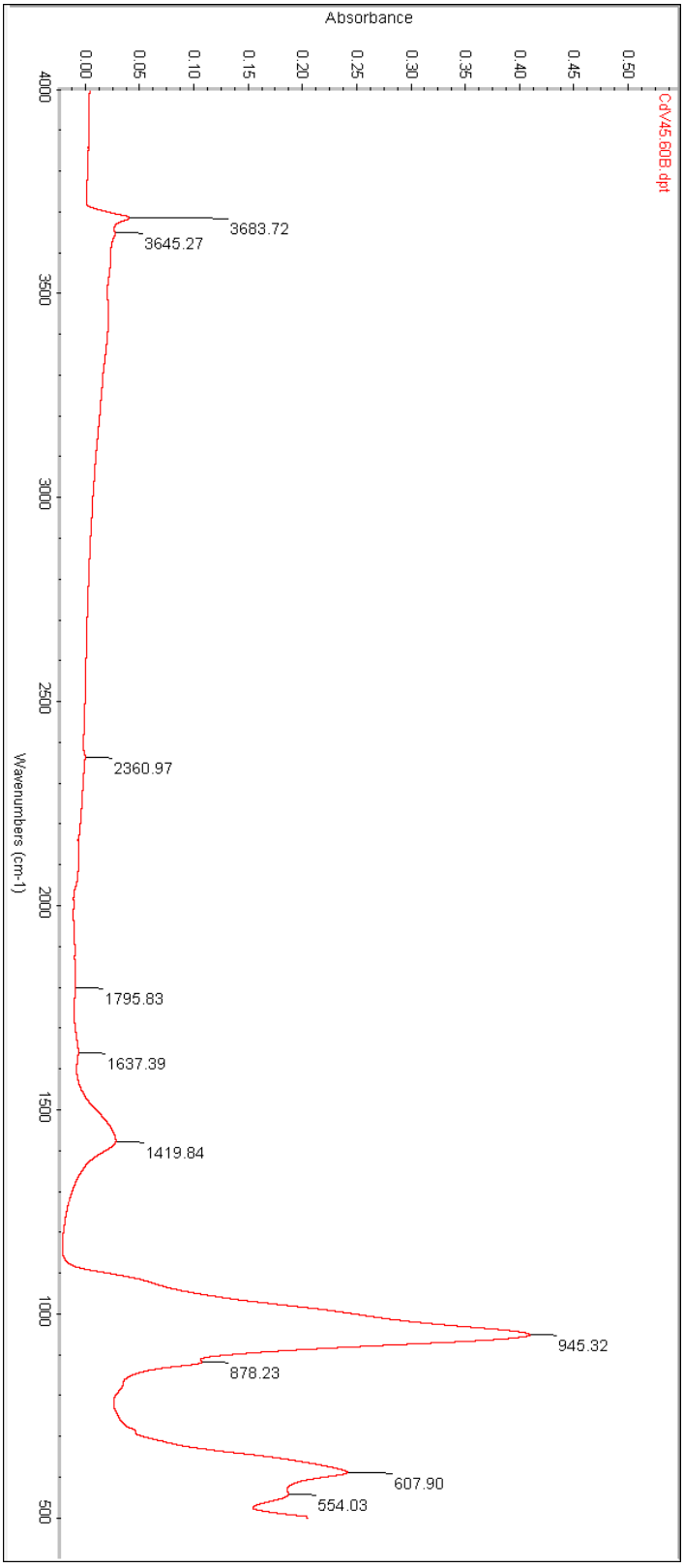

FTIR spectra of partial sample CdV45.60B.

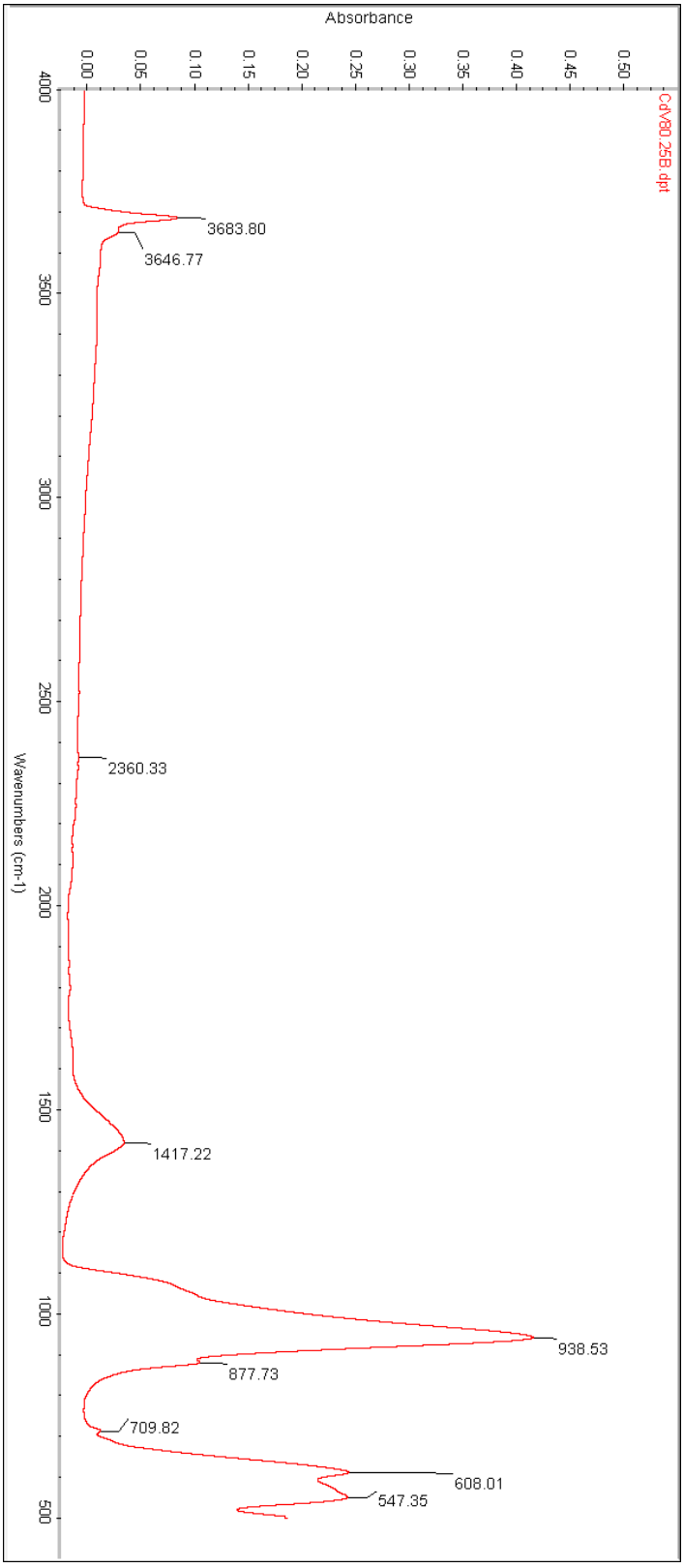

FTIR spectra of partial sample CdV80.25B.

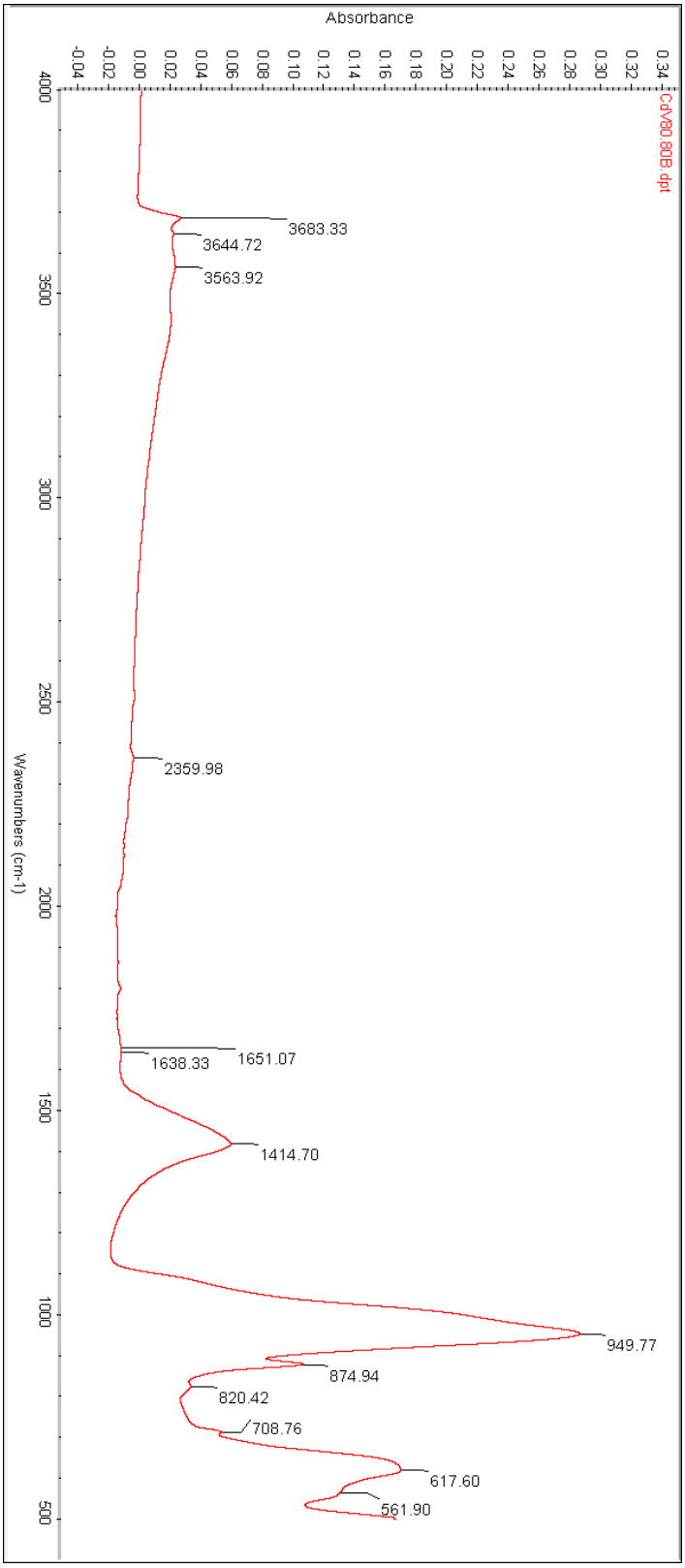

FTIR spectra of partial sample CdV80.80B.

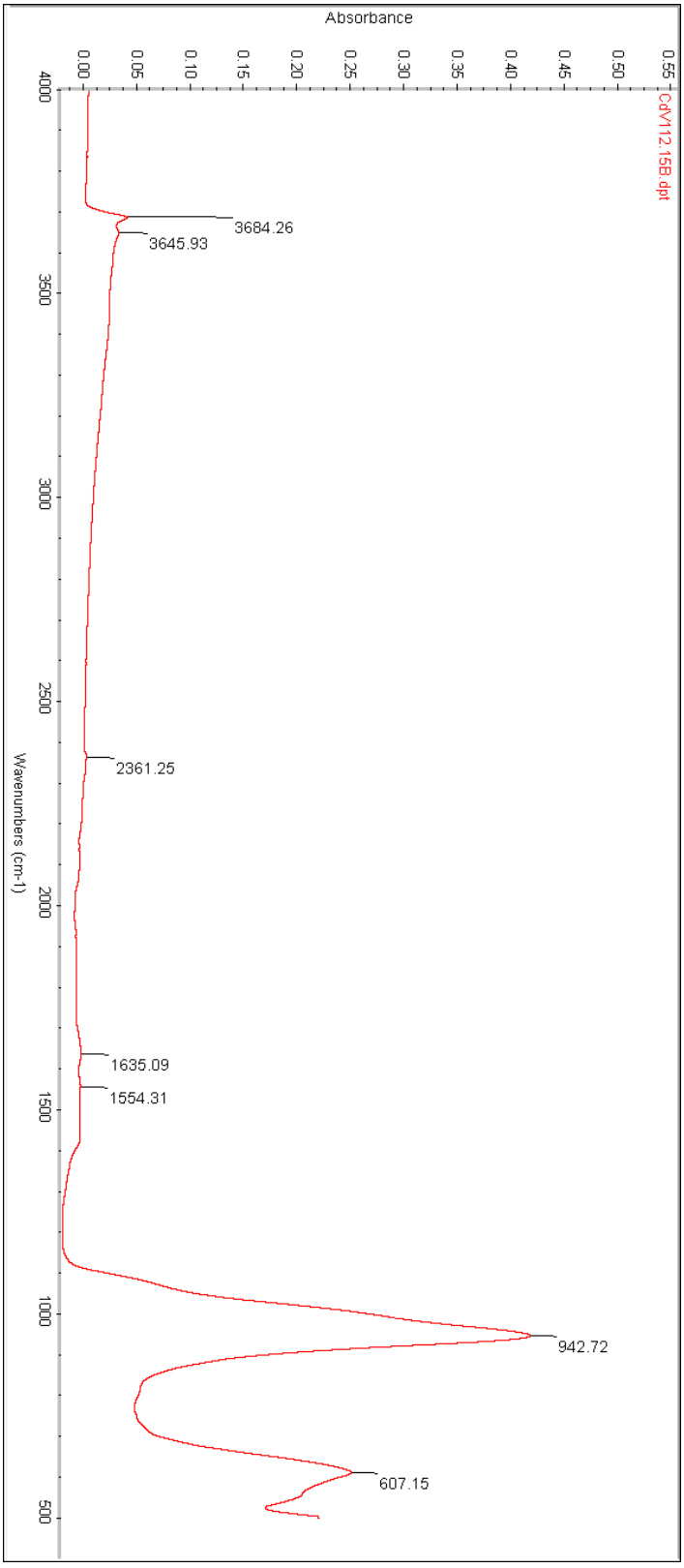

FTIR spectra of partial sample CdV112.00B

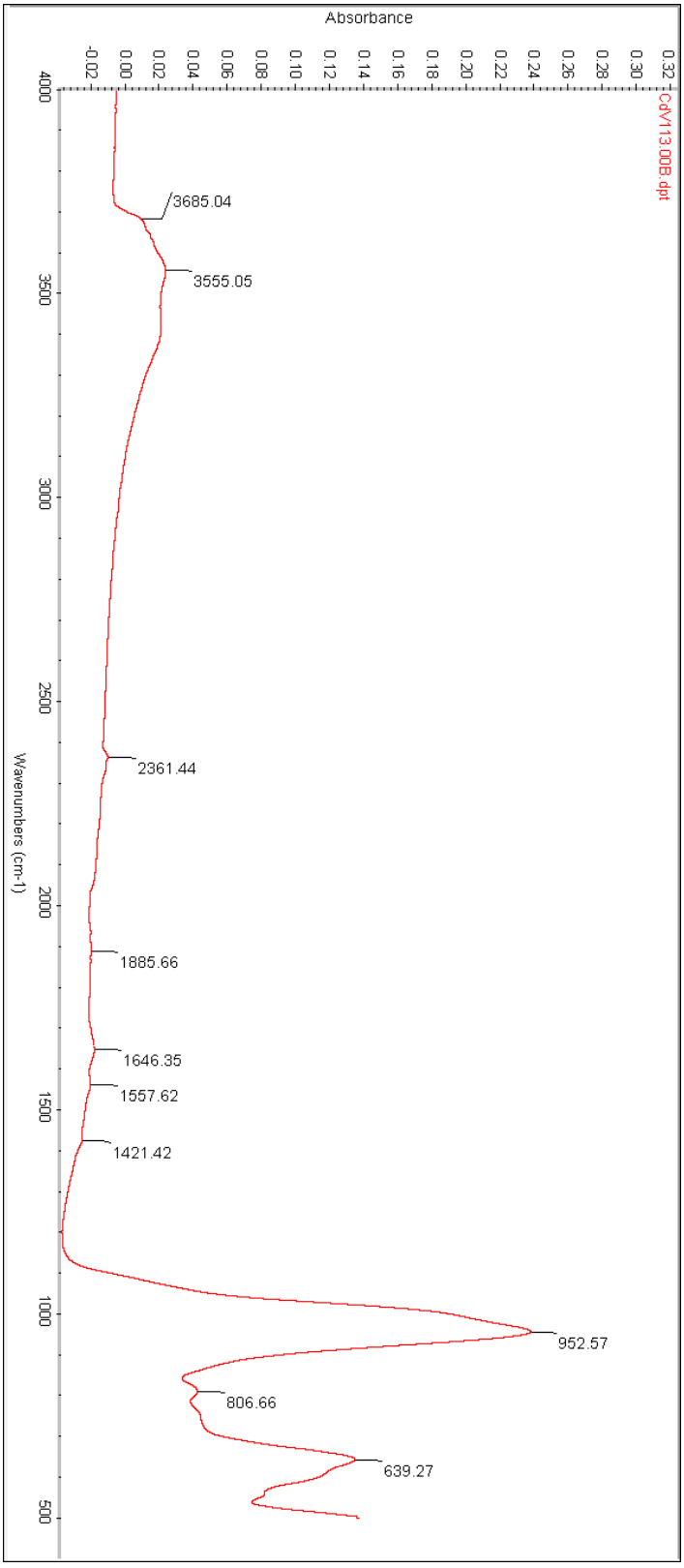

FTIR spectra of partial sample CdV113.15B.

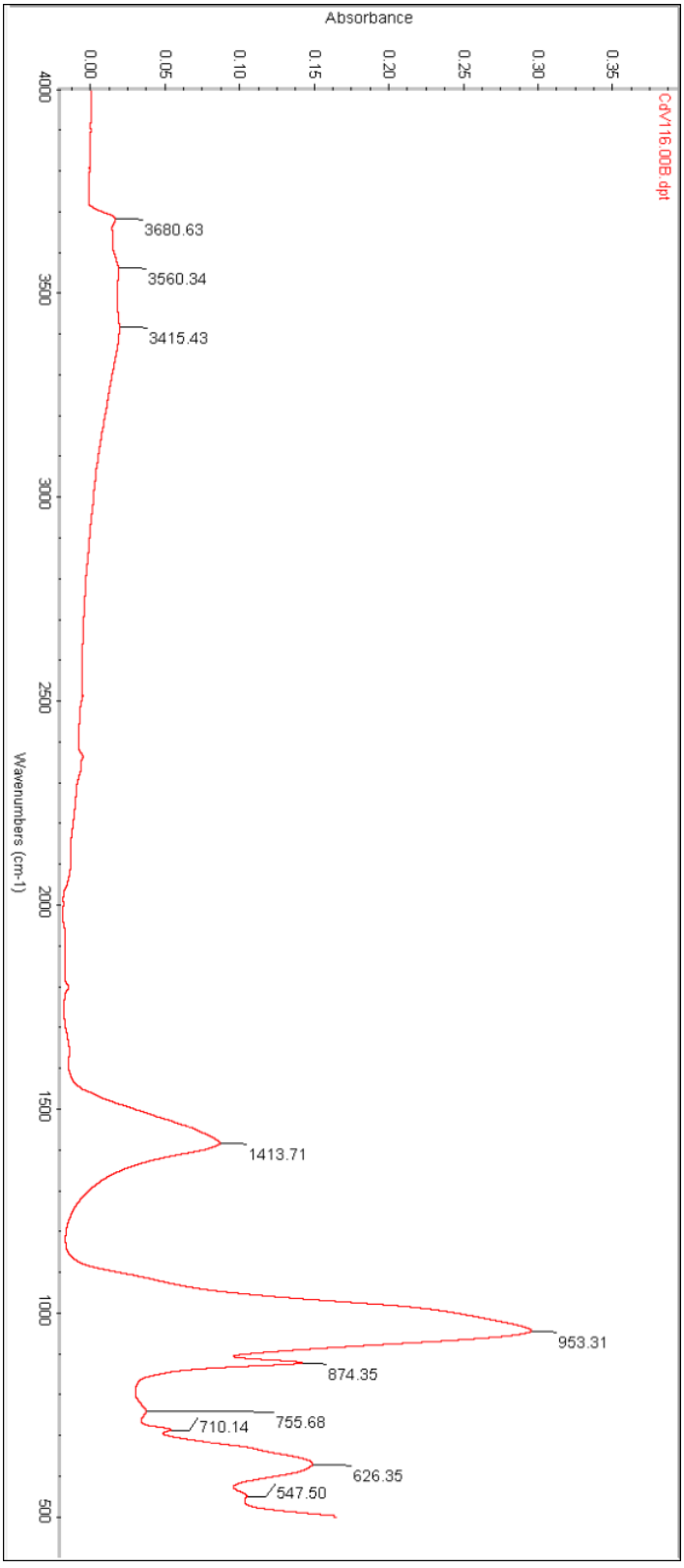

FTIR spectra of partial sample CdV116.00B.

Partial Samples W – Representative of the fractures in the samples

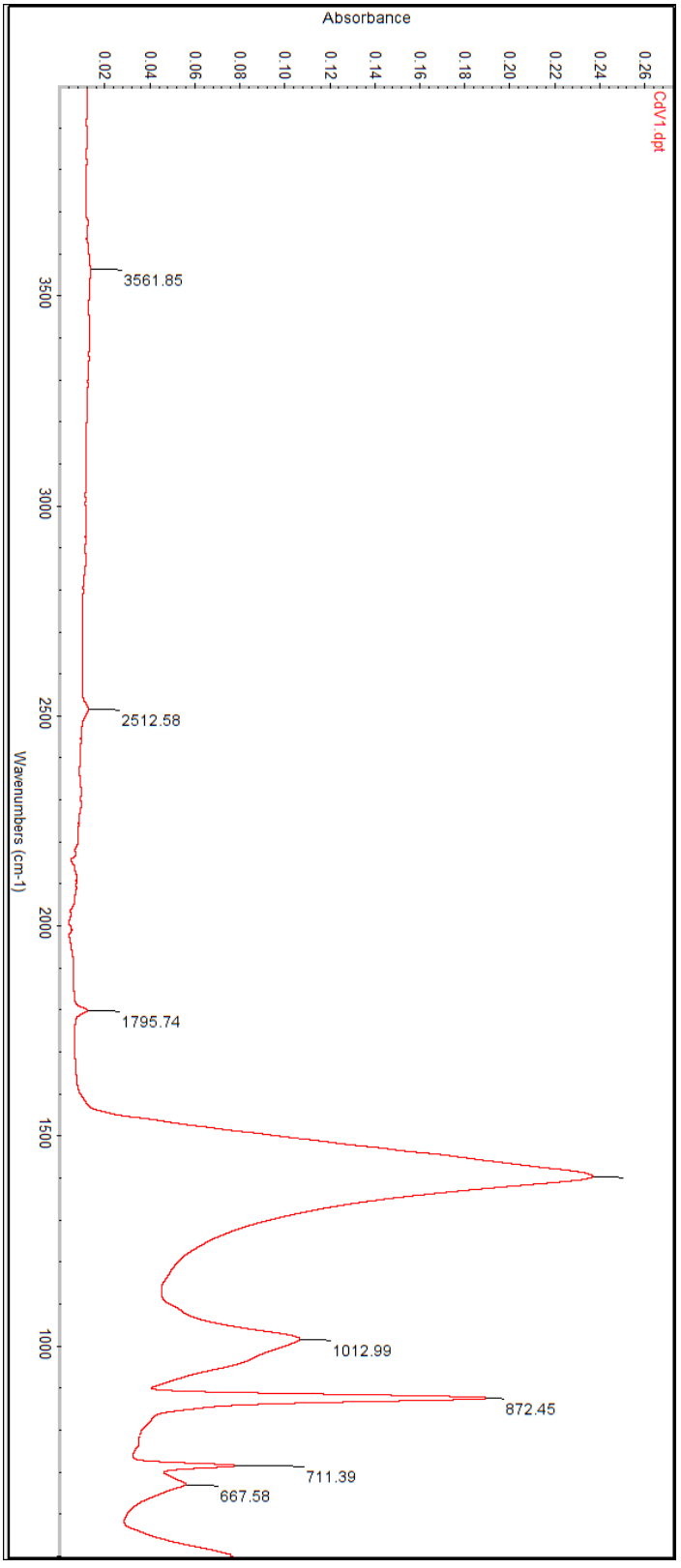

FTIR spectra of partial sample CdV26.80W.

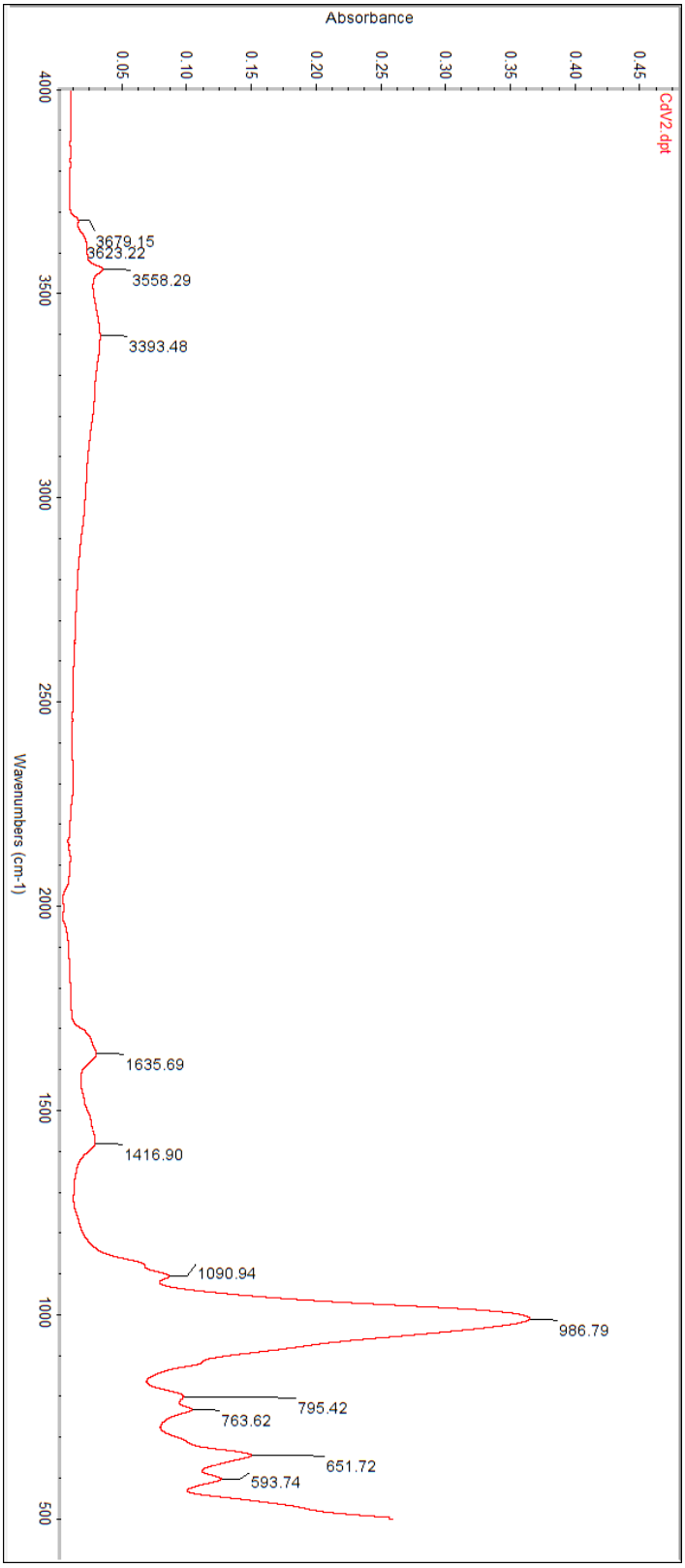

FTIR spectra of partial sample CdV27.00W.

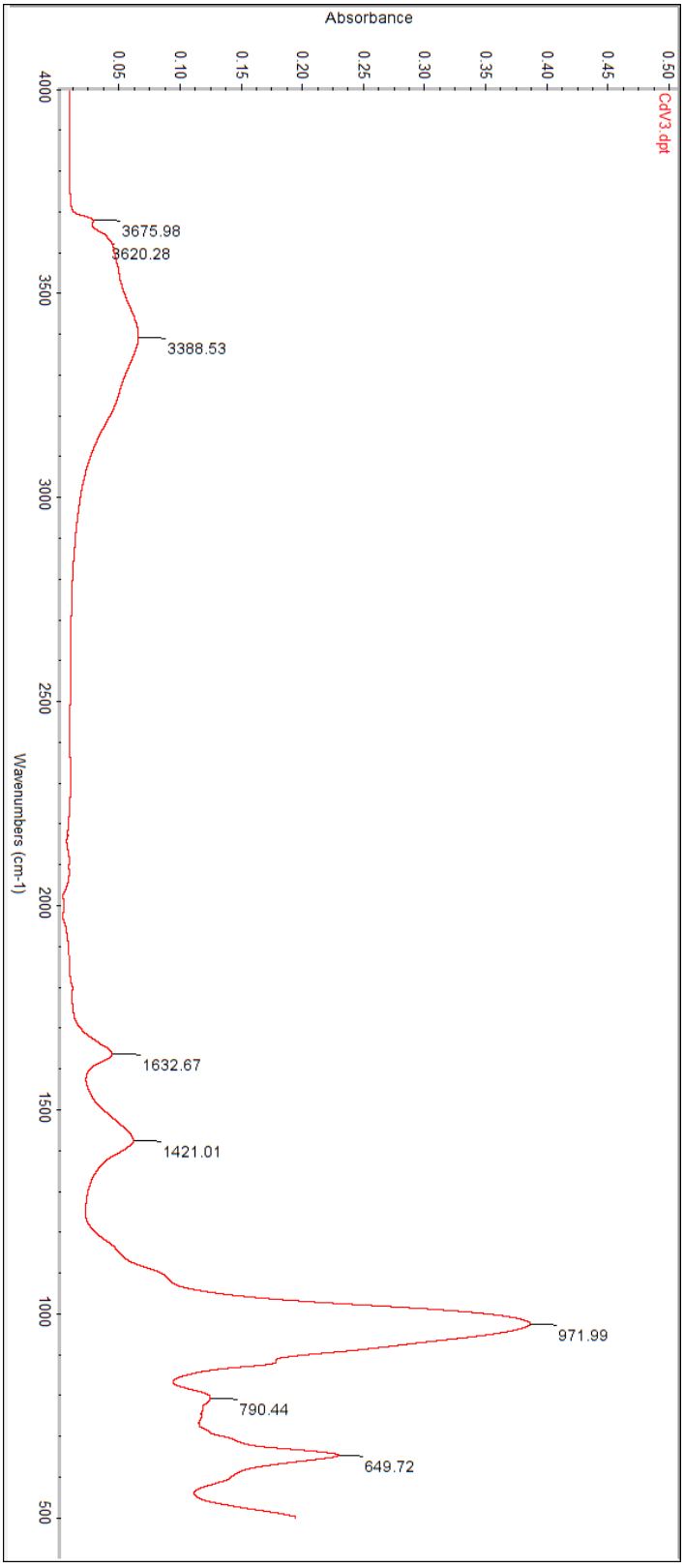

FTIR spectra of partial sample CdV28.00W.

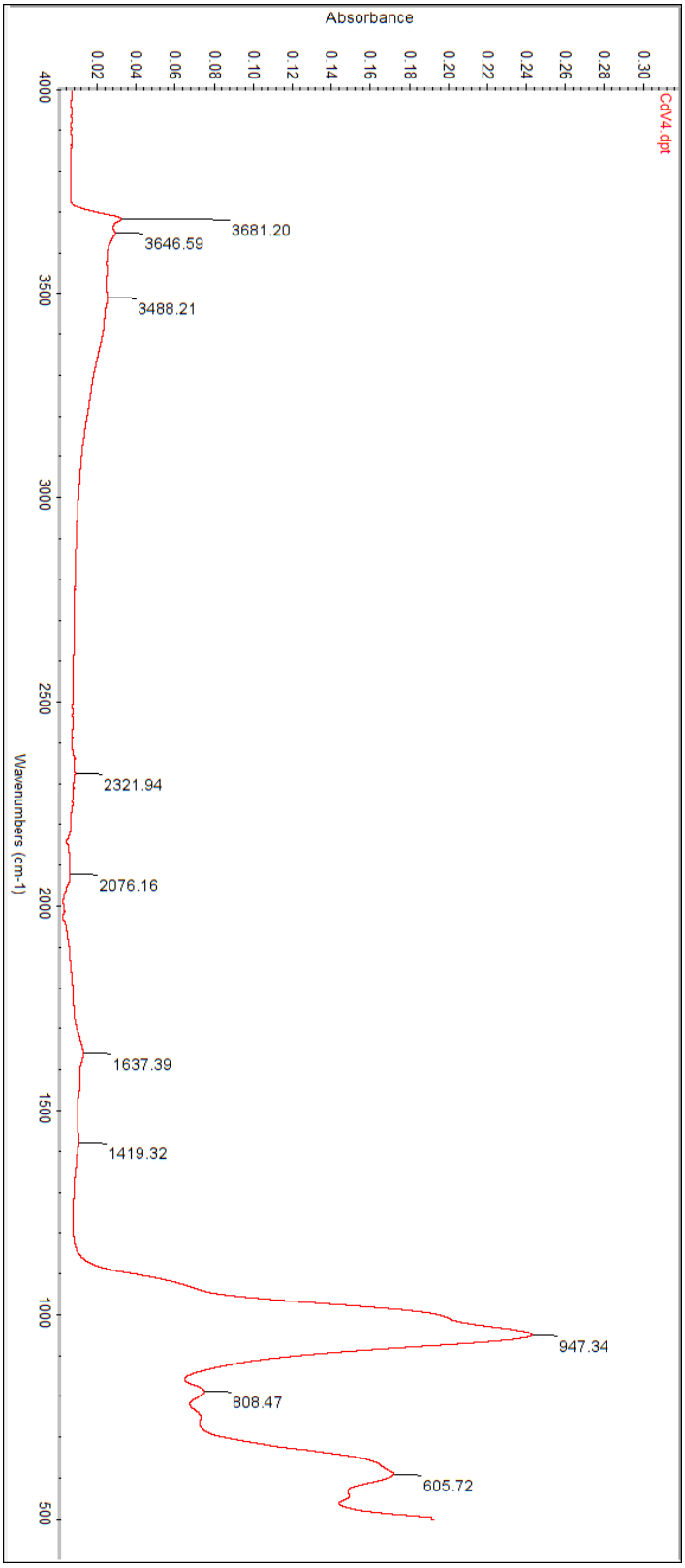

FTIR spectra of partial sample CdV42.85W.

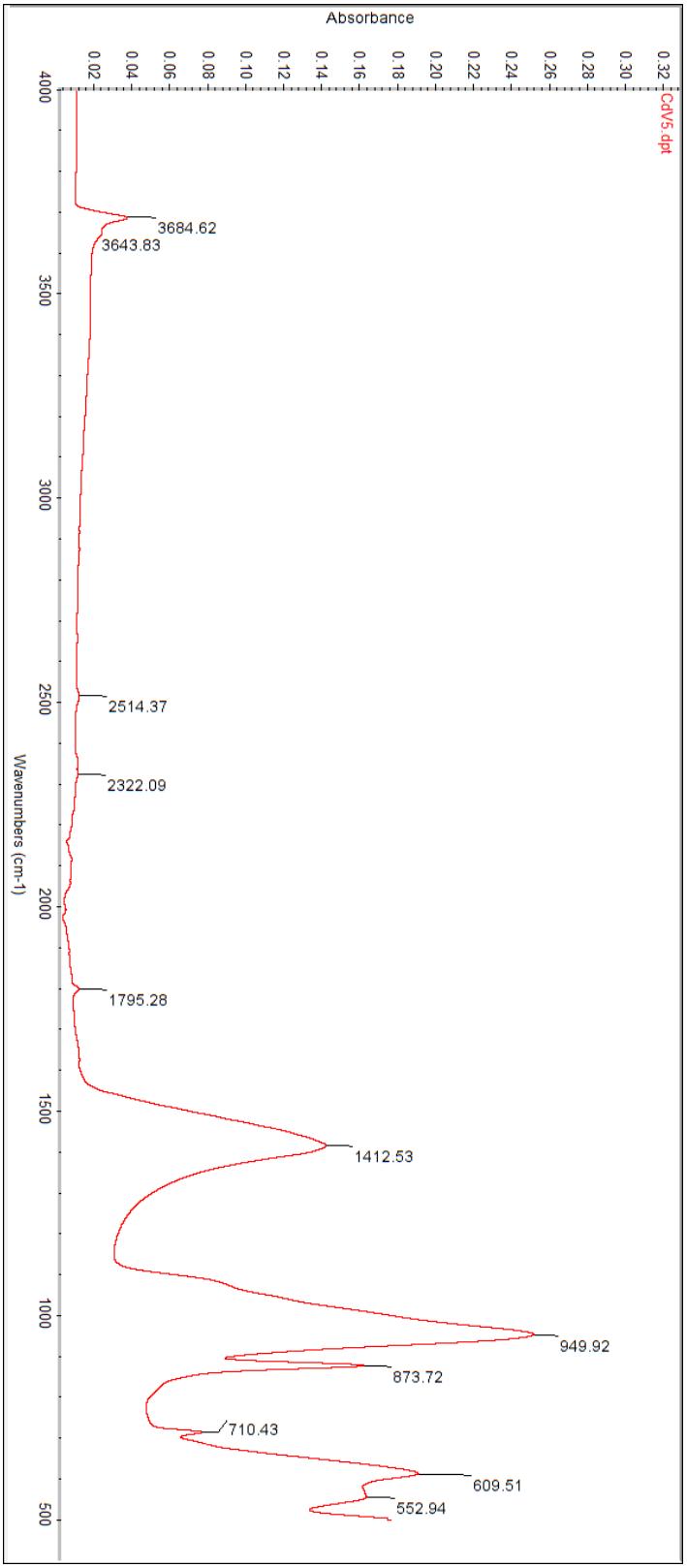

FTIR spectra of partial sample CdV45.60W.

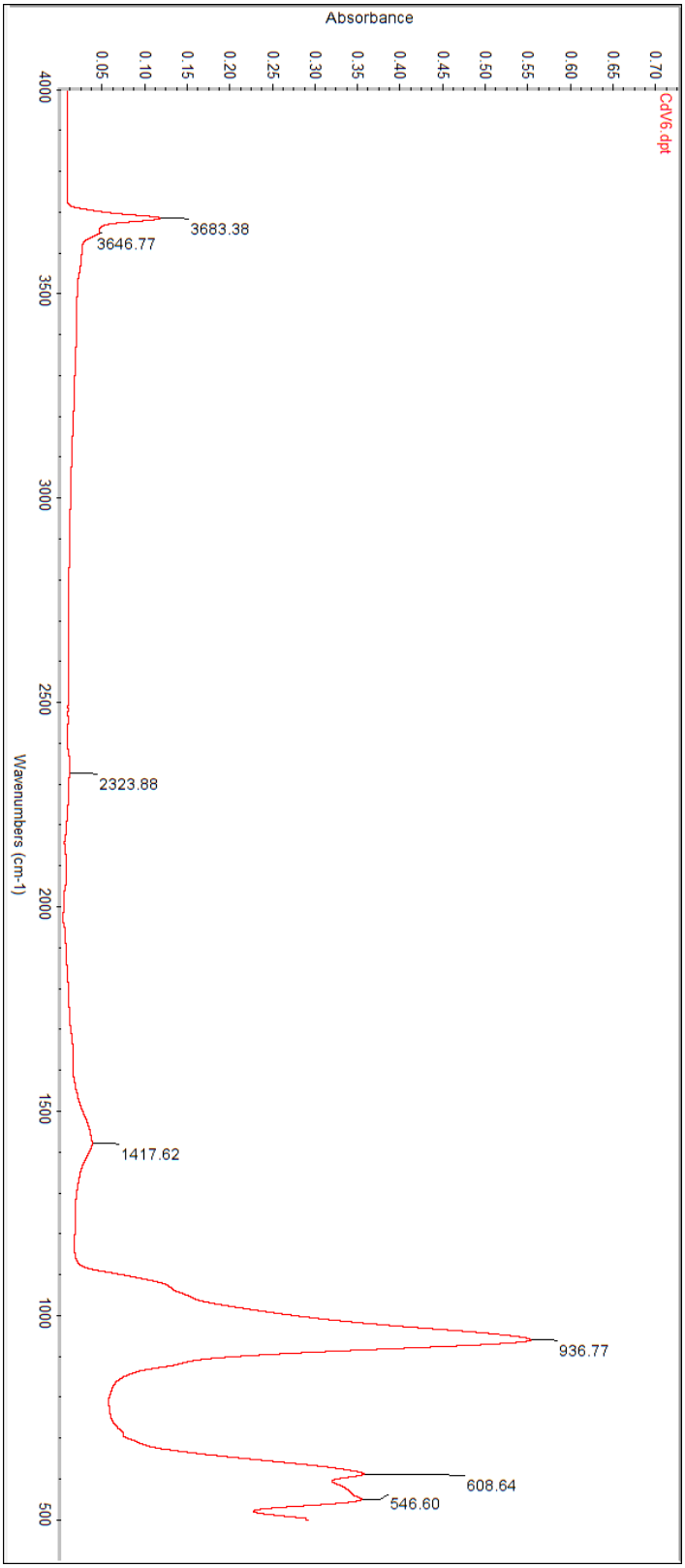

FTIR spectra of partial sample CdV80.25W.

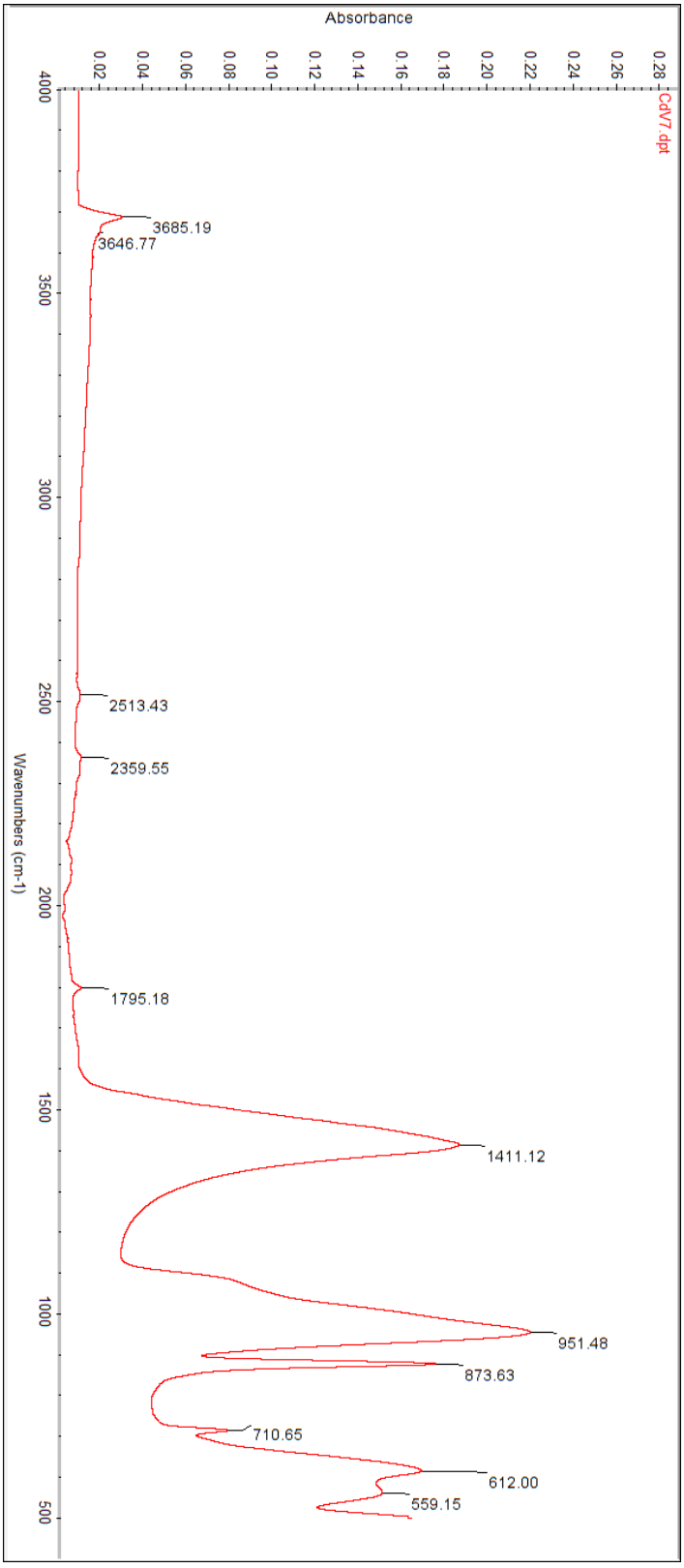

FTIR spectra of partial sample CdV80.80W.

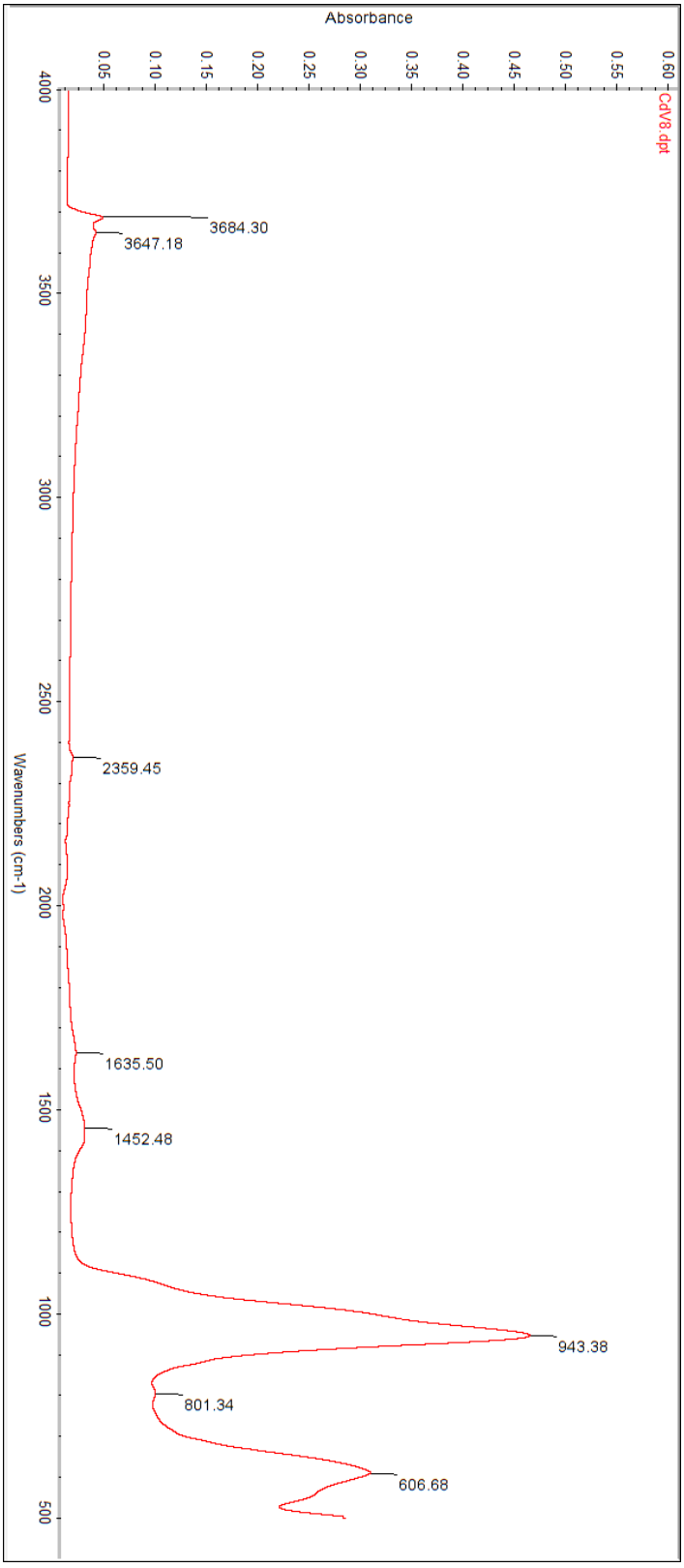

FTIR spectra of partial sample CdV112.00W.

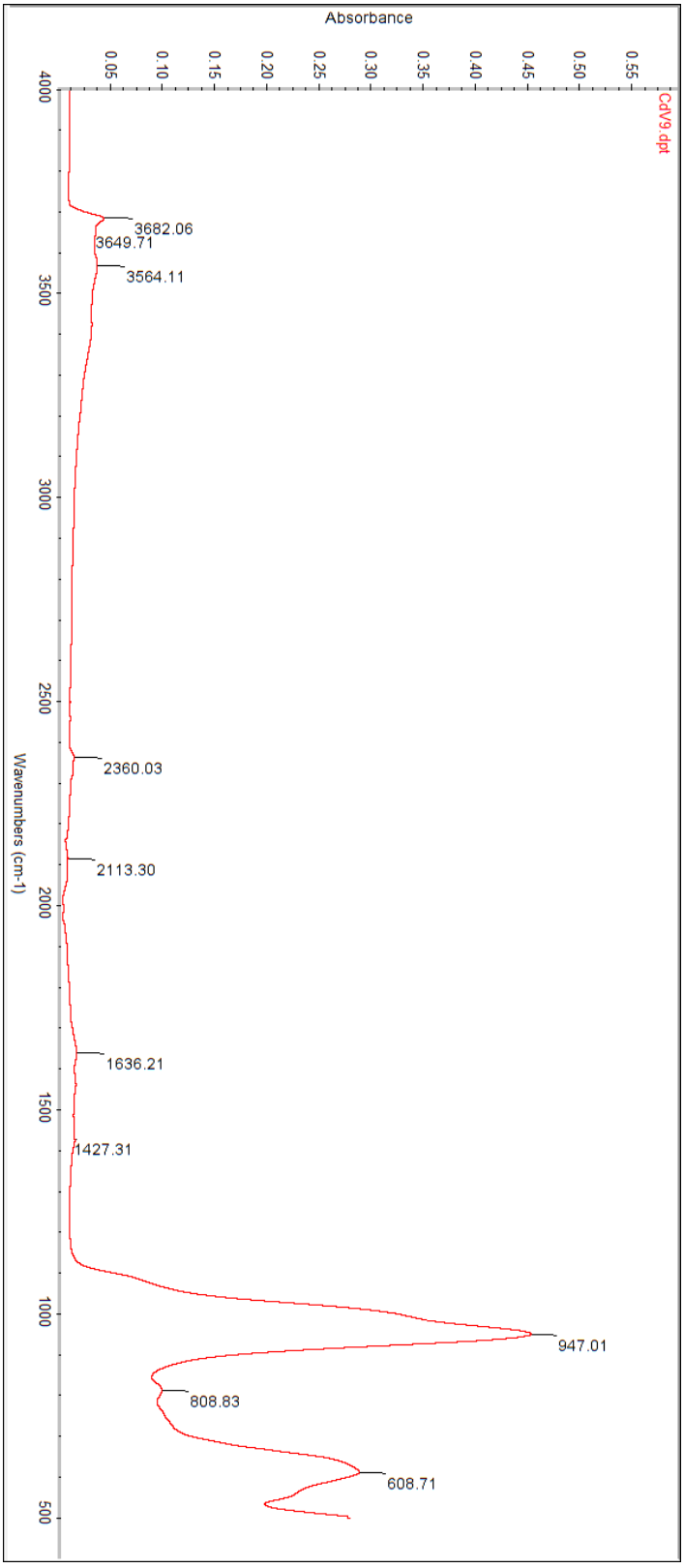

FTIR spectra of partial sample CdV113.15W.

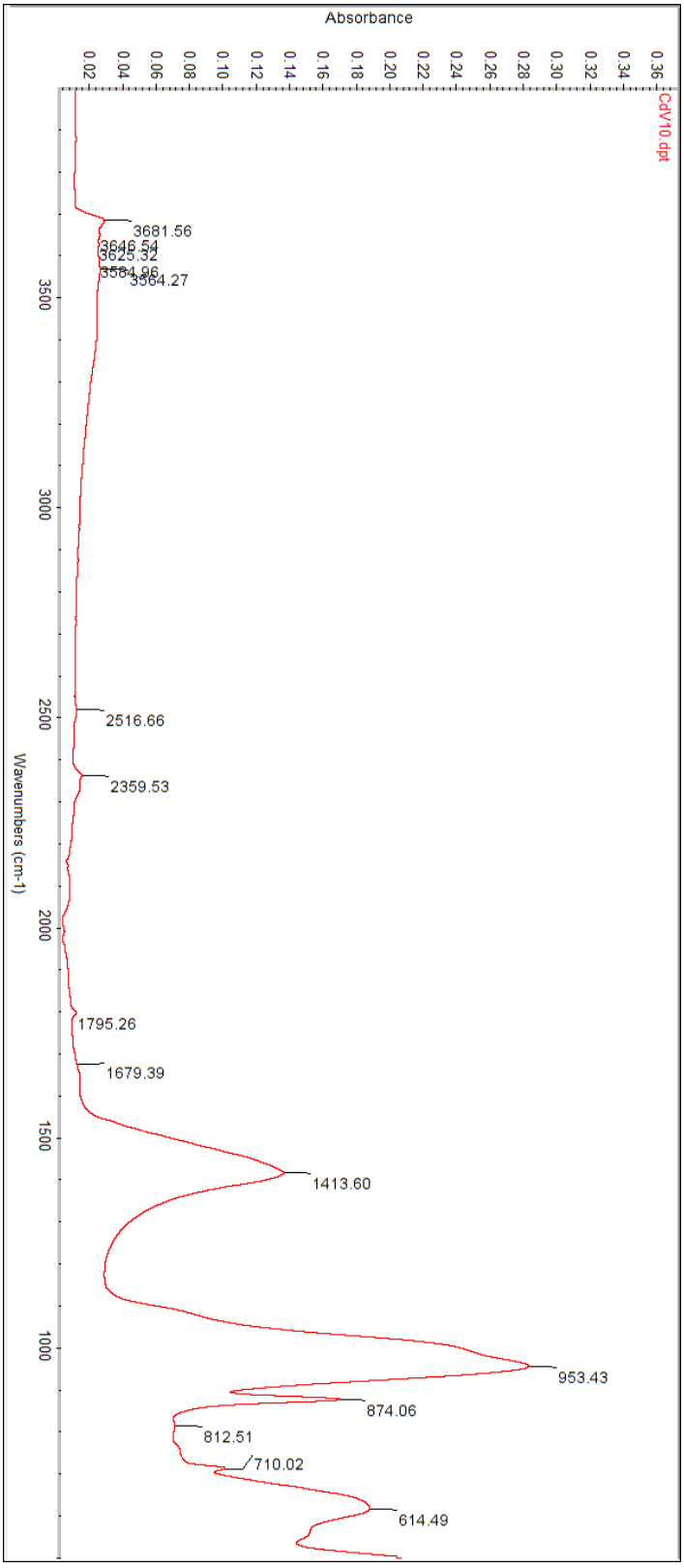

FTIR spectra of partial sample CdV116.00W.